

NUMERICAL AND EXPERIMENTAL ANALYSIS OF FLAPPING MOTION IN  
HOVER. APPLICATION TO MICRO AIR VEHICLES.

A THESIS SUBMITTED TO  
ECOLE DOCTORALE DES SCIENCES POUR L'INGENIEUR  
OF  
ECOLE NATIONALE SUPERIEURE DE MECANIQUE ET  
D'AEROTECHNIQUE  
AND  
THE GRADUATE SCHOOL OF NATURAL AND APPLIED SCIENCES  
OF  
MIDDLE EAST TECHNICAL UNIVERSITY

BY

DİLEK FUNDA KURTULUŞ

IN PARTIAL FULFILLMENT OF THE REQUIREMENTS FOR  
THE DEGREE OF DOCTEUR DE L'UNIVERSITE DE POITIERS  
IN  
MECANIQUE DES MILIEUX FLUIDES

AND

THE DEGREE OF DOCTOR OF PHILOSOPHY  
IN  
AEROSPACE ENGINEERING

JUNE 2005

Approval of the Graduate School of Natural and Applied Sciences

---

Prof. Dr. Canan ÖZGEN

Director

I certify that this thesis satisfies all the requirements as a thesis for the degree of Doctor of Philosophy.

---

Prof. Dr. Nafiz ALEMDAROĞLU

Head of Department

This is to certify that we have read this thesis and that in our opinion it is fully adequate, in scope and quality, as a thesis for the degree of Doctor of Philosophy.

---

Dr. Alain FARCY

Supervisor

---

Prof. Dr. Nafiz ALEMDAROĞLU

Supervisor

Examining Committee Members

Prof. Dr. Roland Decuyper (RMA, Bruxelles) \_\_\_\_\_

Prof. Dr. Kahraman Albayrak(METU, ME, Ankara) \_\_\_\_\_

Prof. Dr. Malik Ba (ENSMA, LEA,Poitiers)\_\_\_\_\_

Prof. Dr. Yusuf Özyörük (METU, AEE, Ankara) \_\_\_\_\_

Dr. Laurent David (Univ. de Poitiers, LEA)\_\_\_\_\_

Dr. Alain Farcy (ENSMA, LEA,Poitiers)\_\_\_\_\_

Prof. Dr. Nafiz Alemdaroğlu (METU, AEE, Ankara) \_\_\_\_\_

Mme. Agnès Luc-Bouhali (ONERA, Paris) \_\_\_\_\_

**I hereby declare that all information in this document has been obtained and presented in accordance with academic rules and ethical conduct. I also declare that, as required by these rules and conduct, I have fully cited and referenced all material and results that are not original to this work.**

Name, Last name : Dilek Funda Kurtuluş

Signature :

## ABSTRACT

### NUMERICAL AND EXPERIMENTAL ANALYSIS OF FLAPPING MOTION IN HOVER. APPLICATION TO MICRO AIR VEHICLES.

Kurtuluş, Dilek Funda

Ph.D, Department of Aerospace Engineering (METU)

Ph.D, LEA (ENSMA/Université de Poitiers)

Supervisor : Dr. Alain Farcy

Supervisor : Prof. Dr. Nafiz Alemdaroğlu

June 2005, 262 pages

The aerodynamics phenomena of flapping motion in hover are considered in view of the future Micro Air Vehicle applications. The aim of this work is to characterize the vortex dynamics generated by the wing in motion using direct numerical simulation and experimental analysis then to propose a simplified analytical model for prediction of the forces in order to optimize the parameters of the motion leading to maximum force. A great number of cases are investigated corresponding to different angles of attack, location of start of change of incidence, location of start of change of velocity, axis of rotation, and Re number. The airfoil used is symmetrical. The flow is assumed to be incompressible and laminar with the Reynolds numbers between 500 and 2000. The experimental results obtained by the laser sheet visualization and the Particle Image Velocimetry (PIV) techniques are used in parallel with the direct numerical simulation results for the phenomenological analysis of the flow. The model developed for the aerodynamic forces is an indicial

method based on the use of the Duhamel Integral and the results obtained by this model are compared with the ones of the numerical simulations.

Keywords: vortex (fluid mechanics), topology, visualization, unsteady aerodynamics, PIV, indicial method

## RESUME

### ETUDE NUMERIQUE ET EXPERIMENTAL DE LA SUSTENTATION PAR VOL VIBRE. APPLICATION AUX MICRO-DRÔNES

Kurtuluş, Dilek Funda

Ph.D, Department of Aerospace Engineering (METU)

Ph.D, LEA (ENSMA/Université de Poitiers)

Superviseur : Dr. Alain Farcy

Superviseur : Prof. Dr. Nafiz Alemdaroğlu

Juin 2005, 262 pages

Les phénomènes aérodynamiques autour d'une aile vibrante dans un fluide au repos (vol stationnaire) sont étudiés en vue des applications aux micro-drônes. L'objectif de ce travail est de caractériser la dynamique tourbillonnaire générée par l'aile en mouvement par simulation numérique directe et analyse expérimentale puis de proposer un modèle analytique simplifié de prédiction des efforts en vue, à terme, d'optimiser les paramètres du mouvement conduisant à une force de sustentation maximale. Un grand nombre de cas ont été examinés correspondant à différentes incidences, lois de vitesse en translation et en rotation, axes de rotation et nombres de Reynolds. Le profil d'aile utilisé est symétrique. L'écoulement est incompressible, laminaire pour des nombres de Reynolds compris entre 500 et 2000. Les résultats expérimentaux, obtenus par visualisation par plan laser et technique anémométrique PIV, sont utilisés conjointement avec les résultats de simulation numérique directe pour l'analyse phénoménologique de l'écoulement. Le modèle développé pour les efforts aérodynamiques est une méthode indicielle basée sur l'utilisation d'intégrales

de Duhamel ; les résultats obtenus par ce modèle sont comparés à ceux des simulations numériques.

Mots-clés : tourbillon (mécanique des fluides), topologie, visualisation aérodynamique instationnaire, PIV, méthode indicielle

## ÖZ

### HAVADA ASILI KONUMDAKİ ÇIRPAN KANAT PROFİLİNİN SAYISAL VE DENEYSEL ANALİZİ. MİKRO HAVA ARAÇLARI'NA UYUGULAMASI.

Kurtuluş, Dilek Funda

Ph.D, Havacılık ve Uzay Mühendisliği Bölümü (METU)

Ph.D, LEA (ENSMA/Université de Poitiers)

Tez Yöneticisi : Dr. Alain Farcy

Tez Yöneticisi : Prof. Dr. Nafiz Alemdaroğlu

Haziran 2005, 262 sayfa

Mikro Hava Araçları'nın geliştirilmesine yönelik havada asılı durumda çırpan kanat hareketinin aerodinamiği incelenmiştir. Bu çalışmadaki amaç, kanat hareketi ile oluşan girdap dinamiğinin direk sayısal simülasyon ve deneysel analizlerle karakterize edilmesi ve maximum kuvveti oluşturacak parametrelerin optimize edilmesi için aerodinamik kuvvetlerin hesaplanabileceği bir analitik modelin oluşturulmasıdır. Hücum açısı, hücum açısı değişme zamanı, hız değişme zamanı, dönme eksen ve Re sayısı değişimleri gibi birçok durum incelenmiştir. Simetrik bir kanat kesiti kullanılmıştır. Akım sıkıştırılmaz ve laminar kabul edilmiş ve Reynolds sayısı 500 ile 2000 arasında alınmıştır. Akımın analizi için deneysel yöntemlerden hem lazer tabakası kullanılarak akımın görüntülemesi yapılmış hem de PIV tekniği kullanılmıştır. Aerodinamik kuvvetler için yaratılmış olan model, Duhamel integrali bazlı bir indisiel metoddur ve bulunan sonuçlar sayısal sonuçlarla karşılaştırılmıştır.

Anahtar Kelimeler: girdap (akışkanlar mekaniği), topoloji, görüntüleme, zamana bağımlı aerodinamik, PIV, indisiel metod



To My Parents Aynur and Yaşar Kurtuluş and To My Brother Bedri

## ACKNOWLEDGMENTS

I wish to express my deepest gratitude to my supervisors Dr. Ing. Alain Farcy and Prof. Dr. Nafiz Alemdaroğlu, for their guidance, advice, criticism and encouragement and insight throughout the research. Without their outstanding ability as research advisors, this work would be impossible.

I also would like to thank to Dr. Laurent David for his guidance and advices during the experimental part of this study.

I would like to specially thank to the reviewers of my thesis and jury members Prof. Dr. Roland Decuypere and Prof. Dr. Kahraman Albayrak. Thanks are also extended to the members of my thesis committee; Prof. Dr. Malik Ba, and Prof. Dr. Yusuf Özyörük and Mme. Agnès Luc-Bouhali for their suggestions, comments and their time.

The technical assistance of François Paillé, Yvan Jolit, Patrice Allary, Jean-François Caperan and all the technical staff of ENSMA and SP2MI during my study is gratefully acknowledged.

I also wish to thank to Mr. Zouheir Hamrouni and all of the French Embassy staff in Turkey for their help during my Ph.D work and for the scholarship of the French Government during 3 years of my study. I also want thank to TÜBİTAK for the Ph.D. scholarship provided. I want to thank to all of my professors and friends in Aerospace Eng. Department of METU and in LEA of ENSMA and of SP2MI. My special thanks goes to Mme Françoise Tournerie, Mme Nilgün Kaplan and Mme Figen Kılıç for their help during the administrative works in France and in Turkey.

Finally, my eternal gratitude to my parents and to my brother Bedri for their endless love and support, I would not have made it this far without them.

## TABLE OF CONTENTS

PLAGIARISM .....	iii
ABSTRACT .....	iv
RESUME .....	vi
ÖZ .....	viii
DEDICATION .....	ix
ACKNOWLEDGEMENTS .....	x
TABLE OF CONTENTS .....	xi
LIST OF TABLES .....	xiv
LIST OF FIGURES .....	xvi
LIST OF SYMBOLS .....	xxv
CHAPTER	
1. INTRODUCTION .....	1
1.1 Background and Objective .....	1
1.2 Literature Survey .....	5
1.2.1 Bio-aerodynamics and Related Studies .....	5
1.2.2 Unsteady Aerodynamic Models .....	16
1.3 Present Approach and Major Goals .....	19
2. ANALYSIS OF NUMERICAL AND EXPERIMENTAL TOOLS .....	21
2.1 Geometry and Motion Definition of the Flapping Motion .....	21
2.2 Two-dimensional Numerical Simulations .....	23
2.2.1 Computational Domain .....	23
2.2.2 Boundary Conditions .....	25
2.2.3 Solver Description .....	25
2.2.4 First Numerical Tests .....	27
2.2.5 Post-Processing of DNS Results .....	28
2.2.5.1 Numerical Visualization .....	28
2.2.5.2 Vortex Identification .....	29

2.2.5.3 Aerodynamic Forces .....	34
2.3 Experimental Model.....	37
2.3.1 Dimensional Analysis .....	37
2.3.2 Displacement System for the Flapping Motion Study .....	39
2.3.3 Laser Sheet Visualization.....	47
2.3.4 Particle Image Velocimetry (PIV) .....	58
3. NUMERICAL STUDY FOR THE INFLUENCE OF DIFFERENT PARAMETERS .....	73
3.1 Configurations.....	73
3.2 Effects of Starting Angle of Attack $\alpha$ and Start of Change of Incidence Position $x_a$ .....	78
3.3 Effects of the Translational Acceleration/Deceleration Position $x_v$ .....	93
3.4 Effects of the Position of Axis of Rotation .....	97
3.5 Effects of Reynolds Number.....	101
3.6 Conclusion .....	102
4. VORTEX DYNAMICS ANALYSIS OF A REFERENCE CONFIGURATION.....	105
4.1 Introduction.....	105
4.2 Comparison of the Different Investigation Techniques.....	107
4.2.1 Experimental Visualization.....	108
4.2.2 Comparison of the Experimental (PIV) and Numerical vorticity/Q values.....	123
4.3 Identification of the Vortices in terms of Pressure Coefficients and Aerodynamic Forces .....	127
4.4 Conclusion .....	134
5. ANALYTICAL MODEL OF FLAPPING MOTION.....	135
5.1 Introduction.....	135
5.2 Choice of Coordinates.....	142
5.3 Formulation of the Problem .....	142
5.4 Results .....	153
5.4.1 Duhamel Integral with Wagner Function.....	153
5.4.2 Duhamel Integral with Wagner Function using DNS results	160

5.4.3 Duhamel Integral with Wagner and Kussner Function by use of Rankine-Froude Momentum Jet using DNS Results .....	163
5.4.4 Discussion of the Results for High Angles of Attack .....	171
5.4.5 Conclusion .....	182
6. CONCLUSION .....	183
6.1 Objective of the Study and the Analysis Tools .....	183
6.2 General Conclusion .....	184
6.3 Perspective .....	185
REFERENCES .....	187
APPENDICES .....	195
A. PRELIMINARY TESTS .....	195
B. DIMENSIONAL ANALYSIS AND SIMILITUDE .....	207
C. EXPERIMENTAL SETUP DETAILS .....	209
D. VISUALIZATIONS OF THE CASE STUDY .....	213
CURRICULUM VITAE .....	262

## LIST OF TABLES

### TABLES

Table 1.1 Different Micro Air Vehicle concepts in DGR-ONERA competition.....	3
Table 1.2 Re number and reduced frequency similitude of Dickinson’s papers about Drosophila.....	8
Table 1.3 Dimensions and parameters calculated by actuator disk theory for some birds and insects performing normal hovering .....	12
Table 2.1 Control parameters.....	27
Table 2.2 Dimensional analysis .....	37
Table 2.3 Similitude results for different Re numbers for air (1) and water (2)....	39
Table 2.4 Comparison of the velocities and periods in air and water for different cases studied.....	39
Table 2.5 Definition of different commands for both of the step motors .....	45
Table 2.6 Experimental periods for Re=1000.....	51
Table 2.7 Image magnification of two CCD cameras.....	61
Table 2.8 Overview of PIV measurements .....	72
Table 3.1 Constants used in the numerical calculations .....	74
Table 3.2 The matrix of the parameter study .....	74
Table 3.3 Case studies (results for configurations in air) .....	74
Table 3.4 Some specifications of the case studies for Re=1000, $x_{T/4}=3c$ .....	77
Table 3.5 Maximum lift and drag coefficients and the maximum angular velocities corresponding to different angles of attack for Re=1000, $x_v=2c$ .....	92
Table 3.6 DNS average force and force coefficient results for different cases for Re=1000 during 7 <sup>th</sup> period with center of rotation at $a=1/4$ .....	102
Table 3.7 DNS average force and force coefficient results for different cases for Re=1000, $x_v=2c$ with a stroke period of 0.09824 sec during 7 <sup>th</sup> period with center of rotation at $a=1/2$ .....	103

Table 3.8 DNS average force and force coefficient results for different cases for Re=1000, $x_v=2c$ with a stroke period of 0.09824 sec during 7 <sup>th</sup> period with center of rotation at $a=3/4$ .....	103
Table 4.1 Characteristic of the numerical and experimental data for case study Re=1000 and $\alpha=45^\circ$ .....	105
Table 4.2 Nomenclature of the vortices generated during the flapping motion...	109
Table 5.1 Summary of the calculations for local downwash and non-circulatory lift .....	153
Table 5.2 Induced velocity calculated by actuator disk theory using DNS average lift results for different cases for Re=1000 and wing beat frequency, $n=1/T=10.18$ Hz .....	164
Table A.1 Oscilating flat plate velocity error norms on the flat plate relative to the exact solution at $t=0.5s$ for the comparison of central and upward diffence schemes used in numerical calculations.....	204
Table A.2 Lift and Drag coefficients for steady state results and impulsive motion result .....	206
Table C.1 Specifications of the step motors used for the setup .....	209
Table C.2 Potentiometer readings .....	209
Table C.3 Specifications of the driver controlling the step motors.....	210

## LIST OF FIGURES

### FIGURES

Figure 1.1 MAV flight regime compared to existing vehicles.....	2
Figure 1.2 Ornithopters .....	4
Figure 1.3 Clap-Fling mechanism .....	6
Figure 1.4 Drosophila wing motion in hover mode .....	9
Figure 1.5 A hummingbird in hover .....	11
Figure 1.6 Superposition of Step Functions to Form an Arbitrary Input.....	20
Figure 2.1 Flapping motion definition .....	21
Figure 2.2 Definitions of parameters .....	22
Figure 2.3 Grid domain .....	24
Figure 2.4 Stroke plane definition for hover.....	36
Figure 2.5 Experimental setup in water tank. ....	40
Figure 2.6 Electronical part of the experimental setup .....	41
Figure 2.7 Translational and rotational mechanism of the setup .....	42
Figure 2.8 Step motor, potentiometer and optocouplers for rotational motion.....	43
Figure 2.9 Direction of the commands.....	45
Figure 2.10 Real-Time control and data acquisition system ADwin-PRO-mini ...	47
Figure 2.11 Flow visualization procedure.....	47
Figure 2.12 The experimental visualization with/without mirror in water tank ...	48
Figure 2.13 Water tank with the whole experimental setup.....	49
Figure 2.14 Automatic photo taken times. A photo is taken each $t^*$ value.....	52
Figure 2.15 Velocity and angular velocity distribution comparison for numerical and experimental data .....	53
Figure 2.16 Velocity and angle of attack distribution for numerical and experimental data for $\alpha=45^\circ$ , $Re=1000$ , $x_v=2c$ , for different $x_a$ values .....	54
Figure 2.17 Velocity and angle of attack distribution for numerical and experimental data for $\alpha=45^\circ$ , $Re=1000$ , $x_v=2.5c$ , for different $x_a$ values. ....	55



Figure 2.18 Pathline, streamline, streakline and timeline definitions.....	57
Figure 2.19 Singularities in the flow topology. ....	57
Figure 2.20 Particle Image Velocimetry (PIV) procedure.....	58
Figure 2.21 Schematic representation of the experimental setup for PIV measurements.....	59
Figure 2.22 Experimental setup for PIV measurements .....	60
Figure 2.23 Timing for double frame cameras.....	62
Figure 2.24 Double frame/double exposure and cross correlation .....	63
Figure 2.25 Interrogation window deformation.....	65
Figure 2.26 Velocity vector is located at the center of the interrogation window (second order interpolation).....	66
Figure 2.27 Kriging for PIV measurements.....	68
Figure 2.28 The original photo which is correlated with the displaced photos. ....	69
Figure 2.29 Average velocities and root mean squares for different translational displacements .....	70
Figure 2.30 Probability density function for different PIV images .....	71
Figure 3.1 Kinematics of the flapping motion .....	75
Figure 3.2 Lift and drag coefficients for $\alpha=5^\circ$ , $x_v=2c$ , $Re=1000$ at $1/4c$ rotation at $7^{th}$ period .....	78
Figure 3.3 Lift and drag coefficients for $\alpha=30^\circ$ , $x_v=2c$ , $Re=1000$ at $1/4c$ rotation at $7^{th}$ period .....	79
Figure 3.4 Lift and drag coefficients for $\alpha=45^\circ$ , $x_v=2c$ , $Re=1000$ at $1/4c$ rotation at $7^{th}$ period .....	80
Figure 3.5 Lift and drag coefficients for $\alpha=60^\circ$ , $x_v=2c$ , $Re=1000$ at $1/4c$ rotation at $7^{th}$ period .....	81
Figure 3.6 Vorticity contours with velocity vectors for $\alpha=30^\circ$ , $x_v=2c$ , $Re=1000$ at $1/4c$ rotation during $7^{th}$ stroke at the end of $1^{st}$ region; $t=0.614532s$ ....	83
Figure 3.7 Vorticity contours with velocity vectors for different angle of attack ( $\alpha$ ) values, $x_v=2c$ , $x_a=2c$ , $Re=1000$ at $1/4c$ rotation during $7^{th}$ stroke at the end of $2^{nd}$ region $t=0.639089s$ .....	84
Figure 3.8 Lift coefficients for different $\alpha$ at $Re=1000$ , $1/4c$ rotation during $7^{th}$ stroke (each graph represent different $x_a$ locations).....	85

Figure 3.9 Drag coefficients for different $\alpha$ at $Re=1000$ , $1/4c$ rotation during 7 <sup>th</sup> stroke (each graph represent different $x_a$ locations).....	87
Figure 3.10 Vorticity contours with velocity vectors for $\alpha=30^\circ$ , $x_v=2c$ , $Re=1000$ with rotation axis at $1/4c$ during 7 <sup>th</sup> stroke.....	89
Figure 3.11 Maximum force coefficients and angular velocity of the airfoil during the flapping motion.....	92
Figure 3.12 Lift and drag coefficients comparing different $x_v$ locations for $\alpha=45^\circ$ , $Re=1000$ , $1/4c$ rotation during 7 <sup>th</sup> stroke for $x_a=1c$ .....	93
Figure 3.13 Lift and drag coefficients comparing different $x_v$ locations for $\alpha=45^\circ$ , $Re=1000$ , $1/4c$ rotation during 7 <sup>th</sup> stroke for $x_a=1.5c$ .....	94
Figure 3.14 Lift and drag coefficients comparing different $x_v$ locations for $\alpha=45^\circ$ , $Re=1000$ , $1/4c$ rotation during 7 <sup>th</sup> stroke for $x_a=2c$ .....	95
Figure 3.15 Lift and drag coefficients comparing different $x_v$ locations for $\alpha=45^\circ$ , $Re=1000$ , $1/4c$ rotation during 7 <sup>th</sup> stroke for $x_a=2.5c$ .....	96
Figure 3.16 Lift and drag coefficients for $\alpha=30^\circ$ , $x_v=2c$ , $Re=1000$ with an axis of rotation at $a=1/4c$ during 7 <sup>th</sup> stroke .....	97
Figure 3.17 Lift and drag coefficients for $\alpha=30^\circ$ , $x_v=2c$ , $Re=1000$ with an axis of rotation at $a=1/2 c$ during 7 <sup>th</sup> stroke .....	98
Figure 3.18 Lift and drag coefficients for $\alpha=30^\circ$ , $x_v=2c$ , $Re=1000$ with an axis of rotation at $a=3/4 c$ during 7 <sup>th</sup> stroke .....	99
Figure 3.19 Vorticity contours with velocity vectors for $\alpha=30^\circ$ , $x_v=2c$ , $x_a=2c$ , $Re=1000$ during 7 <sup>th</sup> stroke.....	100
Figure 3.20 Lift coefficients for $\alpha=30^\circ$ , $x_v=2c$ , $a=1/4c$ for different $Re$ numbers at 7 <sup>th</sup> stroke.....	101
Figure 3.21 Aerodynamic force coefficients averaged during the 7 <sup>th</sup> stroke for $x_v=2c$ , $Re=1000$ for $a=1/4$ , $1/2$ and $3/4$ .....	104
Figure 4.1 Lift and drag coefficient for study case starting from the rest.....	106
Figure 4.2 Comparison of the lift and drag coefficients for the numerical results using $15c$ length and $20c$ length radius of grid domain .....	107
Figure 4.3 Velocity and angle of attack distribution for the numerical simulations (white points), experimental visualization (blue points) and the PIV measurements (orange points).....	108

Figure 4.4 Comparison of the laser sheet visualization with PIV Q values and streamlines in inertial reference frame ( $t^*=0.08$ ).....	110
Figure 4.5 Comparison of the laser sheet visualization with PIV measurement represented with Q values and streamlines in inertial reference frame ( $t^*=0.12$ ).....	111
Figure 4.6 Detachment type separation point is observed close to the airfoil at $t^*=0.12$ .....	112
Figure 4.7 PIV measurements represented with non-dimensional Q values and streamlines in inertial and body-fixed reference frames ( $t^*=0.12$ )....	113
Figure 4.8 Comparison of the laser sheet visualization (A) with PIV non-dimensional vorticity $\omega_{ND}$ (B) and non-dimensional $Q_{ND}$ values (C) at $t^*=0.20$ ...	114
Figure 4.9 Comparison of the laser sheet visualization at $t^*=0.24$ .....	115
Figure 4.10 PIV measurements represented with non-dimensional Q values and streamlines in inertial and body-fixed reference frames a) $t^*=0.24$ , b) $t^*=0.28$ .....	116
Figure 4.11 Laser sheet visualization (A) and PIV measurements represented with non-dimensional Q values and streamlines in inertial reference frame (B) and body- fixed reference frame (C) at $t^*=0.32$ .....	117
Figure 4.12 Laser sheet visualization (A) and PIV measurements represented with non-dimensional Q values and streamlines in inertial reference frame (B) and body-fixed reference frame (C) at $t^*=0.4$ (start of rotation and deceleration of the airfoil).....	118
Figure 4.13 Laser sheet visualization (A) and PIV measurements represented with non-dimensional Q values and streamlines in inertial reference frame (B) and body fixed reference frame (C) at $t^*=0.44$ (during rotation and deceleration of the airfoil).....	119
Figure 4.14 PIV measurements represented with non-dimensional Q values and streamlines in inertial and body-fixed reference frames .....	120
Figure 4.15 Laser plane visualization (A), PIV measurements represented with non-dimensional Q values and streamlines in inertial reference frame (B) and PIV measurements represented with non-dimensional vorticity contours (C) at $t^*=0.56$ .....	122

Figure 4.16 Interpolation with krigging of the numerical grid domain with a rectangular grid domain .....	123
Figure 4.17 PIV measurement and numerical solutions represented with non-dimensional Q values and streamlines in inertial and body-fixed reference frames ( $t^*=0.24$ ).....	124
Figure 4.18 PIV measurement and numerical solutions represented with non-dimensional Q values and streamlines in inertial and body-fixed reference frames ( $t^*=0.28$ ).....	125
Figure 4.19 Comparison of numerical data, experimental visualisation and PIV measurements at $t^*=0.50$ .....	126
Figure 4.20 Comparison of the laser sheet visualization and numerical results at $t^*=0.08$ . .....	128
Figure 4.21 DNS results with non-dimensional Q and pressure coefficient $C_p$ contours at $t^*=0.1330$ .....	129
Figure 4.22 DNS results with non-dimensional Q and pressure coefficient $C_p$ contours at $t^*=0.3581$ .....	130
Figure 4.23 Velocity distributions on the airfoil for two time values after the rotational phase is started .....	131
Figure 4.24 Pressure coefficient $C_p$ contours during rotation of the airfoil at the end of the first half period .....	132
Figure 4.25 Pressure coefficient $C_p$ contours during rotation of the airfoil at the beginning of the second half period .....	133
Figure 5.1 Superposition of step functions to form an arbitrary input.....	136
Figure 5.2 Wagner and Küssner functions.....	137
Figure 5.3 Conformal mapping and the velocities induced at a point P on the circle by a source-sink pair located at $\phi$ above and below the horizontal....	139
Figure 5.4 Coordinates of the problem .....	142
Figure 5.5 Lift coefficient, normal force coefficient and Duhamel Integral solution with Wagner function for $\alpha=5^\circ$ , $x_v=2c$ , $Re=1000$ at $1/4c$ rotation during 7 <sup>th</sup> stroke using $2\pi$ as curve slope .....	154

Figure 5.6 Lift coefficient, normal force coefficient and Duhamel Integral solution with Wagner function for $\alpha=5^\circ$ , $x_v=2c$ , $Re=1000$ at $1/4c$ rotation during 7 <sup>th</sup> stroke using $2\pi$ as curve slope .....	157
Figure 5.7 Lift coefficient, normal force coefficient and Duhamel Integral solution with Wagner function for $\alpha=30^\circ$ , $x_v=2c$ , $Re=1000$ at $1/4c$ rotation during 7 <sup>th</sup> stroke using $2\pi$ as curve slope .....	158
Figure 5.8 Lift coefficient, normal force coefficient and Duhamel Integral solution with Wagner function for $\alpha=5^\circ$ , $x_v=2c$ , $Re=1000$ at $1/4c$ rotation during 7 <sup>th</sup> stroke using DNS curve slope values.....	160
Figure 5.9 Lift coefficient, normal force coefficient and Duhamel Integral solution with Wagner function for $\alpha=30^\circ$ , $x_v=2c$ , $Re=1000$ at $1/4c$ rotation during 7 <sup>th</sup> stroke using DNS curve slope values.....	162
Figure 5.10 Lift coefficient, normal force coefficient and Duhamel Integral solution with Wagner and Küssner function for $\alpha=5^\circ$ , $x_v=2c$ , $Re=1000$ at $1/4c$ rotation during 7 <sup>th</sup> stroke using DNS curve slope values .....	166
Figure 5.11 Lift coefficient, normal force coefficient and Duhamel Integral solution with Wagner and Küssner function for $\alpha=30^\circ$ , $x_v=2c$ , $Re=1000$ at $1/4c$ rotation during 7 <sup>th</sup> stroke using DNS curve slope values without additional correction terms $L_3$ and $L_{3k}$ .....	168
Figure 5.12 Lift coefficient, normal force coefficient and Duhamel Integral solution with Wagner and Küssner function for $\alpha=30^\circ$ , $x_v=2c$ , $Re=1000$ at $1/4c$ rotation during 7 <sup>th</sup> stroke using DNS curve slope values .....	170
Figure 5.13 Lift coefficient, normal force coefficient and Duhamel Integral solution with Wagner and Küssner function for $\alpha=45^\circ$ , $x_v=2c$ , $Re=1000$ at $1/4c$ rotation during 7 <sup>th</sup> stroke using DNS curve slope values .....	172
Figure 5.14 Lift coefficient, normal force coefficient and Duhamel Integral solution with Wagner and Küssner function for $\alpha=60^\circ$ , $x_v=2c$ , $Re=1000$ at $1/4c$ rotation during 7 <sup>th</sup> stroke using DNS curve slope values .....	173

Figure 5.15 Lift coefficient, normal force coefficient and Duhamel Integral solution comparisons function for $\alpha=60^\circ$ , $x_v=2c$ , $x_a=2c$ , Re=1000 at 1/4c rotation during 7 <sup>th</sup> stroke using DNS curve slope values. ....	175
Figure 5.16 Lift coefficient, normal force coefficient and Duhamel Integral solution comparisons function for $\alpha=45^\circ$ , $x_v=2c$ , $x_a=1c$ , Re=1000 at 1/4c rotation during 7 <sup>th</sup> stroke using DNS curve slope values. ....	176
Figure 5.17 Vorticity contours (1 <sup>st</sup> row) and Pressure contours (2 <sup>nd</sup> row) for $\alpha=60^\circ$ , $x_v=2c$ , $x_a=2c$ , Re=1000 at 1/4c rotation during 7 <sup>th</sup> stroke..	177
Figure 5.18 Aerodynamic force coefficients obtained numerically and analytically (Wagner-Kussner) for $\alpha=60^\circ$ , $x_v=2c$ , $x_a=2c$ , Re=1000 at 1/4c rotation during 7 <sup>th</sup> stroke using DNS curve slope values. ....	178
Figure 5.19 Lift coefficient for different $\alpha$ having $x_v=2c$ , $x_a=2c$ , Re=1000 at 1/4c rotation during 7 <sup>th</sup> stroke. ....	179
Figure 5.20 Drag coefficient for different $\alpha$ having $x_v=2c$ , $x_a=2c$ , Re=1000 at 1/4c rotation during 7 <sup>th</sup> stroke. ....	180
Figure 5.21 Vorticity contours for different $\alpha$ values with $x_v=2c$ , $x_a=2c$ , Re=1000 at 1/4c rotation at the beginning of the second region, $t=0.614532$ s, during 7 <sup>th</sup> stroke (point A).....	180
Figure 5.22 Vorticity contours for different $\alpha$ values with $x_v=2c$ , $x_a=2c$ , Re=1000 at 1/4c rotation at the maximum lift coefficient location for $60^\circ$ angle of attack at 2 <sup>nd</sup> region, $t=0.621899$ s during 7 <sup>th</sup> stroke (point B).....	181
Figure 5.23 Vorticity contours for different $\alpha$ values with $x_v=2c$ , $x_a=2c$ , Re=1000 at 1/4c rotation at the end of the rotation and variable velocity region ( $x_a=x_v$ ), $t=0.624355$ s, during 7 <sup>th</sup> stroke (point C)..	181
Figure 5.24 Vorticity contours for different $\alpha$ values with $x_v=2c$ , $x_a=2c$ , Re=1000 at 1/4c rotation at the end of 2 <sup>nd</sup> region during pure translation, $t=0.639089$ s, during 7 <sup>th</sup> stroke (point D).....	182
Figure A.1 Boundary conditions of the grid domain for a flat plate.....	198

Figure A.2 Dimensional velocity profile of an impulsively started flat plate with $U_0=1\text{m/s}$ for different time steps.....	198
Figure A.3 Non-dimensional velocity profile of an impulsively started flat plate with $U_0=1\text{m/s}$ for different time steps.....	199
Figure A.4 Comparison of the drag coefficient $C_d$ between the numerical and exact solutions of impulsively started flat plate with $U_0=1\text{m/s}$ ...	199
Figure A.5 Velocity profile of an oscillatory flat plate for different time steps ..	202
Figure A.6 Drag coefficient $C_d$ between the numerical and analytical compared to exact solutions of oscillating flat plate.....	203
Figure A.7 Velocity profiles for oscillating flat plate for central and upward difference schemes and comparison with exact solution .....	204
Figure A.8 Steady state solutions.....	205
Figure A.9 Comparison of steady state solutions with impulsive start result.....	205
Figure C.1 Clock Signal for drivers controlling step motors.....	210
Figure C.2 Basic Principle (Only the optocoupler n°2 is represented).....	211
Figure C.3 Signal send to computer to find the frequency of the PC .....	212
Figure D.1 Experimental visualization at $t^*=0.08$ , comparison with the numerical solution and PIV measurements.....	214
Figure D.2 Experimental visualization at $t^*=0.12$ , comparison with the numerical solution and PIV measurements.....	216
Figure D.3 Experimental visualization at $t^*=0.16$ , comparison with the numerical solution and PIV measurements.....	218
Figure D.4 Experimental visualization at $t^*=0.20$ , comparison with the numerical solution and PIV measurements.....	220
Figure D.5 Experimental visualization at $t^*=0.24$ , comparison with the numerical solution and PIV measurements.....	222
Figure D.6 Experimental visualization at $t^*=0.28$ , comparison with the numerical solution and PIV measurements.....	224
Figure D.7 Experimental visualization at $t^*=0.32$ , comparison with the numerical solution and PIV measurements.....	226
Figure D.8 Experimental visualization at $t^*=0.36$ , comparison with the numerical solution and PIV measurements.....	228

Figure D.9 Experimental visualization at $t^*=0.40$ , comparison with the numerical solution and PIV measurements.....	230
Figure D.10 Experimental visualization at $t^*=0.44$ , comparison with the numerical solution and PIV measurements.....	232
Figure D.11 Experimental visualization at $t^*=0.48$ , comparison with the numerical solution and PIV measurements.....	234
Figure D.12 Experimental visualization at $t^*=0.52$ , comparison with the numerical solution and PIV measurements.....	236
Figure D.13 Experimental visualization at $t^*=0.56$ , comparison with the numerical solution and PIV measurements.....	238
Figure D.14 Experimental visualization at $t^*=0.60$ , comparison with the numerical solution and PIV measurements.....	240
Figure D.15 Experimental visualization at $t^*=0.64$ , comparison with the numerical solution and PIV measurements.....	242
Figure D.16 Experimental visualization at $t^*=0.68$ , comparison with the numerical solution and PIV measurements.....	244
Figure D.17 Experimental visualization at $t^*=0.72$ , comparison with the numerical solution and PIV measurements.....	246
Figure D.18 Experimental visualization at $t^*=0.76$ , comparison with the numerical solution and PIV measurements.....	248
Figure D.19 Experimental visualization at $t^*=0.80$ , comparison with the numerical solution and PIV measurements.....	250
Figure D.20 Experimental visualization at $t^*=0.84$ , comparison with the numerical solution and PIV measurements.....	252
Figure D.21 Experimental visualization at $t^*=0.88$ , comparison with the numerical solution and PIV measurements.....	254
Figure D.22 Experimental visualization at $t^*=0.92$ , comparison with the numerical solution and PIV measurements.....	256
Figure D.23 Experimental visualization at $t^*=0.96$ , comparison with the numerical solution and PIV measurements.....	258
Figure D.24 Experimental visualization at $t^*=1.00$ , comparison with the numerical solution and PIV measurements.....	260



## LIST OF SYMBOLS

$a$	axis of rotation (=0 at leading edge and =1 at trailing edge)
$b$	semi-chord
$C_D$	drag coefficient
$C_L$	lift coefficient
$C_N$	normal force coefficient
$\bar{C}_{P_{Pro}}$	mean profile power coefficient
$c$	chord
$dt$	time step
$e_{ijm}$	permutation symbol
$f$	feathering parameter
$F_p$	pressure force
$F_s$	shear force
$F_t$	total force
$\sqrt{g}$	determinant of metric tensor
$I$	image intensity
$k$	reduced frequency
$n$	wing beat frequency
$\bar{P}'_{pro}$	mean profile power per unit span
$p$	pressure
$Q$	second invariant of velocity gradient
$Re$	Reynolds number
$s$	reduced time
$s_{ij}$	rate of strain tensor
$t$	time
$t_a$	time corresponding to the $x_a$ location, where the angle of attack changes
$t_v$	time corresponding to the $x_v$ location where the velocity changes
$T$	period
$u_i$	absolute fluid velocity component in direction $x_i$
$V$	velocity of the flapping motion
$V_0$	maximum velocity during the flapping motion
$V_P$	velocity input to the Testpoint program for the photo timing
$x_a$	x position at the beginning of angle of attack change
$x_i$	Cartesian coordinate ( $i=1, 2, 3$ )
$x_v$	x position at the end of constant velocity region
$x_{T/4}$	maximum x location, half-amplitude
$\alpha$	angle of attack
$\dot{\alpha}$	angular velocity of the flapping motion
$\beta$	stroke plane angle
$\delta_{ij}$	Kronecker delta (=1 when $i=j$ and zero otherwise)

$\Gamma$	circulation
$\lambda$	eigenvalue
$\mu$	dynamic viscosity
$\rho$	density
$\nu$	kinematic viscosity
$\omega$	vorticity
$\Omega_{ij}$	rate of rotation tensor
$\tau_{ij}$	stress tensor components
$\tau_w$	wall shear stress

# CHAPTER 1

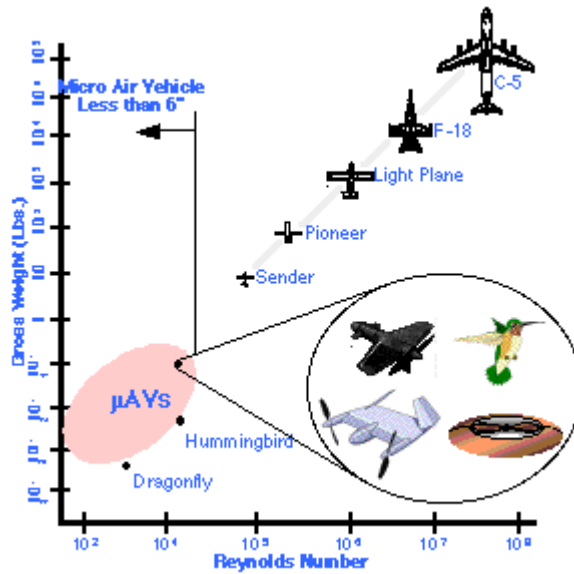
## INTRODUCTION

### 1.1 Background and Objective

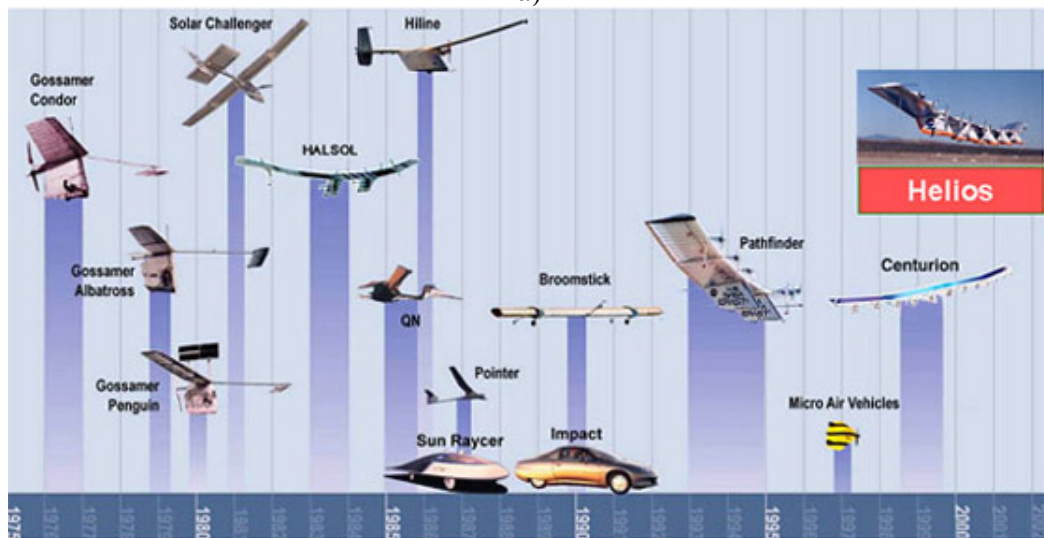
Last ten years, the numerical and experimental studies of low Re number regime become very important due to the advances in micro-technologies enabling the development of Micro Air Vehicles (MAV's). One of the main concerns of these studies is the flapping motion concept. Although, generally the forward flight regime studies are in majority in literature; one of the main objective of MAV applications, i.e. constant position surveillance, reveals the need for more research on hover mode.

Additionally, the MAV's ability to operate in constrained environments like urban canyons and, eventually, even the interior of buildings gives these systems a level of uniqueness unmatched by other concepts. MAVs are not replacements for previously manned air vehicle missions; because of their size, they will be capable of completely new missions not possible with any existing systems [1].

There are three generation of MAV's: Fixed wing, rotating wings (like helicopters) and micro technology (MEMS, flapping or vibrating wings). The definition employed in Defense Advanced Research Projects Agency (DARPA) program limits these craft to a size less than 15 cm (about 6 inches) in length, width or height. This physical size puts this class of vehicle at least an order of magnitude smaller than any missionized UAV developed to date (Figure 1.1).



a)

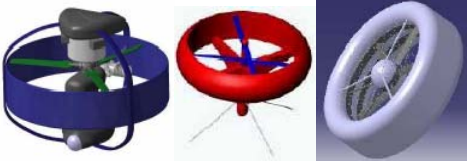
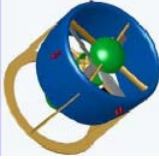
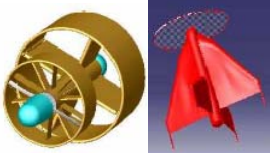


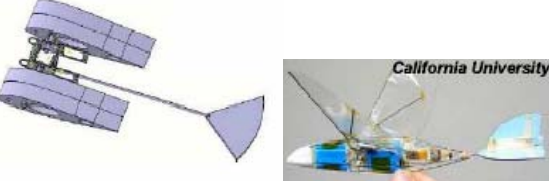




b)

**Figure 1.1** MAV flight regime compared to existing vehicles  
a) in Reynolds number scale (from Ref. [1]) b) in time scale (from Ref. [2]).

DGR-ONERA competition [3] reveals some examples for the base of the different MAV concepts (Table 1.1). The different aerodynamic concepts are such as coaxial ducted rotors with cyclic and collective pitch, tilting wing and body, coaxial ducted rotors with fins, 4 tilting rotors, 4 rotors, flapping wings, fixed wings, ducted main and tail rotors helicopters and R/C helicopter.

**Table 1.1** Different Micro Air Vehicle concepts in DGR-ONERA competition (from Ref.[3])

MAV type	Examples
Coaxial ducted rotors with cyclic and collective pitch	
Tilting wing and body	
Coaxial ducted rotors with fins	
4 tilting rotors	
4 rotors	
Flapping wings	
Fixed wings	
Ducted main and tail rotors helicopters	

The most interesting part of the MAV researches, especially for small dimensional vehicles are to investigate the flapping wing phenomena. Ornithopters (mechanical birds (Fig.1.2)) are especially suited to this type of work [1].



**Figure 1.2** Ornithopters (from Ref.[1]).

The major aim of flapping motion research is based on the understanding of the relation between the temporal and the spatial changes of the wake structure and the resulting instantaneous aerodynamic forces over the flapping wings. In general unsteady aerodynamic effects are relatively local and are a consequence of the time history of the vorticity contained in the shed wake immediately behind the body (behind the blade for a rotor case) [4]. The essential physics of unsteady airfoil problems can be observed from simplified two-dimensional experiments, and the interpretations of the behavior can be supported by theoretical or numerical models.

The aim of this study is to understand the aerodynamical mechanisms and vortex dynamics of flapping motion by using numerical methods, analytical models and experimental techniques.

## **1.2 Literature Survey**

### **1.2.1 Bio-aerodynamics and Related Studies**

The studies on flapping motion flight can be classified into two main parts as the zoological configurations and the simplified configurations. Zoological configuration studies are performed based on the study of the insects or birds. The simplified configurations are mostly the studies based on the aerodynamic studies. The models are simplified such that different airfoil profiles are used instead of the real insect/bird wing geometries.

#### Zoological Configurations

Weis-Fogh [5] analyzed how the dynamic and structural parameters of an oscillating wing system depended on the size of the animals. He used quantitative relationships and performs a dimensional analysis. Flight is a favorable biological activity for studies of scaling because active flapping flight is extremely common in nature and constitutes a large range of forms and sizes. It is demanding in energy and it imposes an absolute, size-dependent requirement in order to lift the body weight. The active flapping flight in terrestrial life has evolved independently at four different occasions: winged insects (Pterygota), pterosaurs (Reptilia, Pterosauria), birds (Aves) and bats (Mammalia, Chiroptera).

The study of the wing motions of a variety of insects and calculation of the forces resulting from these motions are established by Maxworthy [6]. The fluid dynamics of flapping forward flight and hovering flight is summarized. Hovering flight is explained in 4 categories which are the normal hovering, the clap-and-fling mechanism, inclined wing stroke plane and vertical-stroke plane. Normal hovering is where the wing stroke is approximately horizontal. Hummingbirds and the majority of insects are included in this group.

One of the aerodynamic mechanism for the hovering is the “clap and fling” mechanism explained by Weis-Fogh (1973) [7]-Lighthill (1973) [8]. Also, from a series of experiments using simplified mechanical models, explanation of the “clap and fling” mechanism for the generation of large lift coefficients by insects in hovering flight are suggested by Maxworthy [9]. Vortex motion and in particular the motion of vortex pairs and rings are a central concern in any description of the dynamics of hovering flight (Fig.1.3-Ref.[10]).

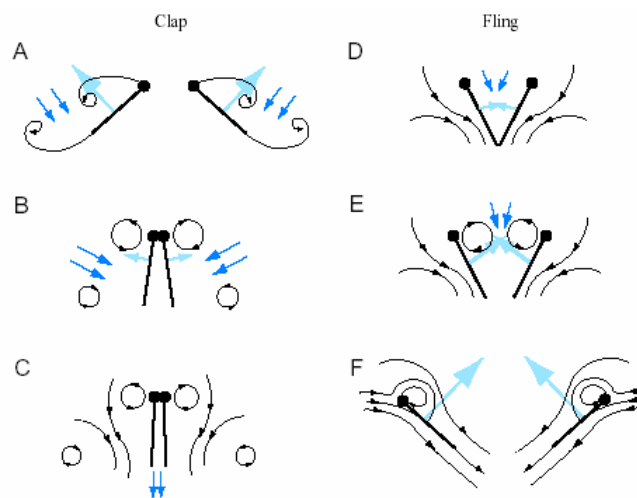


**Figure 1.3** Clap-Fling mechanism (from Ref. [10]) Wings approaching each other to clap (A–C) and flinging apart (D–F). Black lines show flow lines, and dark blue arrows show induced velocity. Light blue arrows show net forces acting on the airfoil.

Trantafyllou et al. [11] reviewed recent experimental and theoretical works identifying the principle mechanism for producing propulsive and transient forces in oscillating flexible bodies and fins in water, the formation and control of large scale vortices.



Dynamic stall or leading edge vortices form when the flow separates near the leading edge. High values of lift coefficient were associated with the formation of the leading-edge vortex (dynamic stall vortex) [6-14].

Liu et al. [13] and Van Den Berg et al. [15] show the three-dimensional formation and evolution of a substantial leading-edge vortex in a wing-simulating hawkmoth hovering.

Dickinson [16] observed by experimental results that four important parameters of stroke reversal influenced the generation of the force during the subsequent stroke. These are the position of the rotational axis, the speed of rotation, the angle of attack of the preceding stroke and the length of the preceding stroke. The motion of the wing profile was divided into three temporally distinct phases: the first translation (downstroke), wing rotation; the second translation in the opposite direction from the first (upstroke). During the experiments carried by Dickinson, a 1mm thick aluminum wing section with a span of 15cm and a chord of 5 cm is used in a 200 liters aquarium filled with 54% sucrose solution with a measured kinematic viscosity of  $0.25 \text{ cm}^2/\text{sec}$ . The pattern of the fluid flow is visualized with aluminum particles and recorded from below with a video tape. A mechanical model which is dynamically scaled to the Reynolds number of the small insects such as *Drosophila* is used in experiments.

*Drosophila* is a fruit fly, a little insect about 3mm long, of the kind that accumulates around spoiled fruit. The translational velocity of the profile is taken to be 12cm/sec in all experiments with a  $Re = 236$ . The rotational velocity is chosen by dynamic scaling of the reduced frequency parameter,  $k = \omega c/U$ ,  $U$  being the velocity during the translational phase. The model is translated and rotated through perpendicular axes by the action of two computer-operated stepper motors. In Sane and Dickinson [17], Birch and Dickinson [14] and Dickinson et al. [18], the dynamically scaled wing in mineral oil is investigated experimentally by using sensors to measure the aerodynamic forces and the digital particle image velocimetry (DPIV) to characterize

the flow around the wing [14]. The Dickinson et al. results for different papers are shown in Table 1.2.

More detailed explanation of the experimental procedure is given in Dickinson and Götz [19] where a two-dimensional model measurement is done for lift and drag calculations with flow visualizations. Time dependency of forces produced by impulsively moved wings are also investigated.

**Table 1.2** Re number and reduced frequency similitude of Dickinson's papers about Drosophila. (In the table U stands for translational velocity, c for chord,  $\nu$  for kinematic viscosity,  $\omega$  for angular velocity, Re for Reynolds number and k for reduced frequency).

	U [cm/s]	c [cm]	$\nu$ [cm <sup>2</sup> /s]	$\omega$ [deg/s]	Re=Uc/ $\nu$	k= $\omega$ c/U
<b>Dickinson et al.</b> [Ref.16]	12	5	0.25 (54% sucrose solution)	625	236 (given) 240 (calc.)	4.5 (given)
<b>Drosophila</b> [Ref.16]	125 (given)	0.0085	(air) 0.1454	$3.8 \cdot 10^5$ (calc.) ( $3 \cdot 10^5$ - $5 \cdot 10^5$ )	236 (given)	4.5 (given) (3.5-6.0)
<b>Dickinson et al.</b> [Ref.17]	15 or 25	6.256 (calculated)	1.15 (mineral oil)	145mHz (frequency)	136	
<b>Drosophila</b> [Ref.17], [Ref.18]	280 (mean velocity of the wing tip)				136	
<b>Sane &amp; Dickinson</b> [Ref. 18]			1.2 (mineral oil)	0.168 Hz (frequency)	in the range of $10^2$	
<b>Birch &amp; Dickinson</b> [Ref.14]			1.15	168 mHz	160 ( mean Re number)	
<b>Dickinson &amp; Götz [Ref.19]</b>	4 to 12 [translation from rest to fixed velocity by a constant acceleration $62.5 \text{ cm/s}^2$ ]	5	0.22-0.25 (54% sucrose solution)		For 10m/s Re=192	

Dickinson et al. [20] reviewed the motion and the creation of aerodynamic forces by a *Drosophila* wing during hovering flight measured on a dynamically scaled model insect (Fig1.4a). The wing of a hovering insect typically flaps back and forth at a high angle of attack during each stroke. The wing path is shown with a black dotted line. Black arrows indicate wing motion. Between strokes, the wing rapidly rotates so that the dorsal surface faces up during the downstroke and the ventral portion faces up during the upstroke. The total aerodynamic force (red) may be decomposed into lift (blue) and drag (green) components. Diagram of wing motion (Fig.1.4b) indicating magnitude and orientation of the total aerodynamic force vector (red) generated throughout the stroke. Black lines indicate instantaneous position of the wing at temporally equidistant points during each stroke. Small circles indicate the leading edge of the wing. Wing moves left to right during downstroke and right to left during upstroke [20].

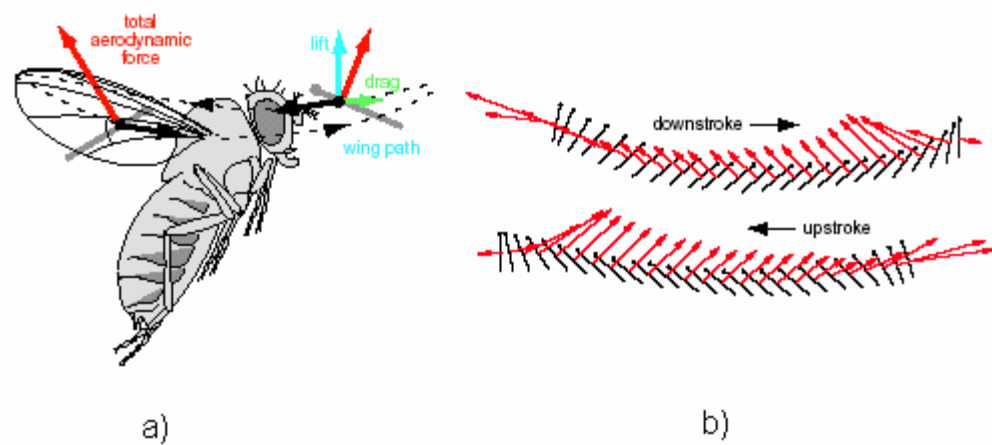


**Fig 1.4** *Drosophila* wing motion in hover mode (from Ref.[20]).

Large animals such as birds appear to operate in the lower frequency regime, while the smaller ones, such as insects in the higher frequency regime. Wang [21] investigated especially the frequency selection in forward flight, the time scales

associated with the shedding of the trailing and leading-edge vortices and the forces corresponding to them. Among the three parameters (Reynolds number  $Re=U_0c/v$ , Strouhal number or advance ratio  $St_a=f a/U_0$  and reduced frequency parameter  $St_c=f c/U_0$  where  $a$  is amplitude and  $c$  is the chord)  $Re$  dependence is expected to be very low for sufficiently high  $Re$  ( $Re \geq 10^3$ ). He defined the optimal flapping to be the one which produced the maximum thrust per unit power input. The thrust exists only at or above a minimum angle of attack  $\alpha_{min}=20^\circ$ . Thrust only occurs in  $t_s \in (0.2, 1.5)$ , where  $t_s$  is the non-dimensional time defined as  $t_s=tU_0/c$ . Lower bound can be associated with the time scale governing the growth of the trailing edge vortex, hence the lift. The upper bound can be attributed to the time scale governing the shedding of the leading edge vortex which reduces the lift. The code developed was validated with an impulsively started flow past a cylinder [21].

Lissaman [22] states that it is not necessary to have a smooth airfoil surface for insects; in fact it is likely that discontinuities are desirable to delay the flow separation.

Most of the studies about the flapping motion in the literature are done with a non-zero freestream velocity. The present study is concerned with the hovering mode, where the freestream velocity is zero.

Hovering is a flight mode where the body is assumed to be fixed in space and the freestream velocity is zero. The fluid motions are only due to the wing motions. In hovering, the main effect is to produce a vertical force in order to balance the weight. Whether a bird can hover or not depends on size, moment of inertia of the wings, degrees of freedom in the movement of the wings and the wing shape [23]. There are only few species which can hover. Hovering may be symmetrical or asymmetrical. Symmetrical hovering, also called normal or true hovering, is performed by hummingbirds (Fig.1.5) and insects like *Drosophila* that hover with fully extended wings during the entire motion which is the case investigated herein. Lift is produced during whole wing stroke. The wings are rotated and twisted at the end of the backstroke so that the leading edge of the wing remains the same throughout the

cycle, but the upper surface of the wing during the forward stroke becomes the lower surface during the backward stroke.



**Figure 1.5** A hummingbird in hover.

Hummingbird and several insects use normal hovering where the wings are moving through a large angle in an approximately horizontal plane making a figure-of-eight motion with a symmetrical half-strokes. Birds, the most successful practitioners employing flapping wings, combine non-steady aerodynamics, variable geometry, flexible surfaces of non-uniform porosity, and rapid, adaptive biological systems to achieve their outstanding flight performance [23]. In order to avoid large drag forces and negative lift forces, these birds flex their wings during the upstroke. The stroke plane is more tilted and this hovering is named as asymmetrical hovering where most of the lift is generated during downstroke.

Table 1.3 shows different parameters concerning hummingbird and some species of insects performing normal hovering. Feathering parameter in Table 1.3 is defined by Rayner [24] as the square ratio between the induced velocity on the wing disk and the mean tip velocity:

$$f = \frac{W_g^2}{u_t^2} \quad (1.1)$$

where the mean tip velocity,  $u_t=6c/(T/2)$  is the distance carried by the wing tips during whole motion divided by the time for which a single vortex ring must support the animal. For Rayner [42], during each stroke two vortex rings are generated during normal hovering.

**Table 1.3** Dimensions and parameters calculated by actuator disk theory for some birds and insects performing normal hovering (from Ref. [24]).

Normal Hovering	Body mass [kg]	Wing semi-span [m]	Disk loading [Nm <sup>-2</sup> ]	Stroke Period [s]	Feathering Parameter, f
Fruit Fly, <i>Drosophila virilis</i>	$2 \times 10^{-6}$	0.003	0.69	0.004	0.0137
Crane fly, <i>Tipula paludosa</i>	$2.8 \times 10^{-5}$	0.0173	0.29	0.018	0.0036
Hover fly, <i>Eristalis tenax</i>	$1.5 \times 10^{-4}$	0.0127	2.90	0.0055	0.0056
Bumble bee, <i>Bombus terrestris</i>	$8.8 \times 10^{-4}$	0.0173	9.18	0.0064	0.0130
Hummingbird, <i>Amazilia fimbriata</i>	$5.1 \times 10^{-3}$	0.059	4.57	0.0285	0.0111

### Simplified Configurations

The mean streamwise velocity field of the wake of a NACA 0012 airfoil oscillating in plunge at zero freestream velocity and at a zero angle of incidence at the neutral position was calculated by Lai and Platzer [25]. When the free stream velocity is zero, both  $k=2\pi fc / U_o$  (reduced frequency) and  $kh=2\pi fa / U_o$  goes to infinity and they are undefined so the only velocity scale is the peak plunge velocity  $V_p=2\pi fa$ , and the relevant length scales are the chord  $c$  and the amplitude of oscillation  $a$ . Non-dimensional frequency parameter can be defined as  $2\pi fc / V_p$  or  $2\pi fa / V_p$  which reduces to  $c/a$  or 1, respectively thus implying that the wake of a plunging airfoil at

zero freestream velocity is independent of the frequency of oscillation. So Lai and Platzer concluded that there is a similarity for mean velocity profiles when non-dimensionalized by  $V_p$  and the lateral distance is non-dimensionalized by  $a$ .

The experiments of Lai and Platzer [25] were conducted in a closed-circuit continuous flow water-tunnel. A shaker was mounted on top of the test section to oscillate the airfoil sinusoidally in plunge within a frequency range of 2.5 to 10 Hz. Dye flow visualization and LDV measurement are carried during the experiments. LDV measurements of a plunging circular cylinder in hover is also done to show the no jet production contrary to airfoil plunging case which is a result obtained by Benett et al., claiming that the thrust generation in hover mode of a plunging airfoil is due to the asymmetry between the round leading and sharp trailing edges of the airfoil.

Flow solutions about single foils are computed using an unsteady, 2-D panel code coupled with a boundary layer algorithm by Jones and Platzer [26]. Results for single mode (pitching and plunging) motions agree with the linear theory for low frequencies and amplitudes. For Strouhal numbers greater than 1, the non-linear wake losses symmetry. Propulsive efficiency of plunging airfoils could be greatly increased by decreasing the reduced frequency and increasing the amplitude while holding the Strouhal number constant. The effect of flapping wing flight near a ground plane was also shown by using the two airfoil code and potential-flow image theory [26]. Comparisons are made between the numerical and experimental wake structures behind airfoils undergoing rapid, oscillatory plunging motion using a low speed watertunnel [27]. A virtual wind tunnel is developed by combining a fast, time-stepping flow solver with an interactive animation interface and aeroelastic response is predicted by a 2-DOF spring/mass system modeling for the analysis of the structural dynamics of a flexible wing [28].

The onset of dynamic stall was also predicted and evaluated due to rapid incidence changes or unsteady pitch and plunge motions [29]. The calculations are mostly carried out at  $Re=400000$ ,  $10^6$  to  $6 \times 10^6$  by using NACA 0012 and other NACA

profiles. A review paper about the application of flapping foils for boundary layer and flow separation control and water tunnel experiments on sinusoidally plunging foils is given in Ref. [30]. For the analysis of flapping wing propulsion, an investigation is undertaken to evaluate the relative merits and limitations of various numerical methods and experimental measurement techniques. A finite aspect-ratio configuration is investigated in a low-speed wind tunnel and direct force measurements are made. The experiment is numerically simulated using the flat-plate theory, two and three dimensional (CMARC) panel codes, and two and three dimensional Euler and Navier-Stokes solvers (Flower) [31]. The inclusion of tip plates was found to reduce the three-dimensional tip losses, showing an additional increase in total thrust, especially at low frequencies [32]. General kinematics, equations of motions, performance criteria of pure plunging, pure pitching, and pitch/plunge motions of single wing and multiple wing configurations that utilize some form of interference to enhance the performance are summarized and some historical perspectives are given in Ref. [33]. Jones et al. [34] investigated numerically and experimentally the ability of a sinusoidally plunging airfoil to produce thrust known as the Knoller-Betz or Katzmayr effect. They observed deflected wake patterns at Strouhal numbers greater than 1.

An experimental and numerical investigation of flapping wing propulsion in ground effect is undertaken by Jones et al. [35]. Experiments were performed in a low speed wind tunnel with approximate flow speed range between 0m/s and 10m/s. Experimental results suggested a rather severe Reynolds number dependence. The Navier-Stokes solver is used with a three block, deforming grid and an unsteady panel code is also used for comparisons.

Anderson et al. [36] showed the results of a series of tests to measure the force and the flow around a harmonically oscillating foil at zero average angle of attack. Conditions for optimal production of thrust are found such as: Operational Strouhal number between 0.25 and 0.4; large amplitude of heave motion-to-chord ratio (of order one); large maximum angle of attack between 15°-25°; phase angle between



heave and pitch (pitch leading heave) of about  $75^\circ$  when the reference point for heave motion is at the one-third chord length from the leading edge.

Numerical simulations of dynamic stall phenomena around an airfoil oscillating in a coupled mode, in which the pitching and heaving oscillations have some phase difference, have been performed using a Navier-Stokes code by Isogai et al. [37]. The propulsive efficiency and the thrust are calculated for various combinations of the phase difference and the reduced frequency for two different amplitude ratios. The effects of the dynamic stall phenomena on the behaviors of the propulsion efficiency and thrust are examined. The highest efficiency has been observed for the case in which the pitching oscillation advances  $90^\circ$  ahead of the heaving oscillation and the reduced frequency is at some optimum value for which no appreciable flow separation appears, in spite of the large amplitude oscillations.

Neef and Hummel [38] showed the time accurate solution of the Euler equations for the inviscid flow around flapping wings in arbitrary motion and calculated the thrust output and propulsive efficiency in order to find the efficient motion parameters. NACA 0012 airfoil in plunging and pitching motions is investigated by focusing especially on phase shifts near  $90^\circ$  between the two motions where the highest efficiencies could be found. They use Mach number of 0.3 for the calculations. In 2-D unsteady flows, the efficiency of the thrust generation is governed by the shedding of vorticity from the trailing edge. Also 3-D Euler equations have been solved for a rectangular wing in a sinusoidal flapping and twisting motion.

The vortical flow patterns in the wake of a NACA 0012 airfoil pitching at small amplitudes are studied by Koochesfahani [39] in a low-speed water channel by considering the effect of both sinusoidal and non-sinusoidal shape of the waveform. Experiments were performed in a low speed water channel using a shaker coil mechanism in conjunction with a closed-loop feedback servo system in order to drive the airfoil to the desired angular position in pitch. Flow visualization pictures are used for qualitative analysis and Laser Doppler velocimetry for quantitative measurements of the mean streamwise velocity component. The structure of the

wake of a pitching airfoil can be substantially modified by controlling the amplitude, frequency and shape of the oscillation waveform. It was found that the magnitude of the axial flow in the cores of the wake vortices increases approximately linearly with both the amplitude and frequency of oscillation.

Water-tunnel tests of a NACA0012 airfoil oscillating sinusoidally in plunge are performed using dye flow visualization and single component LDV by Lai and Platzer [40]. Karman Vortex Street behind stationary airfoil and streamwise velocity profiles are visualized and shown in Ref. [40]. The generation of thrust by a single flapping airfoil and a flapping/stationary airfoil combination in tandem is studied parametrically in Ref. [41]. A multiblock Navier-Stokes solver is employed to compute the unsteady flowfield. The numerical solutions predicted the thrust generation by flapping airfoils and showed a significant augmentation of thrust for flapping/stationary airfoil in tandem configuration. The propulsive efficiency is found to be a strong function of reduced frequency and the amplitude of the flapping motion.

Hovering flight is one of the most energetically demanding forms of animal locomotion. The experimental determination of the thrust generation by the hover-apparatus over a limited parameter range and the visualization of the vertical signature caused by this thrust is analyzed by Freymuth [42]. Three modes are considered. Mode 1 is water trading mode with mean pitch angle  $\alpha_o=0^\circ$  and phase difference between the pitching and plunging  $\phi=90^\circ$ . Mode 2 is degenerate figure eight mode or normal hovering mode with  $\alpha_o=0^\circ$  and  $\phi= -90^\circ$ . Mode 3 is the oblique mode of dragonfly mode where  $\alpha_o$  is oblique and  $\phi= -90^\circ$ . He concluded that large mean vertical force coefficient could be obtained and the force was related to a wake of vortex pairs which results a downward jet of stream.

### **1.2.2 Unsteady Aerodynamic Models**

Earlier an aerodynamic theory was mainly based on small disturbance theory. Using this theory the non-linear aerodynamic equations were linearized making the solution

a possible task. This theory is valid for arbitrary unsteady incompressible motion of an airfoil. It has been proven quite applicable for unsteady flow in the attached region. A second approach for investigating arbitrary motion of subsonic airfoil flow is employing a superposition of indicial response functions, i.e. Fourier-integral superposition of theoretical results for simple harmonic oscillations. This method has also been extended to take non-linear aerodynamic effects into account. Finally, investigation of detailed non-linear aerodynamics has recently been possible using Direct Numerical Simulations (DNS).

Rayner [24] explains the theory for the flight of a hovering animal based on the vorticity present in its wake. A common approach to the problem of hovering flight is the actuator disk and its associated Rankine-Froude momentum jet, as used in propeller theory. Some defects exist: This assumes that there is no vorticity present in the body of the way the geometrical assumptions used in applying conservation laws and the lack of consideration of the mechanism on the disk itself by which a pair of wings oscillating back and forth can generate a steady momentum jet. Blade element theory has been widely applied in the study of propellers. Vortex-Ring theory, which is the classical small-cored circulation of Kelvin, is used to model the elements of the wake. Hovering is defined as the mode of flight in which the body is at rest relative to the undisturbed air, with the wake vertically beneath the animal and with all fluid motions induced by the beating wings. The wing disk is the approximately circular area mapped out by the leading edges of the wings as they oscillate back and forth, it is assumed to be planar and tilted such that the resulting wake momentum is vertical.

Results for unsteady problems have been formulated in both in the time domain and in the frequency domain, primarily by Wagner (1925) [43], Theodorsen (1935) [44], Küssner (1936) [45], and von Karman & Sears (1938) [46]. These solutions are based on the unsteady thin airfoil theory. Theodorsen's approach gives a solution to the unsteady airloads on a 2-D harmonically oscillated airfoil in inviscid, incompressible flow and subject to small disturbance assumption. Theodorsen's by its oscillatory thin airfoil theory [44], used also by Garrick [47], showed that the

propulsive efficiency of a single harmonically plunging airfoil is only about 50 percent for infinitely rapid oscillations and 100 percent for infinitely small flapping (which in turn requires a large airfoil in order to obtain significant thrust values). Theodorsen [44] showed that the effect of the unsteady circulation on the airfoil can be represented as a ratio of Hankel functions which is used for flutter problems. This ratio of Hankel functions was termed the Theodorsen function, popularly represented by the symbol  $C(k)$  where  $k$  is the reduced frequency. Physically, the Theodorsen function is described as a lift deficiency factor since its effect is to reduce the net quasi-steady lift. The unsteady lift on an airfoil subjected to an impulsive change in the angle of attack in incompressible flow is analyzed using the Wagner function approach. The Wagner function [43] is the Fourier Transform of the Theodorsen function and it provides a measure of the circulation growth around the airfoil when the airfoil is impulsively given an angle of attack with respect to the free stream. Von Karman and Sears analyzed the problem of a thin airfoil moving in a sinusoidal vertical gust field with a frequency domain solution [46].

Wagner [43] has obtained a solution for the indicial lift on a thin airfoil undergoing a step change in angle of attack in incompressible flow. The indicial function is the response to a disturbance that is applied instantaneously at time zero and held constant thereafter, that is a disturbance given by a step function. In Wagner's case,  $w=0$  for  $t<0$  and  $w=V\alpha$  for  $t>0$ , where  $w$  is the induced downward velocity.

Beddoes [48] used an indicial response to a step change in the angle of attack leading to a more general approach towards the indicial lift function, which in turn lead to a more general transfer function relating unsteady angle of attack to the forcing experienced by the blades. Some analytical models based on the indicial approach for incompressible and compressible unsteady motions are recently done by Leishman [4], [49] and Zbikowski [50] and the Refs. [51] to [55] show applications and explications of the different unsteady models mostly based on the indicial approach.

### **1.3 Present Approach and Major Goals**

During the first phase of the flapping motion study, it was necessary to simplify the problem in order to understand the complex unsteady aerodynamics of the flapping motion. Therefore, the numerical simulations, analytical modeling and experimental setup are performed in 2-D.

The aim of the present study is to understand the aerodynamics phenomena and the vortex topology of this highly unsteady motion. Instead of the use of real insect/bird wing geometries and motions which are highly complex and difficult to imitate by an exact modeling, a simplified model is used to understand the unsteady aerodynamics and vortex formation during the different phase of the flapping motion.

The present document is composed of 6 chapters. Chapter 1 reviewed some works which has been carried out by the researchers on the flapping motion in view of the zoological configurations, simplified configurations and the unsteady models developed analytically.

The following chapters will explain the results obtained; firstly numerically with a DNS code, secondly experimentally with both by laser sheet visualization and by Particle Image Velocimetry (PIV) measurements and thirdly analytically by developing a model for the simplified flapping motion study in hover. In this view, Chapter 2 explains the numerical tools used for the flapping motion study. Definition of the motion, the numerical tests carried out, different post-processing tools used for the vortex identification and aerodynamic force calculations are explained in the first part of the Chapter 2. The second part of this chapter is concerned to the experimental setup description and visualization techniques (laser plane visualization and PIV). A parametrical study has been performed numerically for the aim of the comparison of the aerodynamic force coefficients. The results are shown in Chapter 3. After a parametrical study, a reference configuration is chosen (one of the configurations where the lift is positive all through the motion) to study the vortex dynamics of the flapping motion phenomena. Different vortex identification methods

such as  $Q$  and  $\lambda$  criterion in addition to the experimental visualizations and PIV measurements are compared. In Chapter 5, the description of the analytical model developed for the aerodynamic force coefficients is given in addition to the comparison of these results with the numerical calculations. Chapter 6 gives the conclusion of the present study and the future works which could be done further.

## CHAPTER 2

### ANALYSIS OF NUMERICAL AND EXPERIMENTAL TOOLS

#### 2.1 Geometry and Motion Definition of the Flapping Motion

The flapping motion is divided into 4 regions with the first region corresponding to the half of the downstroke where the leading edge is pointing in positive direction and second one to the half-upstroke. While the third and fourth regions, are the mirror images of these two regions, corresponding to the second half of upstroke and downstroke respectively. Figure 2.1 shows detailed description of the flapping motion in one period.

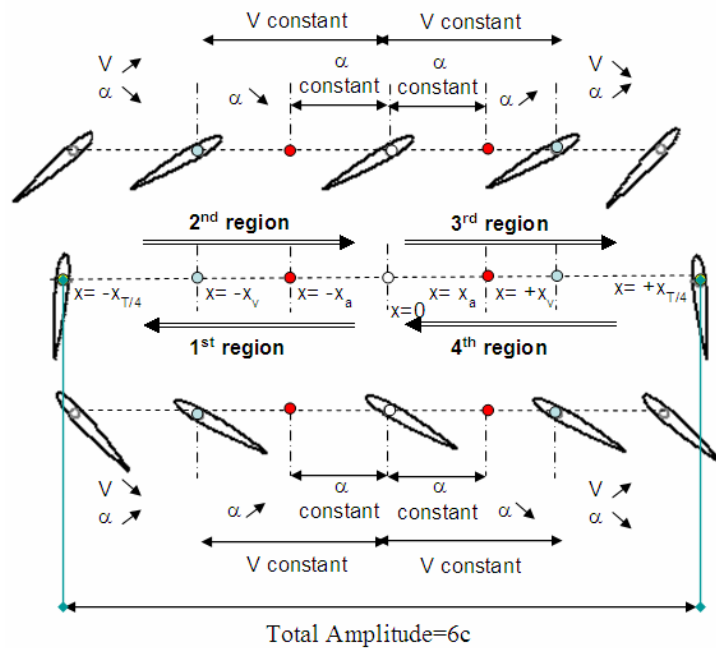
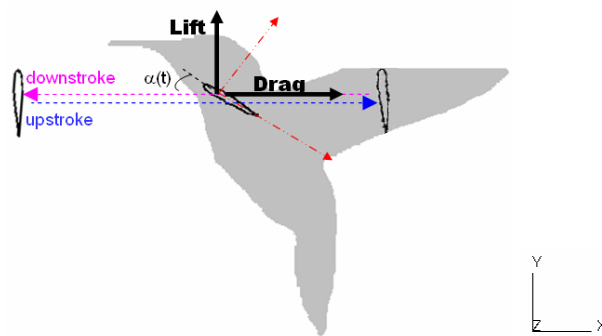


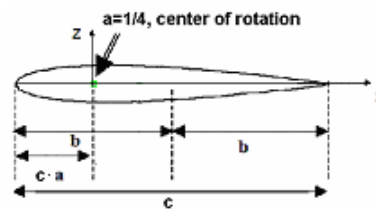
**Figure 2.1** Flapping motion definition.

Each region is composed of a translational phase and a rotational phase. In the translational phase, the airfoil translates with a constant velocity until the time  $t_v$  and position  $x_v$ , where a rotational motion around a point on the chordline is superposed to the translational motion at a predefined time  $t_a$  and position  $x_a$ . Each half cycle starts from rest and comes to a stop. The rotation is such that the leading edge stays as leading edge during all phases of the motion. The semi chord is denoted by  $b$  and the position of the center of rotation with respect to the leading edge of the airfoil is denoted by  $ca$  where  $a=0$  corresponds to the leading edge and  $a=1$  to the trailing edge.

A symmetrical NACA 0012 airfoil section is chosen for this study, so that the symmetry of the motion both during upstroke and downstroke is not lost (Figure 2.2). Total displacement of the airfoil is 6 chord length for all of the cases studied.



a) 2-D cut of a wing section,



b) NACA 0012 airfoil profile with the axis of rotation at  $1/4c$  location,

**Figure 2.2** Definitions of parameters.



T is the period of the simulation. From the mid point until the position  $x_v$  the airfoil has a constant velocity which corresponds to the time  $t_v$ . During the time interval  $[t_v, T/4]$ , the airfoil decelerates where it reaches  $V=0$  at  $t=T/4$ . At a time  $t_a$  and position  $x_a$ , the airfoil also start to rotate around the center of rotation where it reaches  $90^\circ$  angle of attack at the quarter period.

The velocity  $V$  and the angular velocity variation  $\omega$  are given in Eq.2.1 and Eq.2.2 respectively. These type of motion is chosen to ensure that the continuity of the velocities and the accelerations between the two phases of the translational motion.

$$V = V_0 \cos\left(\frac{\pi}{2} \frac{t - t_v}{\frac{T}{4} - t_v}\right) \quad (2.1)$$

$$\omega = -\frac{\omega_{\max}}{2} \left(1 - \cos\left(\frac{\pi(t - t_a)}{\frac{T}{4} - t_a}\right)\right) \quad (2.2)$$

where

$$\omega_{\max} = \frac{2\alpha_0}{\frac{T}{4} - t_a} \quad (2.3)$$

$$T = \frac{4\pi}{2|V_0|} (x_{T/4} - x_v) + t_v \quad (2.4)$$

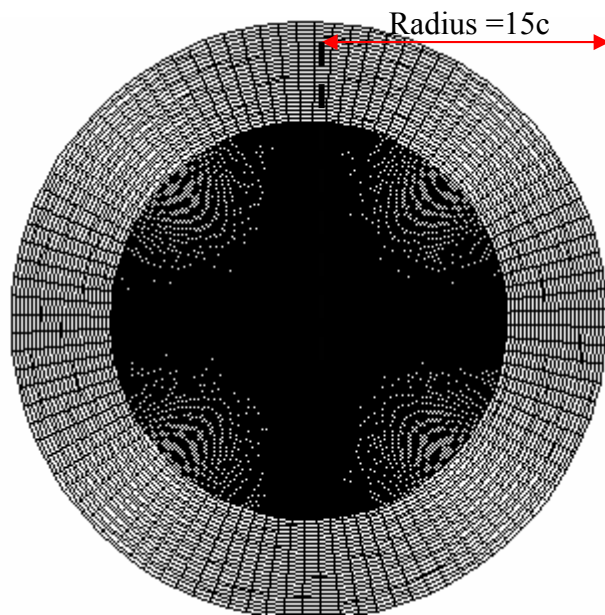
## 2.2 Two-dimensional Numerical Simulations

### 2.2.1 Computational Domain

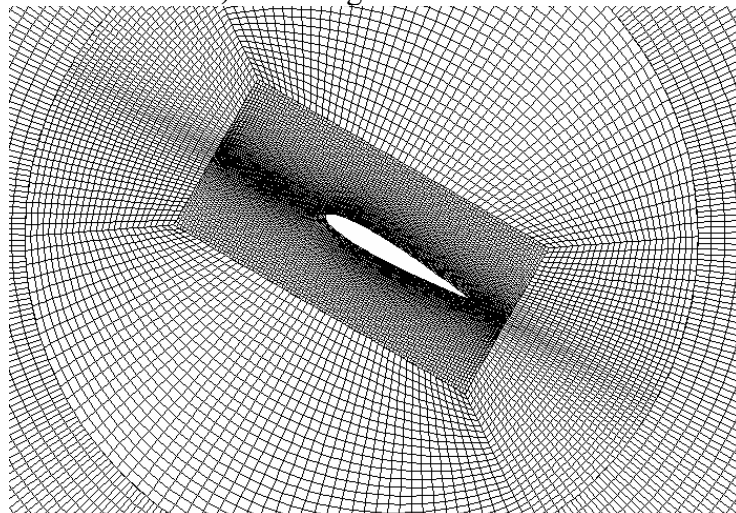
O-type grids are used around the airfoil, with a rectangular region close to the profile (Fig.2.3). The flapping motion is implemented by user-defined subroutines by moving the computational domain. The grid domain consists of 57500 cells with a domain of  $15c$  length diameter. The arbitrary mesh interface option is used to join dissimilar mesh structure, in order to decrease number of cells at the far-field

location. A finer grid domain is used close to the airfoil and a coarser grid is implemented at far-field.

The influence of the radius of disc (meaning the influence of the far-field location) is also investigated with values of  $10c$ ,  $15c$  and  $20c$ . The relative error is found to be small and  $15c$  case is chosen for the numerical calculations.



a) Whole grid domain



b) Grid domain close the airfoil

**Figure 2.3** Grid domain.

### 2.2.2 Boundary Conditions

On the airfoil surface, the instantaneous flow velocity is set equal to the local surface velocity prescribed by user-defined subroutines defining translational and rotational velocities and the no-slip boundary condition is applied. At the farfield, the pressure boundary conditions are applied. In hover condition, the farfield pressure is assumed known and taken to be the standard air pressure. The velocities at the corresponding cell faces are linked to the local pressure gradients by special momentum equations, whose coefficients are equated to those at the cell centre. These equations, together with the continuity constraint, effectively allow the magnitude and direction of the local flow (which may be inwards or outwards) to be calculated. For 2-D calculations, the front and back side of the grid domain are defined as symmetric boundary conditions.

### 2.2.3 Solver Description

The unsteady viscous flowfields are computed using an industrial DNS code (Star-CD). Computations are performed on a HP 4000 workstation. Star-CD has an interface named PROSTAR for use in pre and post processing. PROSTAR can be used as a pre-processor to define the geometry, mesh, boundary conditions, initial conditions, fluid and solid material properties and analysis control. PROSTAR is also a post-processor by which the user can read and manipulate data files, draw graphs of calculated quantities, get 3-D graphical views and animated images.

The code operates by solving the governing differential equations of the flow physics by numerical means on a computational mesh for quite general circumstances. For transient calculations efficient, optimized finite-volume solution algorithms are used. The mass and momentum conservation equations solved for general incompressible and compressible fluid flows (the ‘Navier-Stokes’ equations) are, in Cartesian tensor notation:

$$\frac{1}{\sqrt{g}} \frac{\partial}{\partial t} (\sqrt{g} \rho) + \frac{\partial}{\partial x_j} (\rho u_j) = 0 \quad (2.5)$$

$$\frac{1}{\sqrt{g}} \frac{\partial}{\partial t} (\sqrt{g} \rho u_i) + \frac{\partial}{\partial x_j} (\rho u_j u_i - \tau_{ij}) = - \frac{\partial p}{\partial x_i} \quad (2.6)$$

where for Newtonian fluid, the constitutive relation is:

$$\tau_{ij} = 2\mu s_{ij} - \frac{2}{3} \mu \frac{\partial u_k}{\partial x_k} \delta_{ij} \quad (2.7)$$

with

$$s_{ij} = \frac{1}{2} \left( \frac{\partial u_i}{\partial x_j} + \frac{\partial u_j}{\partial x_i} \right) \quad (2.8)$$

Star-CD can handle general mesh motion and internal sliding mesh with an unsteady flow solution. User-defined subroutines can be used in conjunction with the program.

PISO, SIMPLE and SIMPISO are the three alternative solution procedures available in Star-CD but PISO is mandatory for unsteady calculations where at each iteration (or time step) a predictor step is performed, followed by a number of corrector steps, during which linear equation sets are solved iteratively for each main dependent variable. Standard control parameter settings for Transient PISO Calculations that is used during the calculations are shown in Table 2.1. Scalar solver type and implicit temporal discretization is used during these calculations with an Upward Difference (UD) scheme.

The analyses are done in terms of the flowfield parameters and aerodynamic loads. The equations solved for this study are unsteady, incompressible, laminar and two-dimensional Navier-Stokes equations. The mesh can be made to translate, rotate or distort in any prescribed way, by specifying time-varying positions for some or all of the cell vertices. For this case, an additional equation called the ‘space conservation law’ is solved for the moving coordinate velocity components.

**Table 2.1** Control parameters.

	<b>Used</b>
<b><u>Solver Tolerance</u></b>	
<i>for Velocity</i>	0.01
<i>for Pressure</i>	0.001
<b><u>Sweep (inner iteration) limit</u></b>	
<i>for Velocity</i>	100
<i>for Pressure</i>	1000
<b>Pressure correction relaxation factor</b>	1.0
<b>Corrector step tolerance</b>	0.25

As a result of the decoupling of the equation for each dependent variable and subsequent linearization, large sets of linear algebraic equations are obtained. Each run carried out during this study approximately lasts 10 hours with HP 4000 Workstation. The equations are solved either by Conjugate gradient (CG) type solvers or the algebraic multigrid (AMG) approach.

#### **2.2.4 First Numerical Tests**

First verification studies for the unsteady DNS calculations have been done on an impulsively starting flat plate (Stokes's first problem) and sinusoidally oscillating flat plate (Stokes's second problem) to understand the moving grid options of the program. Both cases have an exact analytical solution which allows for a preliminary validation of the numerical results and the analytical method explained in Chapter 5. The results are shown in Appendix A. It is important to emphasize that the validation is partial since both of the problems studied are linear.

Numerical calculations give exactly same results as the exact analytical solution for the impulsively starting flat plate. For oscillating flat plate results, in addition to the numerical calculations, the analytical model with Duhamel integration is also compared (see Chapter 5 for detailed explanation of Duhamel Integral). Analytical model gives same results with the numerical calculations. For the analytical model, the solution for the impulsively starting flat plate is implemented in to the Duhamel

Integral. The difference between the exact solution of the oscillating flat plate problem (Stokes's second problem) and the numerical solution and the Duhamel integration comes from the fact that the exact solution is not for the impulsive starting oscillating airfoil. The tests lead to a satisfactory conclusion for the validation of the numerical solutions and the analytical modeling with Duhamel integration.

The verification of the numerical scheme used is also done by comparing the central difference and upward difference scheme solutions of an oscillating flat plate and the results are compared with the exact solution (Appendix A).

The verification of the boundary conditions is also carried for 2 different boundary conditions (inlet/outlet and inlet/pressure). The steady state results of the airfoil are compared with the impulsively starting airfoil result at a time where the impulsive start effect disappears. The comparisons are also given in Appendix A.

### **2.2.5 Post-Processing of DNS Results**

The aim of this study is to find optimum parameters to generate maximum lift during this motion and understand the unsteady aerodynamics behind the phenomena. A great number of cases are investigated involving the changes in the parameters such as angle of attack, location of start of change of incidence, location of start of change of velocity, axis of rotation, and Re number. The numerical study is investigated in three sub-section namely, numerical visualization, vortex identification via different methods and calculation of the instantaneous aerodynamic forces and the average lift and drag coefficient values.

#### **2.2.5.1 Numerical Visualization**

The numerical visualization are obtained based on the pressure, vorticity distributions, velocity vectors and streamlines. The influence of different parameters are discussed in following chapters via these visualisations.

### 2.2.5.2 Vortex Identification

Vortex identification is performed by considering second invariant of velocity gradient (Q-criteria) and second eigenvalue  $\lambda_2$ . The demonstrated results are obtained for Direct Numerical Simulations (DNS) for a 2-D, unsteady, laminar flapping motion. High positive values of Q and negative values of  $\lambda_2$  imply vortex regions where the rotation rate is dominant compared to the strain rate.

#### Second Invariant of Velocity Gradient Q-Visualization:

The velocity gradient is made of two parts:

$$u_{i,j} = \frac{\partial u_i}{\partial x_j} = \frac{1}{2} \left( \frac{\partial u_i}{\partial x_j} + \frac{\partial u_j}{\partial x_i} \right) + \frac{1}{2} \left( \frac{\partial u_i}{\partial x_j} - \frac{\partial u_j}{\partial x_i} \right) \quad (2.9)$$

where  $i,j (=1,2)$  are free indices,  $u_i$  is corresponding velocity component and  $x_j$  is the corresponding space coordinate in Cartesian system. The velocity gradient is summation of the symmetrical rate-of-strain (deformation) tensor  $S_{ij}$  and the skew-symmetrical rate-of- rotation tensor  $\Omega_{ij}$  which are given by:

$$S_{ij} = \frac{1}{2} \left( \frac{\partial u_i}{\partial x_j} + \frac{\partial u_j}{\partial x_i} \right) \quad (2.10)$$

$$\Omega_{ij} = \frac{1}{2} \left( \frac{\partial u_i}{\partial x_j} - \frac{\partial u_j}{\partial x_i} \right) \quad (2.11)$$

The vorticity vector  $\omega_i$ , which is twice the angular velocity vector  $\zeta_i$ , is related to the rate-of-rotation tensor by

$$\omega_i = e_{ijm} \Omega_{mj} \quad (2.12)$$

where  $e_{ijm}$  is the permutation symbol.

The strain-rate tensor  $S_{ij}$  can be written as the summation of deviatoric and isotropic tensors which are measures of the rate-of-distortion and the rate-of-dilatation (volumetric expansion) respectively. The vorticity is defined as the curl of the velocity:

$$\vec{\omega} = \vec{\nabla} \times \vec{V} = 2\vec{\zeta} \quad (2.13)$$

The second invariant of velocity gradient (also called as second invariant of the mean rate-of-displacement tensor) is given by Eq.2.14.

$$Q = \frac{1}{2}(\Omega_{ij}\Omega_{ij} - S_{ij}S_{ij}) = -\frac{1}{2} \frac{\partial u_i}{\partial x_j} \frac{\partial u_j}{\partial x_i} \quad (2.14)$$

Once  $u_{i,j}$  is known,  $S_{ij}$ ,  $\Omega_{ij}$ ,  $\zeta_i$ ,  $\omega_i$  and  $Q$  can be calculated from Eq.2.9 to Eq.2.14.  $Q$  criterion technique is used in vortex identification by Hunt et al. [56].

Non-dimensional  $Q$  is defined as:

$$Q_{ND} = \frac{Q \cdot c^2}{(V_0)^2} \quad (2.15)$$

where  $c$  is the chord length and  $V_0$  is the maximum velocity of the profile during the flapping motion.

For the 2D motion:

$$Q = -\frac{1}{2} \left( \left( \frac{\partial u_1}{\partial x_1} \right)^2 + \frac{\partial u_1}{\partial x_2} \frac{\partial u_2}{\partial x_1} + \left( \frac{\partial u_2}{\partial x_2} \right)^2 \right) \quad (2.16)$$

Nondimensional vorticity is defined as

$$\omega_{ND} = \omega \cdot \frac{c}{V_0} \quad (2.17)$$



$Q$  is the balance between the rotation rate and the strain rate. The implication of the latter observation is fairly straightforward: positive  $Q$  iso-surfaces isolate areas where the strength of rotation overcomes the strain rate, thus making those surfaces eligible as vortex envelopes.

Since vorticity should increase as the centre of the vortex is approached,  $Q$  can be expected to remain positive in the core of the vortex.  $Q$  is equal to half the Laplacian of pressure for incompressible flow ( $\rho$  is the density of the fluid and is constant):

$$\begin{aligned} Q &= \frac{1}{2} \left( \frac{1}{2} \omega^2 - S_{ij} S_{ij} \right) = -\frac{1}{2} \left( S_{ij} + \frac{1}{2} \varepsilon_{ijk} \omega_k \right) \left( S_{ij} + \frac{1}{2} \varepsilon_{ijk} \omega_k \right) \\ &= -\frac{1}{2} u_{i,j} u_{j,i} = -\frac{1}{2} \partial_i [u_j u_{i,j}] = -\frac{1}{2} \partial_i \partial_j [u_i u_j] = \frac{1}{2\rho} \nabla^2 p \end{aligned} \quad (2.18)$$

According to the maximum principle, the pressure maximum occurs only on the boundary if  $Q$  is strictly positive and the pressure minimum occurs only on the boundary if  $Q \leq 0$ . However, as stated by Jeong and Hussain [57], there is no necessary implication for the pressure to reach a minimum within a region of positive  $Q$ . Although it has been suggested that a minimum of pressure might not be appropriate within an agglomeration of vortices, it is important to check the correspondence of the pressure criterion with the  $Q$  criterion for an isolated vortex tube which contains a pressure low [57, 58].

#### $\lambda_2$ visualization:

Another criterion has been developed by Jeong and Hussain [57] based on the following arrangement of the inviscid Navier-Stokes equations:

$$\frac{D}{Dt} S_{ij} + \Omega_{ik} \Omega_{kj} + S_{ik} S_{kj} = -\frac{1}{\rho} p_{,ij} \quad (2.19)$$

The Hessian of pressure ( $p_{,ij} = \partial_i \partial_j p$ ) can provide information on the local extrema of pressure. Assuming that unsteady straining ( $DS_{ij}/Dt$ ) is negligible, the study of

pressure minima can be performed with  $S^2 + \Omega^2$ . A local minimum of pressure exists if  $p_{,ij}$  has two positive eigenvalues, i.e.  $S^2 + \Omega^2$  has two negative eigenvalues. The  $\lambda_2$  definition of Ref.[57] was named after the second eigenvalues with  $\lambda_1 < \lambda_2 < \lambda_3$ . Cucitore et al [59] have shown that this definition is strongly related to the  $Q$  criterion, since, in the reference frame of the vortex,  $\lambda_2$  can be written as a balance between local straining and rotation.

Jeong and Hussain [57] show that the second largest eigenvalue of the sum  $A_{ij} = \Omega_{ik}\Omega_{kj} + S_{ik}S_{kj}$  (named as  $\lambda_2$ ) is generally a better parameter than  $Q$  in vortex identification. They define three eigenvalues  $\lambda_1 < \lambda_2 < \lambda_3$  to the corresponding tensor. The pressure attains a local minimum if and only if two eigenvalues are negative. For the definition of vortex core  $\lambda_2$  must be negative.

High positive values of  $Q$  and negative values of  $\lambda_2$  imply vortex regions where the rotation rate is dominant compared to the strain rate.

Non-dimensional eigenvalue is defined as:

$$\lambda_{ND} = \lambda \frac{c^2}{(V_0)^2} \quad (2.20)$$

After some manipulations for 2D flow:

$$A_{ij} = \frac{1}{2} \left[ \frac{\partial u_i}{\partial x_1} \frac{\partial u_1}{\partial x_j} + \frac{\partial u_i}{\partial x_2} \frac{\partial u_2}{\partial x_j} + \frac{\partial u_1}{\partial x_i} \frac{\partial u_1}{\partial x_j} + \frac{\partial u_2}{\partial x_i} \frac{\partial u_2}{\partial x_j} \right] \quad (2.21)$$

Eigenvalues can be found as:

$$|A - \lambda I| = \begin{vmatrix} A_{11} - \lambda & A_{12} & 0 \\ A_{21} & A_{22} - \lambda & 0 \\ 0 & 0 & 0 \end{vmatrix} = 0 \quad (2.22)$$

where

$$A_{11} = \left[ \left( \frac{\partial u_1}{\partial x_1} \right)^2 + \frac{\partial u_1}{\partial x_2} \frac{\partial u_2}{\partial x_1} \right] \quad (2.23)$$

$$A_{12} = \frac{1}{2} \left[ \frac{\partial u_1}{\partial x_1} \frac{\partial u_1}{\partial x_2} + \frac{\partial u_1}{\partial x_2} \frac{\partial u_2}{\partial x_2} + \frac{\partial u_1}{\partial x_1} \frac{\partial u_2}{\partial x_1} + \frac{\partial u_2}{\partial x_1} \frac{\partial u_2}{\partial x_2} \right] \quad (2.24)$$

$$A_{21} = \frac{1}{2} \left[ \frac{\partial u_2}{\partial x_2} \frac{\partial u_2}{\partial x_1} + \frac{\partial u_2}{\partial x_1} \frac{\partial u_1}{\partial x_1} + \frac{\partial u_1}{\partial x_2} \frac{\partial u_1}{\partial x_1} + \frac{\partial u_2}{\partial x_2} \frac{\partial u_1}{\partial x_2} \right] = A_{21} \quad (2.25)$$

$$A_{22} = \left[ \left( \frac{\partial u_2}{\partial x_2} \right)^2 + \frac{\partial u_2}{\partial x_1} \frac{\partial u_1}{\partial x_2} \right] \quad (2.26)$$

$$\lambda_{2,1} = \frac{1}{2} \left( A_{11} + A_{22} \pm \sqrt{(A_{11} + A_{22})^2 - 4(A_{11}A_{22} - A_{12}A_{21})} \right) \quad (2.27)$$

For 3-D calculations,  $\lambda_1 < \lambda_2 < \lambda_3$ . In order to check the results, (Eq. 2.28) can be used.

$$\lambda_{SUM} = \lambda_1 + \lambda_2 + \lambda_3 = -2Q \quad (2.28)$$

It is checked that for 2-D calculations Eq.2.29 also holds.

$$\lambda_{SUM} = \lambda_1 + \lambda_2 = -2Q \quad (2.29)$$

In 2-D calculations, it is observed that the minimum eigenvalue when it is negative shows the vortices generated and the maximum eigenvalue when it is positive represents the shear regions.

#### Circulation around iso-Q curves:

Quantitative formula relating lift to circulation was developed by two researchers, Kutta (1902) and Joukowski (1906). In their work, a model of the flow over a lifting airfoil was conceived to consist of vortical motions; the bound circulation vortex was embedded along chord line. A relation for calculating the lift per unit span of an airfoil was mathematically expressed with Eq.2.30 and named as Kutta-Joukowski theorem.

$$L = \rho V \Gamma \quad (2.30)$$

$\Gamma$  is the bound circulation expressed as line integral of the flow velocity taken around any closed curve encompassing the airfoil.

$$\Gamma = \oint \vec{V} \cdot d\vec{l} \quad (2.31)$$

By using Stokes theorem the circulation can also be written as:

$$\Gamma = \oint \vec{V} \cdot d\vec{l} = \iint \vec{\omega} \cdot d\vec{A} \quad (2.32)$$

Thus, the circulation around a closed contour is the total vorticity enclosed within it. A positive sense corresponds to a counterclockwise path of integration around the curve.

In 2D flow, the circulation of a fluid element at location  $(x_i, y_j)$  is given by

$$\Gamma_{ij} = \oint \vec{V} \cdot d\vec{l} = \iint_{A_{ij}} \vec{\omega} \cdot d\vec{A} \quad (2.33)$$

within the infinitesimal area  $A_{ij}$ , vorticity can be assumed as constant, hence

$$\Gamma_{ij} \approx \omega_{ij} A_{ij} \quad (2.34)$$

Thus the total circulation around the closed contour is:

$$\Gamma = \sum_i \sum_j \Gamma_{ij} \quad \text{for all cells inside the contour} \quad (2.35)$$

### 2.2.5.3 Aerodynamic Forces

The total force is calculated as the sum of the shear force and the pressure force on the wall.

$$\vec{F}_t = \vec{F}_s + \vec{F}_p \quad (2.36)$$

The shear force is:

$$\vec{F}_s = -\tau_w A_b \frac{\vec{V}_{par}}{|\vec{V}_{par}|} \quad (2.37)$$

where  $A_b$  is the elementary wall area and  $\vec{v}_{par}$  is the velocity vector component parallel to the wall and  $\tau_w$  is the wall shear stress.

The pressure force is given by the Equation 2.38.

$$\vec{F}_p = p_b A_b \vec{n}_b \quad (2.38)$$

where  $p_b$  is the pressure on the elementary wall area  $A_b$  and  $\vec{n}_b$  is the outward-pointing unit area vector.

Mean aerodynamic coefficients are calculated as the time average of instantaneous forces throughout one period [Eqs.2.39-2.40]. The integration is done during the 7<sup>th</sup> period region where the first impulsive start effects are highly cancelled.

$$\bar{C}_L = \frac{1}{T} \int_{t=6T}^{t=7T} C_L(t) dt \quad (2.39)$$

$$\bar{C}_D = \frac{1}{T} \int_{t=6T}^{t=7T} C_D(t) dt \quad (2.40)$$

The total mechanical power required to flap the wings is dominated by profile power, which is the power required to overcome the drag on the flapping wings [36]. This power does not include the power required for the rotational motion of the wings. The average profile power coefficient is calculated in one period as in Eq.2.41.

$$\bar{C}_{P_{pro}} = \frac{\bar{P}'_{pro}}{\frac{1}{2} \rho c V_0^3} = n \int_{t=6T}^{t=7T} C_D(t) \cdot \frac{V^3(t)}{V_0^3} dt \quad (2.41)$$

where  $\bar{P}'_{pro}$  is the profile power per unit span and  $n=1/T$  is the wing beat frequency.

Symmetrical hovering is not necessarily done in horizontal plane. There exists a plane named stroke plane making  $\beta$  angle relative to horizontal axis (Figure 2.4). All the calculations are done relative to this stroke plane. But if we take into consideration the hover of an insect or bird, there is a resultant force averaged in a stroke period which must balance the weight of the animal. The resultant force coefficient is:

$$\bar{C}_{Total} = \sqrt{\bar{C}_D^2 + \bar{C}_L^2} \quad (2.42)$$

The angle corresponding to resultant force relative to horizontal plane axis is called stroke plane inclination angle  $\beta$  given by Eq.2.43.

$$\beta = \tan^{-1}\left(\frac{\bar{C}_D}{\bar{C}_L}\right) \quad (2.43)$$

The value of stroke plane inclination is assumed to be between  $20^\circ$  and  $40^\circ$  for a dragonfly who is performing asymmetrical hovering [23]. It is observed that the drag coefficient is approximately the same order of magnitude as lift coefficient. By performing a flapping motion in required stroke plane, considerably high resultant force coefficients can be obtained to overcome the weight of the whole body. If sufficient profile power could be obtained the drag could be overcome in horizontal plane. As will be discussed later, the drag coefficient here is calculated with respect to the motion of the airfoil, the force opposing to the motion. In some circumstances, with respect to the body, this force turns out to be a thrust for the whole body. The first aim of this study is to estimate the lift or the normal force coefficient with respect to the airfoil position during the considered flapping motion.

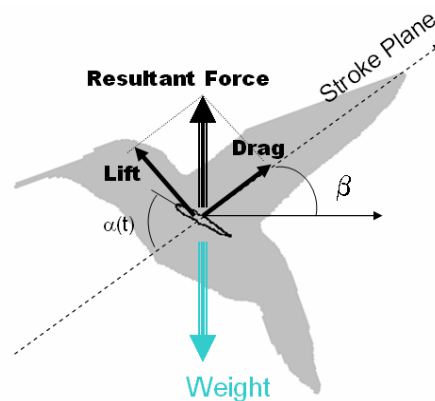


**Figure 2.4** Stroke plane definition for hover.

## 2.3 Experimental Model

In this subsection the experimental procedure carried out is described. The dimensional analysis for the air-water comparison, description of the displacement system, laser plane visualization and PIV measurement procedure are explained.

### 2.3.1 Dimensional Analysis

Dimensional analysis has been performed for this study and the parameters are tabulated in Table 2.2. Eight geometrical and flow parameters are found to be important to determine the force  $F$ . The force is dependent to the velocity of the airfoil (which is considered to be the maximum translational velocity during the flapping motion for dimensional analysis), the density of the fluid  $\rho$ , the chord of the airfoil  $c$ , the fluid viscosity  $\mu$ , the period of the flapping motion  $T$ , the distance carried out by the airfoil during a flapping motion  $x_T$ , angle of attack  $\alpha$  and the angular velocity  $\dot{\alpha}$ .

**Table 2.2** Dimensional analysis.

	<b>F=force/span</b> [kg/s <sup>2</sup> ]	<b>V</b> [m/s]	<b><math>\rho</math></b> [kg/m <sup>3</sup> ]	<b>c</b> [m]	<b><math>\mu</math></b> [kg/ms]	<b>T</b> [s]	<b><math>x_T</math></b> [m]	<b><math>\alpha</math></b> [rad]	<b><math>\dot{\alpha}</math></b> [rad/s]
<b>M</b>	1	0	1	0	1	0	0	0	0
<b>L</b>	0	1	-3	1	-1	0	1	0	0
<b>T</b>	-2	-1	0	0	-1	1	1	0	-1

The dimensional parameters result three dimensions (M L T). The Buckingham Pi theorem can found a relation between the 6 non-dimensional parameters which characterize the physical problem (Eq. 2.44).

$$f(\Pi_1, \Pi_2, \Pi_3, \Pi_4, \Pi_5, \Pi_6) = 0 \quad (2.44)$$

These parameters are given in Eq.2.45 to Eq.2.50. The detailed calculations are given in Appendix B.

$$\Pi_1 = \frac{F}{\rho V^2 c} \quad (\text{non-dimensional force}) \quad (2.45)$$

$$\Pi_2 = \frac{\mu}{\rho V c} = \frac{1}{\text{Re}} \quad (\text{Reynolds number}) \quad (2.46)$$

$$\Pi_3 = \frac{TV}{c} \quad (\text{non-dimensional time}) \quad (2.47)$$

$$\Pi_4 = \frac{x_T}{c} \quad (\text{geometrical similitude}) \quad (2.48)$$

$$\Pi_5 = \alpha \quad (\text{angle of attack}) \quad (2.49)$$

$$\Pi_6 = \frac{\dot{\alpha}c}{V} \quad (\text{reduced frequency}) \quad (2.50)$$

For the simulations in the water tank, the following similitude laws are used for conversions of the air data to the water data. For similitude calculations, subscript <sub>1</sub> stands for air and subscript <sub>2</sub> stands for water. The comparison of the air and water data for different Re numbers and  $x_v$  locations are represented in Table 2.3 and Table 2.4.

$$\frac{\mu_1}{\rho_1 V_1 c_1} = \frac{\mu_2}{\rho_2 V_2 c_2} \text{ or } Re_1 = Re_2 \implies V_2 = V_1 \left( \frac{\mu_2 \rho_1 c_1}{\mu_1 \rho_2 c_2} \right) = V_1 \left( \frac{V_2 c_1}{V_1 c_2} \right) \quad (2.51)$$

$$\frac{T_1 V_1}{c_1} = \frac{T_2 V_2}{c_2} \implies T_2 = T_1 \left( \frac{V_1 c_2}{V_2 c_1} \right) \quad (2.52)$$

$$\frac{x_{T_1}}{c_1} = \frac{x_{T_2}}{c_2} \implies x_{T_2} = x_{T_1} \left( \frac{c_2}{c_1} \right) \quad (2.53)$$

$$\frac{\dot{\alpha}_1 c_1}{V_1} = \frac{\dot{\alpha}_2 c_2}{V_2} \implies \dot{\alpha}_2 = \dot{\alpha}_1 \left( \frac{V_2 c_1}{V_1 c_2} \right) \quad (2.54)$$



**Table 2.3** Similitude results for different Re numbers for air (1) and water (2).

Re	$V_1$ [m/s] air	$V_2$ [m/s] water	$V_2/V_1$	$c_2/c_1$	$T_2/T_1$	$x_{T2}/x_{T1}$	$\dot{\alpha}_2/\dot{\alpha}_1$
<b>500</b>	0.727	0.008	0.011	6	523.4	6	0.0019
<b>1000</b>	1.454	0.017	0.011	6	523.4	6	0.0019
<b>1500</b>	2.181	0.025	0.011	6	523.4	6	0.0019
<b>2000</b>	2.908	0.033	0.011	6	523.4	6	0.0019

**Table 2.4** Comparison of the velocities and periods in air and water for different cases studied.

Re	$x_v$	$V_1$ [m/s] air	$V_2$ [m/s] water	$T_1$ [s] air	$T_2$ [s] water
<b>500</b>	2c	0.727	0.0083	0.196	102.84
<b>1000</b>	2c	1.454	0.017	0.098	51.42
<b>1500</b>	2c	2.181	0.025	0.065	34.28
<b>2000</b>	2c	2.908	0.033	0.049	25.71
<b>500</b>	2.5c	0.727	0.0083	0.1807	94.62
<b>1000</b>	2.5c	1.454	0.017	0.0904	47.31
<b>1500</b>	2.5c	2.181	0.025	0.0602	31.54
<b>2000</b>	2.5c	2.908	0.033	0.045	23.65

### 2.3.2 Displacement System for the Flapping Motion Study

#### Dimensions of the airfoil:

A rectangular wing with a NACA0012 airfoil section is displaced in a tank filled with water by associating a rotational and a translational motion. The chord length is  $c=6$  cm and the span is  $b=50$  cm. The flapping motion investigated is described in detail in Section 2.1. Total displacement of the airfoil is 360mm. The center of rotation is at  $\frac{1}{4}c$  location. The inertial frame of reference is used since the camera is fixed to the ground. The test section is located at the half of the span for whole experiments.

Definition of the flow:

The flapping motion is carried out in zero free-stream velocity, so the flow is steady at the beginning of the motion. Before each experiment minimum 15 minutes is waited for a following experiment in order to achieve a steadiness of the flow in the water tank. A laminar flow is generated with a Reynolds number of 1000 relative to the chord and the maximum velocity of the motion.

Experimental setup:

The experimental setup used is a 1.5m×1m×1m water tank made of altuglas. The wing is delimited by two rectangular plates made of epoxy with 50 cm x 90 cm dimensions in order to obtain a 2D flow. The wing is free to rotate relative to the plates (Figure 2.5).

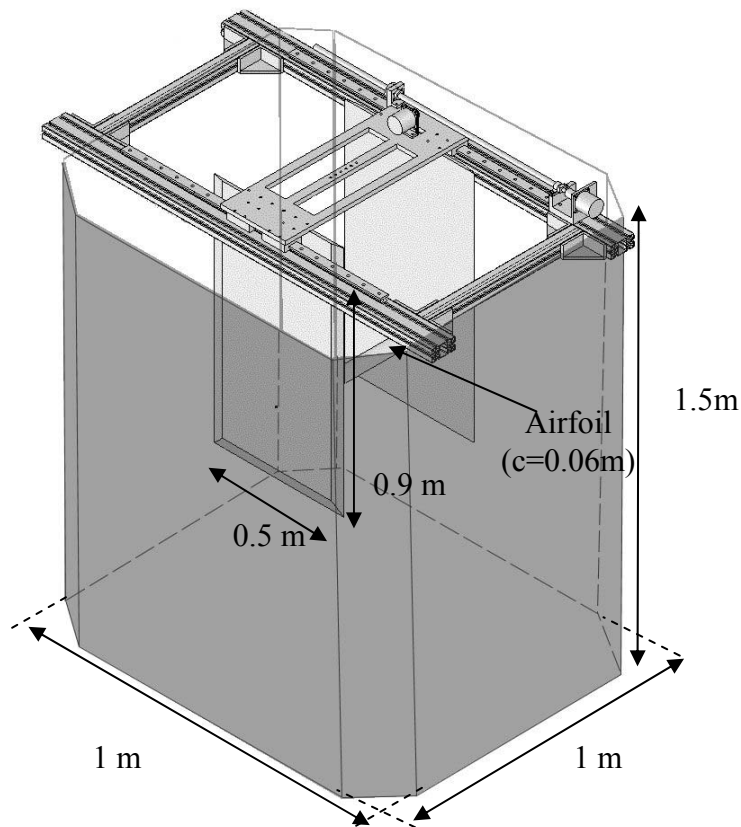


**Figure 2.5** Experimental setup in water tank.

## Motors:

The schema for the electronics of the system is given in Figure 2.6. The solid lines correspond to the signal of the motors and the dashed lines correspond to the signal of the optocouplers. The system consists of 2 step motors (200 step/rev) controlled with a law having variable speed (Table C.1 in Appendix C). The first motor is a high torque brushless motor with integrated electronics (MAC 23 of Midi Ingénierie associated an endless screw (step of 4 mm/rev) allows the translational motion with a maximum linear velocity of 4 cm/s. The second one, associated with 2 pulleys (ratio 14/81) allows the rotation of the profile (Fig. 2.7). The useful race of the translational motion is 600 mm and that of the rotational is of 360°. The second motor is used with two pulleys in order to give the angular velocity variation to the airfoil.

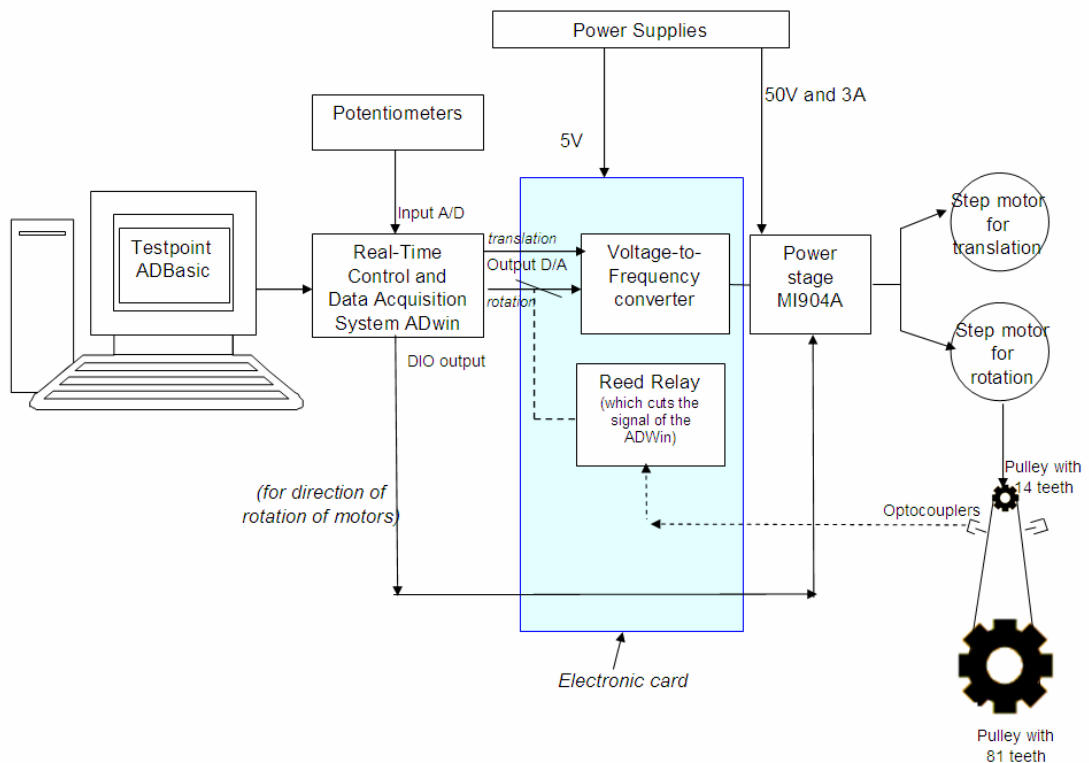


**Figure 2.6** Electrical part of the experimental setup.

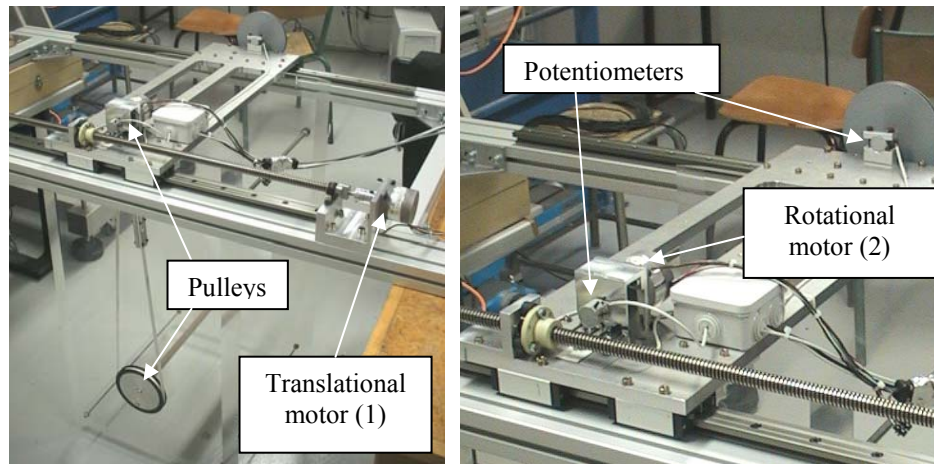


**Figure 2.7** Translational and rotational mechanism of the setup.

Optocouplers:

Two transmissive Optoschmitt sensors HOA2001 limit the angular displacement of the wing in rotation. The sensor consists of an infrared emitting diode facing an Optoschmitt detector encased in a black thermoplastic housing. The delay between each cycle creates zero values of voltage which is harmful for the continuity of the motion. The error of angular displacement during rotation is certainly due to this constraint. The motor is at its maximum speed when the control signal is stopped (zero value). With the new beginning of the cycle, by following its instruction the voltage become again maximum. Under this condition the motor loses steps. To prevent these errors which cumulate by each cycle, two optocouplers are positioned to the carriage (Figure 2.7). These sensors allow the detection of maximum and minimum positions of the rotational motion. Each sensor starts a temporization T1 of 12s, then another temporization T2 of 2 s. T2, by the intermediary of a Power Driver (ULN 2003), command a Reed relay which cuts the signal coming from the ADWin to the motors during 2 seconds. If the relay is activated, the signal voltage coming from converter AD 654 is connected to ground. The motor does not turn any more. A temporization prevents during 12 s a possible oscillation which can occur after 2 seconds. For each case studied (ex: rotation  $\pm 45^\circ$ ), the position of the strips used to start the optocouplers must be adjusted. Their positions on the belt are moved accordingly. The basic working mechanism of one of the optocouplers is given in

Appendix C on Figure C.2. To avoid the mechanical resonance, a flexible nut using a silent-block is assembled to the endless screw (Figure 2.8).

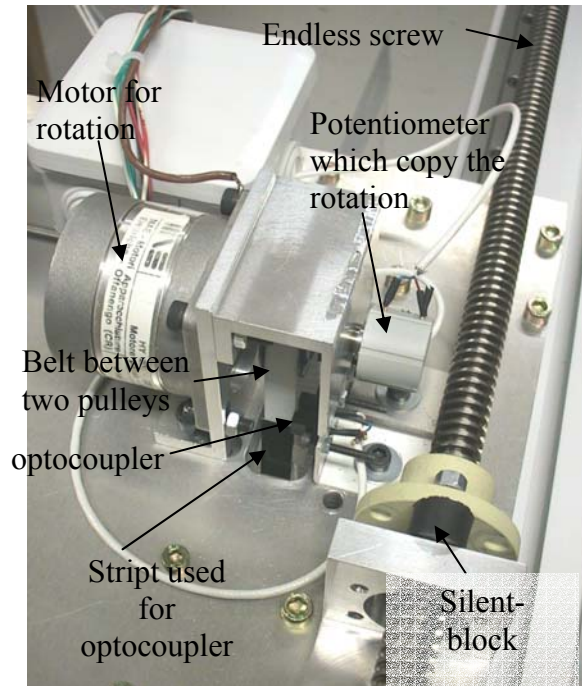


**Figure 2.8** Step motor, potentiometer and optocouplers for rotational motion.

#### Potentiometers:

Two potentiometers are used to control displacements (Figure 2.8). The voltage of the potentiometer used for the rotational motion is measured by use of the controller at  $0^\circ$  and  $360^\circ$  angle of attacks. The same calculation is done for 0mm and 360mm displacements for translation (Appendix C, Table C.2). The preliminary observations show the need for the optocouplers during the rotational motion.

#### Principle of the speed control:

The step motors are controlled by drivers MI 904A of Midi Ingénierie. These are control precision microstep amplifiers. MI 904A control cards integrate the precision microstep amplifier function, based on a chopped current type regulation system, for

two poles (4 or 8 wires) stepper motors (Appendix C, Table C.3).

The two digital/analog channels are used to generate a variable output voltage. Each channel attacks a voltage-to-frequency converter AD 654 which generates clock signals. The frequency is proportional to the input voltage.

Configuration of the step motors:

The carriage in translation must move at a maximum linear speed of 4cm/s. The endless screw has a step of 4 mm/rev. The motors have 200 steps per revolution, the frequency of control command should thus be between 0 and 2000 Hz (10 rev/sec). The low frequency operation of the step motors is incorrect. Towards 200 Hz, the motors enter in resonance. To avoid this phenomenon, it is necessary to run the motors in microstep mode. For the present experiment, 10 microstep is chosen for step motors. The adjustments of the voltage-to-frequency converter must be renewed since each revolution of motor now corresponds to 2000 steps. The frequency of control signal must thus lie between 0 and 20000 Hz (10 rev/sec).

Step Motor 1 (translation)  $5V \rightarrow 20 \text{ kHz} \Leftrightarrow 10 \text{ rev/sec}$

Step Motor 2 (rotation)  $5V \rightarrow 1.2 \text{ kHz} \Leftrightarrow 0.6 \text{ rev/sec}$

For translational motion, the voltage-to-frequency converter is adjusted in order to obtain 5V for 20 kHz. Each motor can perform 2000 step per revolution. The screw displaces 4mm during each revolution so:

$5V \text{ of PC} \Leftrightarrow 20 \text{ kHz} \Leftrightarrow 10 \text{ rev/sec} \Leftrightarrow 40\text{mm/s}$  displacement of the airfoil where 1m/s corresponds to 125V.

For the rotational motion, the voltage-to-frequency converter is adjusted in order to obtain 5V for 1.2 kHz. Each motor can perform 2000 step/rev so:

$5V \text{ of PC} \Leftrightarrow 1.2 \text{ kHz} \Leftrightarrow 0.6 \times 2\pi \text{ rad/s}$

where 1rad/s corresponds to 1.326V.

Choice of the directions of rotation:

To modify the direction of rotation of the motors, two input/output channels (DIO) of Real Time Control and Data Acquisition System (ADWin) is used. Channel 1 regulates the direction of the motor for translational motion. Channel 2 regulates the direction of the motor for rotation. Table 2.5 shows the four possible commands sent to the driver with the directions defined in Figure 2.9.

**Table 2.5** Definition of different commands for both of the step motors.

<b>Command</b>	<b>Motor 1 Translation</b> (in Oxyz coordinate system)	<b>Motor 2 Rotation</b> (in Oxyz coordinate system)
0	Motion toward end of screw (+x direction)	Counter-Clockwise
1	Motion toward support (-x direction)	Counter-Clockwise
2	Motion toward end of screw (+x direction)	Clockwise
3	Motion toward support (-x direction)	Clockwise

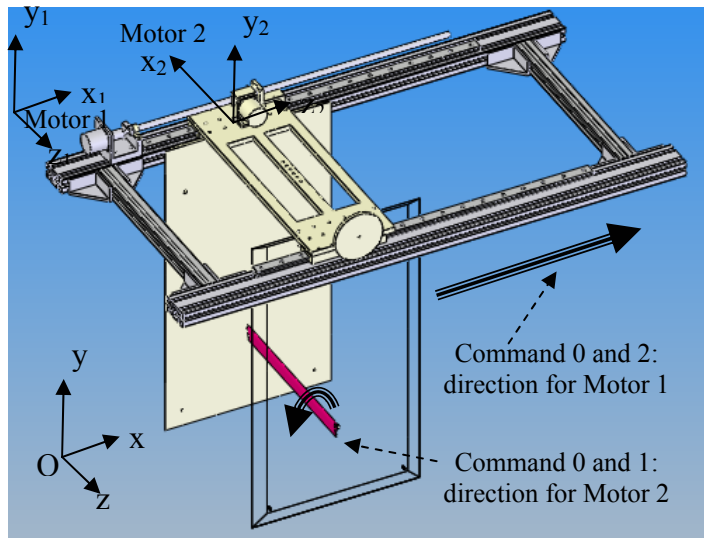


**Figure 2.9** Direction of the commands.

### Control system:

The two motors are controlled with velocity in open loop using a PC. The PC sends an order in tension on a power stage. A converter of tension/ frequency generates the necessary clock signals for the displacement of the motors. By the use of a computer with a real time system of acquisition, the command of the electronic cart developed to make the voltage-frequency conversion is carried out. Clock signals are provided with variable frequency on power stages, on which two step motors are connected.

To command the setup, a real time control and Data Acquisition system (ADWin) is used composed of A/D card of 16 bits, a direct input-output (DIO) channel and a D/A card of 16 bits (Figure 2.10). The system has its own clock, independent of Windows system. Thus, it is possible to impose velocity signals with a constant frequency ( $f = 130 \text{ Hz}$ ).

Knowing the relationship between the voltage of signal and the translational and angular velocities, it is possible to build the command file with the given frequency. A fortran program is developed for this usage. The program give an output of three columns where first column representing the direction of rotation (Table 2.5), second one being the voltage for the motor used for translational motion and the third one being the voltage for the motor used for rotational motion. The generated file with varying voltages are read by the Testpoint program and send to the ADBasic program for the real time data acquisition process which send signals to the motors.

The TestPoint program is composed of two separate processes: Start Manual and Start Auto. With Start Manual option, a manual displacement of each motor can be performed. Start Auto option execute the output file obtained from fortran program for flapping motion. Acquisition of the voltages on the potentiometers is also done with this last option. The number of cycle is a parameter (Nb of cycles) which could be changed in Start Auto program. The two processes are also implemented in ADBasic program (program of the real time data acquisition system ADWin).



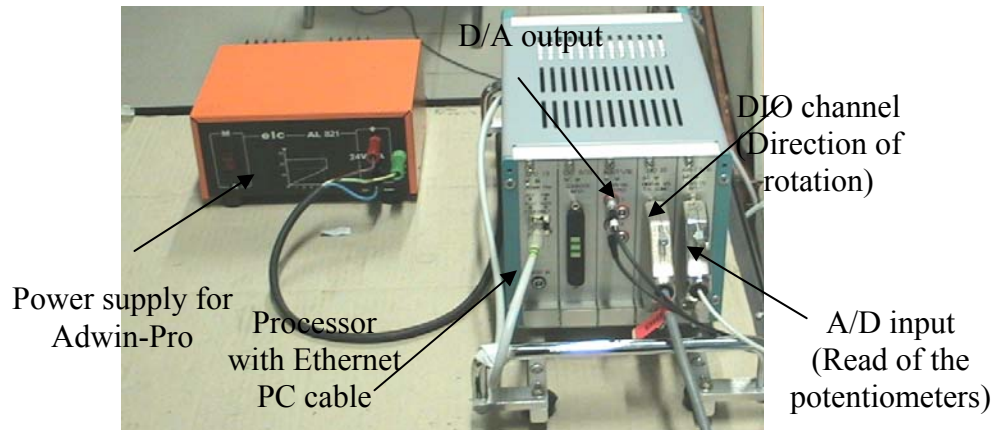


**Figure 2.10** Real-Time control and data acquisition system ADwin-PRO-mini.

### 2.3.3 Laser Sheet Visualization

The assembly has for objective the experimental analysis of the vortex dynamics and validation of the numerical simulations with the help of the visualizations. Figure 2.11 shows the procedure carried out for the flow visualization.

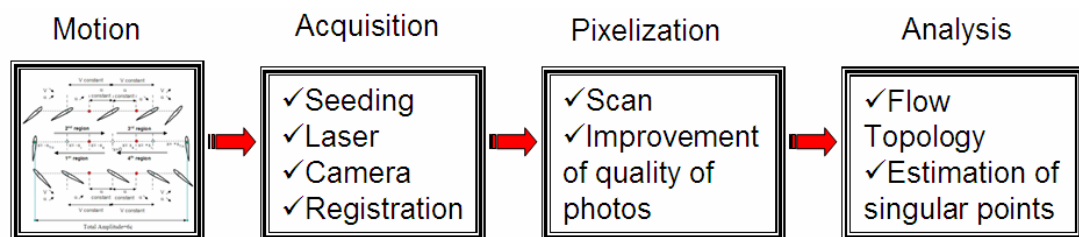


**Figure 2.11** Flow visualization procedure.

#### Seeding:

For this study, micro-spherical hollow particles of glass silver plated on the surface, with an average diameter of 15  $\mu\text{m}$  and a density of  $\rho=1.4 \text{ g/cm}^3$  are used. The

concentration of the particles in the whole volume of the water tank is  $V_{\text{particle}}/V_{\text{tank}}=1.905\times 10^{-6}$ . These particles have the advantage of having a sedimentation test low thus allowing their maintenance in suspension when there is no flow. Moreover, their quasi-spherical form allows an isotropic diffusion of the light. During the exposure time of the apparatus, each tracer describes a motion corresponding to the trajectory of the fluid particle which it replaces.

Laser:

The lighting system chosen for this experiment is a continuous laser system with argon SPECTRA-PHYSICS of 10 W of maximum capacity. The power can be changed by the control panel and during the experiment 1W-3W is used. To obtain the laser sheet, two spherical lenses of focal distance 50 mm are followed by cylinder lens of focal distance 25 mm and a mirror in order to obtain the direction of the luminous plan. This laser plane then is adjusted on the airfoil section perpendicular to the flapping motion direction. At the back side of the water tank, a mirror of 100mm×1500 mm is inserted in order to illuminate the regions of the flow domain in the shadow of the airfoil (Figure 2.12). The whole laser system is shown in Figure 2.13.

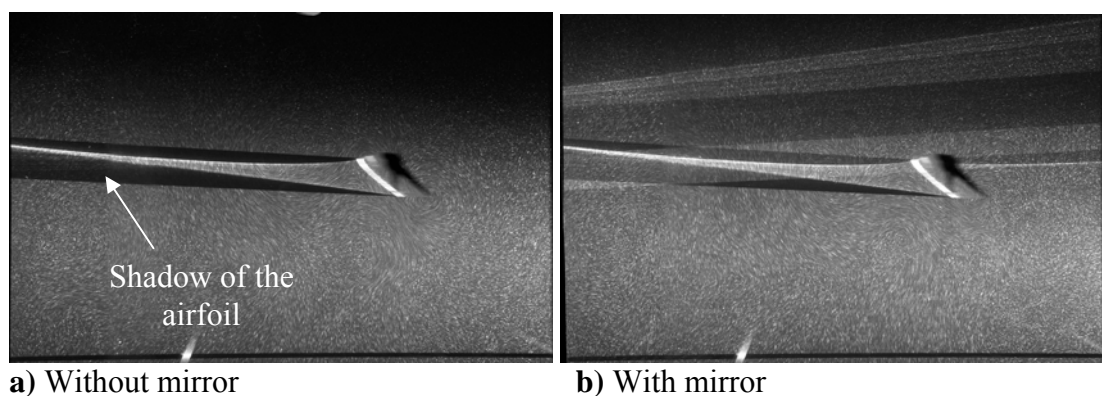
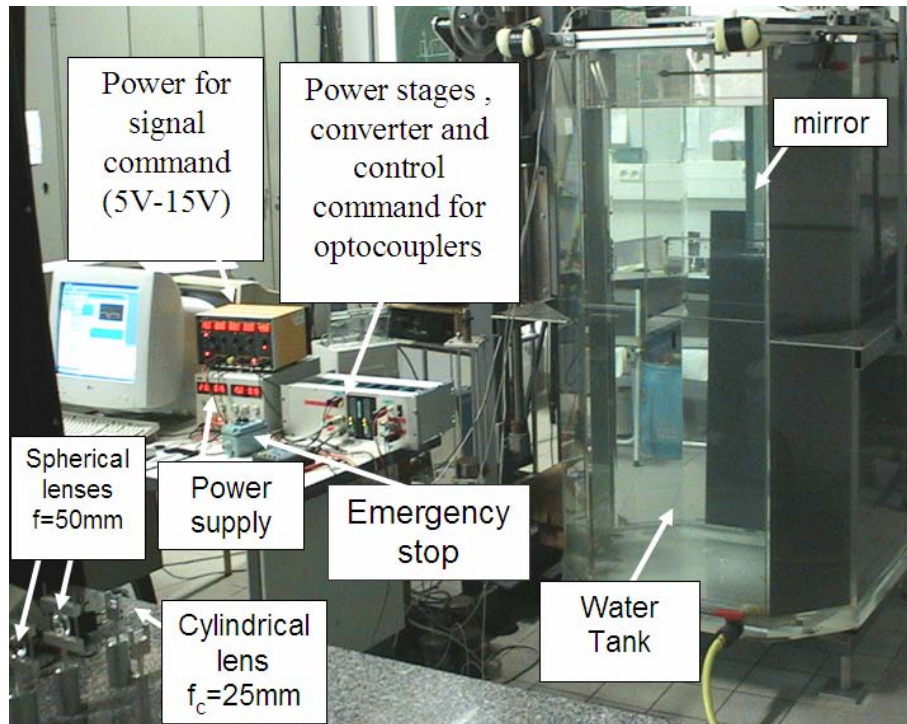
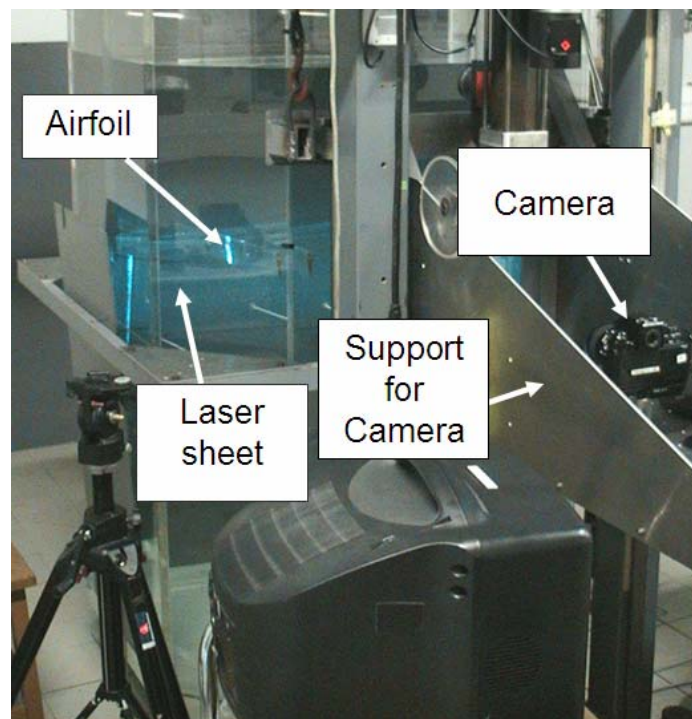


**Figure 2.12** The experimental visualization with and without mirror in the water tank.



a) Front view



b) Side View

**Figure 2.13** Water tank with the whole experimental setup.

### Camera:

The camera used is a NIKON-MB-21, with model F4S. It allows a broad control range (opening, exposure time). It takes the photographs in the 24x36 of format by objective AF-MICRO-NIKOR of 60 mm. The films white-blacks used are ILFORD HP5+. Of a nominal sensitivity of 400 ASA, developments allow us to obtain a sensitivity of about 1600 ASA. The exposure time of 500 ms and F number of 8 are chosen after lots of trials for the whole visualization study. The camera is placed approximately 50 cm from the water tank perpendicular to the laser sheet. All negatives are processed in a dark-room with dark-room equipments. Then, the processed negatives are transmitted into the computer by the Nikon Scanner CoolScan V5. As a last step, the quality improvements of the images are done with Jasc Paint-Shop Pro 8.0 image editor.

In continuation, a digital camera NIKOR-D1 is used with objectives of AF-MICRO-NIKOR of 50 mm and 105 mm to investigate in more detail the flow topology in certain region zooming to a specific region and to investigate also the 3D effects.

Some measurements have been also performed in a water tunnel (with infinite wall distance) to see the free surface and wall influence on the experimental results by using NIKOR-D1 digital camera. The laser plane is feed from the bottom of the water tunnel. It is concluded that there is no wall influence in the water tank.

### Definition of the non-dimensional time:

The non-dimensional time is given by  $t^*$  and defined in Eq.2.55.  $t^*=1$  when time is equal to one period.

$$t^* = \frac{V_P \cdot t}{c} \quad (2.55)$$

The velocity  $V_P$  is the input of the Testpoint program which commands the Nikon F4 SLR film cameras and it can be calculated as:

$$V_P = \frac{c}{T} \quad (2.56)$$

$\bar{T}$  is the average period found experimentally by repeating the experiment three times with each lasting 12 periods. The measures of the real period are done by the use of an oscilloscope (The first two periods are not taken into consideration during averaging). Table 2.6 shows the periods calculated during experiment for the cases investigated. The difference comes due to the step motors which are not suitable for a sudden change from zero velocity to a given value which is the case for the kinematics of the flapping motion studied. For some of the cases, the displacements of cart are measured with respect to two reference point one at the beginning of the movement and one at the end of the motion. Total real displacement is six chords (i.e.360mm). It is observed that total displacement error is less than 3 mm. Due to the usage of the optocouplers, the angles are corrected at each half cycle so the error of the angles is less than  $\pm 1^\circ$ , which is also observed from the protactor glued to the pulley of the airfoil. Non-dimensional  $t^*$  error is less than 1.7%.

**Table 2.6** Experimental periods for  $Re=1000$ .

$\alpha$	$x_v$	$V_1$ [m/s] air	$V_2$ [m/s] water	$T_1$ [sec] air	$T_2$ [sec] water	$\bar{T}$ [sec] (water- exper.)	$V_P$ [m/s] (camera)
45	2c	1.454	0.017	0.098	51.42	50.71	0.012
45	2.5c	1.454	0.017	0.0904	47.31	46.72	0.013

The photos are taken with constant increment  $\Delta t^*$  for two main cases  $x_v=2c$  and  $x_v=2.5c$  with  $\alpha=45^\circ$  by use of a Testpoint program. There is a time delay coming from the camera itself to start take photos (62 ms). The Testpoint program for Nikon F4 is adjusted such that each photo can be taken within the same intervals  $\Delta t^*$  (Fig.2.14).

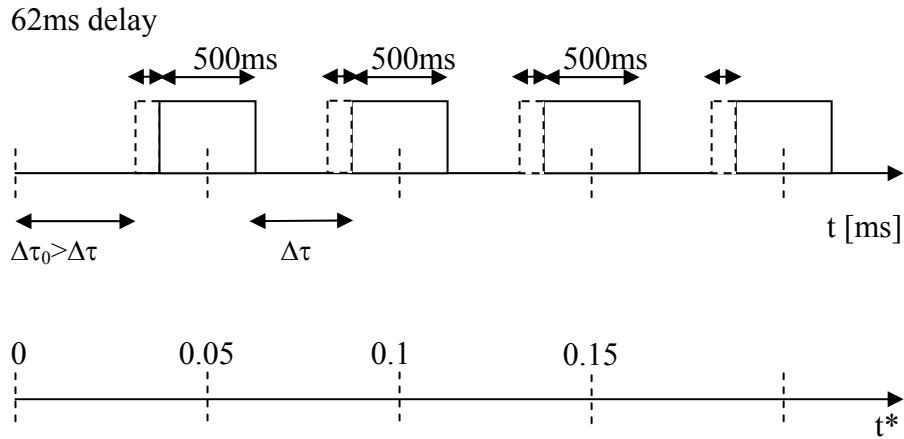
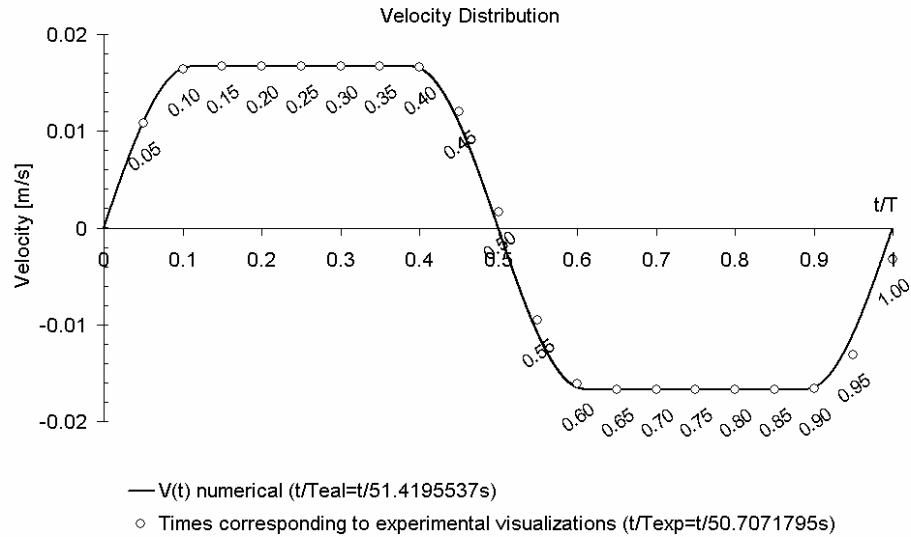
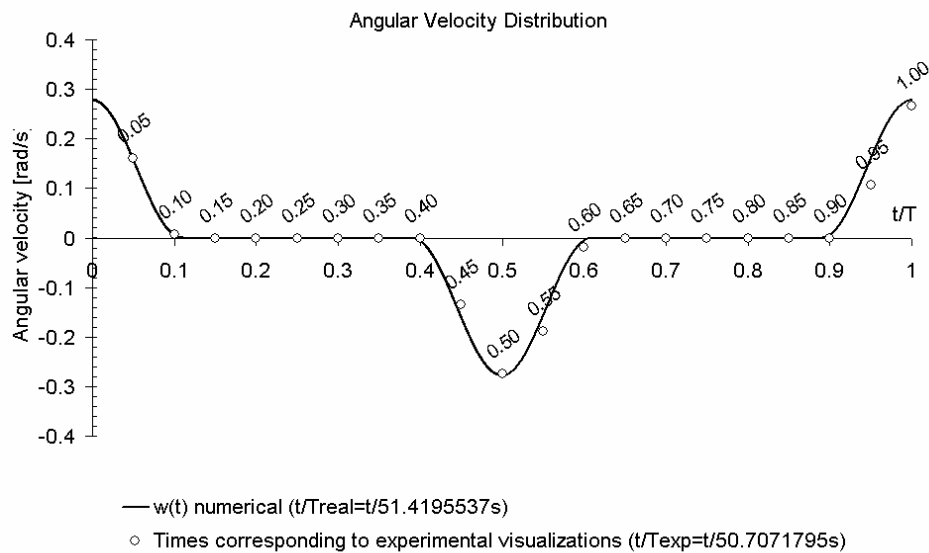


**Figure 2.14** Automatic photo taken times. A photo is taken each  $t^*$  value.

In Figure 2.15, the experimental values of velocity and angular velocity are shown in circles which corresponds to the shooting time of the photograph for  $\Delta t^*=0.05$ . The times are the values corresponding to given  $t^*=t/T_{\text{exp}}$ . The period of the experimental data is obtained by use of an oscilloscope and averaging 12 periods for 4 different measurements for  $\alpha=45^\circ$ ,  $Re=1000$  and  $x_v=2c$  case. For non-dimensionalization of time,  $T_{\text{real}}$  is used for numerical part and  $T_{\text{exp}}$  (experimental period) is used for experimental part. Flow at different periods is investigated to see when the flow reaches a quasi-steady state between different periods. In numerical calculations the results are found to be quasi-steady after 6<sup>th</sup> period and the computations are carried out in 7<sup>th</sup> period. The photos are taken during the 7<sup>th</sup> period so the 0 value on time axis corresponds to the beginning of this period. The labels near the points correspond to the non-dimensional time values. Figure 2.16 and Figure 2.17 show the velocity angle of attack distribution for  $\alpha=45^\circ$ ,  $Re=1000$ ,  $x_v=2c$  and  $\alpha=45^\circ$ ,  $Re=1000$ ,  $x_v=2.5c$  cases respectively for different  $x_a$  parameters.

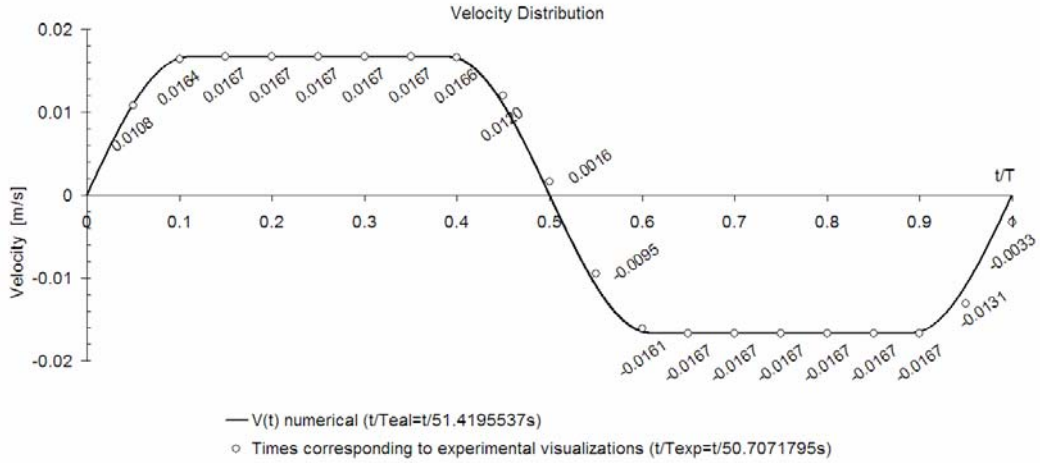


**a) Velocity distribution**

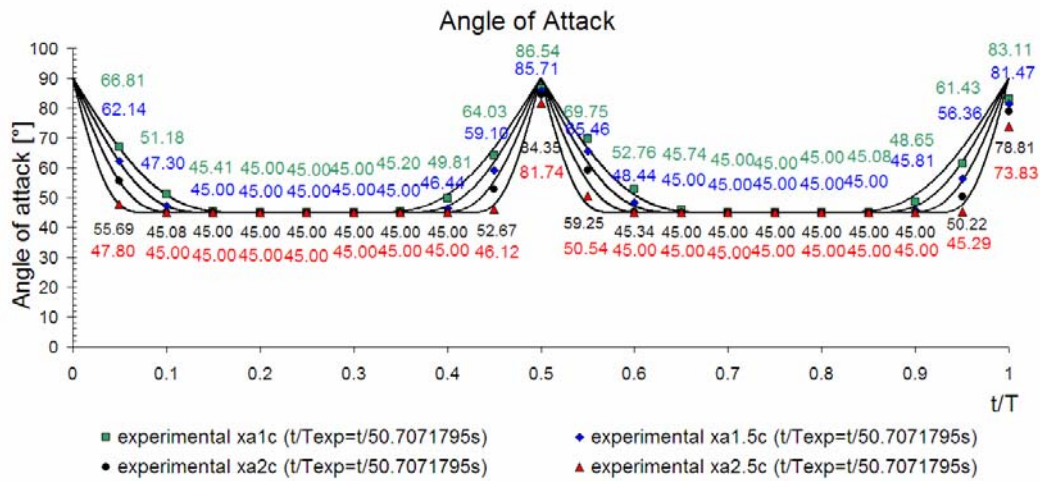


**b) Angular velocity distribution**

**Figure 2.15** Velocity and angular velocity distribution comparison for numerical and experimental data.



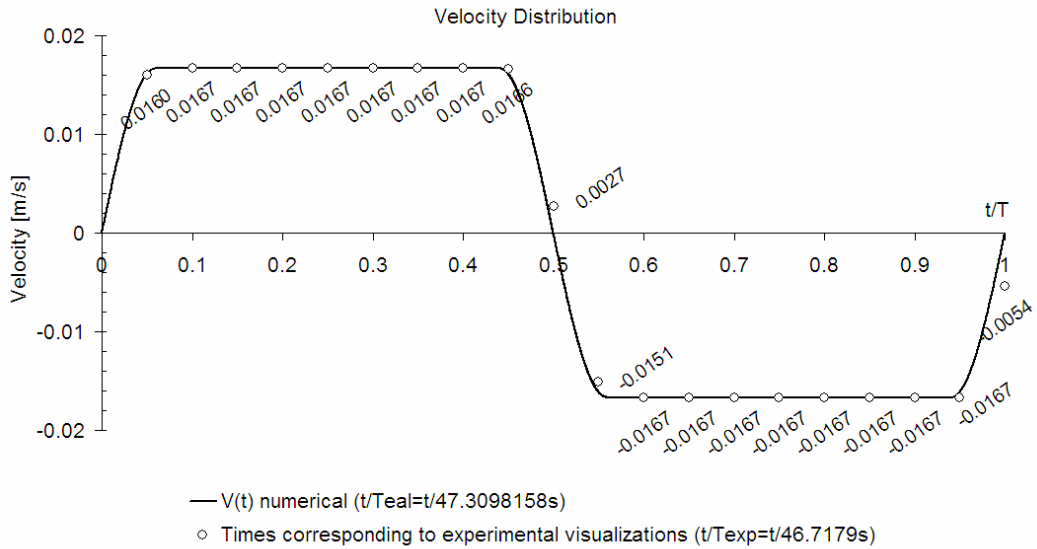
a) Velocity distribution



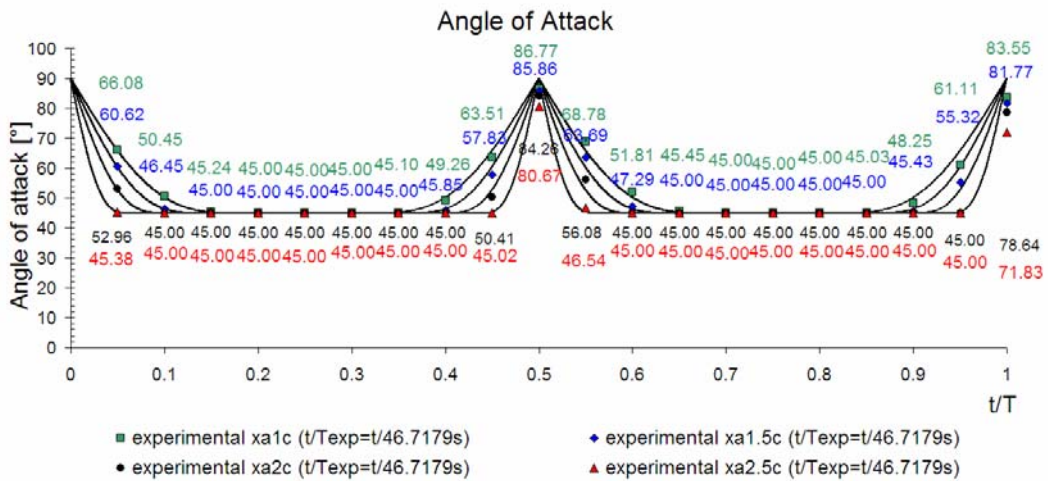
b) Angle of Attack distribution

**Figure 2.16** Velocity and angle of attack distribution for numerical and experimental data for  $\alpha=45^\circ$ ,  $Re=1000$ ,  $x_v=2c$ , for different  $x_a$  values. The values of the graph represent the velocity and angle of attack values at photo taking time. (The photos are taken during the 7<sup>th</sup> period so the 0 value on time axis corresponds to the beginning of 7<sup>th</sup> period.)





a) Velocity distribution



b) Angle of Attack distribution

**Figure 2.17** Velocity and angle of attack distribution for numerical and experimental data for  $\alpha=45^\circ$ ,  $Re=1000$ ,  $x_v=2.5c$ , for different  $x_a$  values. The values of the graph represent the velocity and angle of attack values at photo taking time. (The photos are taken during the 7<sup>th</sup> period so the 0 value on time axis corresponds to the beginning of 7<sup>th</sup> period.)

### Determination of the Flow Topology:

During the visualizations, the photos are taken with an exposure time of 500ms and the displacement of the particles during this time interval draws a part of trajectory giving an idea of the flow topology in the inertial reference frame for this specific experimental visualization. The flow topology and the trajectories are investigated during a whole period of the flapping motion.

Pathline, streamline, streakline and timeline definitions are illustrated in Figure 2.18 Pathline is the path of a particle P over a period of time. It is a long-term exposure of a tracer particle released into the flow field (Lagrange method). A streamline is a smoothly curved line that exists at an instantaneous time, along which the tangent at an arbitrary point coincides with the vector of a particle placed there, i.e., the local flow direction. Streamline give the flow directions of various particles at a particular time. It is the path through the vector field that is tangent to the vectors throughout (Euler method). Streakline is the connection of all particles passing through some point Q (such as a source). It is a simultaneous position of a set of particles released continuously from one or more sources. A streakline is a time-varying curved line (the smoothness depends on the particle release interval) connecting some particles successively released from a fixed position to reveal the change of the flow direction over time. Timeline is the connection of various particles at time t after injection from the source. It is the instant position of a batch of particles released simultaneously.

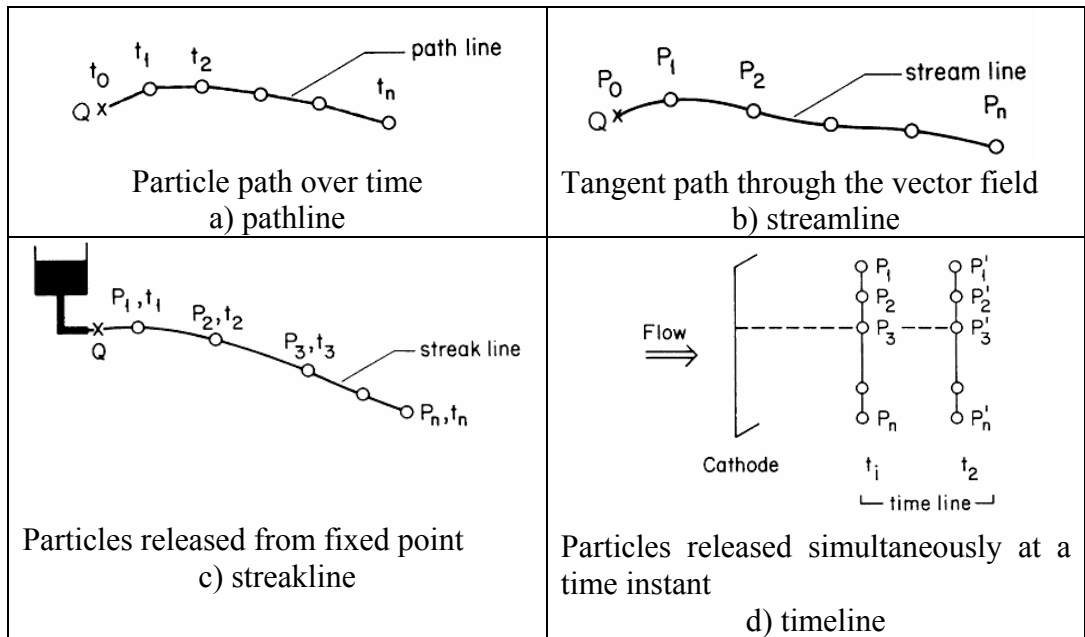


**Figure 2.18** Pathline, streamline, streakline and timeline definitions (from Ref. [60]).

Flow features may be extracted and briefly represented in terms of topology while the complete flow pattern is inferred from oriented streamlines connecting various kinds of critical points and separatrices. Critical points are those points at which the vector magnitude vanishes (Figure 2.19).

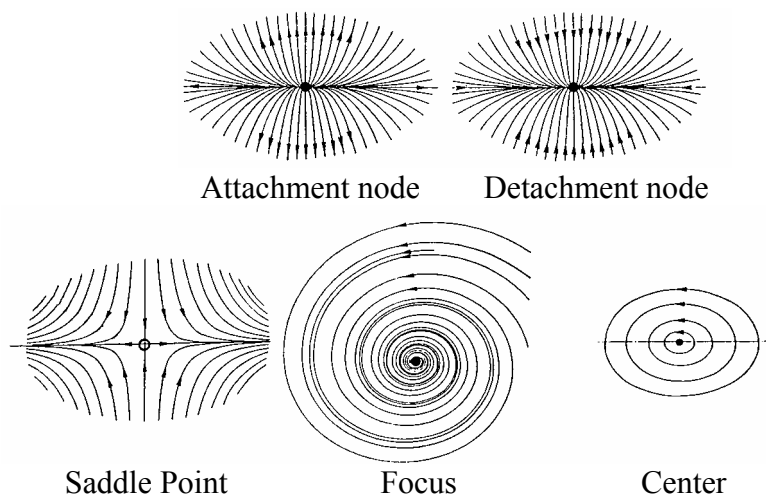


**Figure 2.19** Singularities in the flow topology (from Ref. [61]).

### 2.3.4 Particle Image Velocimetry (PIV)

Particle Image Velocimetry (PIV) is a quantitative method for measuring the instantaneous velocity fields. It is based on the measurement of the displacement of group of particles between two frames. The procedure is summarized in Figure 2.20. Acquisition corresponds to the experimental visualization including the particle seeding, illumination with laser, imaging with CCD cameras and registration of the pictures to the buffer of the computer. Then pixelization and interrogation corresponds to the PIV processing of the double frames obtained from acquisition to obtain a unique velocity field.

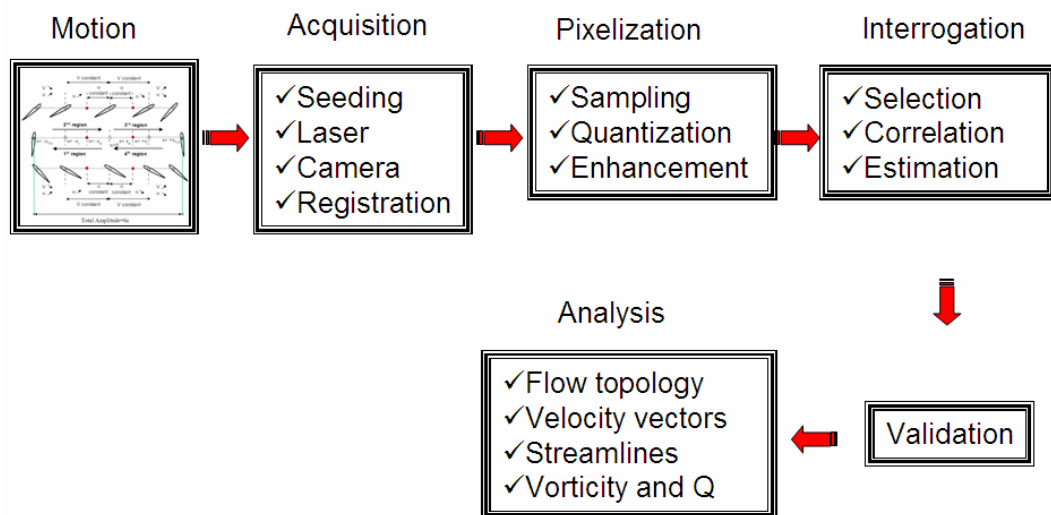


**Figure 2.20** Partice Image Velocimetry (PIV) procedure.

#### Seeding:

The same particles as the flow visualization are used with same concentration of the particles in the whole volume of the water tank being  $1.905 \times 10^{-6}$ . For the evaluation of the particle images it is assumed that the tracers follow the flow into the local flow velocity between the two illuminations (Figure 2.21).

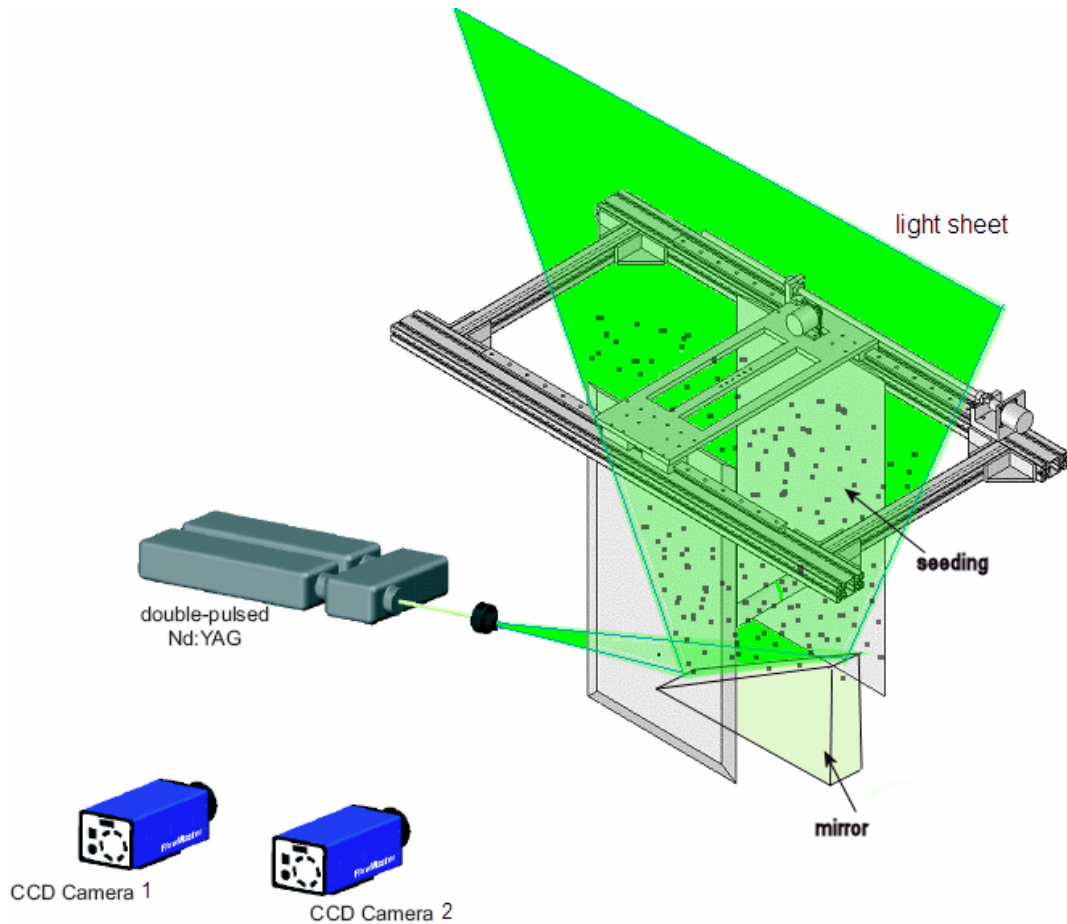
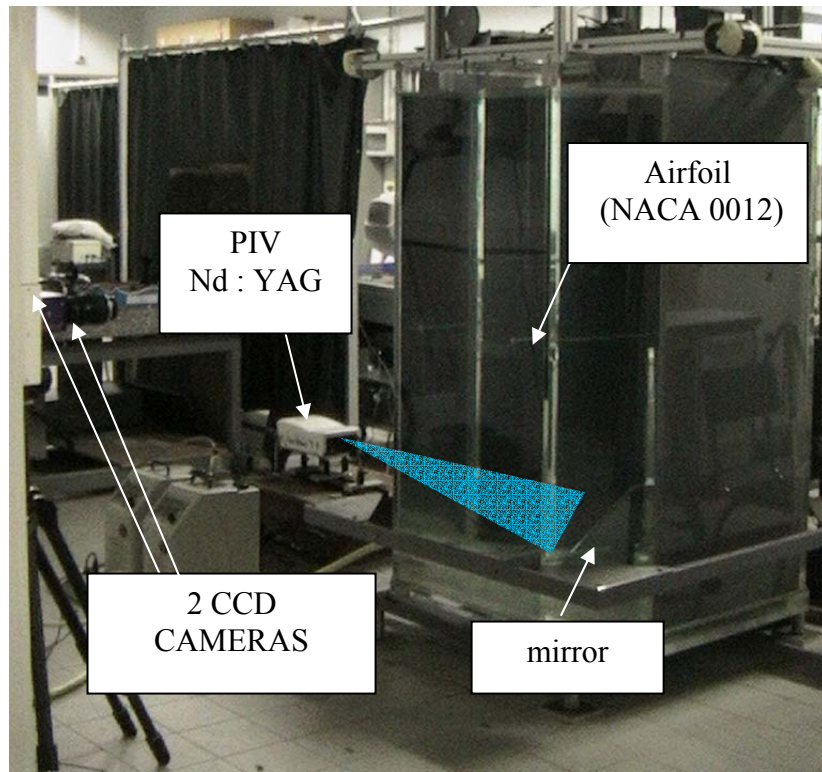


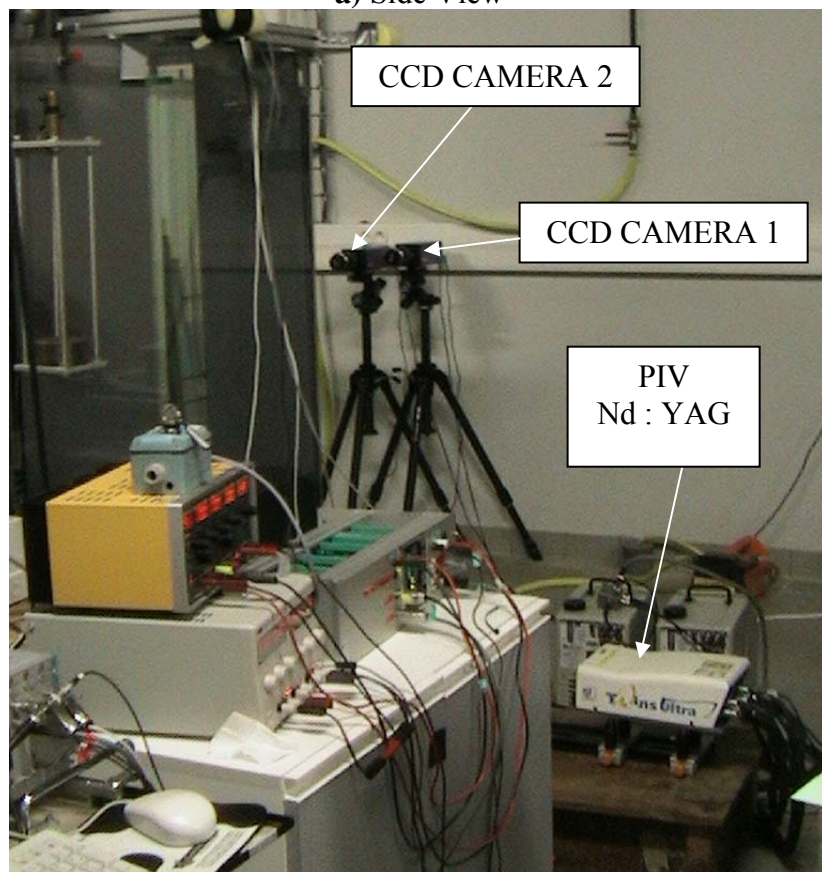
**Figure 2.21** Schematic representation of the experimental setup for PIV measurements.

### Laser:

A check for the light sheet is done to be sure to position it vertically and also at the mid location of the working airfoil section. Laser used is 30mJ pulsed Quantel Twin Ultra Nd:YAG laser. To obtain the laser sheet, a spherical lens followed by a cylinder lens is used. A mirror of 4 cm is located at the bottom center of the water tank (Figure 2.21). The mirror is inserted in order to spread the light of the laser to the whole flow domain as wide as possible and to limit the shadow generated by the model. The experimental setup and the pulsed laser are shown in Figure 2.21 and 2.22.



a) Side View



b) Front view

**Figure 2.22** Experimental set-up for PIV measurements.

### Camera:

Two intensified CCD cameras with 60 mm objectives are used in order to observe the entire flow domain with total displacement of  $6c$  length. Each time, each camera takes two photos. The time is  $81300 \mu\text{s}$  which corresponds to the separation between the two laser flashes to have a displacement of 8 pixel. The F numbers of both cameras are adjusted to 1.8.

The first image that has recorded the 1st laser pulse is moved very quickly to a non-light-sensitive storage area on the CCD. This process is called frame transfer.

The two CCD camera viewing direction is perpendicular to the light sheet. Camera scaling is performed for all of the pictures before post-processing. The distance of the cameras to the water tank is approximately 1.20m. The image magnifications for both cameras are shown in Table 2.7.

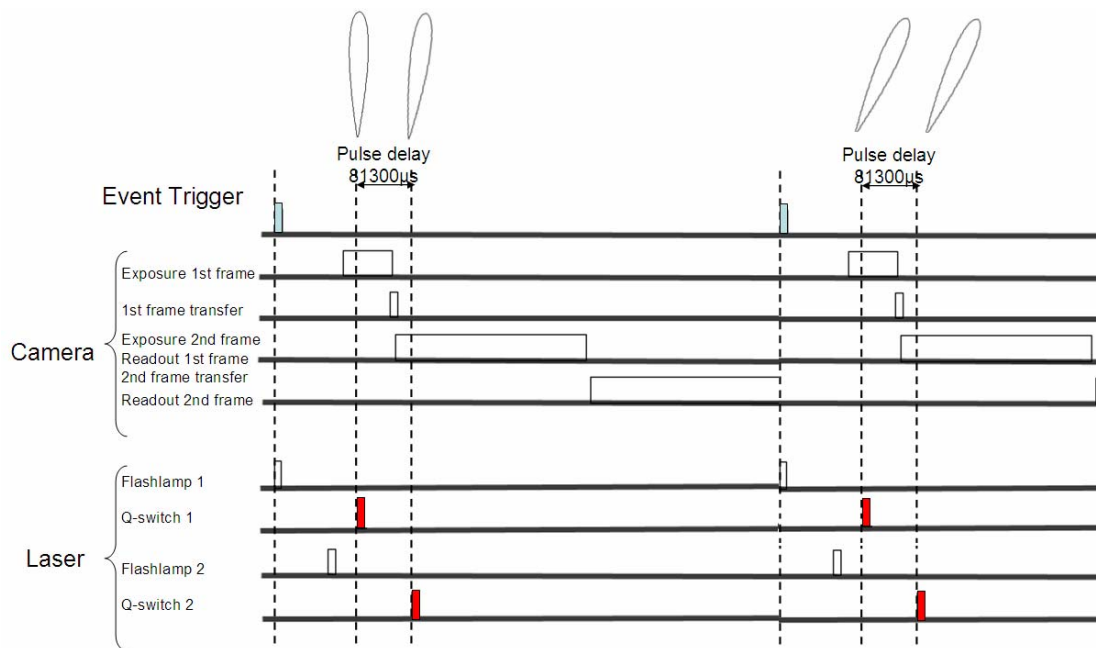
**Table 2.7** Image magnification of two CCD cameras.

	Image magnification
Camera 1	0.038
Camera 2	0.0383

### Registration and Sampling:

The non-dimensional time definition is the same as the laser visualization  $t^*=t/T$ . The evaluation of the particle images depends on the way these images have been recorded by the used camera. The scattered light from the first illumination is recorded in one frame and the scattered light from the second illumination in another frame. This is called double frame / double exposure. The trigger of the acquisition of each image is done by an external event. The trigger time is send via the new

program developed in fortran, Testpoint and ADBasic. For every image acquisition one external trigger signal is needed (Figure 2.23). At each  $\Delta t^*$ , the external trigger sends a signal of 5V to the cameras so that the first picture is taken at this time. The second frame of the picture is taken 81300 $\mu$ s later. The time interval  $\Delta t^*=0.0125$  is chosen for external trigger time of the images which makes 80 double frames per period for each camera.



**Figure 2.23** Timing for double frame cameras.

No pre-processing has been done to the PIV images since after first trials it is found that the shadow of the airfoil and the background does not influence so much the velocity vectors and the pictures are relatively good.



## Correlation:

The main objective of the image interrogation or statistical evaluation of PIV recordings is to determine the displacement between two patterns of particle images. The input signal consists of two frames (upper and lower part). The upper part of the image contains the first exposure. The lower part contains the second exposure. The PIV recordings are divided in small sub-areas (interrogation windows). The local displacement vector for the images of the first and second illumination is determined for each interrogation area by means of cross-correlation via a 2D FFT calculation (Figure 2.24). Essentially the cross correlation function statistically measures the degree of match between the two samples. The highest value in the correlation plane can then be used as a direct estimate of the particle image displacement. For good results the number of particles within one interrogation cell should be at least ten.

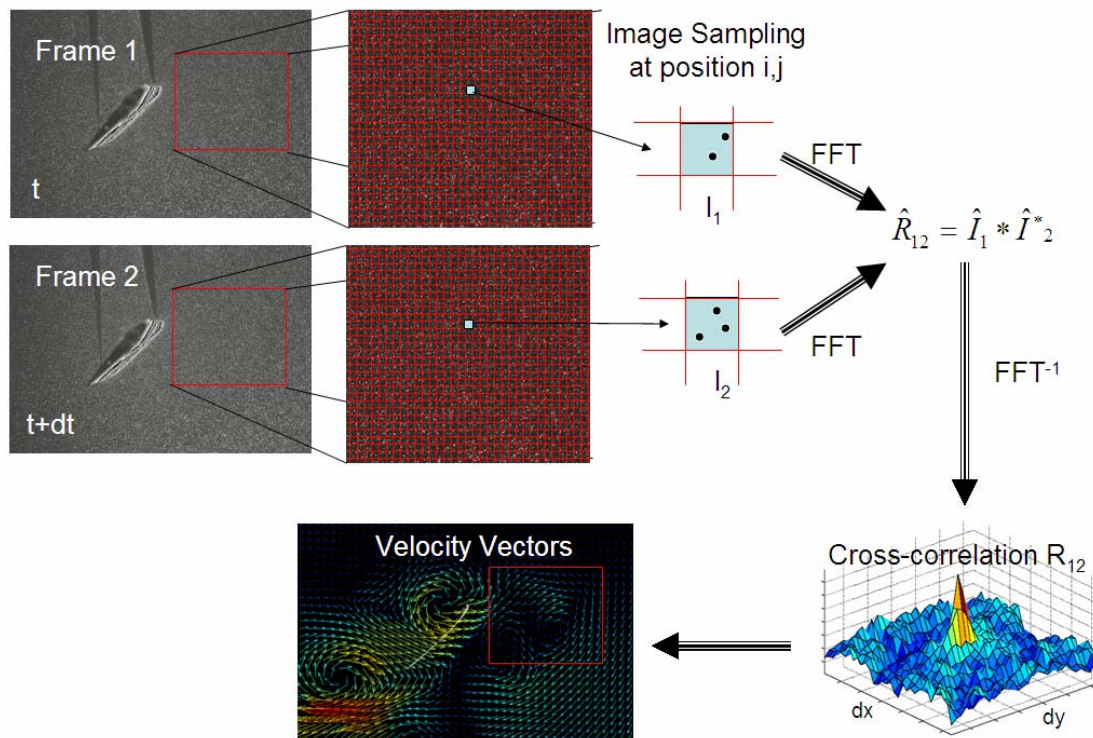


**Figure 2.24** Double frame/double exposure and cross correlation.

The cross-correlation function is defined as:

$$R_{fg}(x, y) = \int_{-\infty}^{\infty} \int_{-\infty}^{\infty} f(\xi + x, \zeta + y)g(\xi, \zeta)d\xi d\zeta \quad (2.57)$$

Since the images recorded are digitalized and are not continuous the integration become summation over the discrete samples with an image size of (M, N)

$$R_{fg} = \sum_{k=0}^M \sum_{l=0}^N f(k + m, l + n)g(k, l) \quad (2.58)$$

m, n can be positive or negative indicating shifts with respect to sampling location. FFT based correlation function is used for the PIV measurements with no zero-padding since it is quicker compared to the equation (2.58).

$$C(x, y) = \sum_{x=0, y=0}^{x<n, y<n} I_1(x, y)I_2(x + dx, y + dy), -\frac{n}{2} < dx, dy < \frac{n}{2} \quad (2.59)$$

where  $I_1$  and  $I_2$  are the image intensity of the first and second interrogation window and the 2D-array  $C$  gives the correlation strength for all integer displacements  $(dx, dy)$  between the two interrogation windows, while  $n$  is the size of the interrogation window and usually also the size of the correlation plane, i.e.  $\pm n/2$  is the maximum displacement computed.

This function is the standard cyclic FFT-based algorithm that calculates a cyclic correlation of the interrogation window which is similar but not exactly the same as the mathematical true correlation as given by the above equation. ‘Cyclic’ means that the correlation is computed as if the two interrogation windows of size  $n \times n$  are repeated again in 2D-space and on this pattern the true correlation is computed. Mathematically from the two  $n \times n$  interrogation windows the complex 2D-FFT is calculated, they are multiplied complex conjugated, and the inverse FFT is computed, which yields the cyclic correlation function.

For this study, the Adaptive multi-pass with decreasingly smaller sizes with an initial interrogation window size of  $64 \times 64$  pixels and final interrogation window size of  $32$

× 32 pixels each with two iterations with a 50% overlap of the final window option is used. The evaluation starts in the first pass with the initial interrogation window size and calculates a reference vector field. In the next pass the window size is half the previous size and the vector calculated in the first pass is used as a best-choice window shift for the second pass. In this manner the window shift is adaptively improved to compute the vectors in the following steps more accurately and more reliably as this ensures the same particles are correlated with each other even if you use small interrogation windows as less particles move inside or outside the interrogation window.

Deformation of the grid domain:

As a velocity region with a vortex is present, the cells of grid domain are deformed by considering the velocity directions of each node of the cell (Figure 2.25). The effect of the deformed interrogation window is a better signal to noise ratio of the correlation function, and increases the accuracy of the velocity measurements.

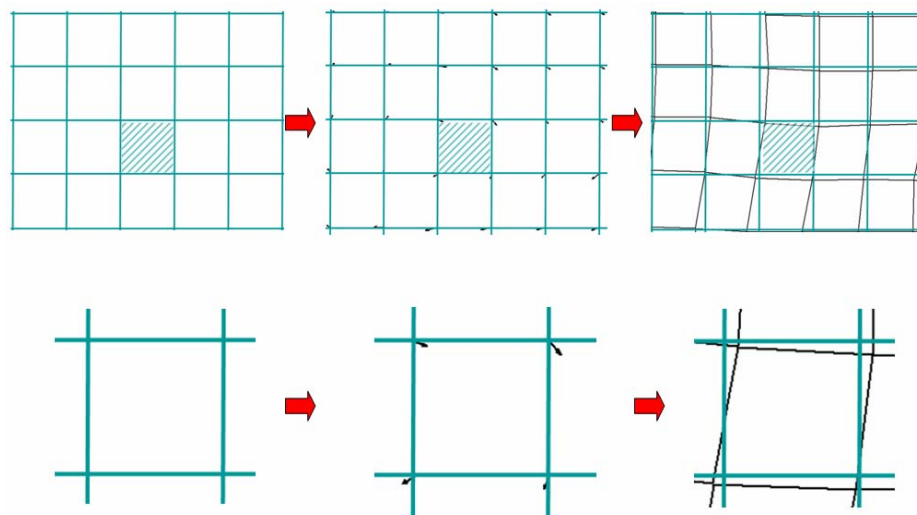


**Figure 2.25** Interrogation window deformation.

Second order difference:

Each interrogation window is shifted by the half of the velocity vector ( $du/2$ ,  $dv/2$ ) calculated in a previous iteration so that the location of the interrogation window in the second frame is shifted by  $(du/dv)$  with respect to the interrogation window in the first frame. The vector computed this way represents an average vector at a time something like  $dt/2$  in the middle between the laser pulses. This ensures a second order interpolation. The time values represented for all PIV measurements in this study correspond to the middle of the two frame times.

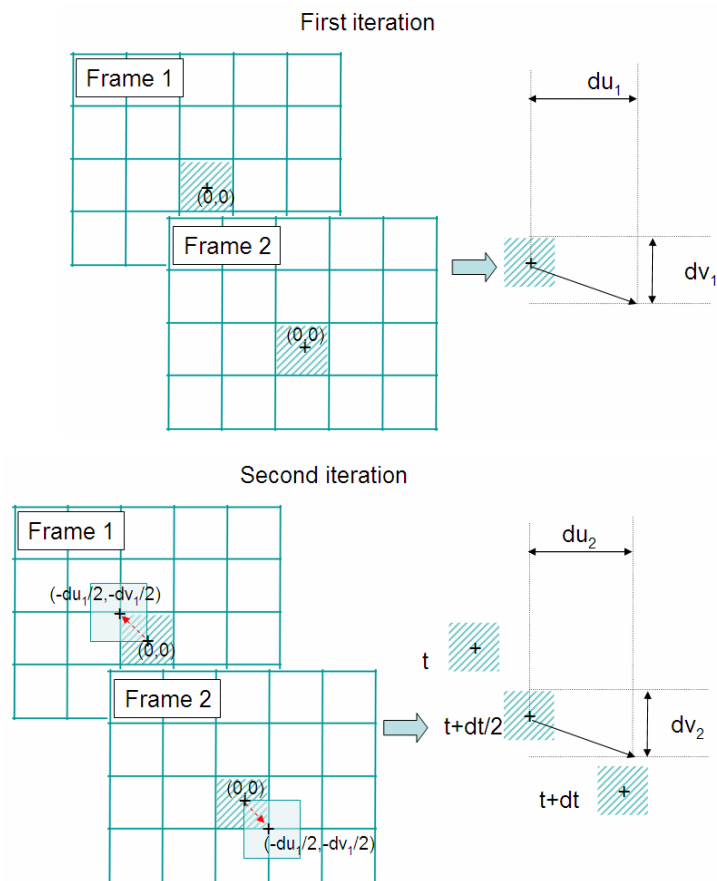


**Figure 2.26** Velocity vector located at the center of the interrogation window (second order interpolation).

### Validation of the velocities:

During processing the values  $Q > 1.3$  removed (Eq. 2.60). Also a median filter, an interpolation to fill the empty spaces which are removed and fill-up all options are used. The peak ratio factor  $Q$  is defined as:

$$Q = \frac{P1 - \min}{P2 - \min} > 1 \quad (2.60)$$

where min is the lowest value of the correlation plane and P1 and P2 are the peak heights of the first and second highest correlation peak.

The empty spaces due to the  $Q > 1.3$  criteria is 1% of the all vectors which is a very low ratio. So the three filters applied namely medial filter, fill-up empty spaces interpolation and fill-up all options do not influence at all the results.

The median filter computes a median vector from the 8 neighboring vectors and compares the middle vector with this median vector  $\pm$  deviation of the neighboring vectors (RMS value of the neighboring vectors). The center vector is rejected when it is outside the allowed range of the average vector  $\pm$  deviation of the neighbor vectors. Once the bad vectors are removed the left over empty spaces can be filled up with the interpolated vectors.

The photos obtained from two CCD cameras are put together in Tecplot to form a single domain (Figure 2.27). Then a rectangular grid domain is formed for each time step over this domain. The rectangular grid is adjusted to have the closest grid domain as the original images obtained from the cameras. Velocity at each airfoil position corresponding to each time step is calculated and imported to the top of the PIV vector domain. All the PIV domain and airfoil boundary velocities are interpolated by kriging on to the rectangular domain. The airfoil point by point velocity is also implemented in order to enforce the streamlines coming parallel to the airfoil boundary during the whole period at each time step.

Kriging is a spatial interpolation technique that assumes that the spatial variation of an attribute may consist of three components: a spatially correlated component, representing the variation of the regionalized variable; a ‘drift’ or structure, representing a trend; and a random error term. Linear drift is used for the calculations. A semivariogram is a function that determines the relationship between distance and the variance of the data. For each variable selected to krig, the variance  $\sigma^2$  is calculated across all source zones. Then, Tecplot calculates the box that will hold the entire source by finding a minimum and maximum x, y. Using this box, the length of the diagonal across the box, L, is determined.

The semivariogram model used by Tecplot is given in Equation 2.61.

$$\begin{aligned} \gamma(h) &= 0.5 * \sigma^2 * h/a * ( 3 - (h/a)^2 ) && \text{for } h < a \\ &= \sigma^2 && \text{for } h \geq a \end{aligned} \quad (2.61)$$

where  $a = L * \text{range\_fraction\_entered\_in\_kriging\_dialog}$  ( $=0.3L$ ) is the actual range and h is the distance between points.

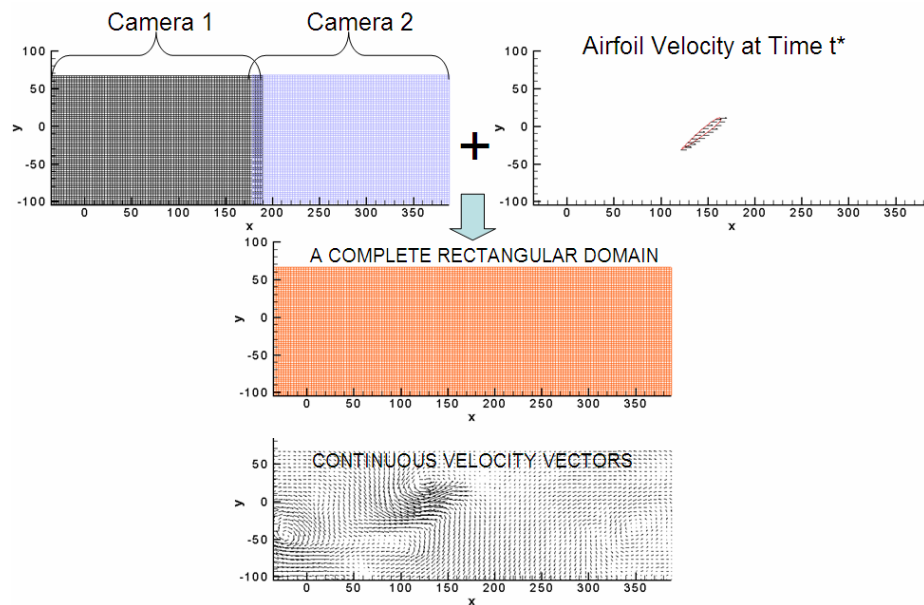


**Figure 2.27** Kriging for PIV measurements.

Estimation of the PIV accuracy:

Accuracy of the images are relative to the lots of parameters such as the perpendicularity of the cameras, scale factor, processing algorithm, particle size...which are very difficult to evaluate. One of the ways of trying to calculate the accuracy of the images is to translate one of the pictures of the measurement in very small pixels and to compare the calculated and translated values. The PIV image selected takes into account all the imperfections. The image is translated in both x and y directions with the very small displacements of  $\Delta x=0.05$  px and  $\Delta y=0.05$  px until a total displacement of  $x=1$  px,  $y=1$  px. (i.e, first photo is translated with a displacement of  $x=0.05$ px,  $y=0.05$ px; second photo is translated with a displacement of  $x=0.1$  px,  $y=0.1$  px; ...). The cross-correlation of each displaced photos with the original photo is performed one by one. The velocities are calculated only in the rectangular region selected shown in Figure 2.28. Total number of vectors in the rectangular region is 1476.

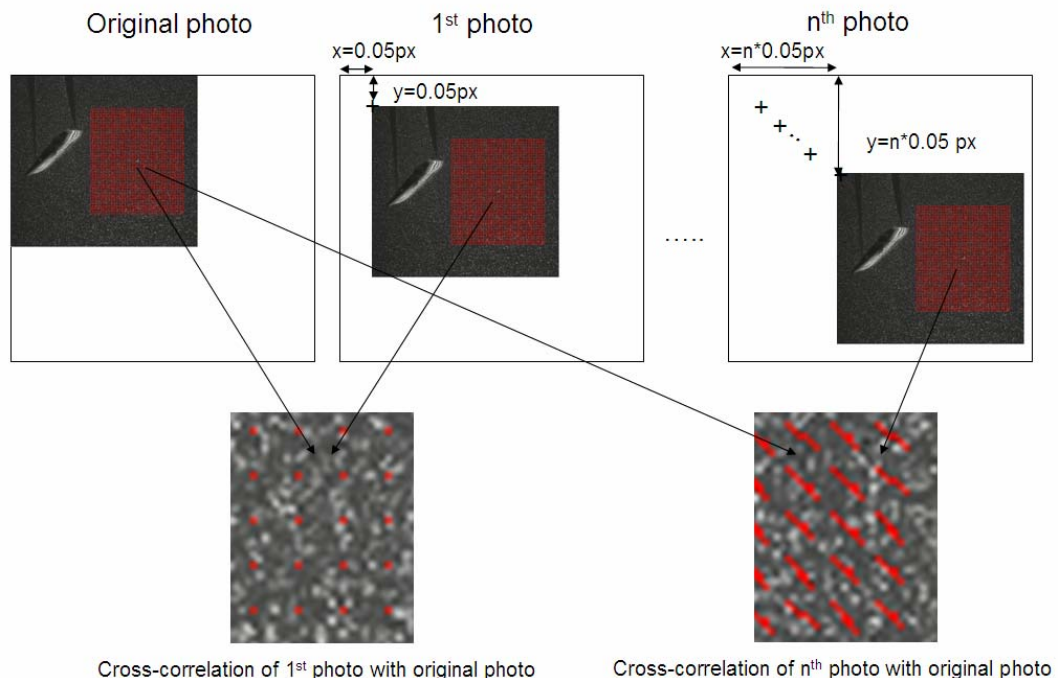
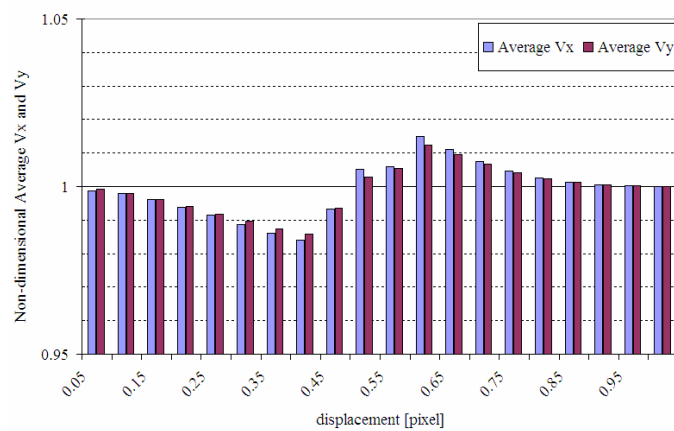


**Figure 2.28** The original photo which is correlated with the displaced photos. Each photo is translated with a displacement of  $\Delta x=0.05$  px and  $\Delta y=0.05$  px. (The displacements  $x$  and  $y$  are exaggerated in the figure for visualization purpose).

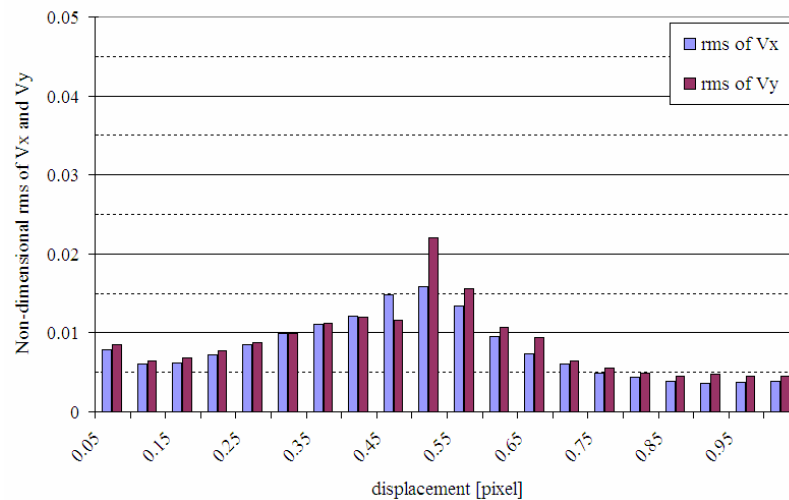
The mean and rms values of the displacement vectors in x direction, in y direction are computed in pixels and given in Figure 2.29. Both the average values and the RMS values in Figure 2.29 are non-dimensionalized with respect to the real displacements  $x$  and  $y$ . It is found that the translation imposed to the images and the displacements calculated are very close (Fig.2.29a). The maximum RMS value is less than 0.011 px.

Non-dimensional Average  $V_x$  and  $V_y$  Values for Different Displacements



a) Non-dimensional average velocities in x and y directions

Non-dimensional Root Mean Square of  $V_x$  and  $V_y$  for Different Displacements

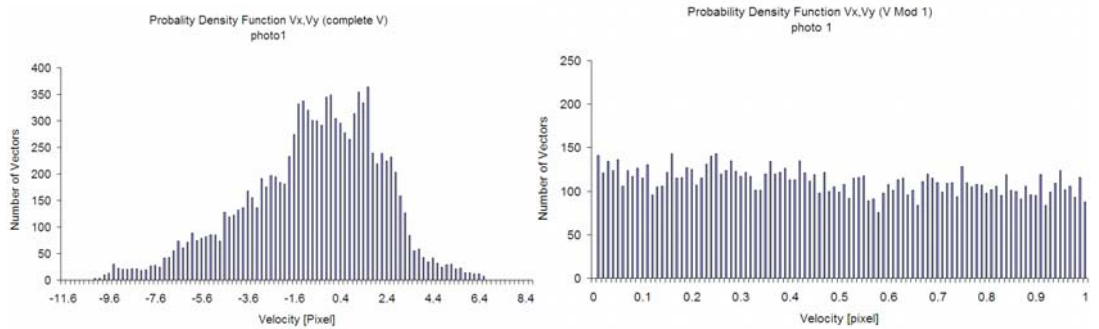


b) Non-dimensional RMS values of the  $V_x$  and  $V_y$

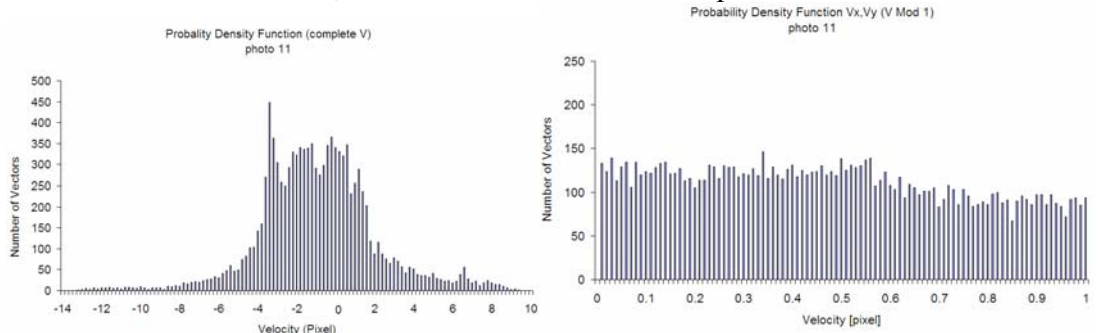
**Figure 2.29** Average velocities and root mean squares for different translational displacements.



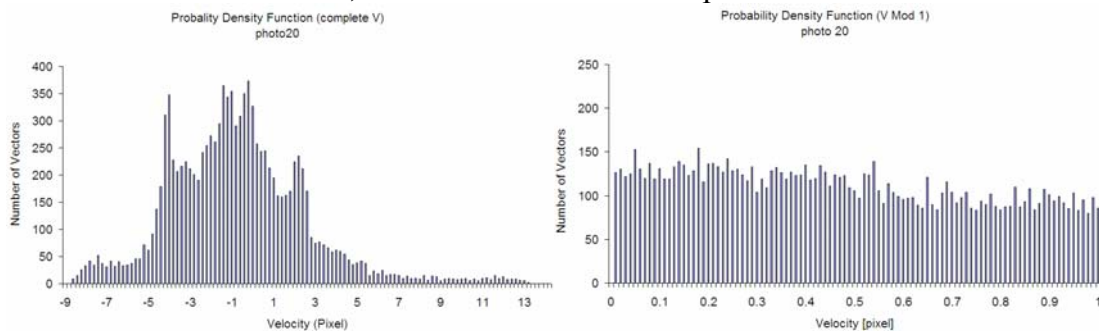
The velocity field computation could have a bias toward integer velocity values, which is called peak locking effect and this could be checked by the probability density function (PDF). PDF computes a histogram of a vector field where the x and y components of the velocity vectors are separated in certain velocity intervals (Figure 2.30). Peak locking can occur when the used seeding particles are too small and produce particle images on the CCD of less than one pixel in diameter. It is concluded that there is no peak locking at the images of the PIV measurements performed.



a) PDF of the velocities for 1<sup>st</sup> photo



b) PDF of velocities for 11<sup>th</sup> photo



c) PDF of velocities for 20<sup>th</sup> photo

**Figure 2.30** Probability density function for different PIV images.

The experimental conditions for PIV measurements are summarized in Table 2.8.

**Table 2.8** Overview of PIV measurements.

<b>Airfoil</b>	type	NACA 0012	
	chord	c=6cm	
<b>Flow</b>	fluid	water	
	Reynolds number range	1000	
	Temperature	18.3°C	
<b>Motion</b>	Period	51.4195s	
	Visualization period	$t^* \in [6,7]$	
	Parameters	$\alpha = 45^\circ, x_v = 2c, x_a = 2c$	
	Max. translational velocity	1.666cm/s	
	Max. Angular velocity	0.2778 rad/s	
<b>Seeding</b>	type	micro-spherical hallow particles of glass silver	
	Concentration	$1.905 \times 10^{-6}$	
	diameter	15 $\mu$ m	
<b>Laser</b>	type	Nd:YAG	
	Maximum power	30mJ/puls	
<b>Recording</b>	Camera type	CCD LaVision intense	
	Number of camera	2	
	Viewing angles	90°	
	Lens focal length	60 mm	
	F number	1.8	
	Frame rate	10 Hz	
	Dynamic Range	12 bit	
	$\Delta t^*$	0.0125 (80 photo/period)	
	resolution	1374 px $\times$ 1040 px	
	Image magnification	0.038	
	Exposure delay time	81300 $\mu$ s	
	Max.particle displacement	8 px	
		synchronization	Via Testpoint and ADBasic
	<b>Interrogation</b>	method	Double Frame/Double Exposure & Cross Correlation
resolution		Adaptive multi-pass with decreasingly smaller sizes initial interrogation window :64 $\times$ 64 pixels final interrogation window :32 $\times$ 32 pixels each with two iterations with a 50% overlap of the final window	

## CHAPTER 3

### NUMERICAL STUDY FOR THE INFLUENCE OF DIFFERENT PARAMETERS

#### 3.1 Configurations

The aim of this study is to analyze the influence of the different parameters to aerodynamic forces and to find optimum parameters for flapping motion studied which generate maximum force, by using numerical methods. A great number of cases are investigated involving the changes in the parameters such as angle of attack, location of start of change of incidence, location of start of change of velocity, axis of rotation, and Re number. In addition to the instantaneous aerodynamic forces, pressure distributions and vorticity contours, the average lift and drag coefficient values are also calculated.

In the calculations, air is used as the fluid, and constants used in the calculations are given in Table 3.1. Cases investigated for parametrical study are tabulated in Table 3.2 which makes approximately 216 cases. Each run is performed in three steps (i.e., two restart has been done) to get the entire calculation domain in the 7<sup>th</sup> period. The Table 3.3 shows the period and the maximum velocity during translational phase of the motion for the parametrical studies carried out for different Re numbers. The Reynolds number is based on the maximum velocity and the chord length. The quarter period is prescribed directly by defining the time  $t_v$ , displacement  $x_v$ , translational velocity  $V_o$  and maximum amplitude  $x_{T/4}$ .

$$\frac{T}{4} = \frac{\pi}{2 \cdot V_o} (x_{T/4} - x_v) + t_v \quad (3.1)$$

**Table 3.1** Constants used in the numerical calculations.

	Air	Water (for experiment)
$\mu$ [kg/m.s]	0.00001781	0.001
$\rho$ [kg/m <sup>3</sup> ]	1.225	1000
$\nu$ [m <sup>2</sup> /s]	$1.454 \cdot 10^{-5}$	$10^{-6}$
$c$ [m] (chord)	0.01	0.06
$a$ (rotation center)	$\frac{1}{4}$ or $\frac{1}{2}$ or $\frac{3}{4}$	$\frac{1}{4}$

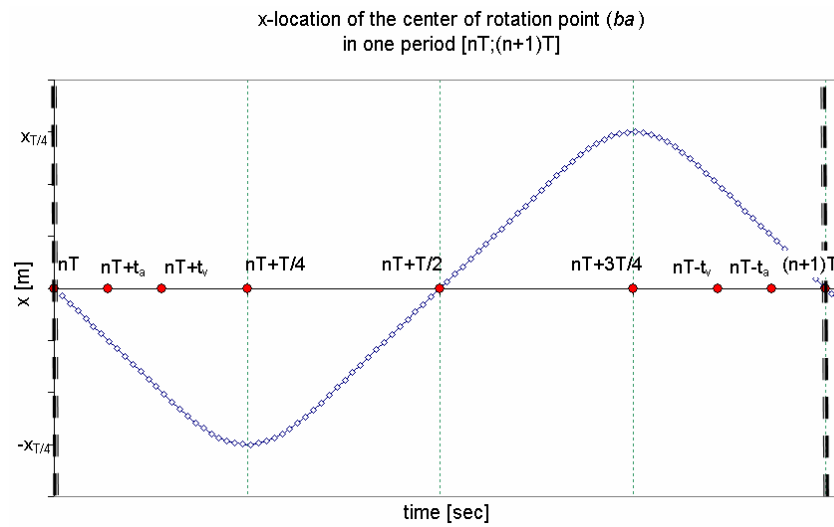
**Table 3.2** The matrix of the parameter study.

	Center of rotation, $a$		
	$\frac{1}{4}c$	$\frac{1}{2}c$	$\frac{3}{4}c$
<b>Re</b>	500, 1000, 2000	500, 1000, 2000	500, 1000, 2000
<b><math>x_v</math></b>	$2c, 2.5c$	$2c$	$2c$
<b><math>x_a</math></b>	$1c, 1.5c, 2c, 2.5c$	$1c, 1.5c, 2c, 2.5c$	$1c, 1.5c, 2c, 2.5c$
<b><math>\alpha</math></b>	$5^\circ, 10^\circ, 15^\circ, 30^\circ, 45^\circ, 60^\circ$	$5^\circ, 30^\circ, 45^\circ, 60^\circ$	$5^\circ, 30^\circ, 45^\circ, 60^\circ$

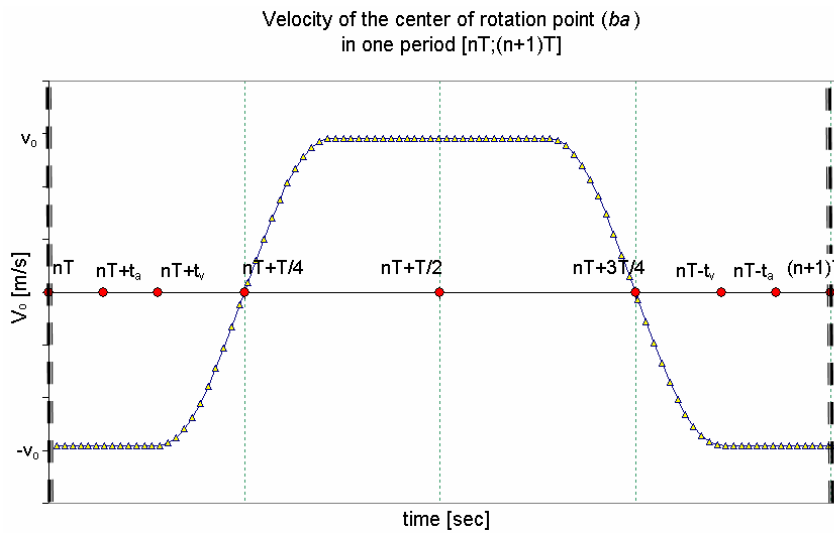
**Table 3.3** Case studies (results for configurations in air).

	Re	$V_o$ [m/s]	T [sec]
$x_{\Gamma/4}=3c$ $x_v=2c$	500	0.727	0.1965
	1000	1.454	0.098
	2000	2.908	0.049
$x_{\Gamma/4}=3c$ $x_v=2.5c$	500	0.727	0.180
	1000	1.454	0.090
	2000	2.908	0.045

Fig. 3.1 shows the x position, velocity, angle of attack and angular velocity of the airfoil at the center of rotation.

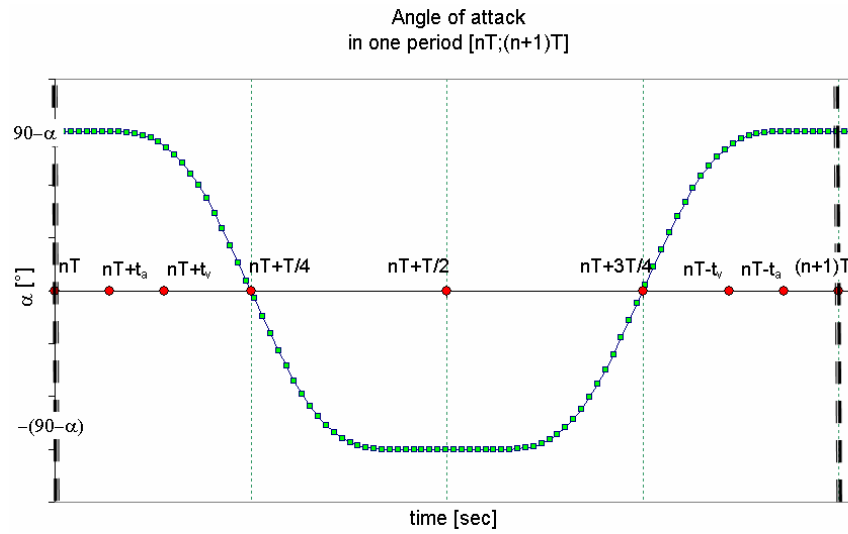


**a) Translational displacement**

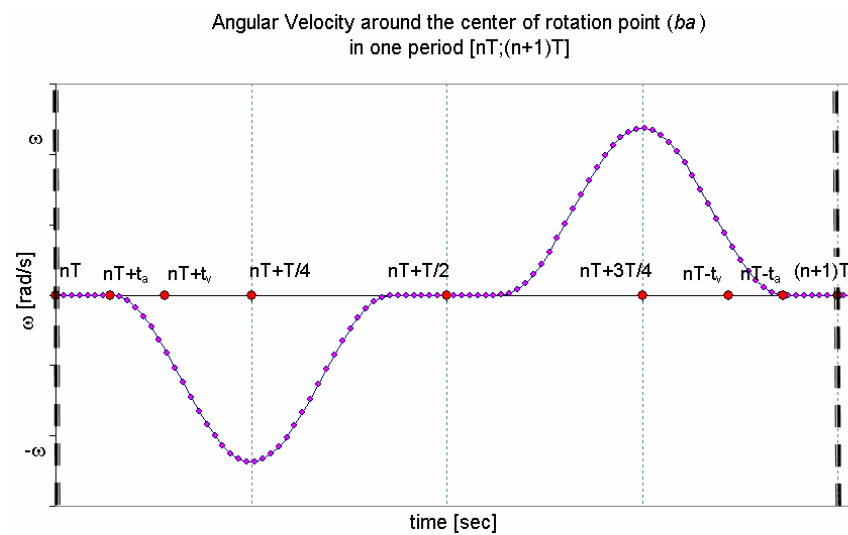


**b) Velocity**

**Figure 3.1** Kinematics of the flapping motion.



c) Angle of Attack



d) Angular Velocity

**Figure 3.1 (continued)** Kinematics of the flapping motion.

Table 3.4 shows the maximum angular velocity during the flapping motion of the studied cases. The maximum frequency and angular velocities for some cases studied are also given in the same table.

**Table 3.4** Some specifications of the case studies for  $Re=1000$ ,  $x_{T/4}=3c$ . (The table is applicable for all three center of rotations  $a= \frac{1}{4}c$ ,  $\frac{1}{2}c$  and  $\frac{3}{4}c$ )

$\alpha$	$x_v$	$x_a$	$Vo[m/s]$	$T [s]$	$T/4 [s]$	$t_v=x_v/Vo [s]$	$t_a[sec]$	<b>Max. <math>\omega</math>[rad/s]</b>	<b>Frequency <math>f=\omega/2\pi</math> [Hz]</b>
5	2c	1c	1.454	0.098	0.025	0.014	0.0069	167.8	26.71
		1.5c					0.0103	208.3	33.15
		2c					0.0138	274.6	43.71
		2.5c					0.0172	402.9	64.12
	2.5c	1c	1.454	0.090	0.023	0.017	0.0069	188.8	30.04
		1.5c					0.0103	241.6	38.45
		2c					0.0138	335.6	53.41
		2.5c					0.0172	549.2	87.41
30	2c	1c	1.454	0.098	0.025	0.014	0.0069	118.4	18.85
		1.5c					0.0103	147.0	23.40
		2c					0.0138	193.9	30.85
		2.5c					0.0172	284.4	45.26
	2.5c	1c	1.454	0.090	0.023	0.017	0.0069	133.2	21.21
		1.5c					0.0103	170.5	27.14
		2c					0.0138	236.9	37.70
		2.5c					0.0172	387.7	61.70
45	2c	1c	1.454	0.098	0.025	0.014	0.0069	88.8	14.14
		1.5c					0.0103	110.3	17.55
		2c					0.0138	145.4	23.14
		2.5c					0.0172	213.3	33.94
	2.5c	1c	1.454	0.090	0.023	0.017	0.0069	99.3	15.90
		1.5c					0.0103	127.9	20.36
		2c					0.0138	177.7	28.28
		2.5c					0.0172	290.8	46.28
60	2c	1c	1.454	0.098	0.025	0.014	0.0069	59.2	9.43
		1.5c					0.0103	73.5	11.70
		2c					0.0138	96.9	15.43
		2.5c					0.0172	142.2	22.63
	2.5c	1c	1.454	0.090	0.023	0.017	0.0069	66.6	10.60
		1.5c					0.0103	85.3	13.57
		2c					0.0138	118.4	18.85
		2.5c					0.0172	193.9	30.85

### 3.2 Effects of Starting Angle of Attack $\alpha$ and Start of Change of Incidence Position $x_a$

Figure 3.2 shows the values of the lift and drag coefficients for  $5^\circ$  starting angle of attack case where the rotation is at quarter chord location. This case is particularly used for comparison of analytical model where small angle of attack assumption is applied and has no other practical interest because of the low value of the mean lift generated.

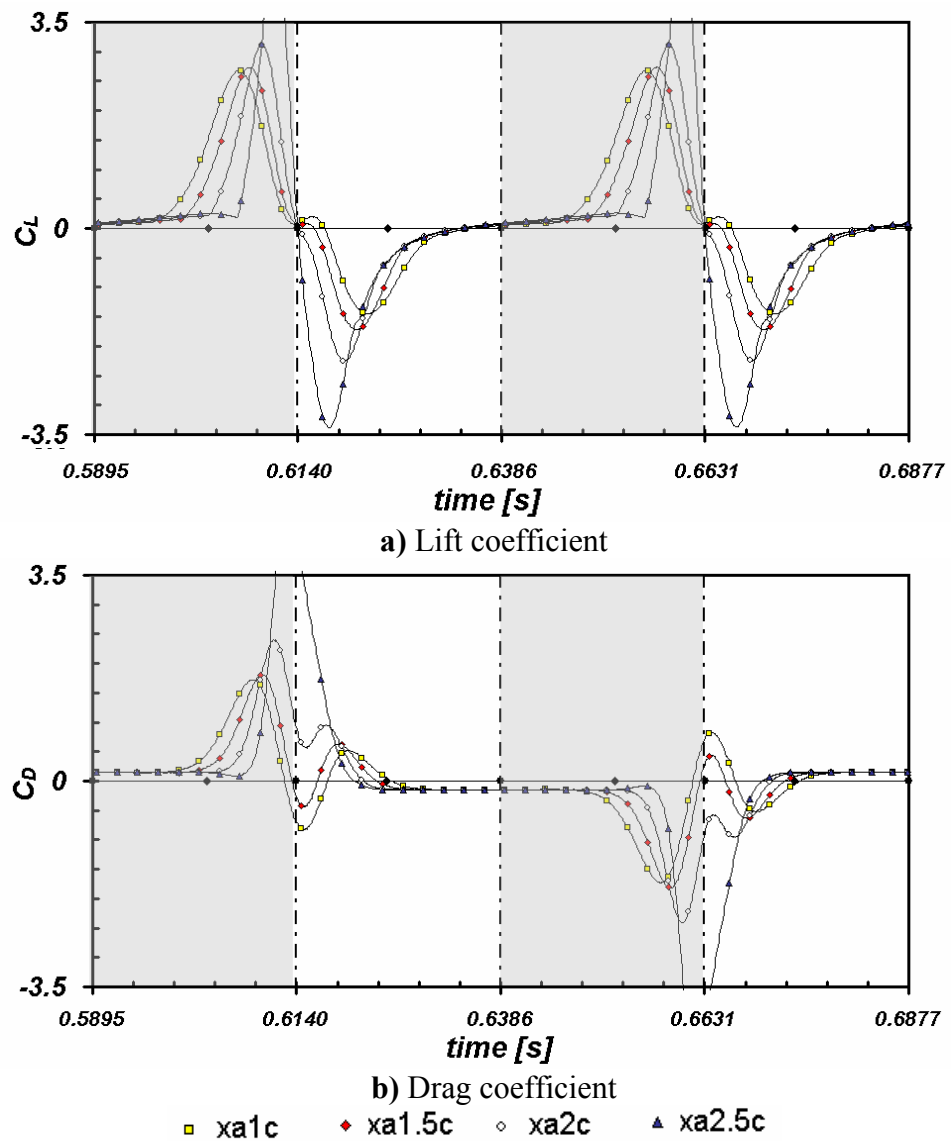
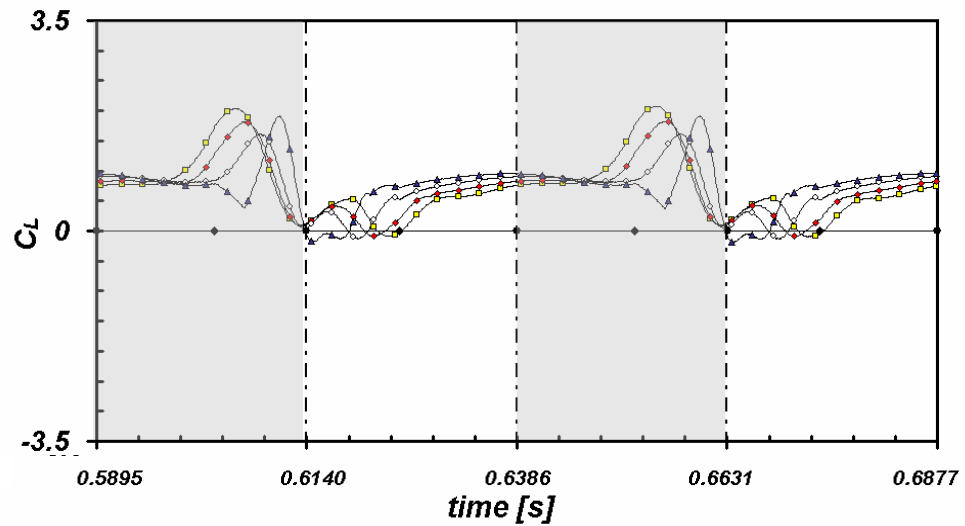


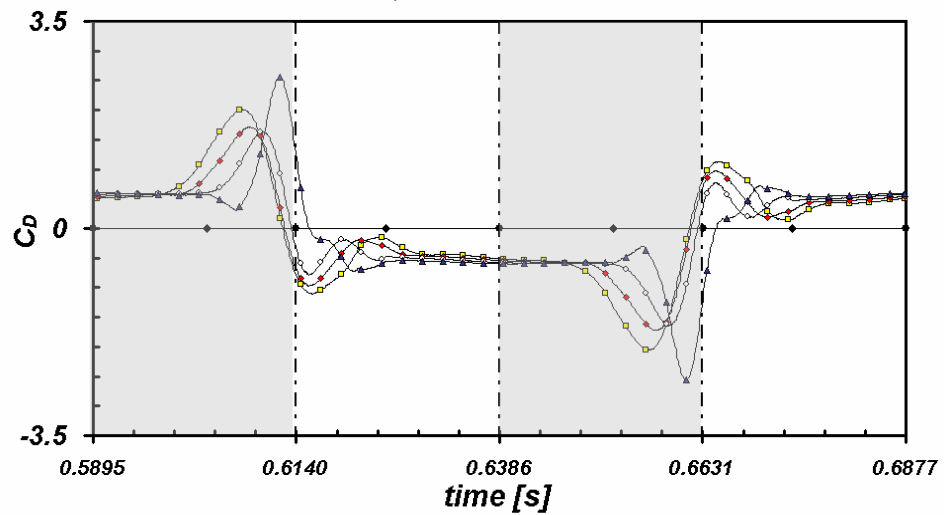
**Figure 3.2** Lift and drag coefficients for  $\alpha=5^\circ$ ,  $x_v=2c$ ,  $Re=1000$  at  $1/4c$  rotation at  $7^{\text{th}}$  period.



The lift and drag coefficients for  $30^\circ$  angle of attack are compared for different  $x_a$  locations having  $x_v=2c$  with a  $Re=1000$  (Figure 3.3). As the angle of attack increases to  $30^\circ$ , the negative lift values disappear and during the whole motion, positive lift values are obtained.



a) Lift coefficient



b) Drag coefficient

■  $x_{a1c}$     ◆  $x_{a1.5c}$     ○  $x_{a2c}$     ▲  $x_{a2.5c}$

**Figure 3.3** Lift and drag coefficients for  $\alpha=30^\circ$ ,  $x_v=2c$ ,  $Re=1000$  at  $1/4c$  rotation at  $7^{\text{th}}$  period.

Same comparison is done for  $45^\circ$  and  $60^\circ$  starting angle of attack in Fig.3.4 and Fig.3.5 respectively. It is observed that as the starting angle of attack increases the drag coefficient increases as well. Also, with further increase of the angle of attack from  $30^\circ$ , the start of half-stroke locations gives a second positive peak lift values. The peak value gets bigger as the angle of attack increases to  $60^\circ$ .

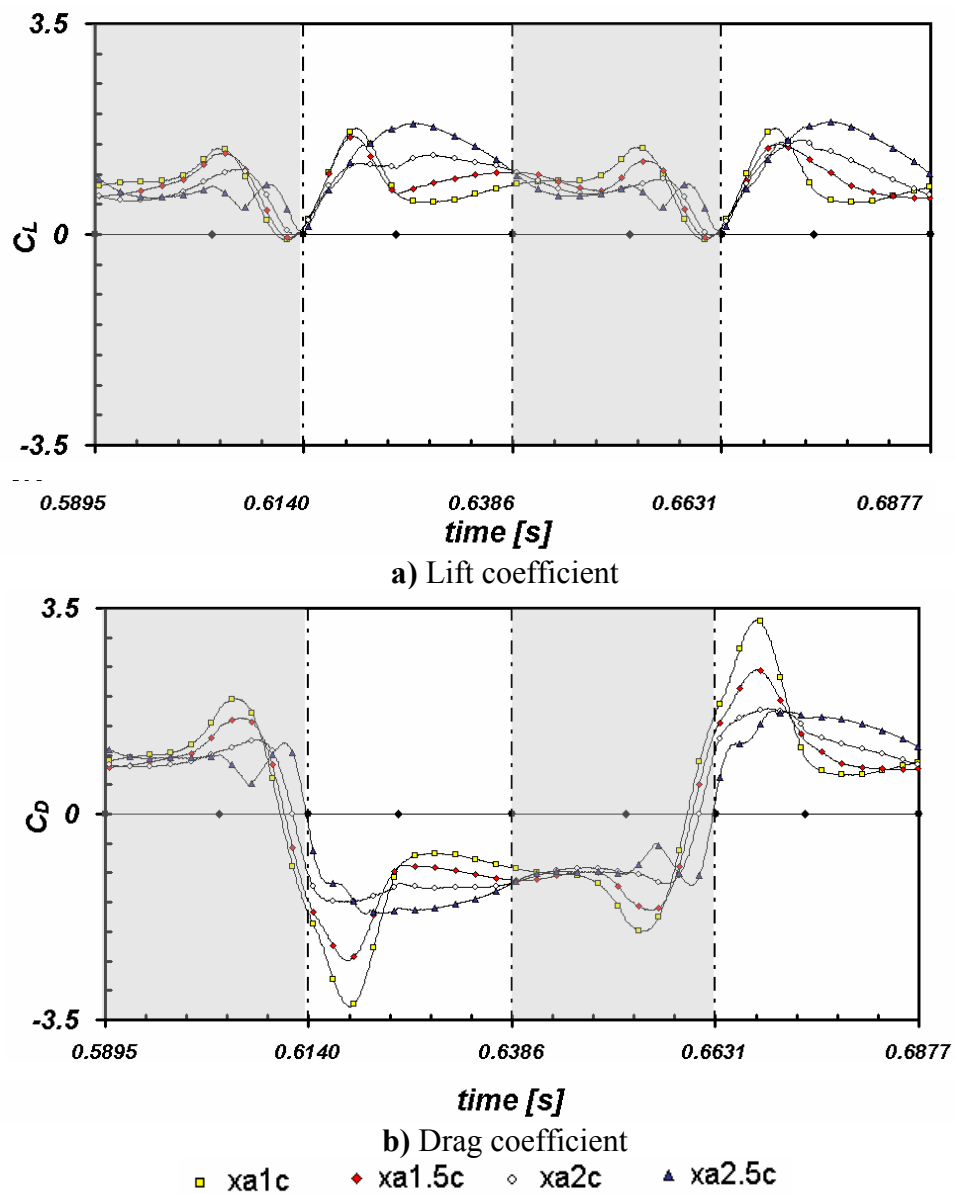
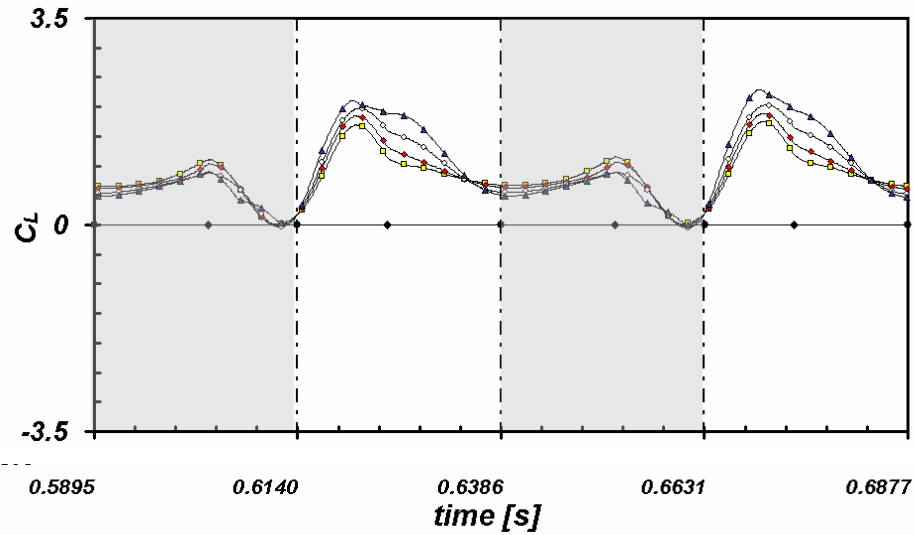
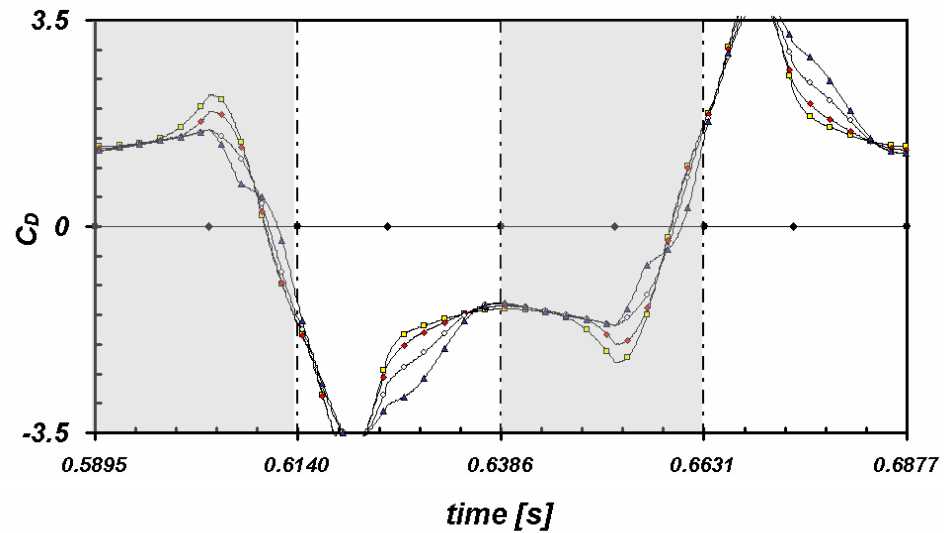


**Figure 3.4** Lift and drag coefficients for  $\alpha=45^\circ$ ,  $x_v=2c$ ,  $Re=1000$  at  $1/4c$  rotation at  $7^{\text{th}}$  period.



a) Lift coefficient



b) Drag coefficient

■ xa1c    ◆ xa1.5c    ◇ xa2c    ▲ xa2.5c

**Figure 3.5** Lift and drag coefficients for  $\alpha=60^\circ$ ,  $x_v=2c$ ,  $Re=1000$  at  $1/4c$  rotation at 7<sup>th</sup> period.

As the angle of attack increase, the first peak value at the end of the first region for lift coefficients decreases but the second peak value at the beginning of the 2<sup>nd</sup> region increases. At  $5^\circ$  angle of attack, this second peak is negative but at  $30^\circ$  we obtain a positive value and this become to be a peak at  $45^\circ$  and  $60^\circ$  angle of attacks. As  $x_a$  increase, these peaks approaches to the times corresponding to  $T/4$  and  $3T/4$ , where the velocity is zero and the airfoil is at  $90^\circ$  angle of attack at  $x=x_{max}$ .

For normal hovering, where the strokes are symmetrical, the wing strokes produce two periodic pressure pulses and these symmetric pulses are observable for all cases studied. The vortex attached to the airfoil's leading edge increases the production of lift during the translational phase of the motion. When the angle of attack is very small in translational phase as in  $5^\circ$ , negative lift peak values are obtained at the beginning of a half-stroke and a positive peak value at the end of the half-stroke (both for upstroke and downstroke).

For  $5^\circ$  angle of attack cases (Figure 3.2), it is observed that the lift distribution is variable especially during the rotational phase so this is the influence of the angular velocity change for this angle of attack regime. However, it is observed that for  $60^\circ$  angle of attack cases (Figure 3.5), the different  $x_a$  parameters do not influence the lift coefficient distribution. This comes from the fact that, for  $60^\circ$  angle of attack there is small angular velocity changes in order to reach  $90^\circ$  angle of attack at the end of the stroke.

For  $5^\circ$  angle of attack, it is also observed that the rotational phase and translational phase are two different phases. They do not influence each other in terms of the aerodynamic force coefficients. They are separate phenomena. During translational phase the Wagner function, step response on a 2-D wing in incompressible flow resulted from the impulsively changing velocity, is highly visible in an increasing manner. As the rotation starts, a peak is generated in lift and drag coefficient distributions (Figure 3.2). However as the starting angle of attack increases to  $30^\circ$ ,  $45^\circ$  and  $60^\circ$ , it is considered that the rotational phase and translational phase cannot be investigated separately, one influence the other one considerably. The widths of the peaks widen up towards the translational region in view of the lift and drag coefficient distributions.

Vorticity contours with velocity vectors are drawn approximately at quarter period of 7<sup>th</sup> stroke for 30° starting angle of attack in Fig.3.6 for different  $x_a$  locations. For this case the starting location of velocity change is at  $x_v=2c$ . For  $x_a=2.5c$  where the rotational motion starts at 2.5c distance from the origin, at this time minimum  $C_L$  value is obtained in the whole stroke, however for  $x_a$  locations corresponding to 1c, 1.5c and 2c a negative value of lift coefficient is observed. Same contours are shown for half period of 7<sup>th</sup> stroke of the flapping motion in Fig.3.7 for different starting angle of attacks. For small angles of attack, the trace of the vortices generated in the previous stroke is very small and the airfoil is entered to a weak, approximately zero velocity vector field. However, as the starting angle of attack increases, the induced velocity region due to these vorticities become more important and stronger so the profile pass through a highly induced velocity region. As a result, for 30° and 45° starting angle of attacks, the lift coefficients, as well as, the  $C_D$  values increase compared to the small angle of attack cases. As the angle increase to 60°, a decrease of lift is observed due to clockwise vorticity region (blue trace in Fig.3.7) remained from the previous stroke. The influence of this clockwise vorticity starts at 45°. In the vorticity contours, warm tones (reds) correspond to counter-clockwise vorticity and cool tones (blues) correspond to clockwise vorticity.

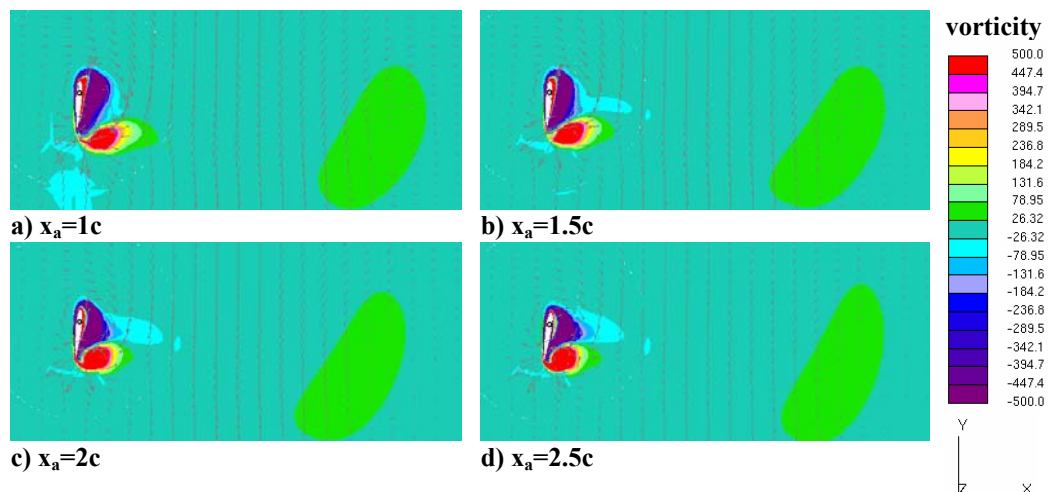


**Figure 3.6** Vorticity contours with velocity vectors for  $\alpha=30^\circ$ ,  $x_v=2c$ ,  $Re=1000$  at  $1/4c$  rotation during 7<sup>th</sup> stroke at the end of 1<sup>st</sup> region;  $t=0.614532s$  (at approximately quarter period,  $x \approx -x_{T/4}$ ).

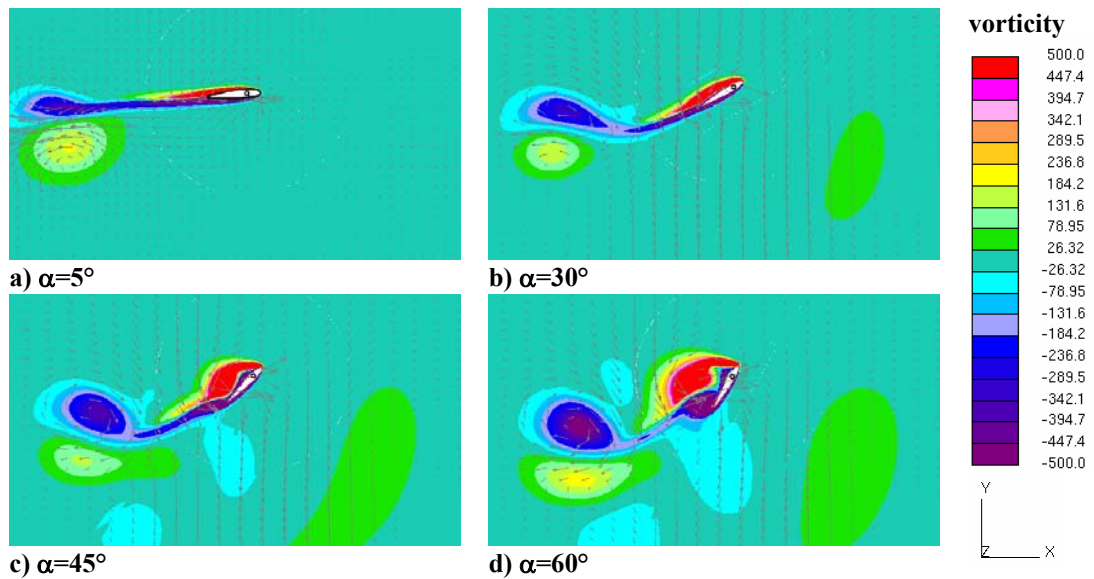


**Figure 3.7** Vorticity contours with velocity vectors for different angle of attack ( $\alpha$ ) values,  $x_v=2c$ ,  $x_a=2c$ ,  $Re=1000$  at  $1/4c$  rotation during  $7^{\text{th}}$  stroke at the end of  $2^{\text{nd}}$  region,  $t=0.639089s$  (at approximately half period,  $x \approx 0$ ).

It is also observed from Fig.3.2 that the sign of the drag coefficient does not oppose the motion direction only for  $x_a=2.5c$  where the rotational motion starts after the change of velocity position (i.e.  $x_a > x_v$ ).

The definition of thrust is a bit confusing in this case, since if we are defining thrust relative to the motion of the wings, we can say that only for  $5^\circ$  angle of attack values, we obtained some thrust data (Fig.3.2) at the beginning of the upstroke. For this definition, the drag is the force opposing to the airfoil motion and thrust is the force in the direction of motion. So during the downstroke negative  $C_D$  means thrust and during upstroke positive  $C_D$  means thrust. But if we define the thrust relative to the body of the insect/bird in hover, the thrust can also be defined as the force directing the front of the body. In this case, during both downstroke and upstroke positive  $C_D$  corresponds to thrust.

In Figure 3.8, the lift coefficients are demonstrated for same  $x_a$  locations having different angles of attack. It is obvious that as the starting angle of attack gets bigger, the negative lift region disappears. The lift peaks start just at time  $t_a$ , where the angular change occurs. At the end of 1<sup>st</sup> and 3<sup>rd</sup> regions, the amplitude of these peaks increase as the  $\alpha$  value decreases since the airfoil must reach 90° at the end of the stroke in the same time interval. So big angular velocities result high peaks in lift coefficients.

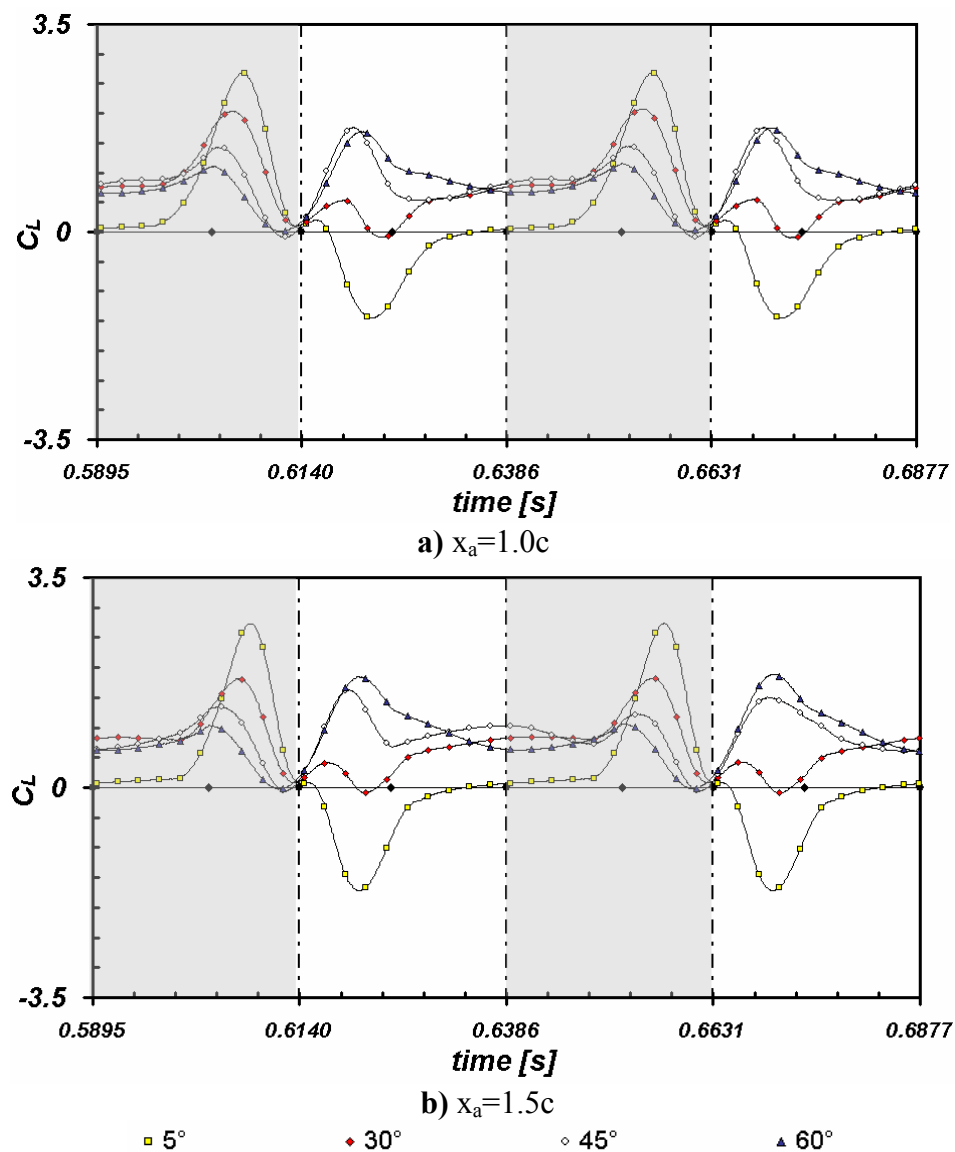
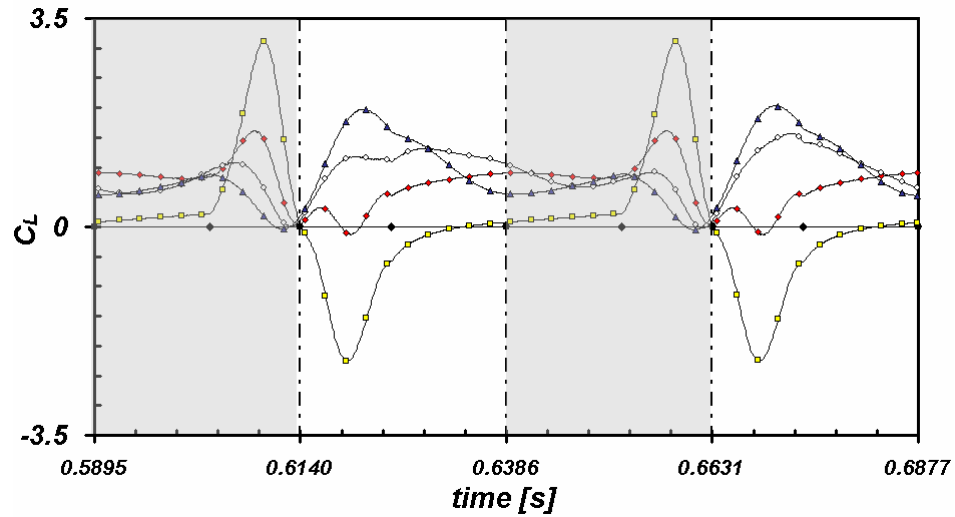
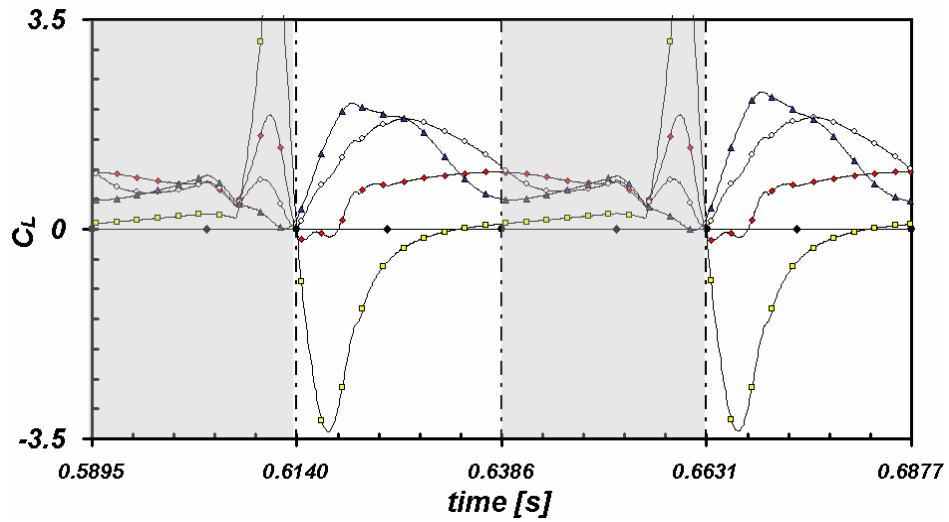


**Figure 3.8** Lift coefficients for different  $\alpha$  at  $Re=1000$ ,  $1/4c$  rotation during 7<sup>th</sup> stroke (each graph represent different  $x_a$  locations).



c)  $x_a=2c$



d)  $x_a=2.5c$

■  $5^\circ$       ◆  $30^\circ$       ◇  $45^\circ$       ▲  $60^\circ$

**Figure 3.8 (continued)** Lift coefficients for different  $\alpha$  at  $Re=1000$ ,  $1/4c$  rotation during 7<sup>th</sup> stroke (each graph represent different  $x_a$  locations).

At the beginning of 2<sup>nd</sup> and 4<sup>th</sup> regions, there exists a negative peak of lift coefficient for  $\alpha=5^\circ$  case. As the angle of attack increases to  $30^\circ$ , this peak disappears and with more increase of  $\alpha$ , it transforms to a positive peak of lift coefficient. It is observed that for  $60^\circ$  angle of attack, although the maximum lift coefficient value is bigger than all other cases, in translational region the lift coefficient value drops abruptly.



The width of the peaks occurring in lift coefficient decreases also as  $x_a$  value increases, and they become sharper in amplitude at the end of 1<sup>st</sup> and 3<sup>rd</sup> regions. But the width of the peaks forming at the beginning of 2<sup>nd</sup> and 4<sup>th</sup> regions for lift coefficient data is increasing for the same decrease of  $x_a$  value. For 60° angle of attack, the peak for lift coefficient at the end of 1<sup>st</sup> region is relatively small and change of  $x_a$  does not influence so much. For other  $\alpha$  values, as the  $x_a$  location increases, the peak value shifts toward the quarter-period location. Fig.3.9 shows the drag coefficients for same configurations as Fig.3.8.

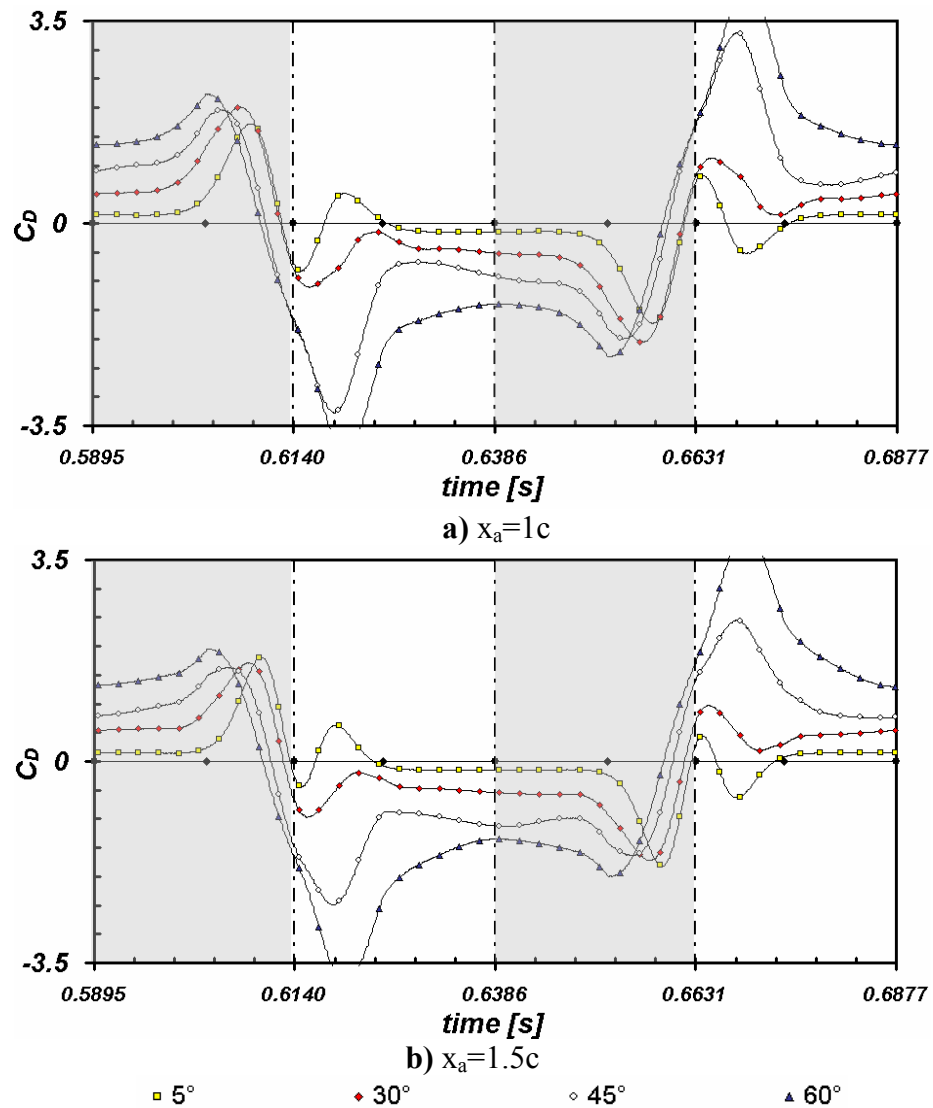


**Figure 3.9** Drag coefficients for different  $\alpha$  at  $Re=1000$ ,  $1/4c$  rotation during 7<sup>th</sup> stroke (each graph represent different  $x_a$  locations).

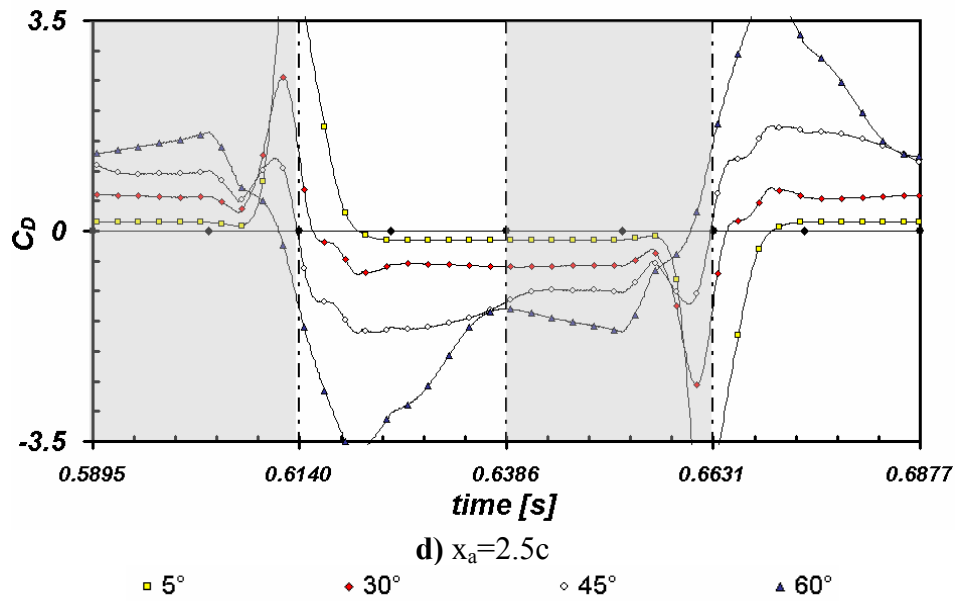
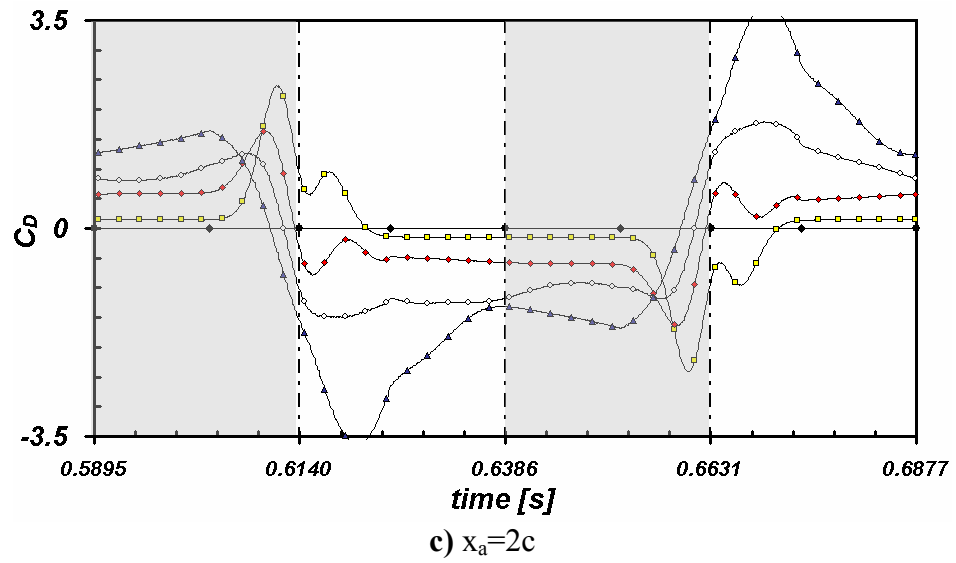


**Figure 3.9 (continued)** Drag coefficients for different  $\alpha$  at  $Re=1000$ ,  $1/4c$  rotation during 7<sup>th</sup> stroke (each graph represent different  $x_a$  locations).

Figure 3.10 shows vorticity distribution with velocity vectors. Different time instants are represented for  $x_a=1c$  (A),  $x_a=1.5c$  (B),  $x_a=2c$  (C),  $x_a=2.5c$  (D). It is observed that, as the  $x_a$  location increase, the cores of the translational vortices are located toward upwards (Fig.3.10a). The angle between the core of the counter rotating vortices are also shifting from the vertical axis as  $x_a$  increases. The trace of the translational vortex from the previous stroke disappears more as the rotation of the airfoil is done quicker, more distinguishable in Figure 3.10f.

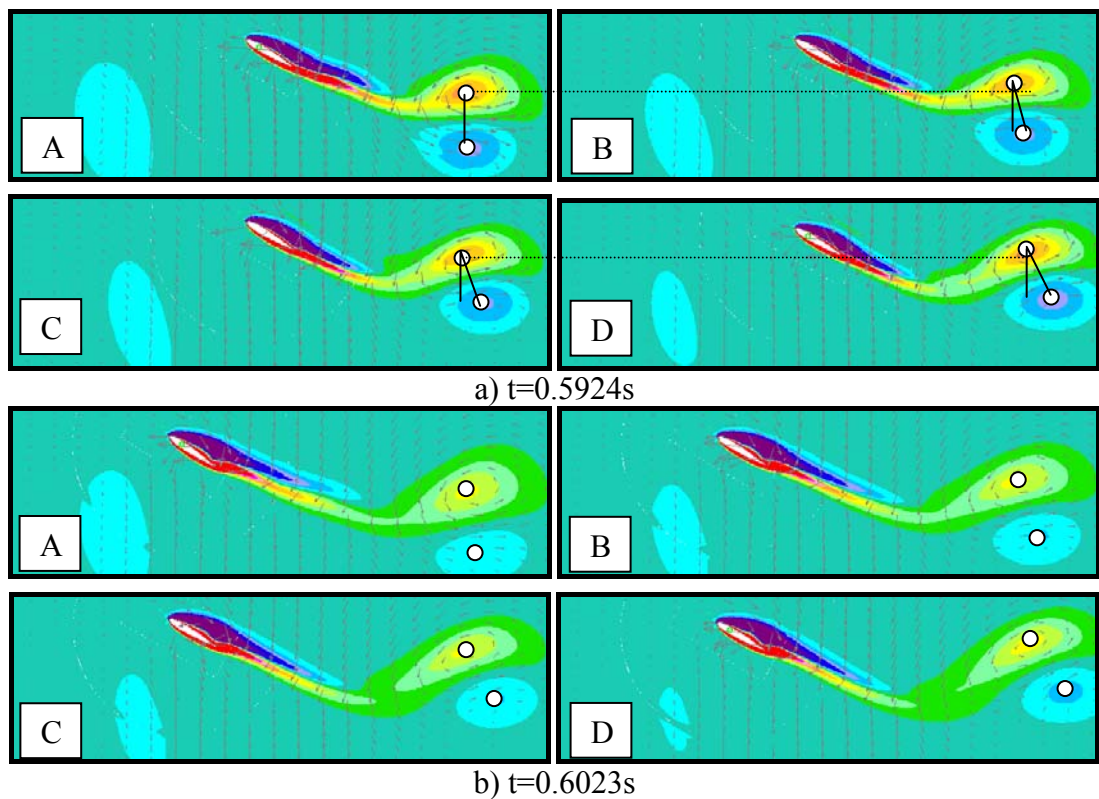


**Figure 3.10** Vorticity contours with velocity vectors for  $\alpha=30^\circ$ ,  $x_v=2c$ ,  $Re=1000$  with rotation axis at  $1/4c$  during 7<sup>th</sup> stroke. A)  $x_a=1c$ , B)  $x_a=1.5c$ , C)  $x_a=2c$ , D)  $x_a=2.5c$  [Vorticity contours have the same scale as Fig.3.6 or 3.7]

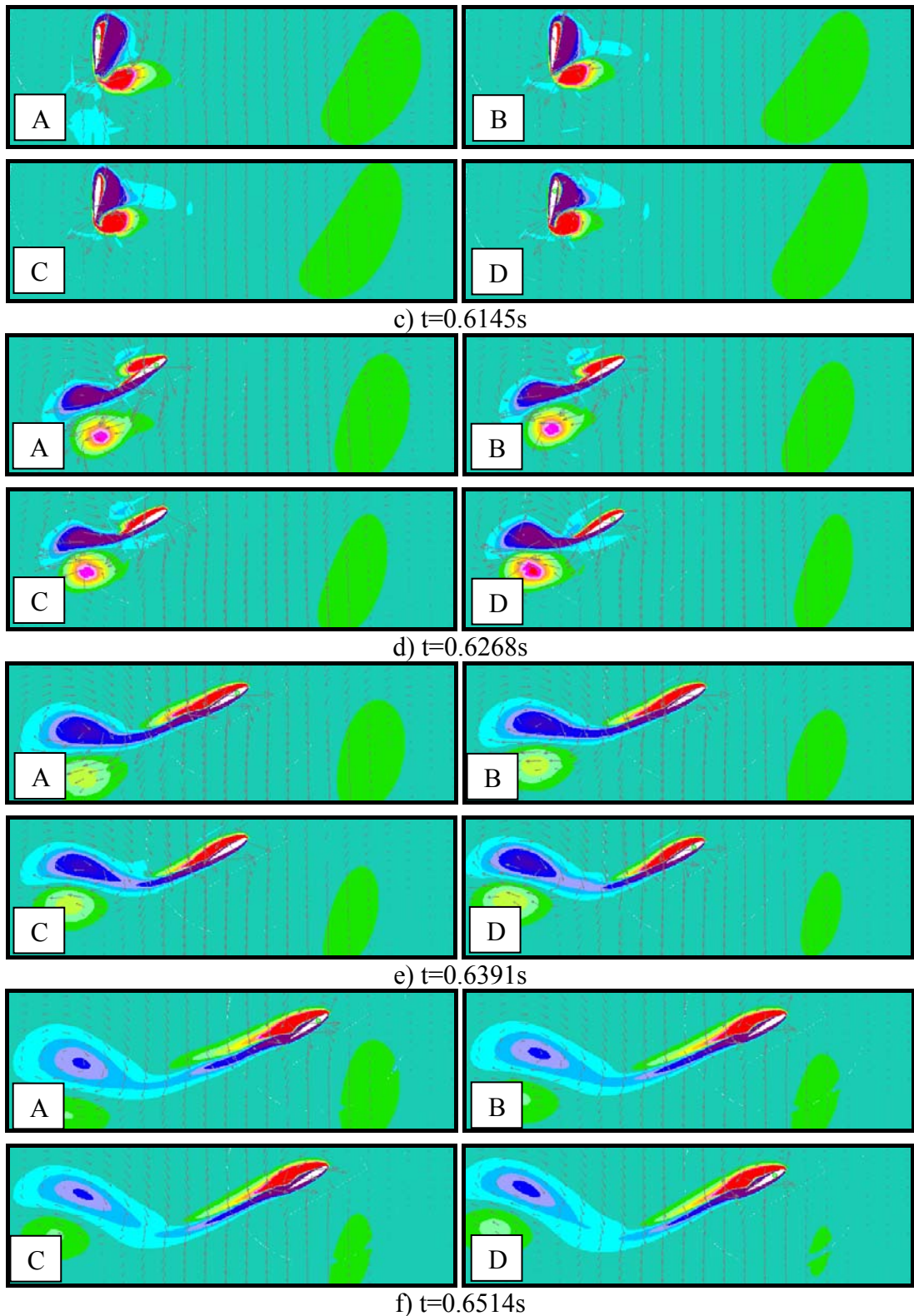


**Figure 3.10 (continued)** Vorticity contours with velocity vectors for  $\alpha=30^\circ$ ,  $x_v=2c$ ,  $Re=1000$  with rotation axis at  $\frac{1}{4}c$  during 7<sup>th</sup> stroke. A)  $x_a=1c$ , B)  $x_a=1.5c$ , C)  $x_a=2c$ , D)  $x_a=2.5c$  [Vorticity contours have the same scale as Fig.3.6 or 3.7]

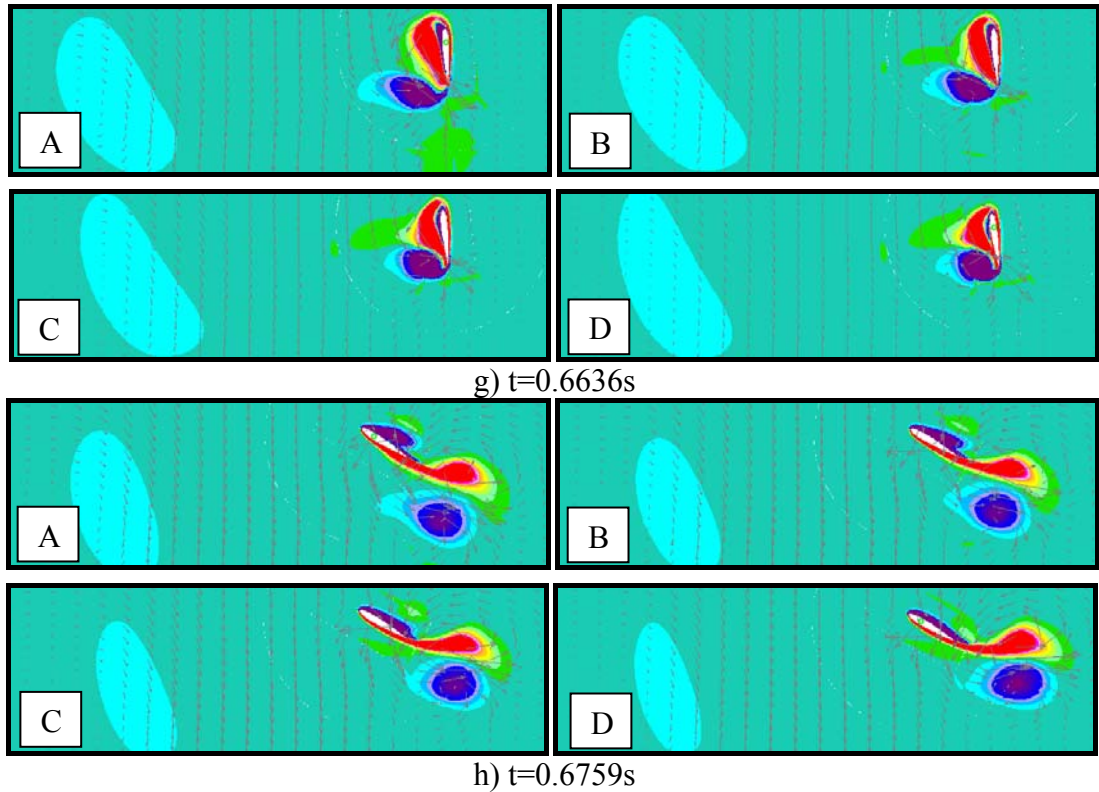


**Figure 3.10 (continued)** Vorticity contours with velocity vectors for  $\alpha=30^\circ$ ,  $x_v=2c$ ,  $Re=1000$  with rotation axis at  $\frac{1}{4}c$  during 7<sup>th</sup> stroke. A)  $x_a=1c$ , B)  $x_a=1.5c$ , C)  $x_a=2c$ , D)  $x_a=2.5c$  [Vorticity contours have the same scale as Fig.3.6 or 3.7]

Table 3.5 shows maximum force coefficients (lift, drag and normal force coefficients) in comparison with the maximum angular velocity values during the flapping motion of the corresponding case. The 16 case shown are also represented in Figure 3.11. For a fixed angle of attack case, it is obvious that for all of the cases studied maximum lift occurs when the maximum angular velocity is highest. For  $5^\circ$  angle of attack case, the increasing behavior of the maximum angular velocity is exactly observable on the aerodynamic force coefficients, which validate the fact that for  $5^\circ$  angle of attack the rotational and translational phase does not influence each other. For the other angle of attacks, although the maximum angular velocity at  $x_a=1.5c$  is bigger than the  $x_a=1c$  case, there is a decrease of the aerodynamic force coefficients. Same decrease also continue for  $x_a=2c$ . At  $x_a=2.5c$ , the angular velocity become more important as in the case of  $5^\circ$  angle of attack. There is an increase of lift and drag coefficients for all of the  $x_a=2.5c$  cases.

**Table 3.5** Maximum lift and drag coefficients and the maximum angular velocity values corresponding to different angles of attack for  $Re=1000$ ,  $x_v=2c$ .

Case	$\alpha$	$x_v$	$x_a$	Max. $\omega$ [rad/s]	$C_{L\ MAX}$	$C_{D\ MAX}$	$C_{N\ MAX}$
1	5	2c	1c	167.7979	2.67891	1.72444	3.0641
2			1.5c	208.3132	2.73298	1.81429	3.12447
3			2c	274.6213	3.10807	2.40271	3.64208
4			2.5c	402.8536	4.73188	5.07541	6.06383
5	30	2c	1c	118.4456	2.03744	2.01151	2.78457
6			1.5c	147.0446	1.81121	1.71208	2.42593
7			2c	193.8503	1.61307	1.63792	2.22139
8			2.5c	284.3672	1.91435	2.55142	3.00906
9	45	2c	1c	88.8342	1.76451	3.29291	3.69017
10			1.5c	110.2834	1.50634	2.45035	2.83103
11			2c	145.3878	1.57313	1.79558	2.31802
12			2.5c	213.2754	1.86831	1.75627	2.48647
13	60	2c	1c	59.2228	1.88982	3.9588	4.3682
14			1.5c	73.5223	1.50634	2.45035	2.83103
15			2c	96.9252	2.04132	3.78376	4.29013
16			2.5c	142.1836	2.29159	4.07758	4.67711

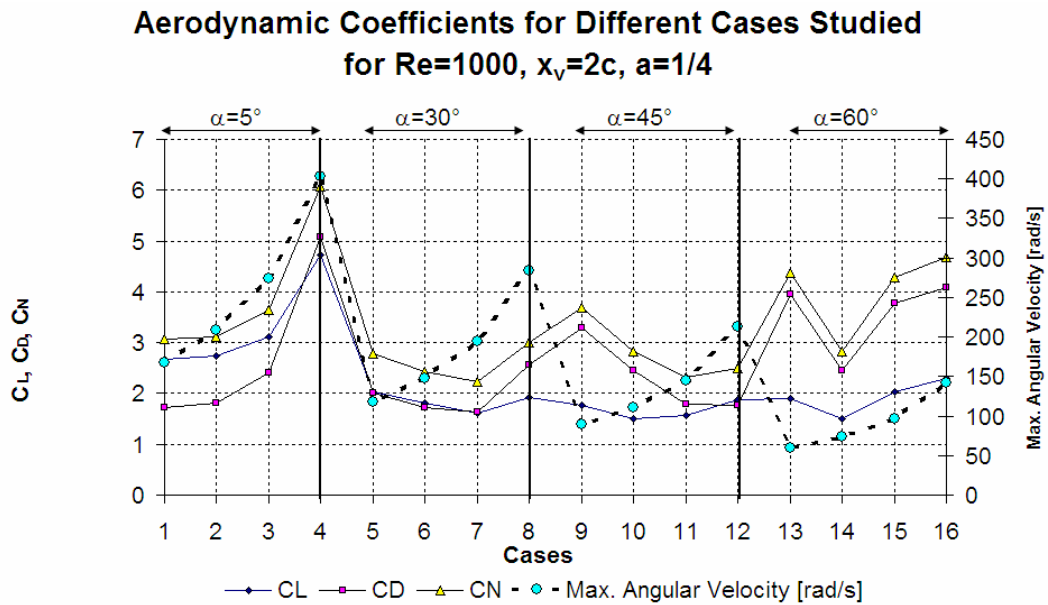


**Figure 3.11** Maximum force coefficients and angular velocity of the airfoil during the flapping motion.

### 3.3 Effects of the Translational Acceleration/Deceleration Position $x_v$

In addition to the position of the angle of attack change ( $x_a$ ), the position of the velocity decrease/increase ( $x_v$ ) is also investigated as a parameter. From Figure 3.12 to Figure 3.15, the lift and drag coefficients for different  $x_a$  locations are shown for comparison of  $x_v=2c$  and  $x_v=2.5c$  cases.

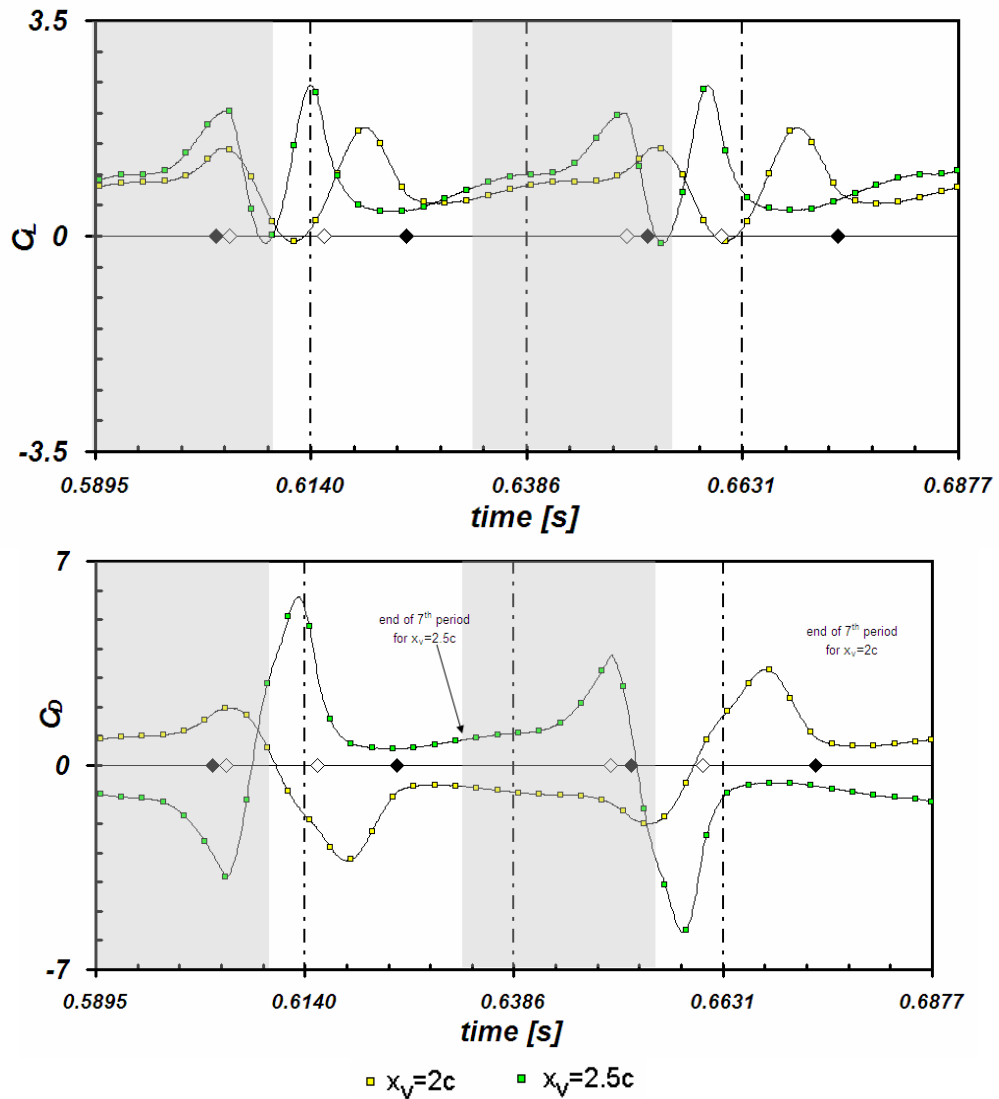


**Figure 3.12** Lift and drag coefficients comparing different  $x_v$  locations for  $\alpha=45^\circ$ ,  $Re=1000$ ,  $1/4c$  rotation during 7<sup>th</sup> stroke for  $x_a=1c$ .

The gray regions in the Figures 3.12 to 3.15 correspond to the quarter period of the  $x_v=2.5c$  cases and the vertical dashed lines correspond to the quarter-periods of  $x_v=2c$  cases. The diamond signs on the x-axis are the positions of the time  $t_v$  location for cases  $x_v=2c$  (black) and  $x_v=2.5c$  (white). As the  $x_v$  location gets closer to the maximum amplitude location (end of the stroke), for the same Reynolds number, the period gets smaller in order to obtain same velocity at the end of acceleration/deceleration region.

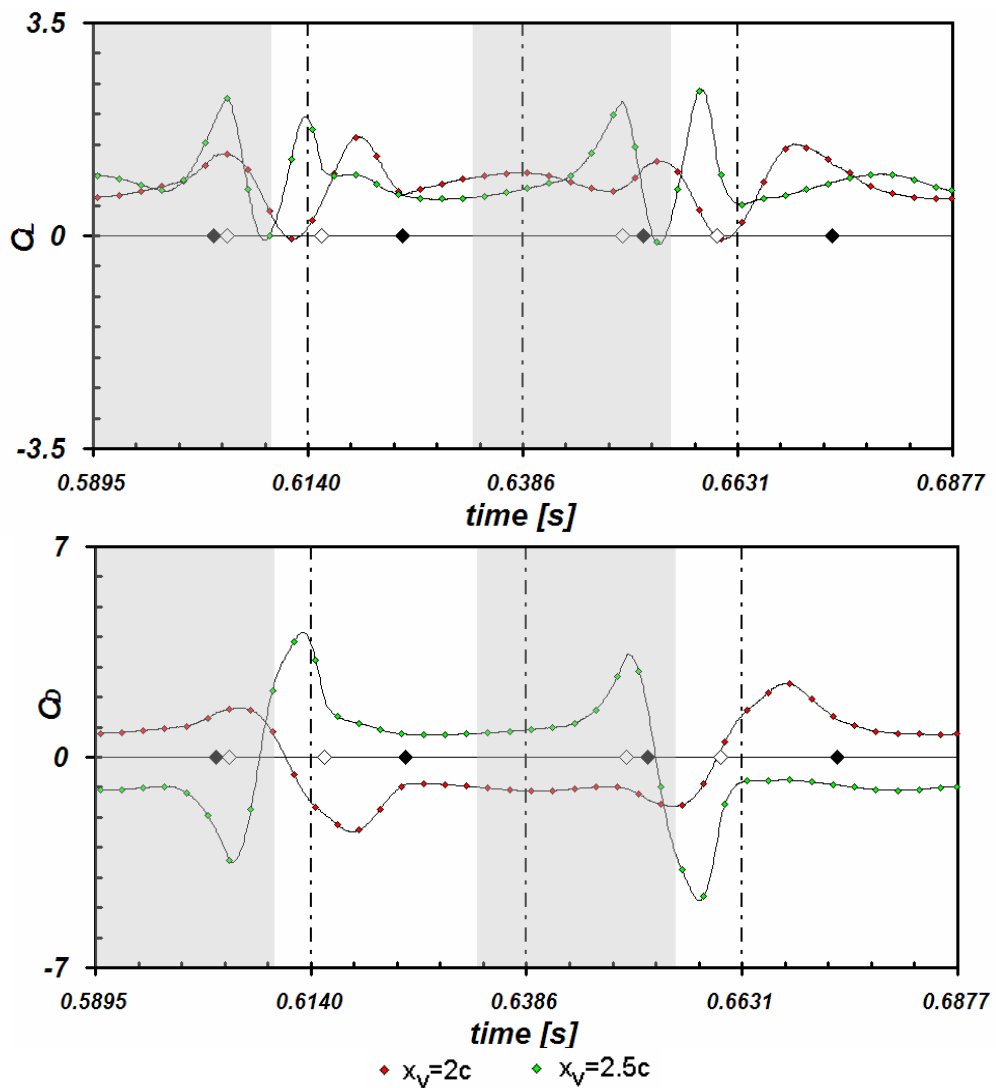


**Figure 3.13** Lift and drag coefficients comparing different  $x_v$  locations for  $\alpha=45^\circ$ ,  $Re=1000$ ,  $1/4c$  rotation during 7<sup>th</sup> stroke for  $x_a=1.5c$ .



The first observation is that the peak values for lift and drag coefficients are bigger as the velocity deceleration/acceleration is done close to the end of the stroke. However, when  $x_a$  increase, the maximum lift coefficient for  $x_v=2.5c$  decreases and tends towards the  $x_v=2c$  case.

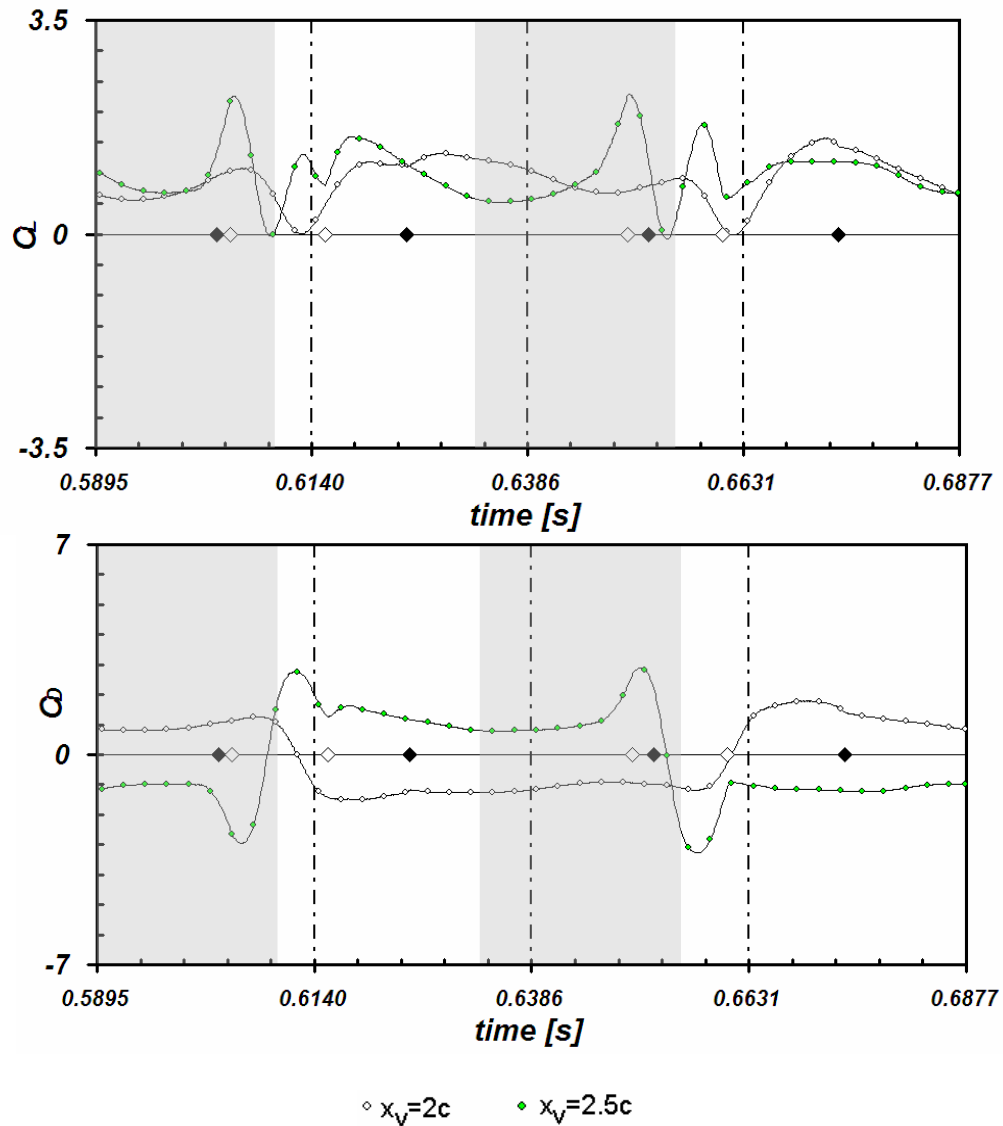


**Figure 3.14** Lift and drag coefficients comparing different  $x_v$  locations for  $\alpha=45^\circ$ ,  $Re=1000$ ,  $1/4c$  rotation during 7<sup>th</sup> stroke for  $x_a=2c$ .

At the beginning of translation, there is a sudden decrease of  $C_L$  for slow rotational velocities (Fig.3.12) but the decrease of the lift coefficient values is gradual for high angular velocities expending to a bigger time interval (Fig.3.15). The peak observed in drag coefficient value where the angular displacement is slow (Fig.3.12) is due to the circulation effect. This is a drag due to an airfoil in translation with a constant velocity by changing its angle of attack. In the mean time, the drag coefficient for Figure 3.15, where the angle of attack is changing very quickly, the drag can be explained as the drag due to the inertia of the fluid.

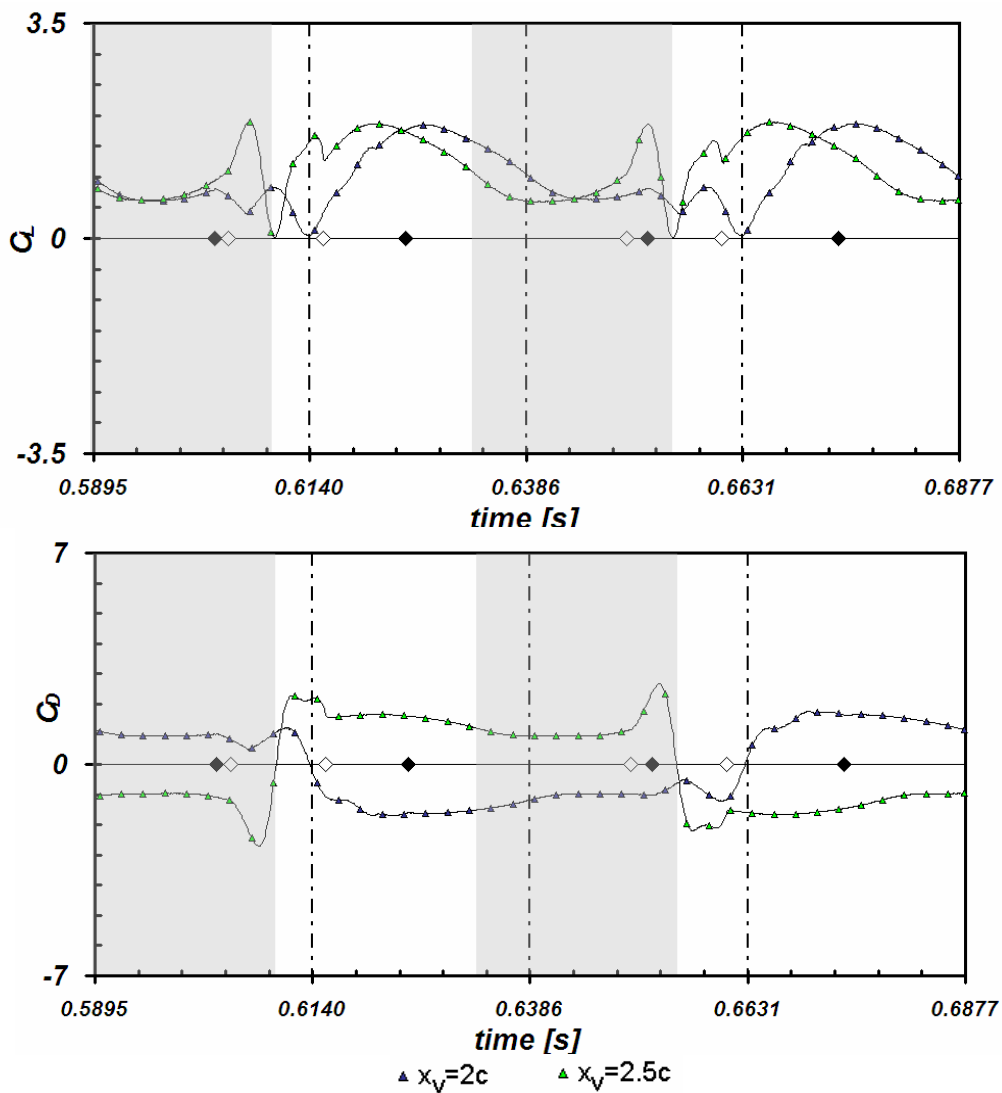


**Figure 3.15** Lift and drag coefficients comparing different  $x_v$  locations for  $\alpha=45^\circ$ ,  $Re=1000$ ,  $1/4c$  rotation during 7<sup>th</sup> stroke for  $x_a=2.5c$ .

### 3.4 Effects of the Position of Axis of Rotation

Three different axis of rotation positions are investigated namely  $\frac{1}{4}$ ,  $\frac{1}{2}$  and  $\frac{3}{4}$  chord locations. At  $\frac{1}{2}$  chord rotation, two positive peak values are observed at the beginning and at the end of each stroke (Fig. 3.17). For  $\frac{1}{4}$  chord position (Fig.3.16), this lift peak is at the end of a stroke and for the  $\frac{3}{4}$  c position (Fig.3.18), it is at the beginning of the stroke. For this last case, at the end of the stroke a negative peak forms. On Figures 3.16 to 3.18 in addition to the axis of rotation change, different position of change of angular displacement,  $x_a$  are also demonstrated to show their influence on aerodynamic force coefficients for a constant  $x_v=2c$  parameter.

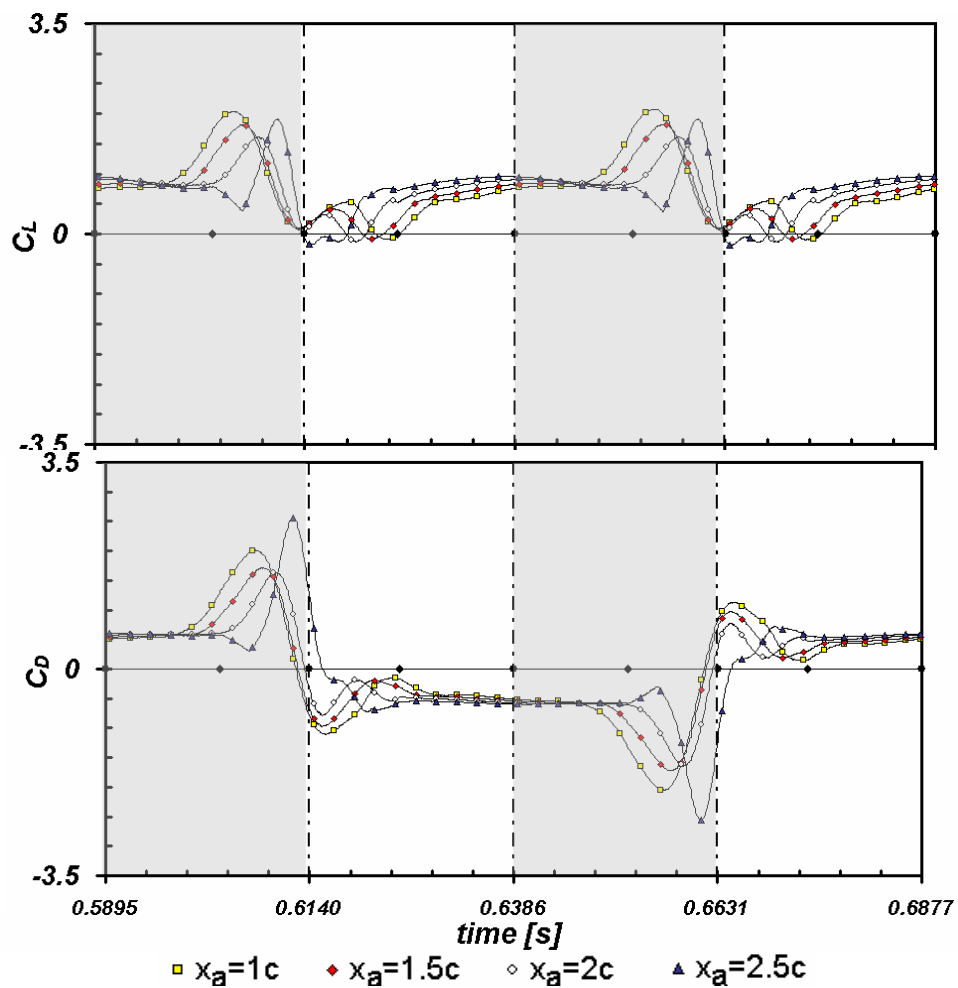


**Figure 3.16** Lift and drag coefficients for  $\alpha=30^\circ$ ,  $x_v=2c$ ,  $Re=1000$  with an axis of rotation at  $a=\frac{1}{4}c$  during 7<sup>th</sup> stroke.

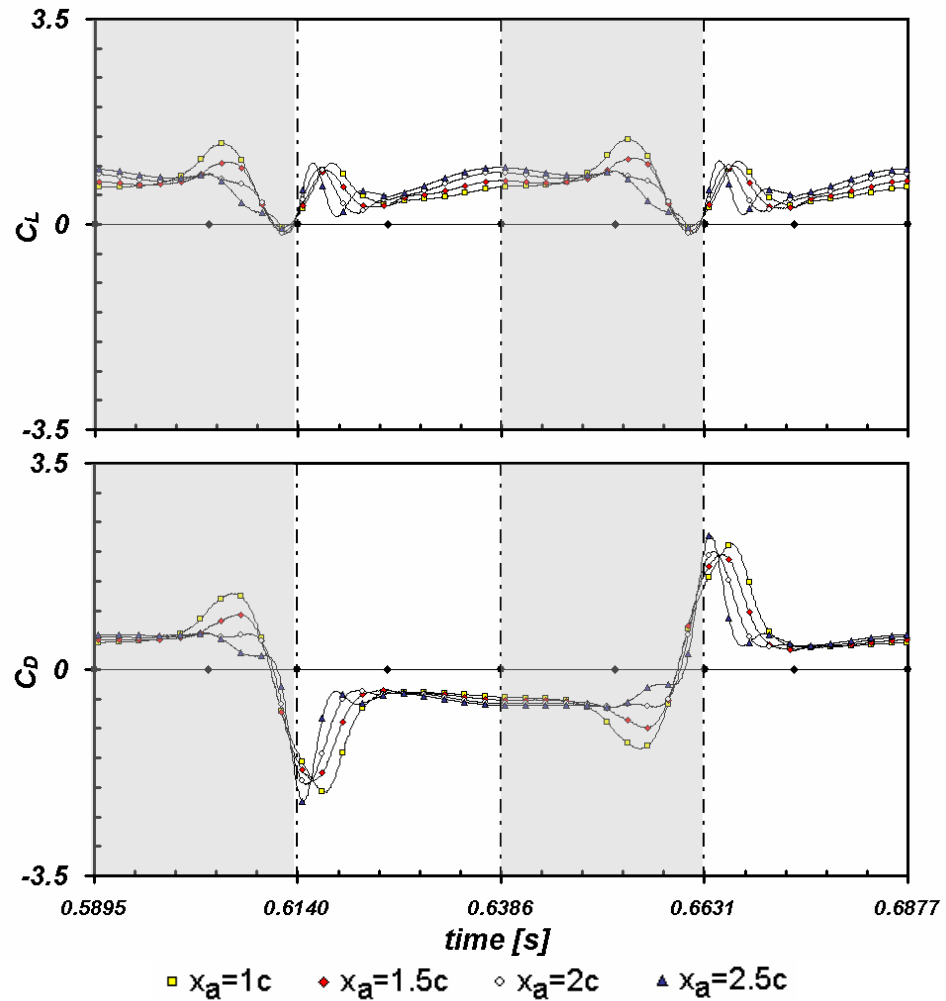


**Figure 3.17** Lift and drag coefficients for  $\alpha=30^\circ$ ,  $x_v=2c$ ,  $Re=1000$  with an axis of rotation at  $a= \frac{1}{2} c$  during 7<sup>th</sup> stroke.

The drag coefficient values for three axis of rotation during the translational phase are almost constant for  $\frac{1}{4} c$  and  $\frac{1}{2} c$  cases but there is a visible slope (increasing or decreasing according to the period) for  $\frac{3}{4} c$  axis of rotation. Always positive values for lift coefficient obtained for  $\frac{1}{4} c$  and  $\frac{1}{2} c$  is not observed for  $\frac{3}{4} c$  case during whole period. Especially for  $x_a=2.5c$  in Figure 3.18, highly big negative values for lift coefficient are obtained.

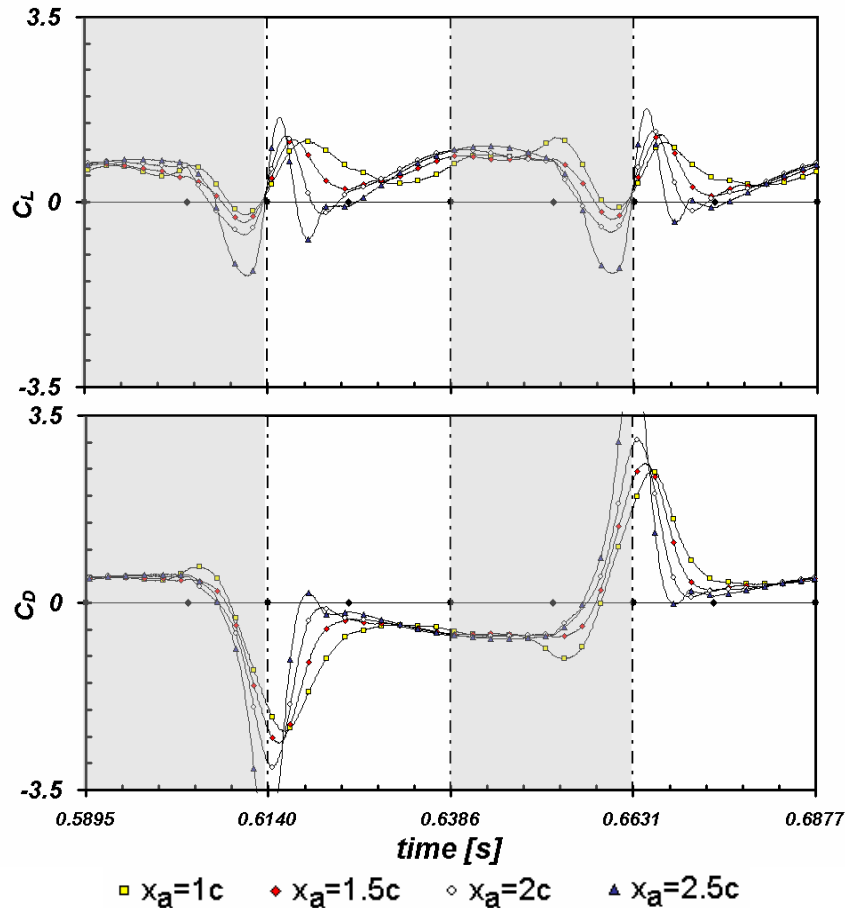
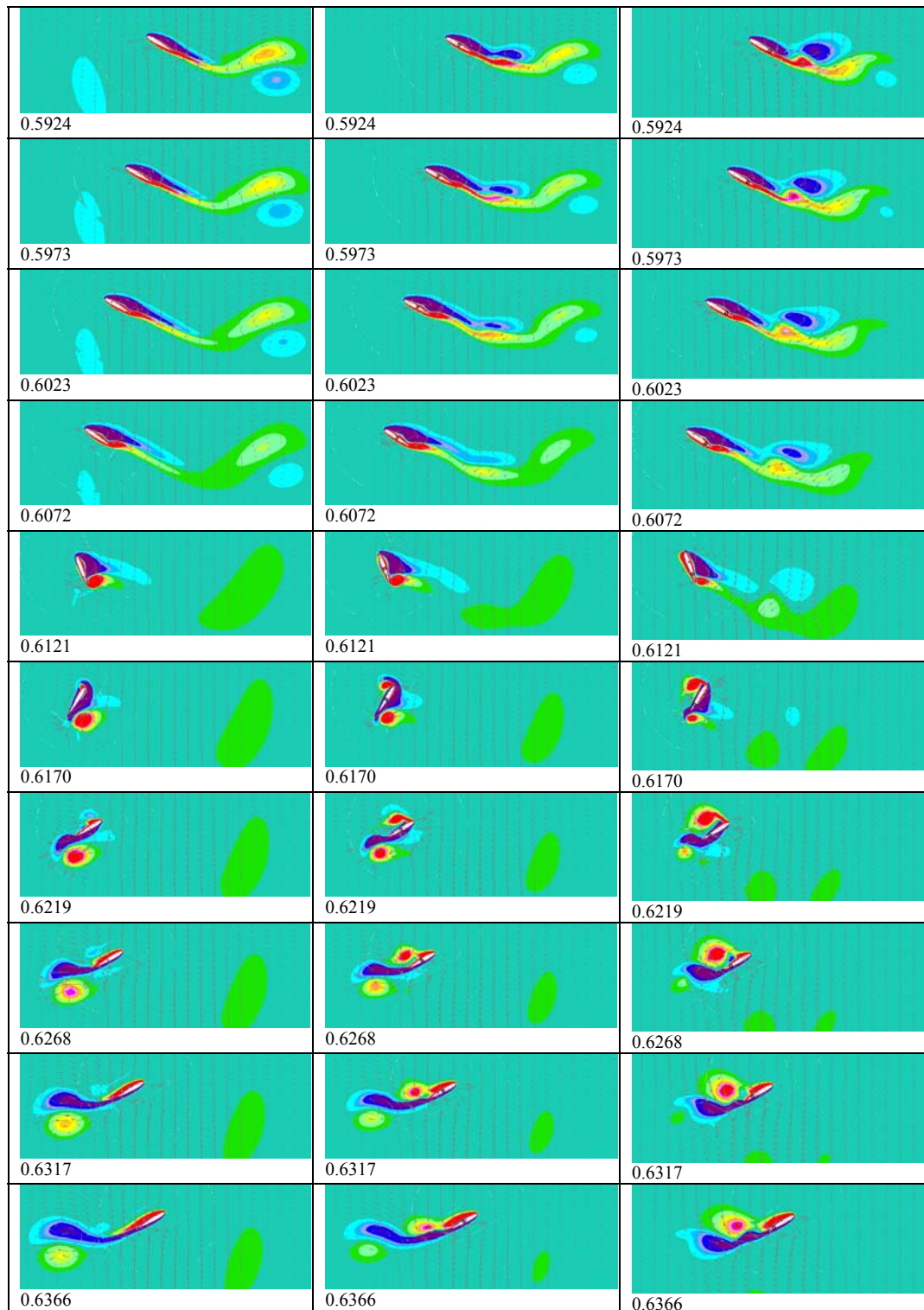


**Figure 3.18** Lift and drag coefficients for  $\alpha=30^\circ$ ,  $x_v=2c$ ,  $Re=1000$  with an axis of rotation at  $a=3/4 c$  during 7<sup>th</sup> stroke.

Figure 3.19 show the vorticity contours with velocity vectors for  $1/4 c$ ,  $1/2c$  and  $3/4c$  position of rotation axis during the 7<sup>th</sup> stroke. For  $30^\circ$  case, the symmetry of the aerodynamic forces is obtained for all of the cases studied so the half of the motion is represented in Figure 3.19. The induced velocity at the leading edge for  $1/2 c$  is more important than the case of  $1/4 c$  axis of rotation and  $3/4 c$  leading edge velocity is more important than the  $1/2c$  case. So at  $t=0.6170$ , at the beginning of upstroke, the counter-clockwise leading edge vortex is highly important for  $3/4 c$  axis of rotation and its importance decrease as the center of rotation gets closer to the leading edge. This leading edge vortex is detached from the airfoil surface after a while. The trace of the detached vortex is highly visible for  $3/4 c$  center of rotation case ( $t=0.6121$  in Figure 3.19). The rotational stopping vortex at the trailing edge of the airfoil becomes less important as the center of rotation displaced toward the trailing edge.



a)  $\frac{1}{4}c$  center of rotation      b)  $\frac{1}{2}c$  center of rotation      c)  $\frac{3}{4}c$  center of rotation

**Figure 3.19** Vorticity contours with velocity vectors for  $\alpha=30^\circ$ ,  $x_v=2c$ ,  $x_a=2c$ ,  $Re=1000$  during 7<sup>th</sup> stroke. (The numbers in the lower left-hand corners represent the time in second).

### 3.5 Effects of Reynolds Number

The calculations have been performed for  $Re=500$ ,  $1000$  and  $2000$  cases. It is found that in this regime of Reynolds number the force coefficients are not affected. For an example, lift coefficient for  $\alpha=30^\circ$ ,  $x_v=2c$ ,  $a=1/4c$  case is shown in Figure 3.20 for  $Re=500$  and  $Re=2000$  which are also the same as the  $Re=1000$  studied earlier. The force coefficients are non-dimensionalized with respect to maximum velocity corresponding to each  $Re$  number.

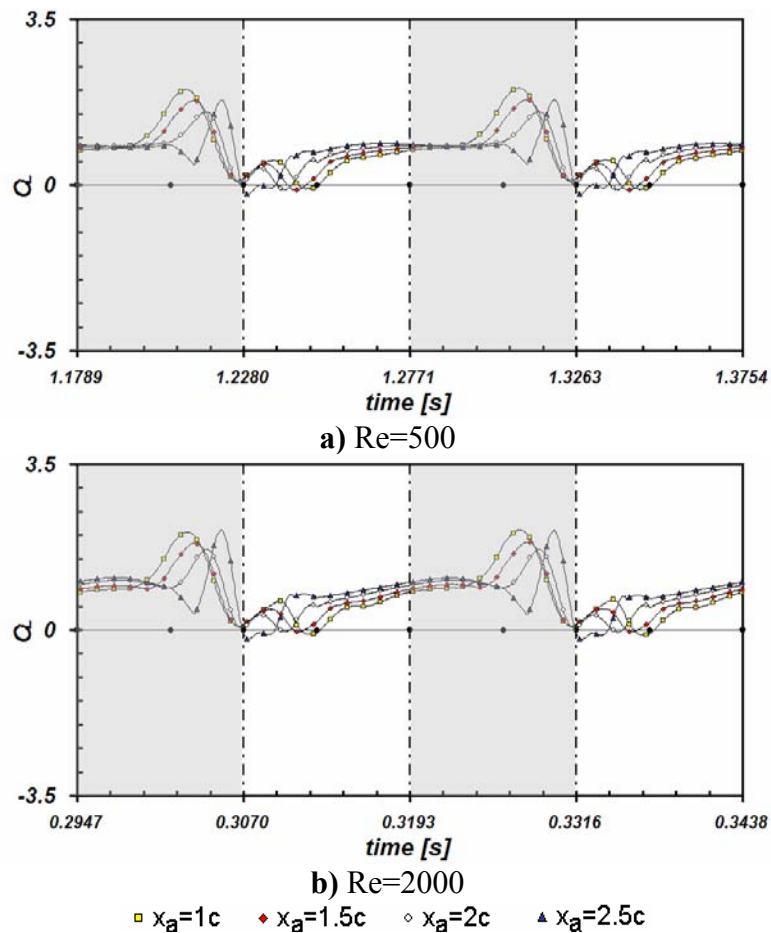


**Figure 3.20** Lift coefficients for  $\alpha=30^\circ$ ,  $x_v=2c$ ,  $a=1/4c$  for different  $Re$  numbers at 7<sup>th</sup> stroke.

### 3.6 Conclusion

The mean force coefficients for different configurations studied are represented in Table 3.6 to 3.8. Figure 3.24 shows the comparison of the data in these tables. It is observed that the drag coefficient and lift coefficients are approximately the same order of magnitude for most of the cases and they increase with angle of attack. In the tables, average stroke plane value  $\beta$ , and the profile power and its coefficient are also tabulated. For  $a=1/2c$  case the average drag coefficient is highly big compared to the other two center of rotations  $1/4c$  and  $3/4c$ .

**Table 3.6** DNS average force and force coefficient results for different cases for  $Re=1000$  during 7<sup>th</sup> period with center of rotation at  $a=1/4c$ .

$\alpha$ [°]	$x_v$	$x_a$	$\bar{C}_D$	$\bar{C}_L$	$\bar{C}_{Ftotal}$	$\beta$	$\bar{C}_{Ppro}$
5	2c	1c	0.2847	0.2266	0.3639	51.48	0.1584
5	2c	1.5c	0.2524	0.1662	0.3022	56.64	0.1328
5	2c	2c	0.2282	0.094	0.2468	67.61	0.1142
5	2c	2.5c	0.1993	0	0.1993	90.14	0.1017
30	2c	1c	0.714	0.7273	1.0192	44.47	0.4936
30	2c	1.5c	0.6422	0.7083	0.9561	42.2	0.4492
30	2c	2c	0.6244	0.7205	0.9534	40.91	0.4344
30	2c	2.5c	0.6452	0.7466	0.9868	40.83	0.43
45	2c	1c	1.2062	0.8301	1.4642	55.46	0.8758
45	2c	1.5c	1.1291	0.8536	1.4155	52.91	0.8428
45	2c	2c	1.0778	0.8806	1.3918	50.75	0.8322
45	2c	2.5c	1.1745	1.0078	1.5476	49.37	0.9211
60	2c	1c	1.7386	0.8107	1.9183	65	1.3494
60	2c	1.5c	1.6852	0.849	1.887	63.26	1.3384
60	2c	2c	1.6941	0.88345	1.9106	62.46	1.3558
60	2c	2.5c	1.7793	0.9502	2.0171	61.9	1.4163
45	2.5c	1c	1.5771	0.9708	1.8520	58.3838	1.3130
45	2.5c	1.5c	1.4028	0.9572	1.6983	55.6930	1.1746
45	2.5c	2c	1.3323	1.0099	1.6718	52.8372	1.1255
45	2.5c	2.5c	1.4328	1.1872	1.8608	50.3569	1.1668
60	2.5c	1c	2.0926	0.9183	2.2852	66.3070	1.8485
60	2.5c	1.5c	2.0294	0.9583	2.2443	64.7220	1.7787
60	2.5c	2c	2.0397	1.0292	2.2846	63.2246	1.7843
60	2.5c	2.5c	2.2440	1.2222	2.5552	61.4243	1.9605



**Table 3.7** DNS average force and force coefficient results for different cases for  $Re=1000$ ,  $x_v=2c$  with a stroke period of 0.09824 sec during 7<sup>th</sup> period with center of rotation at  $a=1/2c$ .

$\alpha$ [°]	$x_a$	$\bar{C}_D$	$\bar{C}_L$	$\bar{C}_{Ftotal}$	$\beta$	$\bar{C}_{Ppro}$
5	1c	0.2554	0.1917	0.3193	53.1101	0.1550
5	1.5c	0.2186	0.1233	0.2510	60.5816	0.1254
5	2c	0.1966	0.0651	0.2071	71.6626	0.1092
5	2.5c	0.1750	0.0023	0.1750	89.2420	0.1009
30	1c	0.6577	0.6419	0.9190	45.6938	0.4507
30	1.5c	0.5655	0.6097	0.8316	42.8461	0.3992
30	2c	0.5270	0.6199	0.8136	40.3671	0.3871
30	2.5c	0.5122	0.6470	0.8252	38.3657	0.3962
45	1c	2.4903	1.2383	2.7812	63.5612	1.9737
45	1.5c	1.9744	1.1271	2.2734	60.2801	1.6152
45	2c	2.2220	1.3362	2.5928	58.9797	1.8438
45	2.5c	2.2978	1.4690	2.7272	57.4095	1.9566
60	1c	1.7343	0.8162	1.9168	64.7986	1.3720
60	1.5c	1.6672	0.8352	1.8647	63.3896	1.3192
60	2c	1.6308	0.8571	1.8423	62.2755	1.3030
60	2.5c	1.6272	0.8862	1.8528	61.4275	1.3222

**Table 3.8** DNS average force and force coefficient results for different cases for  $Re=1000$ ,  $x_v=2c$  with a stroke period of 0.09824 sec during 7<sup>th</sup> period with center of rotation at  $a=3/4c$ .

$\alpha$ [°]	$x_a$	$\bar{C}_D$	$\bar{C}_L$	$\bar{C}_{Ftotal}$	$\beta$	$\bar{C}_{Ppro}$
5	1c	0.2905	0.1101	0.3106	69.2467	0.1478
5	1.5c	0.2270	0.0194	0.2278	85.1101	0.1085
5	2c	0.1681	-0.0964	0.1938	119.8200	0.0827
5	2.5c	0.1202	-0.2814	0.3059	156.8710	0.0730
30	1c	0.6024	0.5828	0.8381	45.9491	0.4235
30	1.5c	0.4709	0.5026	0.6887	43.1376	0.3415
30	2c	0.3647	0.4366	0.5689	39.8725	0.3044
30	2.5c	0.2472	0.3338	0.4154	36.5177	0.2871
45	1c	0.1042	-0.0887	0.1368	130.4	0.0034
45	1.5c	-0.013	-0.0932	0.0946	7.6086	-0.064
45	2c	1.2063	1.1218	1.6472	47.0794	0.8479
45	2.5c	1.6953	0.9020	1.9194	62.0321	1.4993
60	1c	1.4779	0.7092	1.6393	64.3636	1.2387
60	1.5c	1.3645	0.6829	1.5259	63.4125	1.1548
60	2c	1.2360	0.6543	1.3985	62.1066	1.0634
60	2.5c	1.1283	0.6341	1.2943	60.6647	1.0242

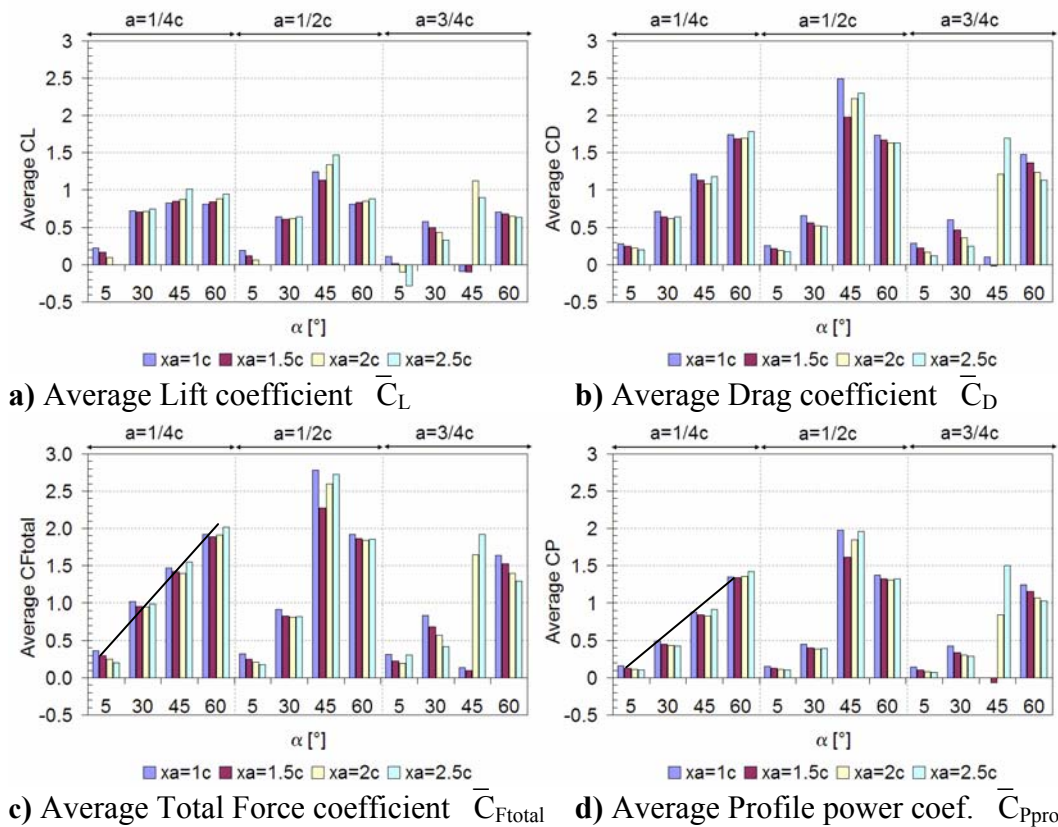


**Figure 3.21** Aerodynamic force coefficients averaged during the 7<sup>th</sup> stroke for  $x_v=2c$ ,  $Re=1000$  for  $a=1/4c$ ,  $1/2c$  and  $3/4c$ .

It can be concluded that in order to obtain maximum average total force the most important parameter for the flapping motion studies is the angle of attack. As the angle of attack is bigger than  $30^\circ$ , positive lift values are obtained during the whole period of the motion. And as the angle of attack is increased, it is observed from Fig.3.21 that the average lift coefficient is bigger for  $45^\circ$  angle of attacks and total force coefficients are bigger for  $60^\circ$  angle of attack. The average drag coefficient is highly big for  $60^\circ$  angle of attack which contributes so much to the total force coefficient. From  $5^\circ$  to  $60^\circ$  angles of attack, for  $a=1/4c$  center of rotation, there is an approximately linear increasing trend for average total force and average profile power coefficient values (Fig.3.21c and Fig.3.21d). The second important parameter is the axis of rotation. It is observed that at  $a=1/2c$  axis of rotation at  $45^\circ$  angle of attacks there exist high values of total force coefficient which is due to the high drag coefficient values. It is observed that  $x_a$  parameter has very small influence on average force coefficients for a given angle of attack.

## CHAPTER 4

### VORTEX DYNAMICS ANALYSIS OF A REFERENCE CONFIGURATION

#### 4.1 Introduction

The vortex dynamics and the aerodynamics phenomena are investigated for a reference configuration. The studied case is  $Re=1000$ ,  $\alpha=45^\circ$ ,  $x_v=2c$ ,  $x_a=2c$  with the rotation center at  $\frac{1}{4}c$ . In addition to the numerical studies, laser sheet visualization and PIV measurements are also performed for this reference study. This case is a first, fundamental step toward understanding the more complicated flow of hovering flight. Characteristics of the flow and the motion are summarized in Table 4.1.

**Table 4.1** Characteristics of the numerical and experimental data for case study  $Re=1000$  and  $\alpha=45^\circ$ .

	Air data	Water Data
$V_0$ [m/s]	1.454	0.017
$x_v$ [m]	0.02	0.12
$x_a$ [m]	0.02	0.12
$t_v$ [s]	0.014	7.20
$t_a$ [s]	0.014	7.20
$T/4$ [s]	0.025	12.85
$T$ [s]	0.098	51.42
$\dot{\alpha}_{max}$ [rad/s]	145.39	0.28

Numerical calculations are beginning from the half amplitude position, however the experimental visualization are started from the one end of the cycle. Therefore, there exist a one-half period of shift between the time definitions. All of the measurements are carried out during the 7<sup>th</sup> cycle. In order to compare both results, the non-dimensional times below are started from  $t^*=0$  instead of  $t^*=6$  but one must have in mind that the results are for the 7<sup>th</sup> period (Figure 4.1).

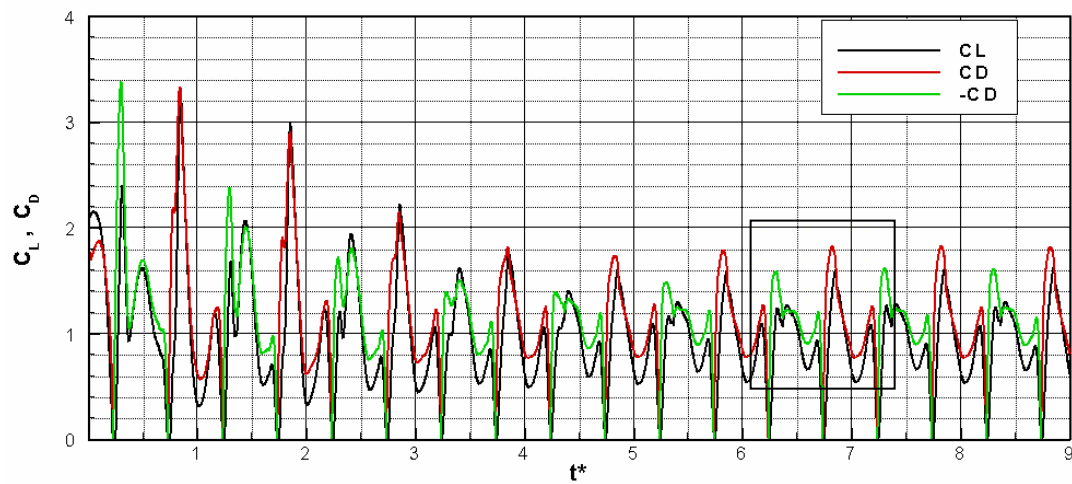


**Figure 4.1** Lift and drag coefficient for study case starting from the rest.

For the numerical simulations, the 15c radius length grid domain and 20c radius length grid domain are also compared in terms of force coefficients. The grid for 15c is sufficient for the solutions so the different configuration's numerical solutions are done with the 15c radius grid domain. The study case results are shown for 20c solution (Figure 4.2).

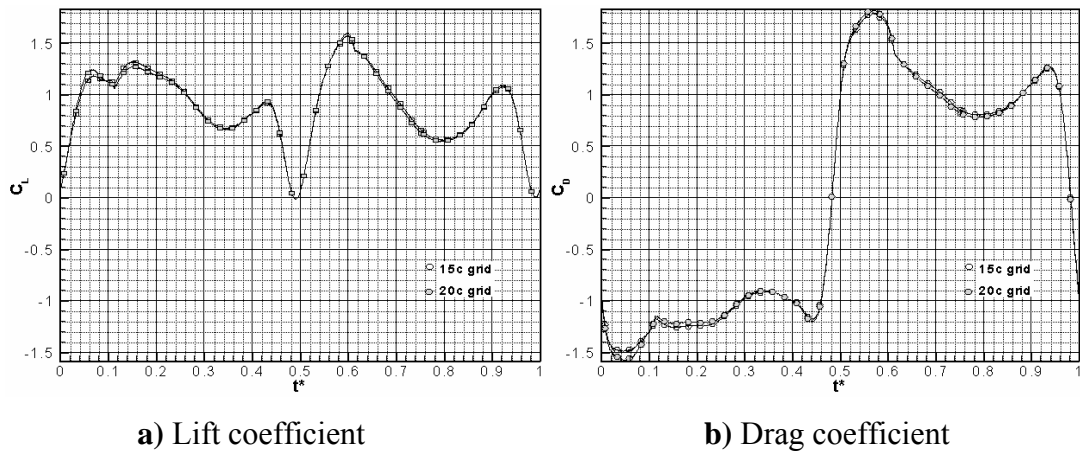


**Figure 4.2** Comparison of the lift and drag coefficients for the numerical results using 15c length and 20c length radius of grid domain for study case.

## 4.2 Comparison of the Different Investigation Techniques

In this section, firstly the experimental visualizations are compared to ensure that both the visualization with particles and PIV measurements give the same results since the experiments are done separately. Then the experimental results are compared with the numerical simulations in order to comment the results in view of aerodynamic forces and pressure distributions. The angle of attack and velocity distribution for all different measurement techniques investigated are shown in Figure 4.3. The points represent the times corresponding to each technique for comparison with each other.

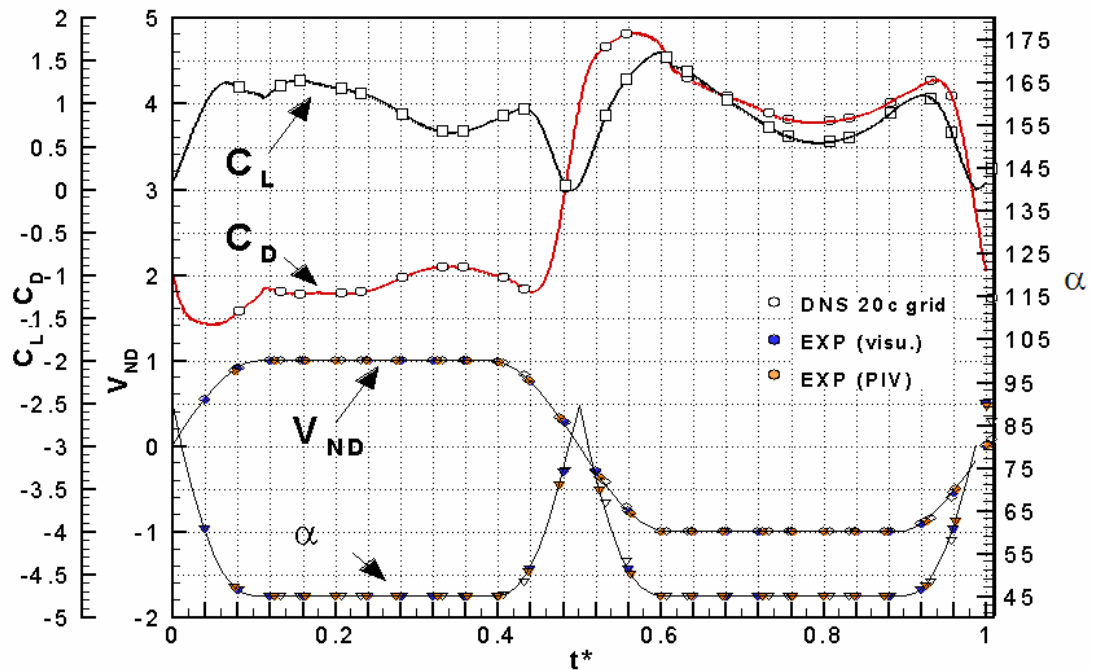


**Figure 4.3** Velocity and angle of attack distribution for the numerical simulations (white points), experimental visualization (blue points) and the PIV measurements (orange points). The force coefficients are the numerical results.

#### 4.2.1 Experimental Visualization

The two experiments namely visualization with discrete tracers using laser sheet and Particle Image Velocimetry (PIV) are compared in this section in view of streamlines and vortex identification. In visualization, the closed streamlines are visible with respect to the inertial reference frame.

It is checked that all the vortices observed at the time  $t^*=1.00$  corresponding to the beginning of the 8<sup>th</sup> period and are also observable at the time  $t^*=0$ , corresponding to the beginning of the 7<sup>th</sup> period, which implies that the motion is periodical.

The vortices are better distinguished via the non-dimensional  $Q$  contours for the PIV measurements. The streamlines are drawn to see if the closed curves obtained from the laser sheet visualization are also observable from the velocity component measurements of the flow field via PIV measurements.

During the whole period, three types of vortices are generated: Leading Edge Vortex (LEV) at the leading edge of the airfoil, Translational Vortex (TV) at the trailing edge of the airfoil and Rotational Stopping Vortex (RSV) at the trailing edge of the airfoil also. The LEV and TV are the vortices generated during the translation of the airfoil and RSV is generated due to the rotation of the airfoil and detached from the airfoil at the return. During experimental visualizations it is observed that some vortices are also generated due to the interaction of different vortices and shear between these vortices. The cores of the vortices are represented with points at the particle visualization photos. The blue colors represent the clockwise vortices and the red colors represent the counter-clockwise vortices. Nomenclature of the vortices is given in Table 4.2.

**Table 4.2** Nomenclature of the vortices generated during the flapping motion.

<b>Vortex</b>	<b>Explanation</b>	<b>Vortex Generation Phase</b>
LEV1	Leading Edge Vortex 1	Before translational phase starts
LEV2	Leading Edge Vortex 2	At the beginning of translational phase
TV1	Translational Vortex 1	Before translational phase starts
LEV3	Leading Edge Vortex 3	During pure translation
TV2	Translational Vortex 2	During pure translation
TV3	Translational Vortex 3	At the mid-of the translational phase (it rest attached to the airfoil until the rotational phase starts)
LEV4	Leading Edge Vortex 4	At the beginning of rotational phase
LEV5	Leading Edge Vortex 5	At the end of the rotational phase
RSV1	Rotational Stopping Vortex 1	At the end of the rotational phase

The explanation of the motion is started from the end of the rotational phase and the beginning of translational phase. During rotation there is a formation of a counter-clockwise leading edge vortex LEV1 which detaches very quickly from the surface of the airfoil when a new LEV2 is generated. At the beginning of the translation ( $t^*=0.08$ ), a counter-clockwise leading edge vortex starts to form (LEV2). In the mean time there is a newly generated translational vortex TV1 which is clockwise. All the other vortices (written in yellow color) shown in Figure 4.4 are the trace of the vortices generated during the previous period.

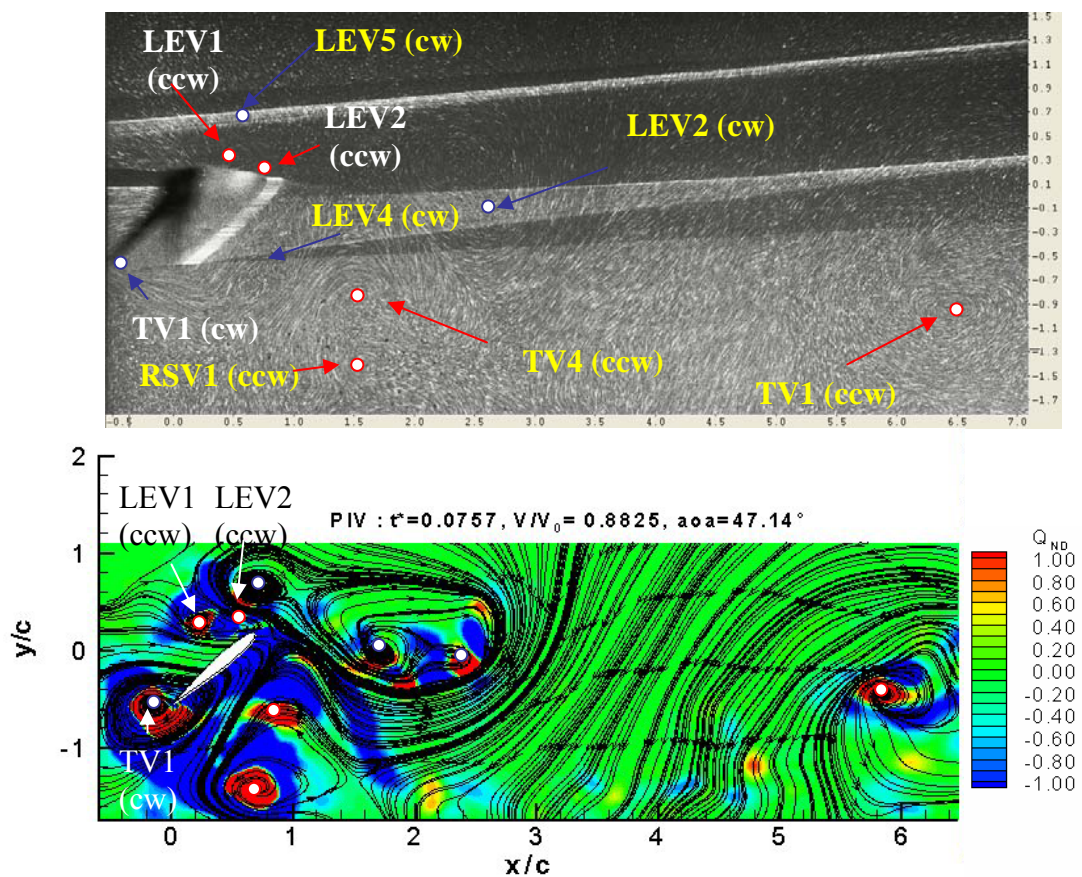


**Figure 4.4** Comparison of the laser sheet visualization with PIV non-dimensional  $Q$  values and streamlines in inertial reference frame ( $t^*=0.08$ ).



At  $t^*=0.12$ , LEV2 which is always attached to the airfoil grows as shown in the Figure 4.5. The LEV1 is separated from the airfoil. The translational vortex TV1 is started to detach from the airfoil. As the airfoil translates, the translational vortex TV1 stretches. There is always a wake left behind the airfoil which is the trace of TV1 until the mid-amplitude of the motion.

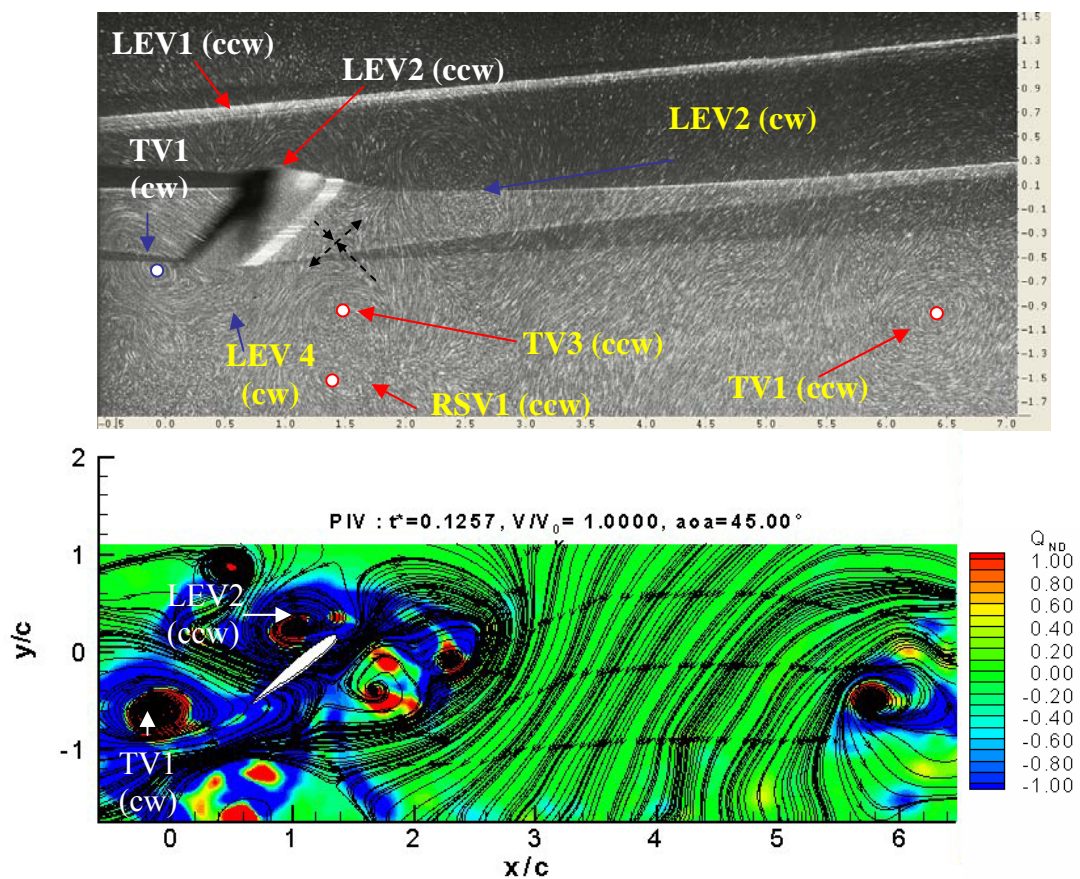


**Figure 4.5** Comparison of the laser sheet visualization with PIV non-dimensional  $Q$  values and streamlines in inertial reference frame ( $t^*=0.12$ ).

There exists a highly visible separation line in front of the airfoil both in experimental visualization and PIV measurements. It is surrounded with 4 vortices.

At the left side of the singularity, there is the clockwise leading edge vortices generated during previous stroke (LEV2); at the bottom side, there is the translational vortex (TV3) which is counter-clockwise. At the top, the newly generated leading edge vortex LEV2 (ccw) is observable and at the right side there is the influence of the new clockwise translational vortex (TV1). The type of singularity is the detachment separation point since the flow is detaching from the airfoil (Figure 4.6), it does not flow towards the wall of the airfoil but in the opposite direction.

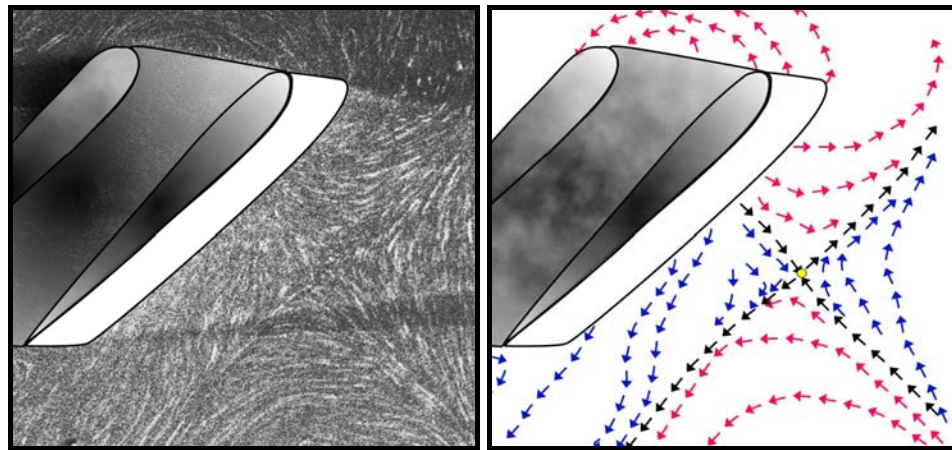


**Figure 4.6** Detachment type separation point is observed close to the airfoil at  $t^*=0.12$ .

It is known that the streamlines are dependent on the choice of the coordinate system, as it is shown in Figure 4.7; the separation point highly visible in inertial frame disappears completely in body fixed reference frame. For this reason, the vortex identification is carried out mostly with vorticity and  $Q$  contours.

In Figure 4.7, PIV measurements are represented with the  $Q_{ND}$  contours and streamlines both in inertial frame and body fixed frame at  $t^*=0.12$ . It is observed that the LEV2 is attached to the airfoil and its core velocities is the same as the velocity of the airfoil since it is forming closed curves of streamlines in body fixed

coordinate frame. Trailing vortex TV1 which is detached from the airfoil has approximately zero core velocity since it is visible in closed contours in inertial reference frame.

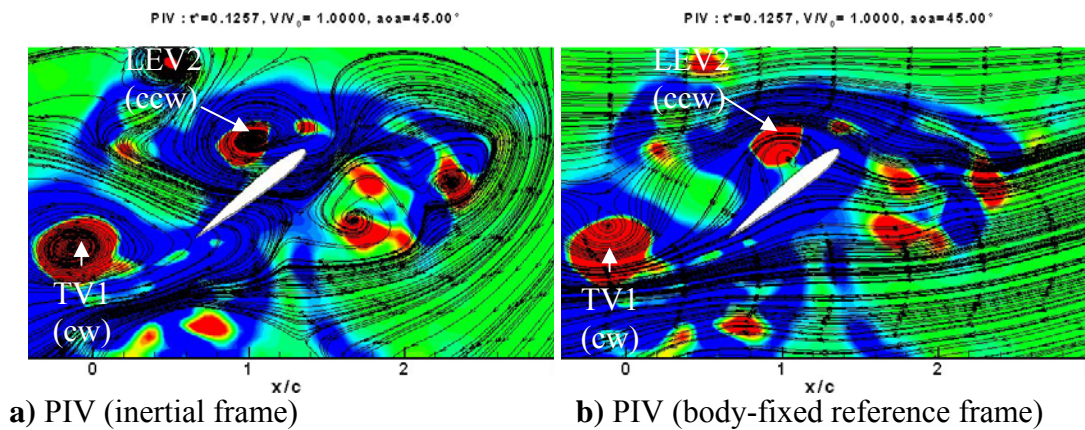


**Figure 4.7** PIV measurement represented with non-dimensional  $Q$  values and streamlines in inertial and body-fixed reference frames ( $t^*=0.12$ ).

A new leading edge vortex LEV3 is generated at  $t^*=0.20$  approximately (Figure 4.8). This new leading edge vortex generated during pure translation of the airfoil pushes the LEV2 towards the trailing edge of the airfoil. A new translational vortex TV2 is also formed at the same time. Non-dimensional vorticity values obtained from PIV measurements are also shown in Figure 4.8b. TV2 is in continuation with TV1 which forms a form of wake at the trailing edge of the airfoil. So it could be noted that  $Q$  contours are important for the detection of the cores of the vortices (Figure 4.8c). The different vortices can not be detected so easily from the vorticity contours when there is a continuous shear region behind the airfoil.

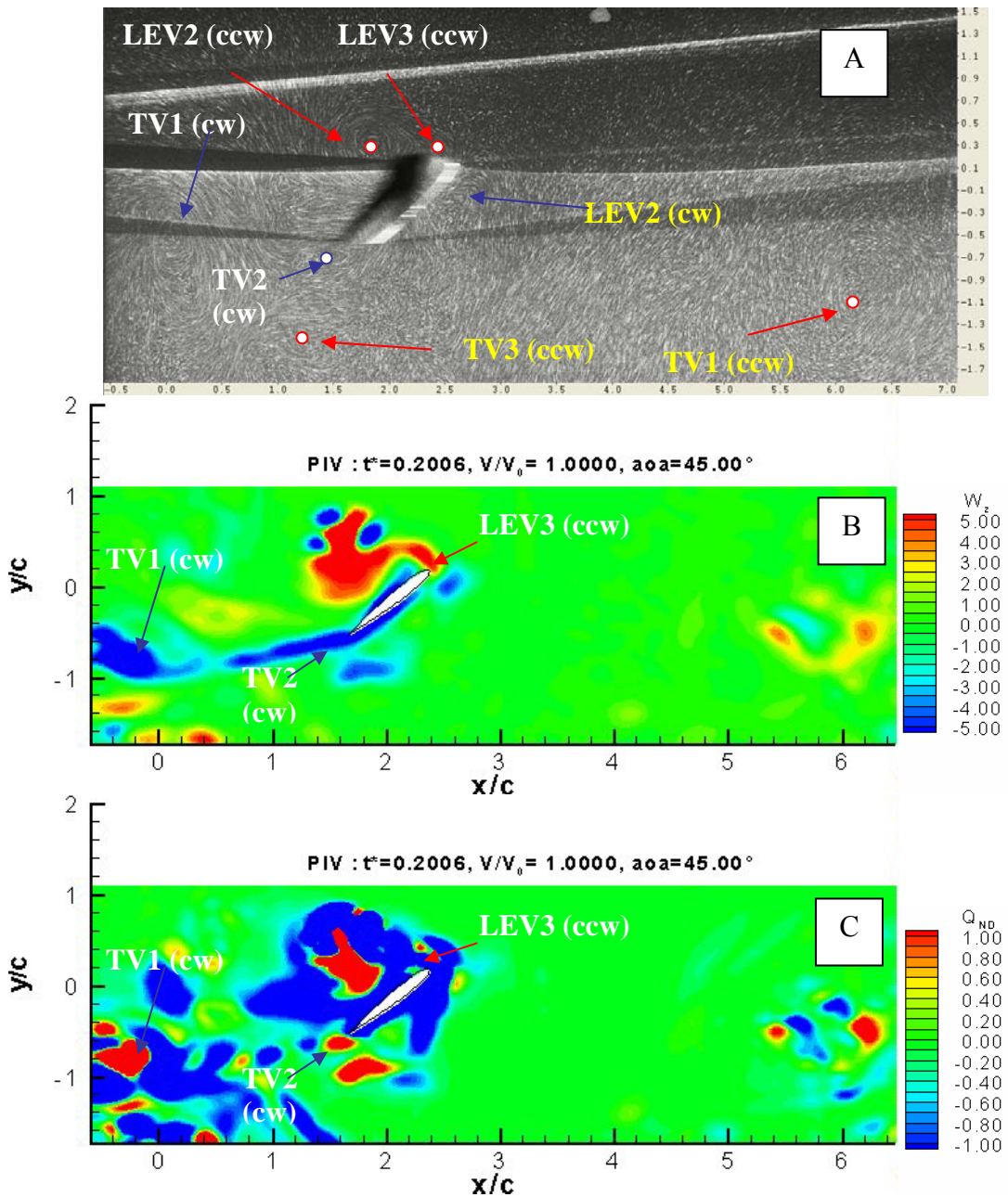


**Figure 4.8** Comparison of the laser sheet visualization (A) with PIV non-dimensional vorticity  $\omega_{ND}$  (B) and non-dimensional  $Q_{ND}$  values (C) at  $t^* = 0.20$ .

Negative  $Q$  values imply a shear region and the positive  $Q$  values shows vortex regions. There is a very thick shear region in front of the airfoil at  $t^* = 0.2$ , which seems to be due to the interaction between the airfoil and the vortices generated during previous stroke (visible on Fig.4.7).

LEV2 gets bigger and bigger during the translational phase of the motion at  $t^*=0.24$  (Figure 4.9). At the same time a new translational vortex TV3 is formed. A big trace of the vortices is formed at the back side of the airfoil from the combination of the vortices TV1 and TV2.

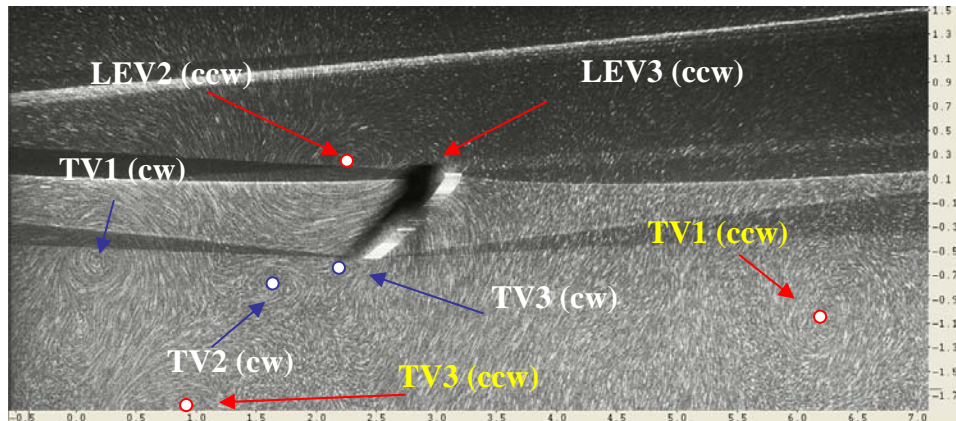


**Figure 4.9** Laser sheet visualization at  $t^*=0.24$ .

It is also observed that in body fixed frame LEV2 displaced toward the trailing edge of the airfoil at  $t^*=0.24$  (Figure 4.10b) and it detaches completely from the airfoil surface at  $t^*=0.28$  (Figure 4.10d). Since the close contour of the streamlines is obtained in body fixed frame for LEV2, it is concluded that at these instants the LEV2 is displacing with a core velocity equal to the translational velocity of the airfoil (Figure 4.10).

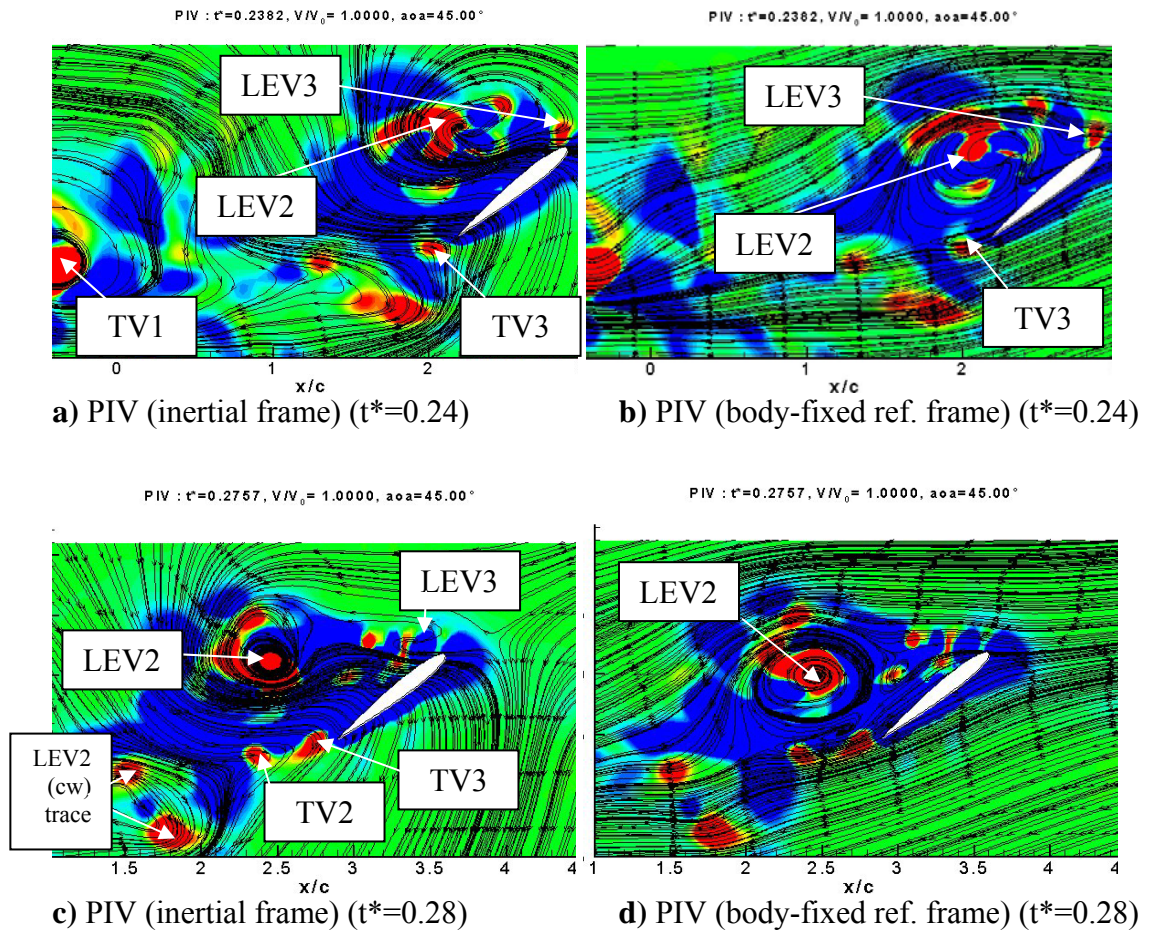


**Figure 4.10** PIV measurements represented with non-dimensional  $Q$  values and streamlines in inertial and body-fixed reference frames a)  $t^*=0.24$ , b)  $t^*=0.28$ .

The vortex detachment observed in the body-fixed frame in Figure 4.10 over the surface of the airfoil is also observable in literature in impulsively starting airfoils at high angles of attack.

Trailing vortex TV3 also highly visible at  $t^*=0.32$  (Figure 4.11). TV3 is in closed streamline form in body fixed reference frame (Fig.4.11c). LEV2 is situated at the top of the TV3.  $Q$  contours for LEV3 is visible at PIV measurements and closed streamline for LEV3 is much more visible in inertial reference frame.

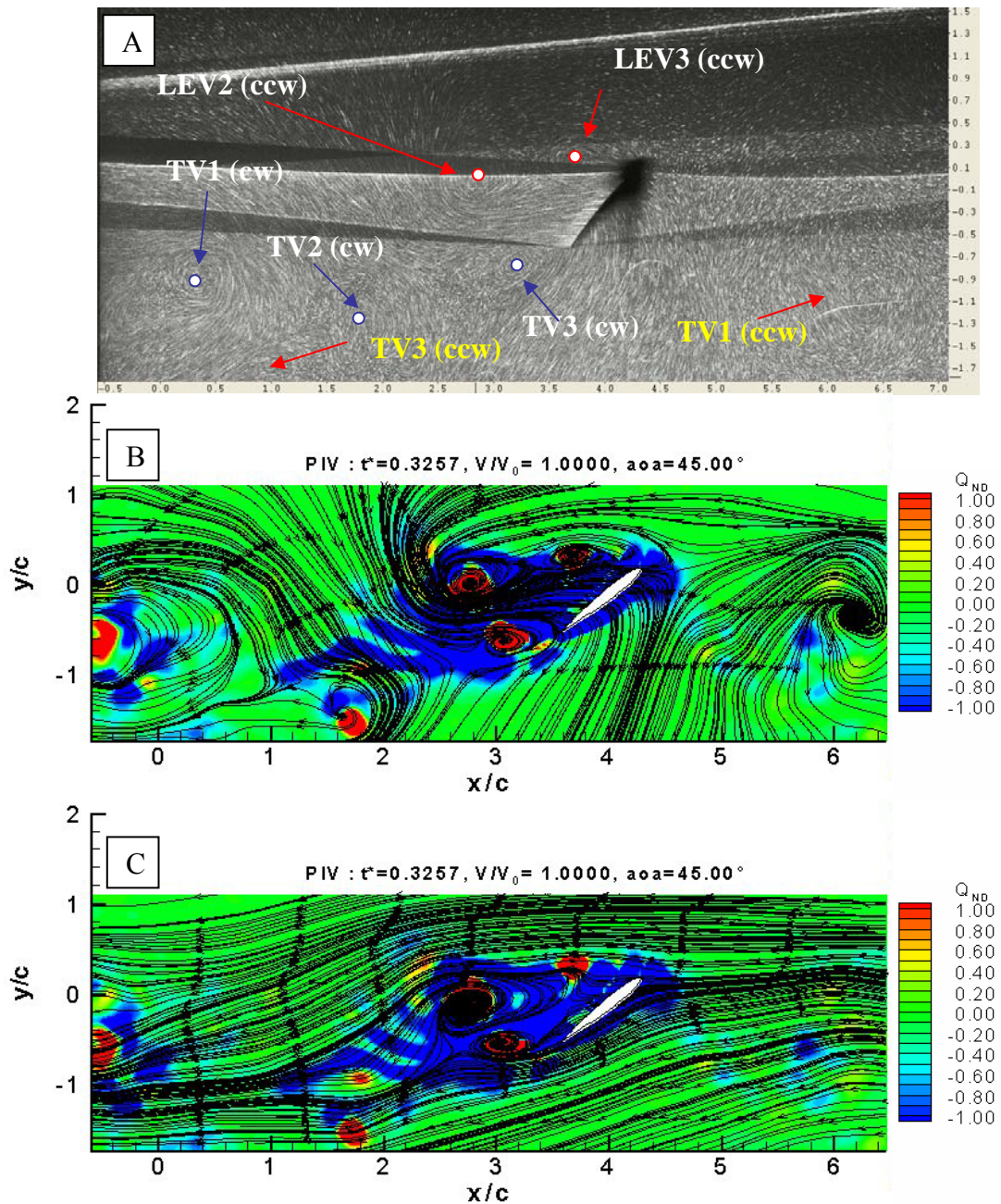


**Figure 4.11** Laser sheet visualization (A) and PIV measurements represented with non-dimensional  $Q$  values and streamlines in inertial reference frame (B) and body-fixed reference frame (C) at  $t^*=0.32$ .

The rotation of the airfoil is started at  $t^*=0.4$  (Figure 4.12). A new leading edge vortex LEV4 is formed at this time. LEV3 and LEV4 are shown coupled in the streamlines of PIV measurement and laser sheet visualization. The translational vortex TV3 and the sum of LEV3-LEV4 are positioned half by half on the airfoil

upper surface and they are translating with the airfoil velocity (Figure 4.12c). LEV2 is more visible at inertial reference frame. So, the core velocity of the LEV2 goes to zero since it is detached from the airfoil. It is observed that the trace of this LEV2 will influence this mid-amplitude location of the flapping motion domain.

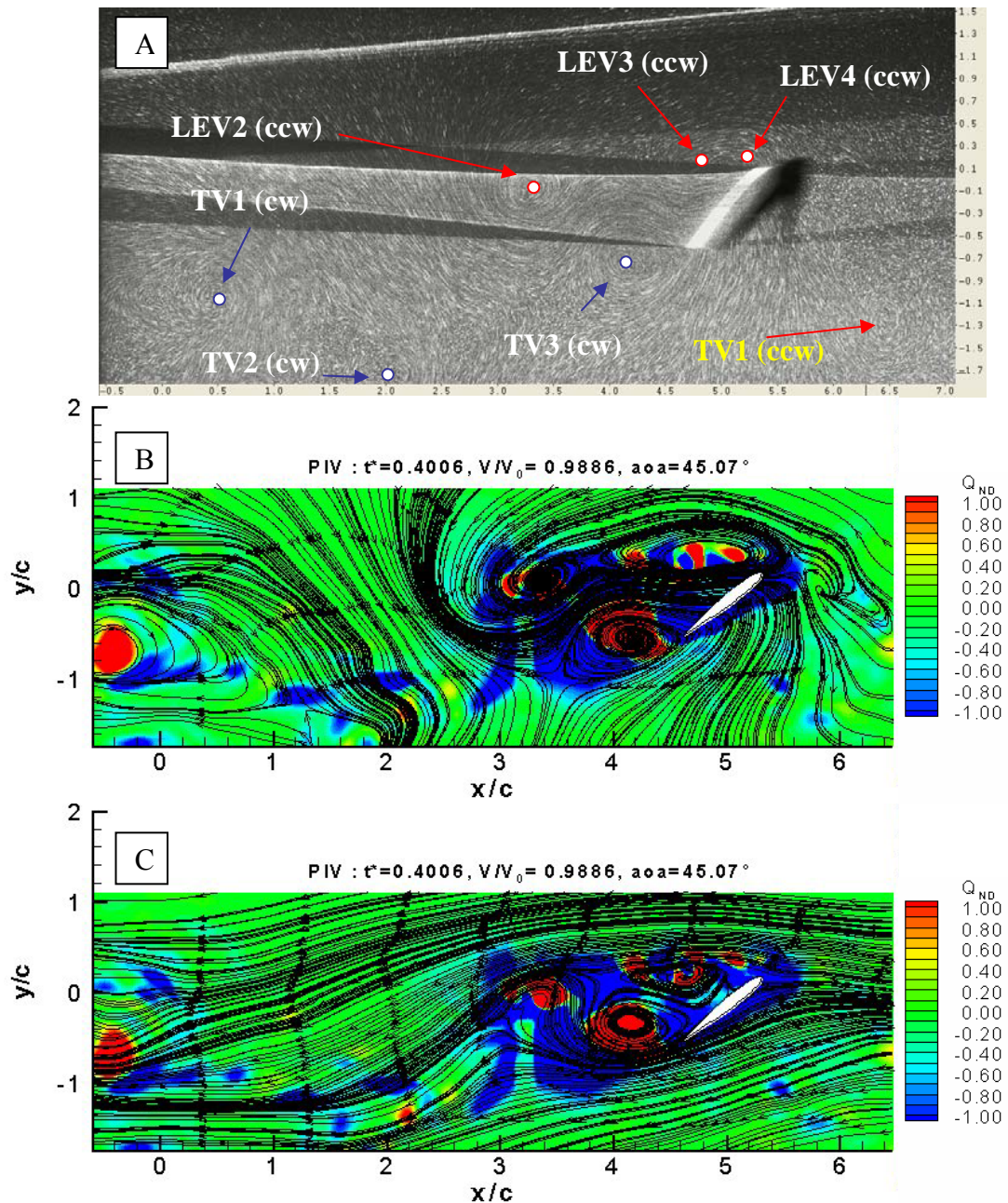


**Figure 4.12** Laser sheet visualization (A) and PIV measurements represented with non-dimensional  $Q$  values and streamlines in inertial reference frame (B) and body-fixed reference frame (C) at  $t^*=0.4$  (start of rotation and deceleration of the airfoil).



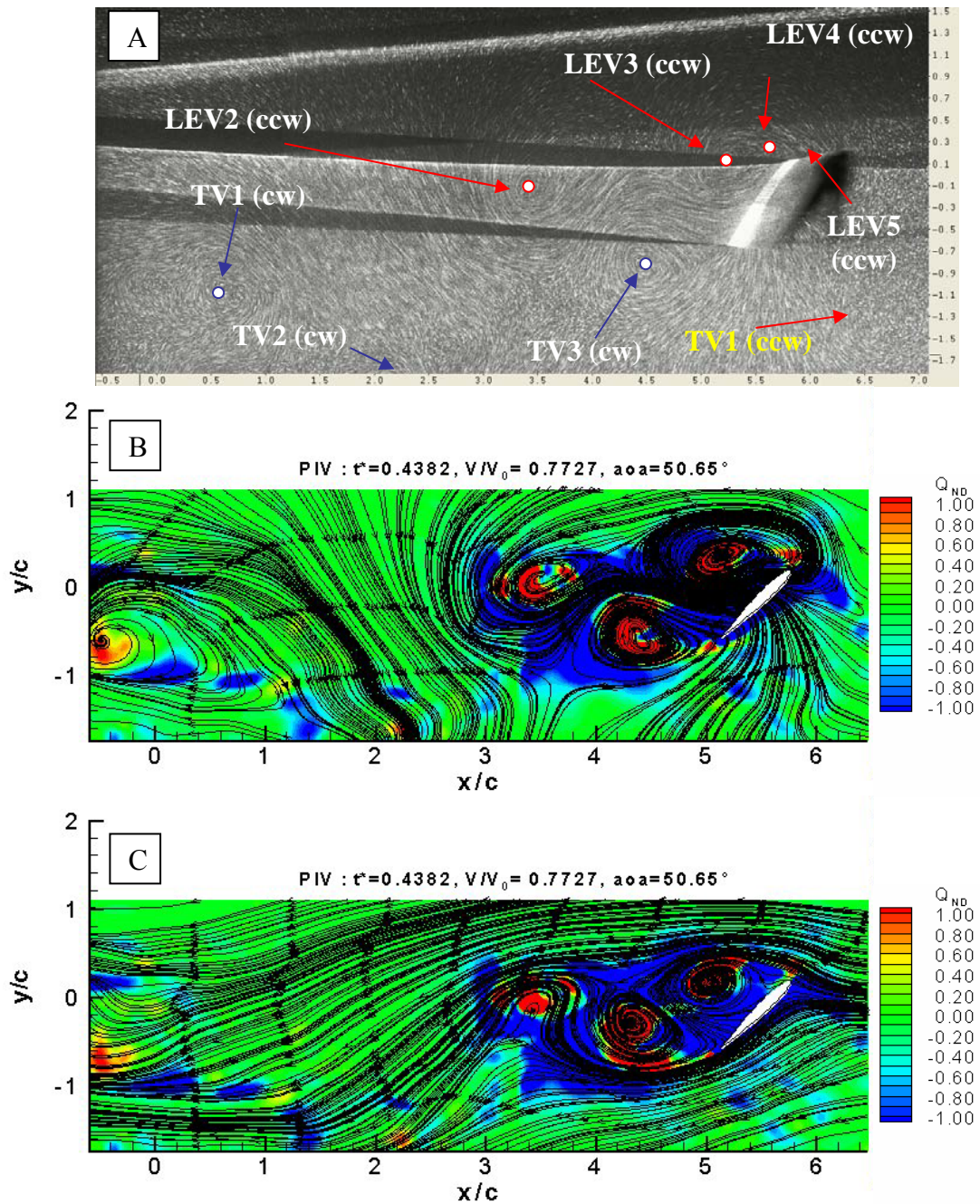


**Figure 4.13** Laser sheet visualization (A) and PIV measurements represented with non-dimensional  $Q$  values and streamlines in inertial reference frame (B) and body fixed reference frame (C) at  $t^*=0.44$  (during rotation and deceleration of the airfoil).

At  $t^*=0.44$ , a new LEV5 is formed (Figure 4.13). The velocity of the airfoil is decreased to 77% of the maximum velocity. It is observed that the body fixed frame and inertial frame streamlines are observed approximately similarly concerning the vortex structures. The translational vortex TV3 is detached from the airfoil surface

(Fig. 4.13c). There is a big leading edge vortex covering the entire upper surface of the airfoil. LEV4 and LEV5 are the small continuations of the LEV3 but are visible in  $Q$  distribution of PIV measurements and experimental visualisation. LEV5 disappears very quickly due to the rotation of the airfoil towards on it. At the end of the rotational phase, a Rotational Stopping Vortex (RSV1) is formed (Figure 4.14a). Both RSV1 and the leading edge vortices are separated from the airfoil surface at the end when the airfoil is at  $90^\circ$  angle of attack. The RSV1 forms a big vortex by interacting with the trace of the TV3 at the return of the airfoil at  $t^*=0.52$  (Figure 4.14c).

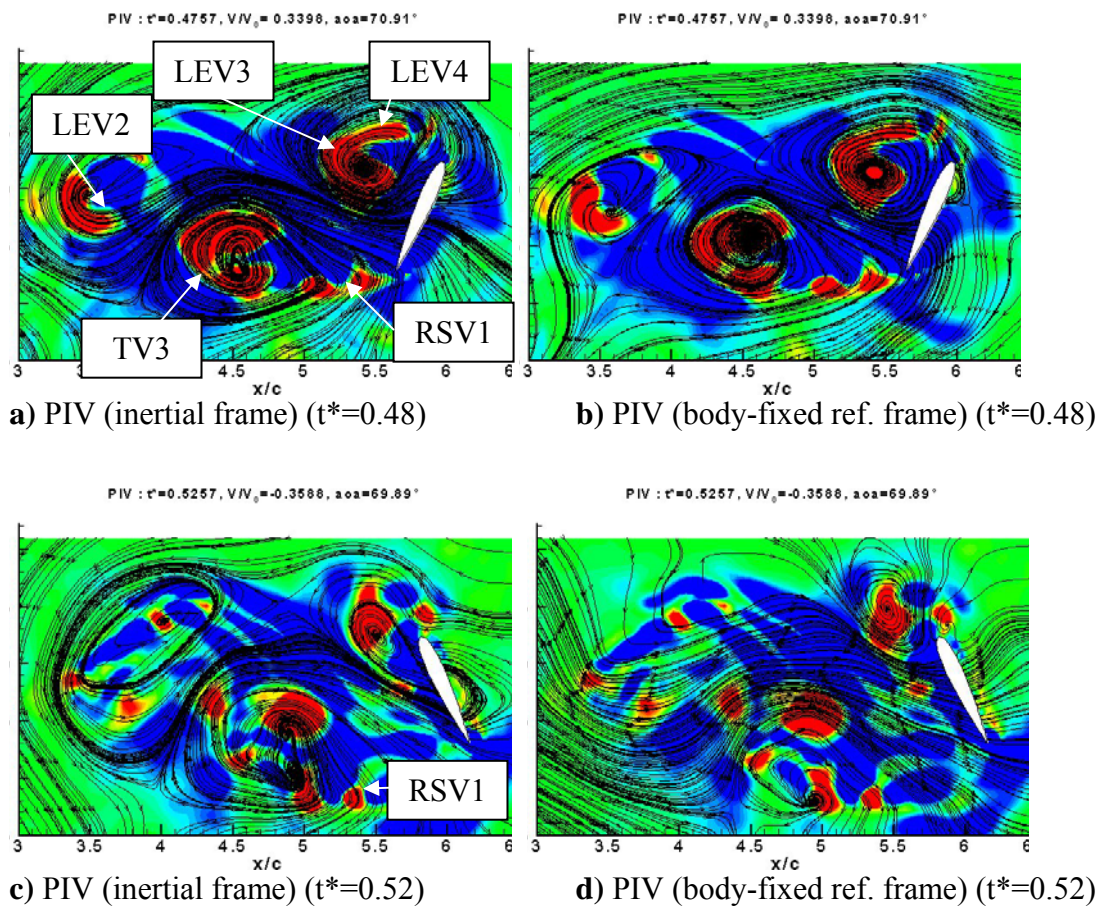
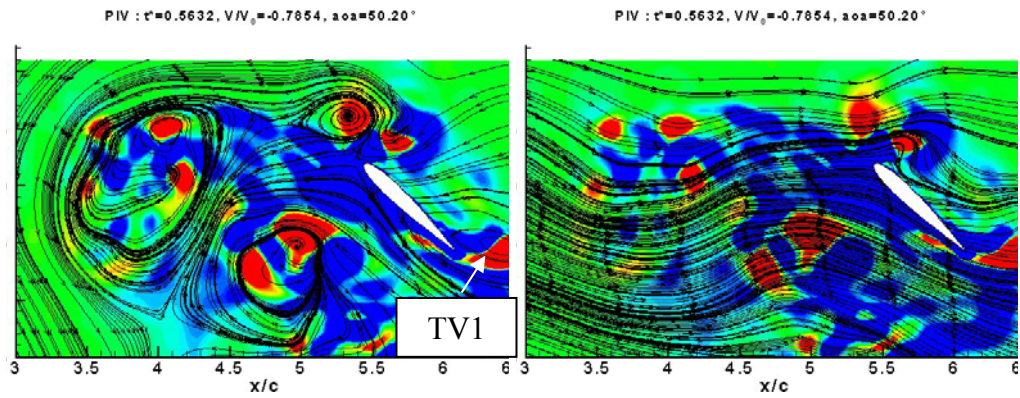


**Figure 4.14** PIV measurements represented with non-dimensional  $Q$  values and streamlines in inertial and body-fixed reference frames.



e) PIV (inertial frame) ( $t^*=0.56$ )

f) PIV (body-fixed ref. frame) ( $t^*=0.56$ )

**Figure 4.14 (continued)** PIV measurements represented with non-dimensional  $Q$  values and streamlines in inertial and body-fixed reference frames.

When the new rotational phase is started at the opposite direction at  $t^*=0.56$  (Figure 4.14e), the airfoil pushes these combined trailing edge vortices towards downward. All the vortices which are not attached to the airfoil during the return of the airfoil are not visible in the body fixed coordinate system, implying that their velocity is close to zero.

At  $t^*=0.56$ , the new counter-clockwise translational vortex TV1 and the clockwise leading edge vortex LEV2 are formed (Figure 4.15). The non-dimensional vorticity contours are also drawn in order to distinguish between the clockwise and counter-clockwise vortices (Figure 4.15c). The newly generated vortices LEV1 and TV1 are more visible in vorticity contours. The trace of the leading edge vortices from the previous stroke (LEV4 and LEV5) are pushed toward upwards. The trace of the LEV2 (ccw) is always visible at the mid location of the domain. At the left end of the domain the trace of the TV1 (cw) is also visible.

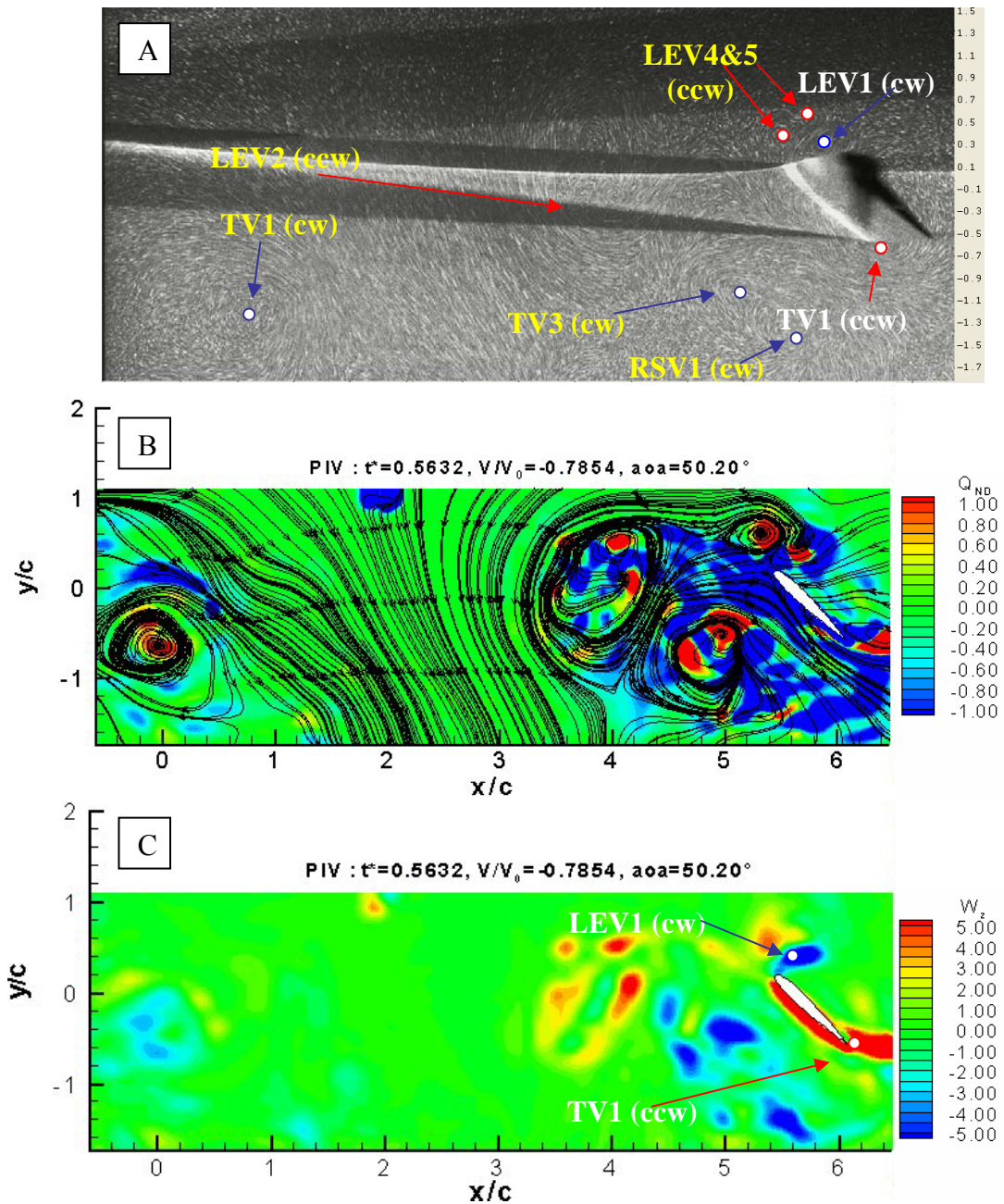


**Figure 4.15** Laser plane visualization (A), PIV measurements represented with non-dimensional  $Q$  values and streamlines in inertial reference frame (B) and PIV measurements represented with non-dimensional vorticity contours (C) at  $t^*=0.56$ .

The motion is performed in similar way in the opposite direction. The vortices generated are the same. A good agreement is found between the two independent experiments in terms of the vortex identification. The flow is quite complex. The

main features are the development of the lots of vortices attached or detached to the airfoil, in interaction with each other and with the airfoil itself.

#### 4.2.2. Comparison of the Experimental (PIV) and Numerical vorticity/ $Q$ values

Same rectangular grid domain is used for numerical solutions as the experimental PIV data in order to compare the results. An interpolation of the circular numerical domain to the rectangular region in concern is done with kriging. The velocity contours are represented before (red lines) and after kriging (black lines) in Figure 4.16 to validate the interpolation. The value at each source zone data point is weighted by the inverse of the distance between the source data point and the destination data point. The closest 8 points are selected so they are distributed as evenly as possible throughout the eight octants. This reduces the chance of using source points which are all on one side of the destination point. Kriging generally produces superior results to the inverse-distance algorithm but requires more computer memory and time.

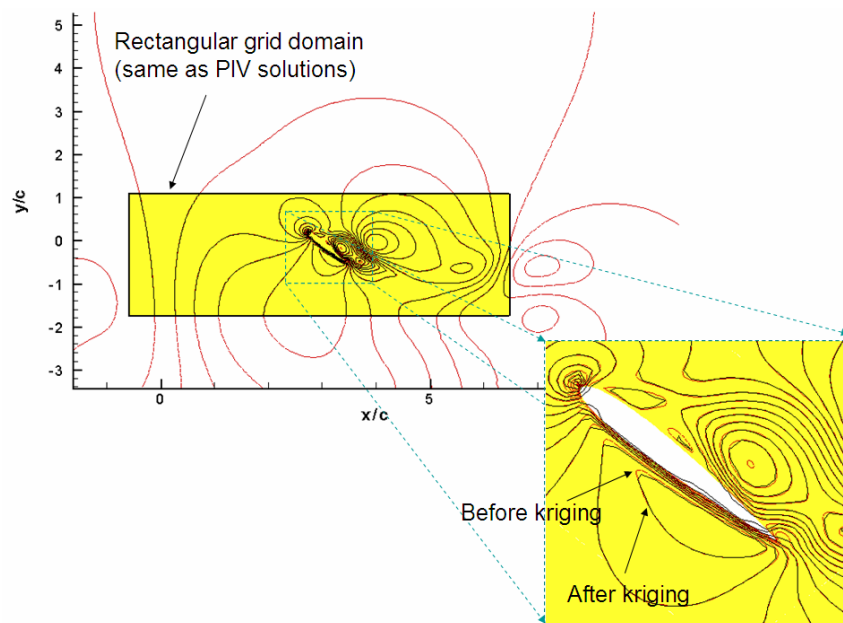


**Figure 4.16** Interpolation with kriging of the numerical grid domain with a rectangular grid domain.

With a general point of view, the same principle structures of vortices and their general topology are distinguishable both in experiment and numerical solutions but it is observed that there exist big abundance of the topology in view of  $Q$  and vorticity in experiments. Figure 4.17 shows the PIV measurements and numerical solutions during the translational phase of the motion. The LEV2 has the same behavior both in inertial reference frame and body fixed frame of references in the numerical and experimental data.

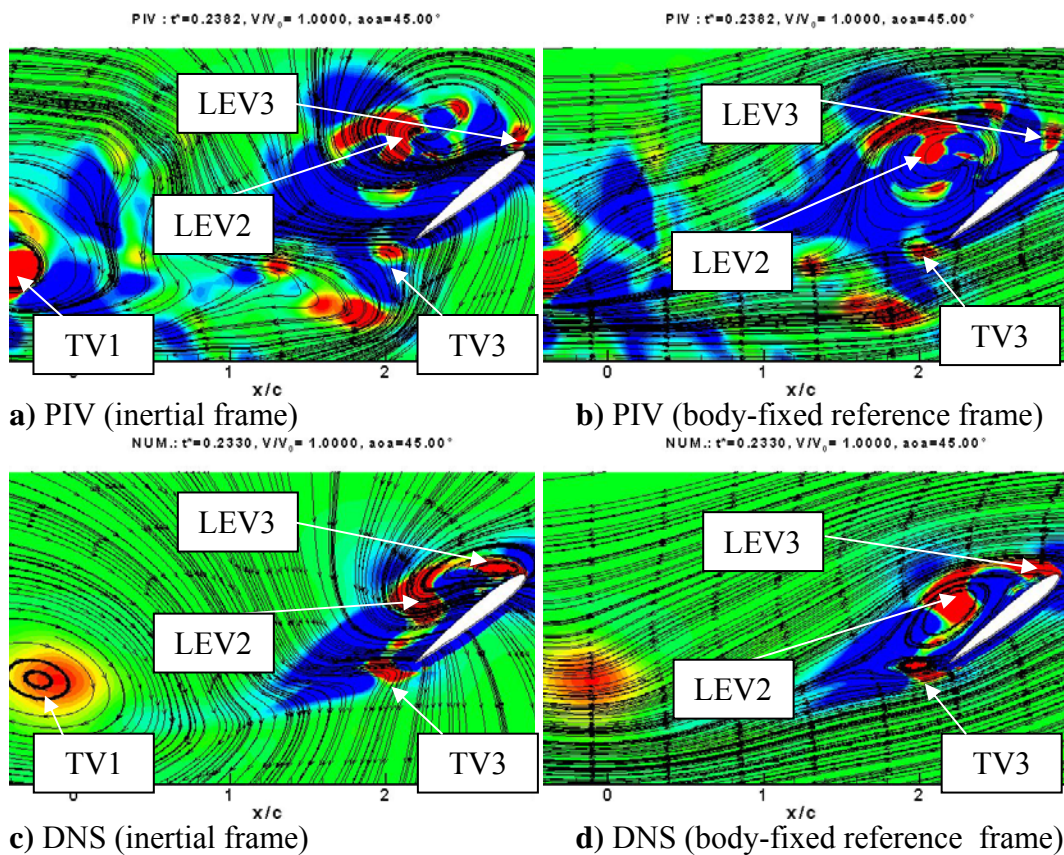
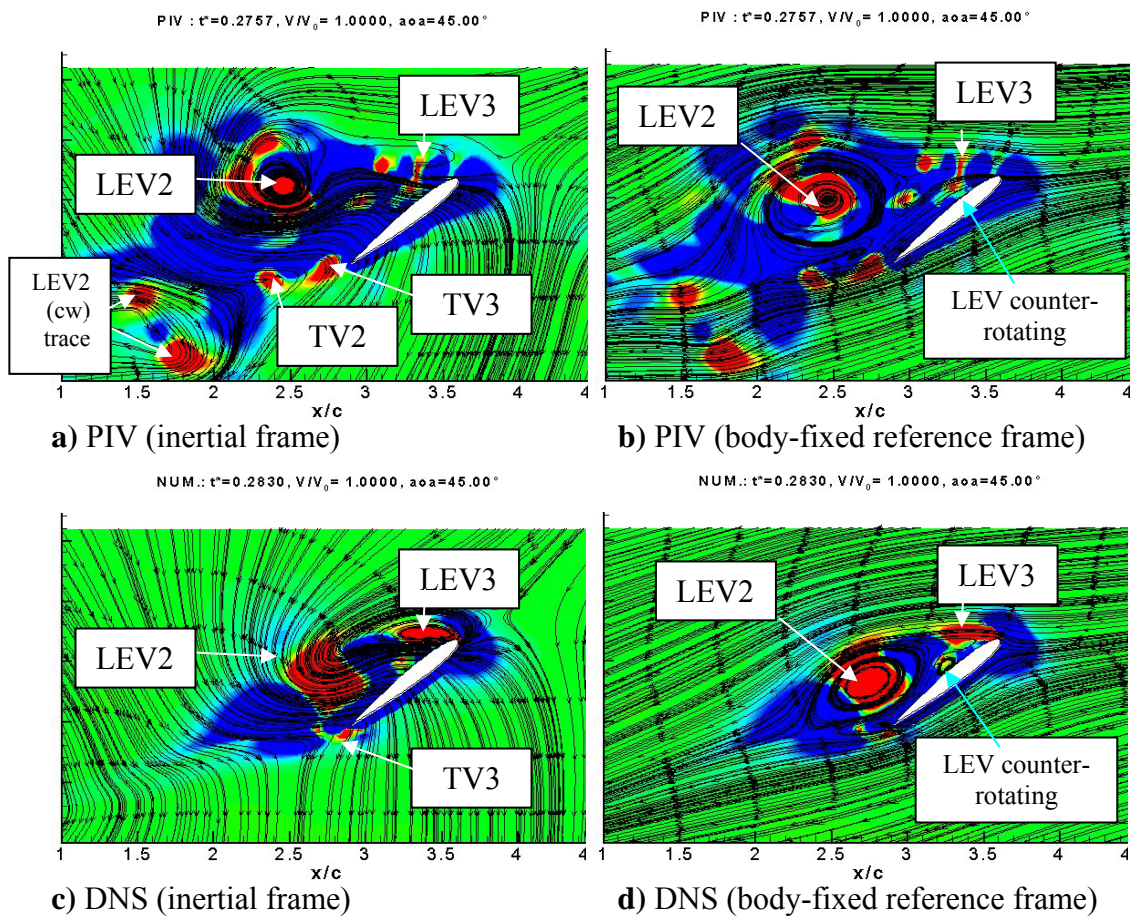


**Figure 4.17** PIV measurement and numerical solutions represented with non-dimensional  $Q$  values and streamlines in inertial and body-fixed reference frames ( $t^*=0.24$ ).

Translational vortex TV3 is also visible in both reference frames in numerical and PIV measurements where the  $Q_{ND}$  contours are drawn with streamlines. The trace of

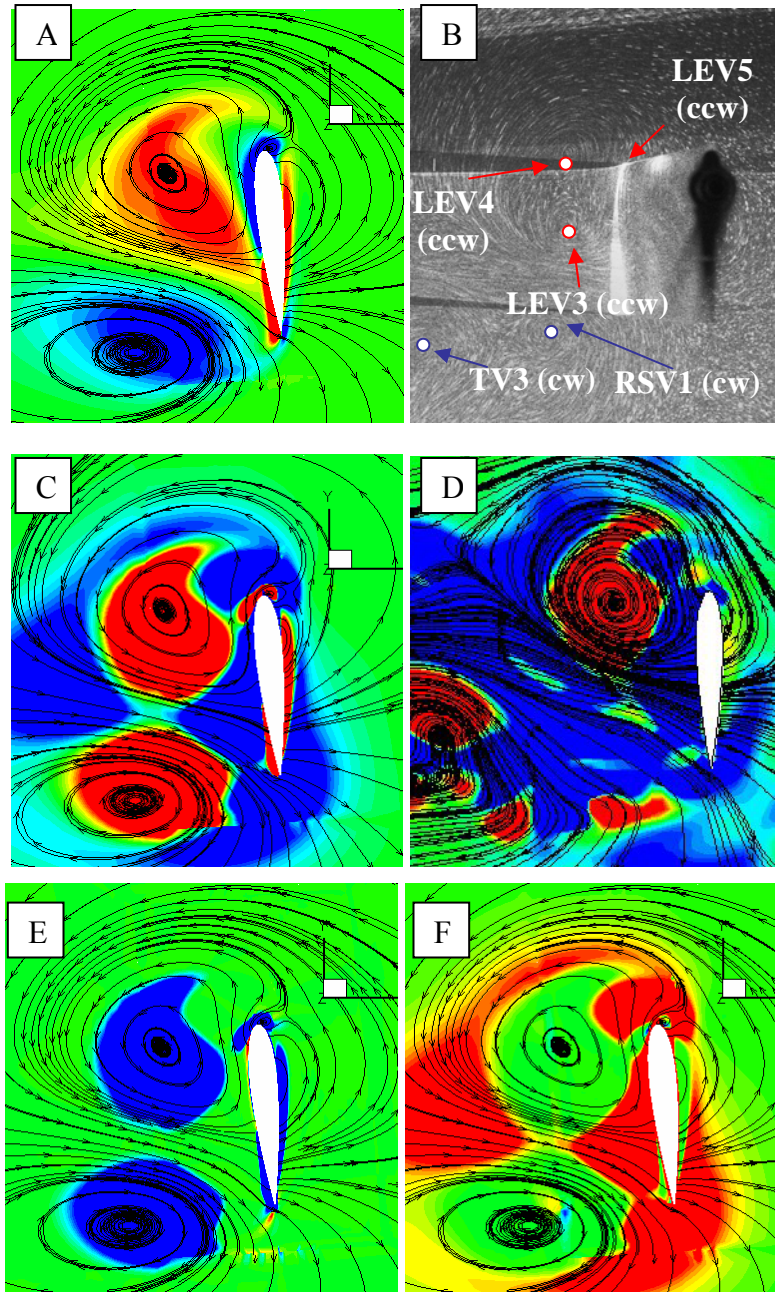
the translational vortex is observed only in inertial reference frame both in numerical and experimental solutions. The aerodynamic forces are mostly dependent on the vortices close to the airfoil, since these are the one that influences the pressure values on the airfoil surface.

Figure 4.18 shows the position where a counter-rotating vortex is generated on the airfoil surface which is only visible on the body fixed coordinate system and the  $Q$  and vorticity contours. The formation of this vortex could be responsible of the decrease in the aerodynamic forces.



**Figure 4.18** PIV measurement and numerical solutions represented with non-dimensional  $Q$  values and streamlines in inertial and body-fixed reference frames ( $t^*=0.28$ ).

Figure 4.19 shows the numerical results, experimental visualization and PIV measurements at  $t^*=0.5$ .



**Figure 4.19** Comparison of numerical data, experimental visualisation and PIV measurements at  $t^*=0.50$ . A. DNS Vorticity contours with streamlines  $t^*=0.508106$ . B. Experiment visualization of particles  $t^*=0.5$ . C. DNS  $Q_{ND}$  contours with streamlines  $t^*=0.508106$ . D. PIV measurements with  $Q_{ND}$  contours with streamlines  $t^*=0.5$ . E. DNS  $\lambda_1$  contours with streamlines  $t^*=0.508106$ . F. DNS  $\lambda_2$  contours with streamlines  $t^*=0.508106$ .



In addition to the vorticity and  $Q_{ND}$  contours,  $\lambda_1$  and  $\lambda_2$  contours are also shown in Figure 4.19-E and 4.19-F respectively for numerical simulations. It is concluded that  $Q$  contours are sufficient for the identification of the vortices in 2D simulations. It is also verified that  $\lambda_1 + \lambda_2 = -2Q$ .

With regard to the experimental solutions, we are not sure that the structures stay two-dimensional. This can cause a splitting up of the vortices. The numerical simulations are strictly two-dimensional.

The diffusion of vortices in numerical results is too fast and this phenomenon is highly visible during translational phase. The trace of the rotation stays visible in experimental visualizations but disperses in numerical solutions. But also in the numerical solutions, it is observed that the pressure is more persistent.

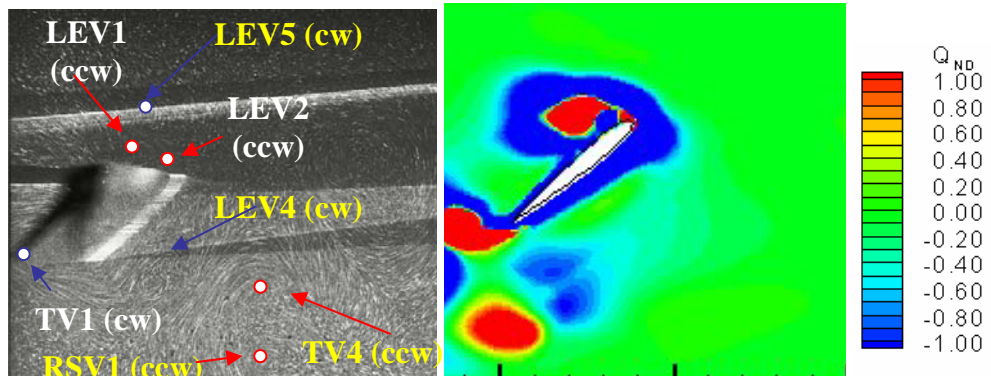
The vortices which are more energetical are highly visible both in numerical solutions, experimental visualizations and PIV measurements, in particular near the airfoil. They are also influencing the aerodynamic forces on the airfoil. The two-dimensional analysis of numerical solutions reveals obviously the presence of these most energetical vortices which are close to the airfoil, so this is a validation of the numerical simulations.

### **4.3 Identification of the Vortices in terms of Pressure and Aerodynamic Forces**

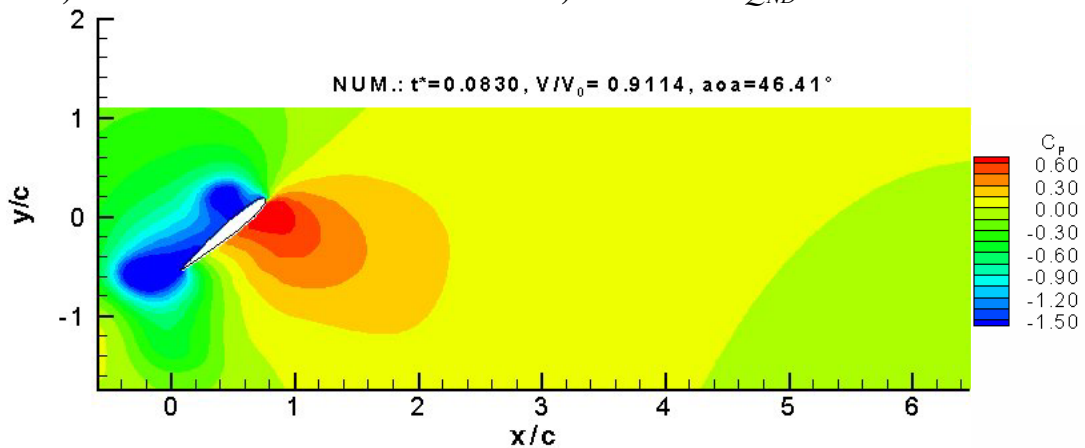
The PIV measurements and the laser sheet visualizations are compared with numerical results in order to identify the vortices generated during the flapping motion and to interpret the results in terms of the pressure and aerodynamic force coefficients.

$Q$  values are the laplacian of the pressure. So the centres of the vortices are the center of suction peaks. At the end of the rotation ( $t^*=0.08$ ), on the upper surface of the airfoil there is two suction regions resulted from the LEV1 and TV1 (Figure 4.20).

Lower surface of the airfoil is surrounded with a shear region where the  $Q$  values are negative (Fig.4.20b). Stagnation point is at the lower surface of the airfoil and is very close to the leading edge. Lift coefficient is approximately equal to the drag coefficient at this time so the resultant force is approximately normal to the airfoil.



a) Laser sheet visualization at  $t^*=0.08$  b) DNS results  $Q_{ND}$  contours at  $t^*=0.083$



c) DNS results Pressure Coefficient  $C_p$  contours at  $t^*=0.083$

**Figure 4.20** Comparison of the laser sheet visualization and numerical results at  $t^*=0.08$ .

At  $t^*=0.1330$ , during translational phase, there is a slight diminution of the lift and drag coefficients. From the visualization, it is observed that the trailing edge vortex

(Translational Vortex TV) moves away from the airfoil (Figure 4.21). The lift coefficient is also approximately equal to the drag coefficient.

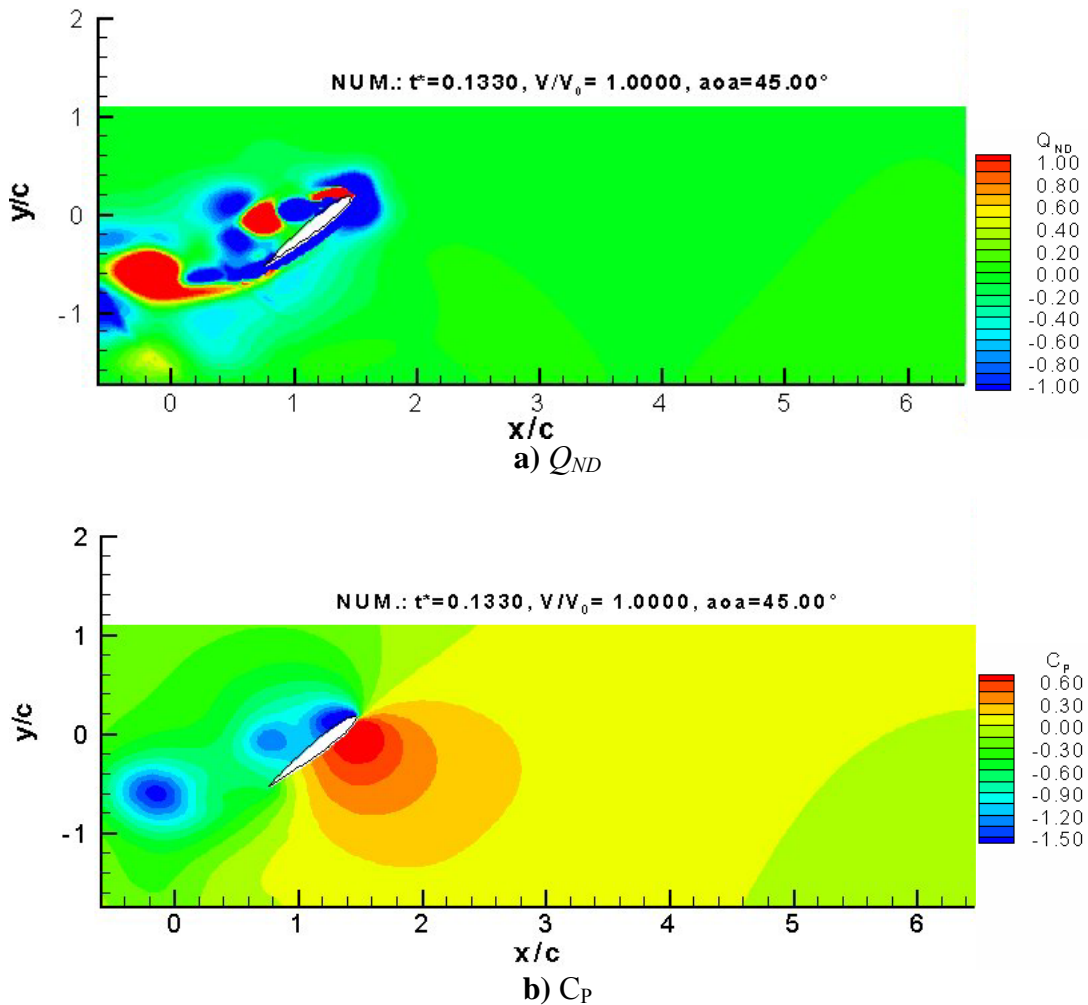


**Figure 4.21** DNS results with non-dimensional  $Q$  and pressure coefficient  $C_p$  contours at  $t^*=0.1330$ .

At  $t^*=0.3581$ , a separation phenomena during the translational phase is observed. A weak counter rotating vortex is generated on the upper surface of the airfoil. Negative pressure region on the upper surface of the airfoil also moves from the

leading edge toward to the trailing edge (Figure 4.22). Lift coefficient is minimum at this time.

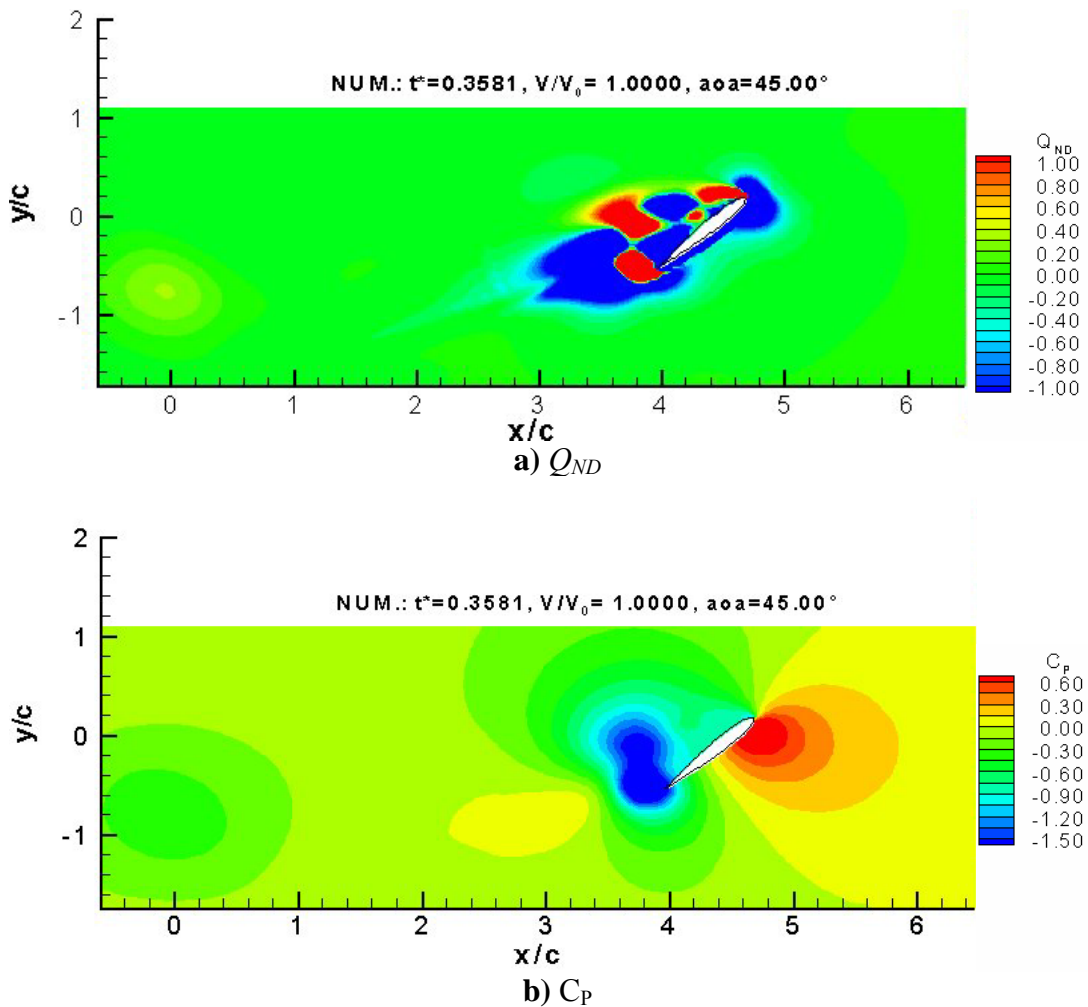


**Figure 4.22** DNS results with non-dimensional  $Q$  and pressure coefficient  $C_p$  contours at  $t^*=0.3581$ .

At the beginning of the rotation, there is also an abrupt reduction of the velocity. The rotation reinforces the vortex at the trailing edge and weakens the vortex at leading edge since there is an increase of the rotational velocity at the trailing edge and a decrease of the rotational velocity at the leading edge (Figure 4.23).

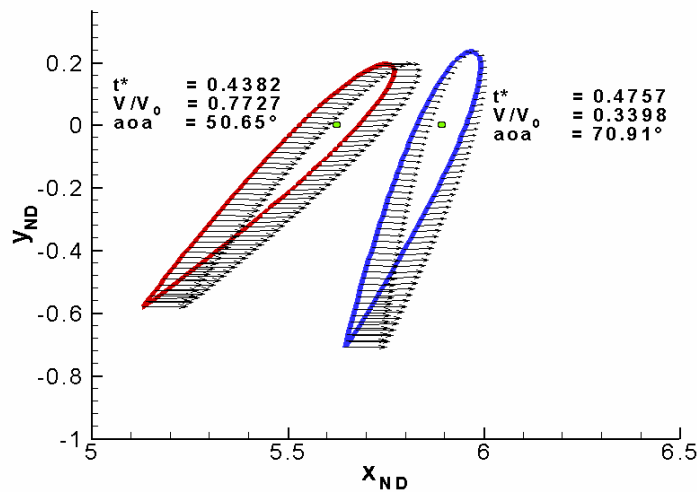


**Figure 4.23** Velocity distributions on the airfoil for two time values after the rotational phase is started.

At the end of a stroke, when the airfoil is  $90^\circ$  angle of attack, there is an annulation of the influence of the two big vortices on the airfoil. The airfoil is moving away of these two vortices resulting with zero lift and drag coefficient values in numerical simulations, which is seen also on the pressure contours close to the airfoil (Figure 4.24). This phenomenon is also visible in PIV measurements. The lift and drag coefficients are equal to zero at the end of the stroke.

At the beginning of rotation (Fig.4.24a), the suction region is situated at the trailing edge of the airfoil. As the angular velocity increases and angle of attack approaches to  $90^\circ$ , this suction peak gets bigger and spread out toward the leading edge. The suction region on the upper surface of the airfoil becomes stronger. After a while, the pressure regions are detached from the airfoil upper surface. Firstly, the leading edge vortex region moves away from the airfoil seen from the pressure contours at  $t^*=0.4581$  (Figure 4.24d) and then the trailing edge suction region moves away from the airfoil surface at  $t^*=0.4831$  (Figure 4.24e).

At the beginning of the second stroke (Figure 4.24f and Figure 4.25), the traces of the two big vortices are always present and could be seen by the two levels of suction regions. The airfoil is accelerating in this region. The pressure on the lower surface of the airfoil starts to increase. This overpressure helps to eject the two suction zones one towards downwards and the other one toward upwards. As a result, there is a very small interaction between these two suction regions and the airfoil. As going from Figure 4.24a to Figure 4.24f, the lift and drag coefficients decreases until zero value at the end of the stroke.

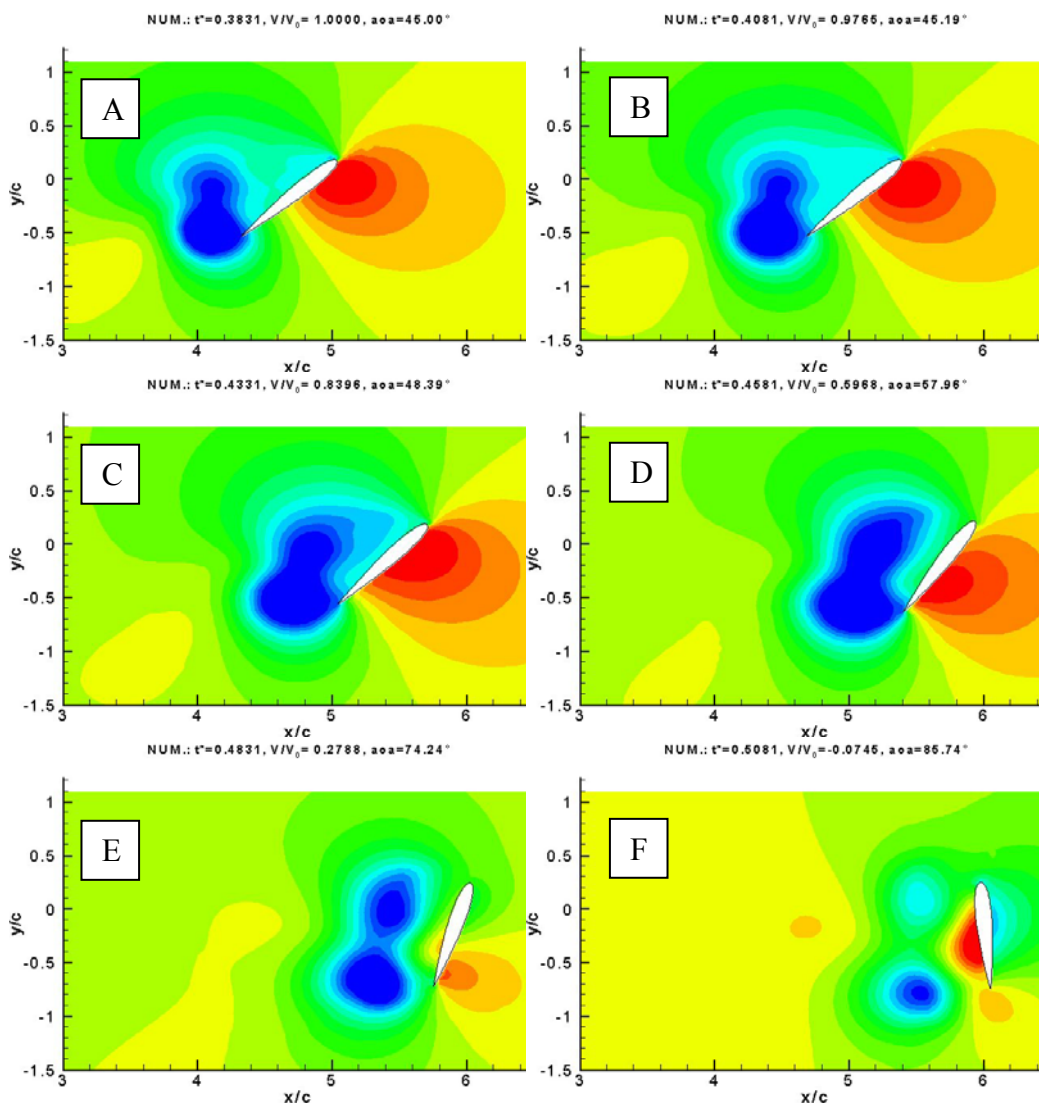


**Figure 4.24** Pressure coefficient  $C_p$  contours during rotation of the airfoil at the end of the first half period.

The two suction center of the vortex created during the previous stroke is ejected by the newly created overpressure region. This results a positive lift during the whole flapping motion (Figure 4.25). From Figure 4.25a to Figure 4.25b, the lift and drag coefficients increase and the lift coefficient is maximum at the time corresponding to Figure 4.25b. Then the lift and drag coefficients decreases until  $t^*=0.8$  approximately.

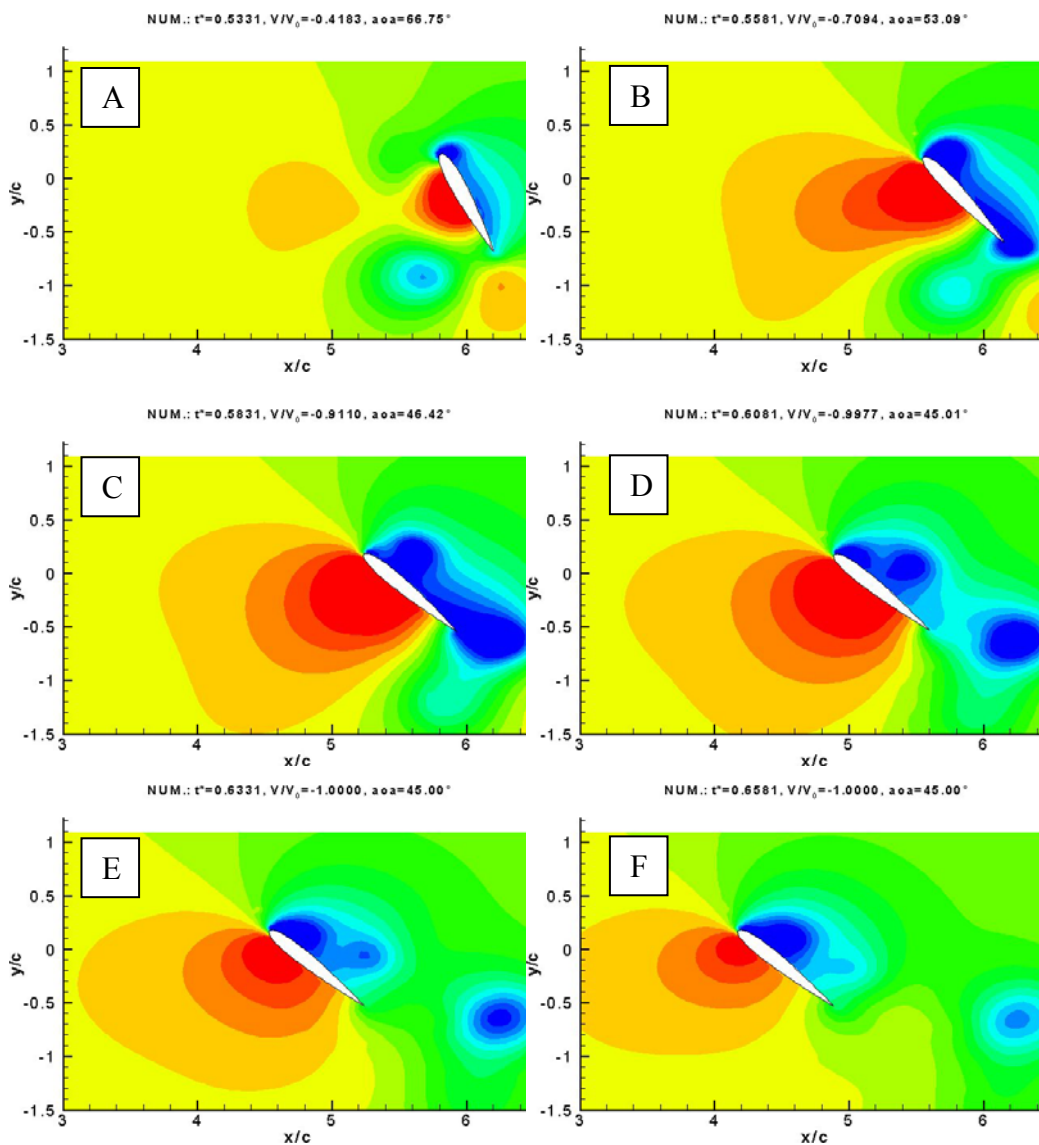


**Figure 4. 25** Pressure coefficient  $C_p$  contours during rotation of the airfoil at the beginning of the second half period.

The comparison of laser sheet visualizations, PIV measurements and numerical results during a period at different time values are represented in Appendix D from Figure D.1 to Figure D.24. Each figure represents the experimental visualization with laser sheet, non-dimensional vorticity contours for PIV measurements, non-dimensional vorticity contours for numerical simulations, non-dimensional  $Q$  contours for PIV measurements, non-dimensional  $Q$  contours for numerical simulations, pressure coefficient for the numerical simulations and the aerodynamic force coefficients for numerical simulations.

#### **4.4 Conclusion**

There is a good agreement between different types of visualizations in phenomenological point of view. Numerical simulations give significant values with respect to the forces calculated. This allows the perspective for the optimization of the aerodynamic forces. The time of the rotation  $t_a$  is an important parameter for the formation of detachment (dynamic stall). If the rotation starts earlier, there will be less time for the formation of the counter-rotating vortex on the upper surface of the airfoil which is created during translation.

PIV give more complicated topology compared to numerical simulations. We are not sure that the flow is 2-D throughout the motion. There is also a certain, very quick numerical diffusion in terms of the vortices due to the moving grid system. When the airfoil is moved away, the grid domain becomes coarser. Since the grid domain is not uniform, it is finer close to the airfoil and enlarges as it goes far away. The vortices could enter to a domain where the grid is coarser.

The vortices which are more energetical are very similar to each other for both the experimental results (laser sheet visualization and PIV) and the numerical simulations. The analysis of the forces in DNS is significant.



## CHAPTER 5

### ANALYTICAL MODEL OF FLAPPING MOTION

#### 5.1 Introduction

The analytical model developed for the analysis of the flapping motion is described in the present chapter. Brief description of the unsteady models has been done in Section 1.1.2. The model presented in this chapter is compared with the parametrical study performed in Chapter 3 with numerical simulations.

The indicial response of a quantity (e.g. lift, drag) with respect to any of its influencing parameters (e.g. angle of attack  $\alpha$  or pitch rate  $\dot{\alpha}$ ) is the response to a step input of the influencing parameter. Given this indicial response for a linear system, the indicial approach provides a methodology for computing the response of the system to any arbitrary input using the principle of superposition. This methodology is based on the fact that any arbitrary input can be approximately reconstructed by superimposing a series of step functions as shown in Figure 5.1. The response of the system to this arbitrary input is then approximated by linearly superimposing the system response to each step function making up the reconstructed input.

By decreasing the time interval  $\Delta t$  a more accurate function can be obtained and at the limit letting  $\Delta t \rightarrow 0$ , the exact response of the system could be computed using Duhamel's integral (Eq.5.1).

$$x(t) = f(0)A(t) + \int_0^t \frac{d}{d\tau} f(\tau)A(t-\tau)d\tau \quad (5.1)$$

$A(t)$  is the response of linear system to a unit step function and called "indicial admittance". Then the response  $x(t)$  to an arbitrary forcing function  $f(t)$  is found from Duhamel's Integral. Equation (5.2) is in terms of the indicial admittance and the derivatives of the forcing function but in some cases the analytical form of it can not be available so an alternative form is obtained using integration by parts.

$$x(t) = A(0)f(t) + \int_0^t f(\tau)A'(t - \tau)d\tau \quad (5.2)$$

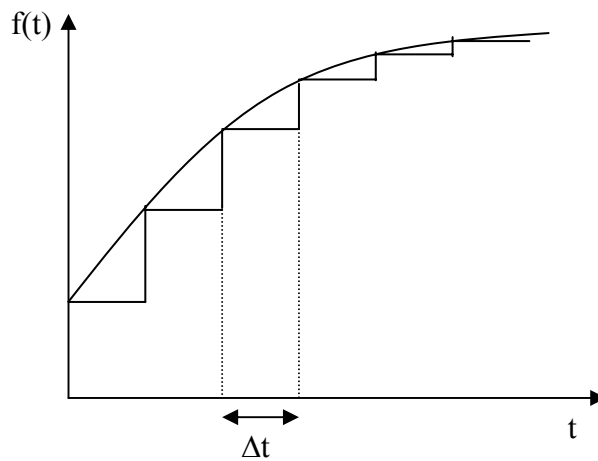


**Figure 5.1** Superposition of step functions to form an arbitrary input.

The indicial lift on a 2-D wing in incompressible flow was first derived by Wagner [43]. He has obtained a solution for the indicial lift on a thin airfoil undergoing a step change in angle of attack in incompressible flow. The indicial function is the response to a disturbance that is applied instantaneously at time zero and held constant thereafter, that is a disturbance given by a step function. In Wagner's case,  $w=0$  for  $t<0$  and  $w=V\alpha$  for  $t>0$ , where  $w$  is the induced downward velocity.

Küssner function [45] represents the dimensionless lift development due to a sharp-edged gust striking the leading edge of the airfoil at  $t=0$ . Both Wagner and Küssner functions are represented in Figure 5.2.

In this study,  $\phi_w$  is taken to be the Wagner Function with

$$\phi_w(s) = 1.0 - 0.165e^{-0.0455s} - 0.335e^{-0.3s} \quad (5.3)$$

and  $\psi$  is the Küssner Function which is approximated with exponential form as:

$$\psi(s) = 1.0 - 0.5e^{-0.13s} - 0.5e^{-1.0s} \quad (5.4)$$

where  $s$  is the reduced time defined as:

$$s = \frac{1}{b} \int_0^t V dt \quad (5.5)$$

which represents relative distance traveled by the airfoil through the flow in terms of the airfoil semi-chords during a time interval  $t$  and is called as reduced time.

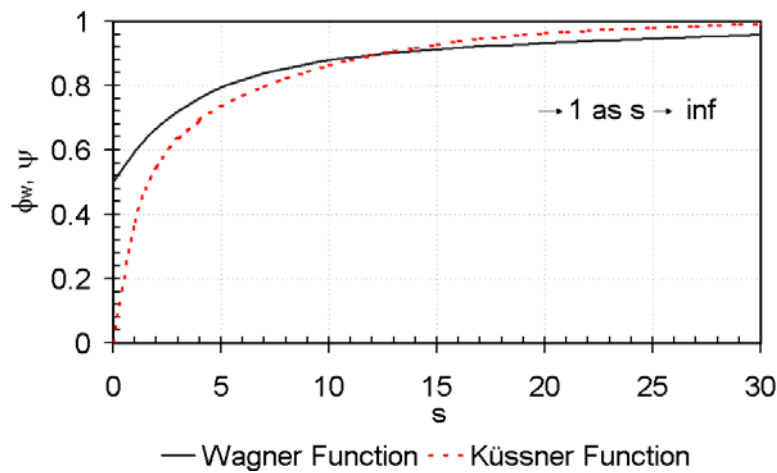


**Figure 5.2** Wagner and Küssner functions.

One important parameter used in the description of unsteady aerodynamics and unsteady airfoil behavior is the reduced frequency. This parameter is used to characterize the degree of unsteadiness of the problem. The reduced frequency in turn is expressed as  $k=\omega b/V$  where  $\omega$  is the frequency of oscillation of the airfoil with  $b$  as the semi-chord and  $V$  as the free-stream velocity or the maximum velocity of the airfoil during translation for the hover case. For more transient problems, the concept of a single reduced frequency in terms of characterizing the degree of unsteadiness of the problem begins to lose its significance. For these cases, the reduced time  $s$  is defined.

The indicial functions can be used to calculate the lift and moment on a wing undergoing an arbitrary motion by means of Duhamel's Integral assuming inviscid, potential flow conditions and based on the linear superposition assumption. Arbitrary variations in free-stream are mostly implemented by use of Eq.5.6. In this equation  $\phi$  can be replaced by either Wagner function  $\phi_w$  or Küssner function  $\psi$  according to the problem considered.

$$L_{circulatory} = \pi\rho V(t) \cdot S \cdot \left[ w_{3/4c}(0)\phi(s) + \int_0^s \frac{dw_{3/4c}}{d\sigma}(\sigma) \cdot \phi(s-\sigma)d\sigma \right] \quad (5.6)$$

In the literature it is observed that, even for high angle of attack values (as helicopter aerodynamics or MAV applications)  $3/4c$  location is used as position of downwash velocity (Theodorsen [44], Leishman [4], Zbikowski [50]). So we handle the same approach during this study and use the induced velocity value at  $3/4c$  location ( $w_{3/4c}$ ).

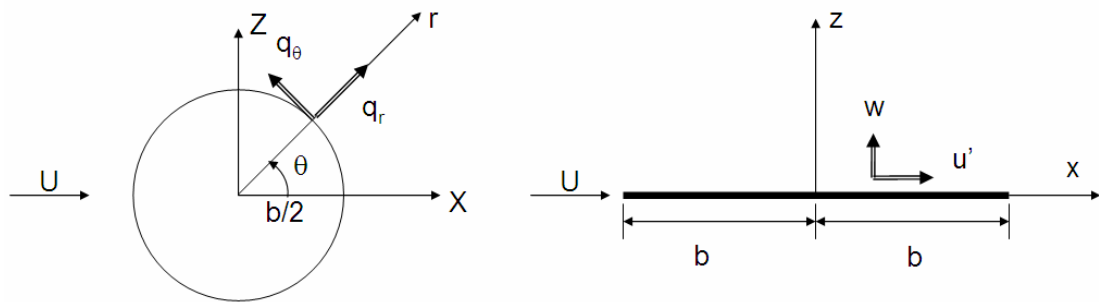
The non-circulatory or apparent mass terms arise from the  $\partial\Phi/\partial t$  term contained in the unsteady Bernoulli equation and account for the pressure forces required to accelerate the fluid in the vicinity of the airfoil. . It is the results of instantaneous local accelerations.

For example, for a thin airfoil of chord  $c=2b$ , moving normal to the surface at velocity  $w(t)$ , the noncirculatory fluid force  $F_{NC}$ , acting on the surface is:

$$F_{NC} = -M_a \frac{dw}{dt} \quad (5.7)$$

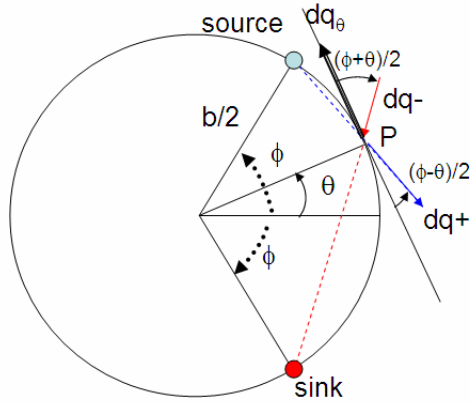
The term  $M_a$  is known as the apparent mass and in this case is given by  $M_a = \pi \rho b^2$ .

Thin airfoils oscillating in incompressible flow problem is explained in detail in Ref.62. The small-disturbance theory is considered and the Laplace equation is solved for the disturbance velocity potential  $\phi'$  along the airfoil of chord length  $2b$  subjects to two dimensional boundary condition of zero normal velocity across the body's solid boundaries. Kutta's hypothesis of finite, continuous velocities and pressure at the trailing edge is also applied in the equations. Theodorsen's solution is such that to satisfy the boundary condition, he put an appropriate distribution of source and sinks above and below the chordline. In addition, a pattern of vortices is put on this line with counter-vortices along the wake to infinity to satisfy the Kutta condition. The calculations are done by using the Joukowski's conformal mapping transformation to map a circle of radius  $b/2$  onto the airfoil's projection (Figure 5.3a). The normal velocity on the surface of the chordline ( $z=0$ ) is named  $w_a$ .



a) Conformal mapping

**Figure 5.3** Conformal mapping and the velocities induced at a point P on the circle by a source-sink pair located at  $\phi$  above and below the horizontal (reproduced from Ref.[62]).



**b) Velocity induced at point P by source-sink pair**

**Figure 5.3 (continued)** Conformal mapping the velocities induced at a point P on the circle by a source-sink pair located at  $\phi$  above and below the horizontal (reproduced from Ref.[62]).

The tangential velocity  $q_\theta$  is found from the integration of  $dq_\theta$  resulted from all possible source-sink pairs by varying  $\phi$  from 0 to  $\pi$  (Figure 5.3b)

$$\phi'(\pi, t) - \phi'(\theta, t) = \int_\theta^\pi q_\theta \frac{b}{2} d\theta \quad (5.8)$$

The disturbance velocity potential  $\phi'_U$  at an arbitrary point on the upper half of the circle, and at the corresponding point on top of the chordline is given by Equation 5.9. It is assumed that  $\phi'(\pi, t) = 0$  (at the leading edge). The detailed explanation of the calculations can be found in Ref.[62]

$$\phi'_U(\theta, t) = -\frac{b}{\pi} \int_0^\pi \int_0^\pi \frac{w_a \sin^2 \phi d\phi d\theta}{(\cos \phi - \cos \theta)} \quad (5.9)$$

Because of the anti-symmetry with respect to X-axis (axis of the circle) of the flow pattern due to the source-sink sheet, the value of  $q_\theta$  is the same at symmetrically located points on the upper and lower halves of the circle. Therefore, the change in

$\phi'$  going from any upper point around to  $\theta = \pi$  must be equal to the change of  $\phi'$  going from  $\theta = \pi$  to the corresponding lower point. That is,

$$\phi'(\pi, t) - \phi'_U(\theta, t) = \phi'_L(-\theta, t) - \phi'(\pi, t) \quad (5.10)$$

from which it follows, because of the vanishing of  $\phi'(\pi, t)$ , that

$$\phi'_L(-\theta, t) = -\phi'_U(\theta, t) \quad (5.11)$$

This equation is useful for calculating the pressure distribution on the slit representing the airfoil. The linearized Bernouilli equation for unsteady flow is:

$$p - p_\infty = -\rho U u' - \rho \frac{\partial \phi'}{\partial t} = -\rho \left( U \frac{\partial \phi'}{\partial x} + \frac{\partial \phi'}{\partial t} \right) \quad (5.12)$$

Since we can replace the lower limit  $\theta$  in Eq.(5.10) by the equivalent value of  $x = b \cos \theta$ , then the equations (5.11) and (5.12) gives the pressure difference between the upper and lower surfaces:

$$\begin{aligned} p_U - p_L &= -\rho \left( U \left( \frac{\partial \phi'_U}{\partial x} - \frac{\partial \phi'_L}{\partial x} \right) + \left( \frac{\partial \phi'_U}{\partial t} - \frac{\partial \phi'_L}{\partial t} \right) \right) \\ &= -2\rho \left( U \frac{\partial \phi'_U}{\partial x} + \frac{\partial \phi'_U}{\partial t} \right) = -2\rho \left( \frac{\partial \phi'_U}{\partial t} - \frac{U}{b \sin \theta} \frac{\partial \phi'_U}{\partial \theta} \right) \end{aligned} \quad (5.13)$$

By integration Eq.(5.13), the lift and per unit span, due to source-sink part of the flow, are found to be:

$$L_{NC} = - \int_{-b}^b (p_U - p_L) dx = 2\rho b \frac{\partial}{\partial t} \int_0^\pi \phi'_U \sin \theta d\theta \quad (5.14)$$

The total force is the summation of the non-circulatory force and the circulatory force obtained from the Duhamel Integral.

## 5.2 Choice of the Coordinates

It is useful to describe the unsteady motion of the surface on which the zero normal flow boundary condition is applied in a body-fixed coordinate system  $(x,y,z)$ . The motion of the origin  $O$  of this coordinate system  $(x,y,z)$  is then prescribed in an inertial frame of reference  $(X,Y,Z)$  and is assumed to be known (Fig.5.4).

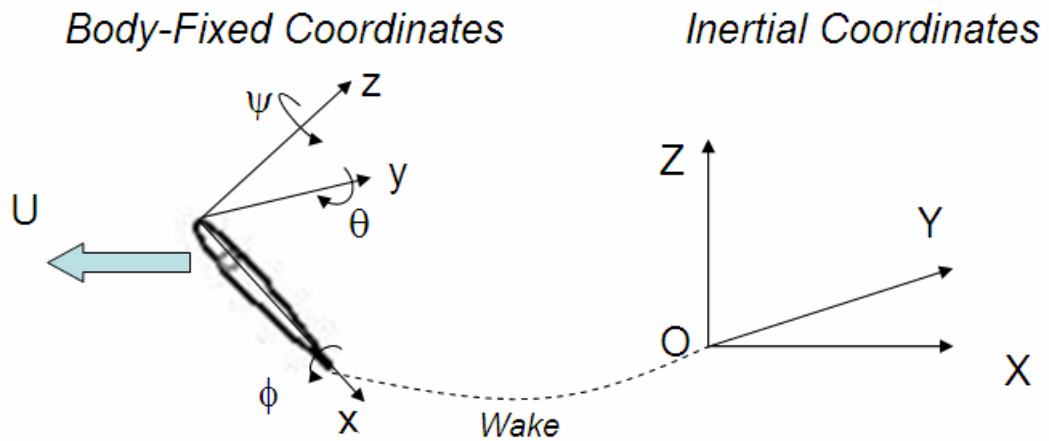


**Figure 5.4** Coordinates of the problem.

For simplicity, assume that at  $t=0$ , the inertial frame  $(X, Y, Z)$  coincides with the frame  $(x,y,z)$ . Then at  $t>0$ , the relative motion of the origin of the body fixed frame of reference is prescribed by its location  $\vec{r} = (x, y, z)$ . The rate of rotation of the body's frame of reference is  $\vec{\Omega} = (\dot{\phi}, \dot{\theta}, \dot{\psi})$ . For a 2-D flow,  $\vec{\Omega}$  reduces to  $(0, \dot{\theta}, 0)$ .

## 5.3 Formulation of the Problem

The fluid surrounding the body is assumed to be inviscid, irrotational, and incompressible over the entire flowfield, excluding the body's solid boundaries and its wakes. A velocity potential  $\Phi(X,Y,Z)$  can be defined in the inertial frame and the continuity equation, in this frame of reference becomes:



$$\nabla^2\Phi = 0 \quad (\text{in } X,Y,Z \text{ coordinates}) \quad (5.15)$$

and the first boundary condition requiring zero normal velocity across the body's solid boundaries is

$$(\nabla\Phi + \vec{v}) \cdot \vec{n} = 0 \quad (\text{in } X,Y,Z \text{ coordinates}) \quad (5.16)$$

Here  $-\vec{v}$  is the surface's velocity and  $\vec{n} = \vec{n}(X,Y,Z,t)$  is the vector normal to this moving surface, as viewed from the inertial frame of reference. Since the Eq. (5.15) does not depend directly on time, the time dependency is introduced through this boundary condition (e.g. the location and orientation of  $\vec{n}$  can vary with time) [63].

The second boundary condition requires that the flow disturbance, due to the body's motion through the fluid, should diminish far from the body (or wing).

For the unsteady flow case the use of the Kelvin condition will supply an additional equation that can be used to determine the streamwise strength of the vorticity shed into the wake. In general, it states that in the potential flow region the angular momentum cannot change, thus the circulation  $\Gamma$  around a fluid curve enclosing the wing and its wake is conserved:

$$\frac{d\Gamma}{dt} = 0 \quad (\text{for any } t) \quad (5.17)$$

The solution of this problem, which becomes time-dependent because of the boundary condition (Eq.5.16), is easier in the body-fixed coordinate system. The kinematic velocity  $\vec{v}$  of the surface due to the motion of the wing, as viewed in the body frame of reference, is given by [63]:

$$\vec{v} = -(\vec{V} + \vec{\Omega} \times \vec{r}) \quad (5.18)$$

where  $\vec{V}$  is the velocity of the (x,y,z) system's origin. As explained before,  $\vec{r} = (x,y,z)$  is the position vector and  $\vec{\Omega} = (\dot{\phi}, \dot{\theta}, \dot{\psi})$  is the rate of rotation of the body's frame of reference. To an observer in the (x,y,z) frame, the velocity direction is opposite to the flight direction (as observed in the X,Y,Z frame) and therefore the minus sign appears in Eq. 5.18.

At any moment the continuity equation is independent of the coordinate system orientation and the mass should be conserved. Therefore, the quantity  $\nabla^2\Phi$  is independent of the instantaneous coordinate system and the continuity equation in terms of (x,y,z) remains unchanged. Also the boundary conditions should state the same physical conditions

Therefore, the zero-velocity normal to a solid surface boundary condition, in the body frame becomes:

$$(\nabla\Phi + \vec{v}) \cdot \vec{n} = 0 \quad (\text{in } x,y,z \text{ coordinates}) \quad (5.19)$$

where  $\vec{n}$  is the normal to the body's surface, in terms of the body coordinates (x,y,z). So by using Eq.5.18, Eq.5.19 becomes:

$$(\nabla\Phi - \vec{V} - \vec{\Omega} \times \vec{r}) \cdot \vec{n} = 0 \quad (\text{in } x,y,z \text{ coordinates}) \quad (5.20)$$

Each region of the flapping motion, represented in Figure 2.1, is investigated separately in terms of the calculation of the downwash velocity at 3/4 c location, circulatory lift and the non-circulatory lift.

### 1<sup>st</sup> region:

#### *1. Calculation of Downwash:*

The velocity components of the airfoil expressed in body-fixed coordinate system are:

$$\vec{V} = (-U \cos \alpha, 0, -U \sin \alpha) \quad (5.21)$$

The position vector of the airfoil center of rotation is given by  $\vec{r} = (x, y, z)$  and angular velocity is given by  $\vec{\Omega} = (\dot{\phi}, \dot{\theta}, \dot{\psi}) = (0, \dot{\theta}, 0)$ .

$$\vec{\Omega} \times \vec{r} = \begin{vmatrix} i & j & k \\ 0 & \dot{\theta} & 0 \\ x-ba & y & z \end{vmatrix} = (\dot{\theta}z, 0, -\dot{\theta}(x-ba)) \quad (5.22)$$

In analytical part, the definition of  $a$  is different from the numerical DNS part. The range of  $a$  is  $-1 \leq a \leq 1$ . At the leading edge  $a=-1$  and at trailing edge  $a=1$ . The center of rotation for the calculations are at quarter chord ( $a= -0.5$ ). The normal direction of the linearized body surface in body fixed coordinate system is  $\vec{n} = (0,0,1)$ .

As a result, equation 5.20 becomes:

$$\left( \frac{\partial \Phi}{\partial x} + U \cos \alpha - \dot{\theta}z, 0, \frac{\partial \Phi}{\partial z} + U \sin \alpha + \dot{\theta}(x-ba) \right) \cdot (0,0,1) = 0 \quad (5.23)$$

$$\frac{\partial \Phi}{\partial z} + U \sin \alpha + \dot{\theta}(x-ba) = 0$$

So the local downwash is given by:

$$w_a = -U \sin \alpha - \dot{\theta} \cdot (x-ba) \quad (5.24)$$

It must be paid attention that the signs of  $U$  and  $\dot{\theta}$  are already taken into consideration. So they are treated as in absolute value.

The calculations for circulatory lift are always carried out relative to the 3/4 chord location. So downwash at this location is:

$$w_{3/4c} = -U \sin \alpha - \dot{\theta} \cdot b/2 \quad (5.25)$$

## 2. Calculation of the Circulatory Lift:

$$L_{\text{circulatory}} = \pi\rho V(t) \cdot c \cdot \text{span} \cdot \left[ w_{3/4c}(0)\phi_w(s) + \int_0^s \frac{dw_{3/4c}}{d\sigma}(\sigma) \cdot \phi_w(s-\sigma) d\sigma \right] \quad (5.26)$$

$$= \pi\rho V(t) \cdot c \cdot \text{span} \cdot [w_{3/4c} - X(s) - Y(s)]$$

where

$$X(s) = A_1 \int_0^s \frac{dw_{3/4c}}{d\sigma}(\sigma) \cdot e^{-b_1(s-\sigma)} d\sigma \quad (5.27)$$

$$Y(s) = A_2 \int_0^s \frac{dw_{3/4c}}{d\sigma}(\sigma) \cdot e^{-b_2(s-\sigma)} d\sigma \quad (5.28)$$

Numerically, the recursive integrations of the Eq.5.27 and Eq.5.28 give:

$$X(s) = X(s-\Delta s)e^{-b_1\Delta s} + \frac{A_1}{6}(w_{3/4c}(s) - w_{3/4c}(s-\Delta s)) \cdot \left( 1 + 4e^{-b_1\frac{\Delta s}{2}} + e^{-b_1\Delta s} \right) \quad (5.29)$$

$$Y(s) = Y(s-\Delta s)e^{-b_2\Delta s} + \frac{A_2}{6}(w_{3/4c}(s) - w_{3/4c}(s-\Delta s)) \cdot \left( 1 + 4e^{-b_2\frac{\Delta s}{2}} + e^{-b_2\Delta s} \right) \quad (5.30)$$

## 3. Calculation of the Non-Circulatory Lift:

$$L_{NC} = -\int_{-b}^b (p_U - p_L) dx = 2\rho b \frac{\partial}{\partial t} \int_0^\pi \phi'_U \sin \theta d\theta \quad (5.31)$$

So for the 1<sup>st</sup> region, the disturbance velocity potential  $\phi'_U$  is:

$$\phi'_U(\theta, t) = -\frac{b}{\pi} \int_0^\pi \int_0^\pi \frac{w_a \sin^2 \phi d\phi d\theta}{(\cos \phi - \cos \theta)} \quad (5.32)$$

$$\phi'_U(\theta, t) = -\frac{b}{\pi}(-U \sin \alpha)(\pi \sin \theta) - \frac{b}{\pi}(-\dot{\theta})(b \frac{\pi}{2} \sin \theta \cos \theta) - \frac{b}{\pi}(-\dot{\theta})(-ba)\pi \sin \theta$$

with local downwash  $w_a$  given by Eq.5.24.

By using the equalities in Equation 5.33,

$$\int_0^{\pi} \sin^2 \theta d\theta = \frac{\pi}{2} \quad \text{and} \quad \int_0^{\pi} \sin^2 \theta \cos \theta d\theta = 0 \quad (5.33)$$

The non-circulatory lift at the first region can be calculated as:

$$\begin{aligned} L_{NC} &= 2\rho b \frac{\partial}{\partial t} \int_0^{\pi} \left( -\frac{b}{\pi} (-U \sin \alpha) (\pi \sin \theta) - \frac{b}{\pi} (-\dot{\theta}) \left( b \frac{\pi}{2} \sin \theta \cos \theta \right) - \frac{b}{\pi} (-\dot{\theta}) (-ba) \pi \sin \theta \right) \sin \theta d\theta \\ &= 2\rho b \frac{\partial}{\partial t} \left( -\frac{b}{\pi} (-U \sin \alpha) \left( \frac{\pi^2}{2} \right) - \frac{b}{\pi} (-\dot{\theta}) (-ba) \left( \frac{\pi^2}{2} \right) \right) \\ &= 2\rho b \left( -\frac{b}{\pi} \right) \left( \frac{\pi^2}{2} \right) \frac{\partial}{\partial t} \left( (-U \sin \alpha) + (-\dot{\theta}) (-ba) \right) \\ &= \pi \rho b^2 \sin \alpha \frac{\partial}{\partial t} (U) - \pi \rho b^3 a \frac{\partial}{\partial t} (\dot{\theta}) \end{aligned} \quad (5.34)$$

$$L_{NC} = \pi \rho b^2 \sin \alpha \frac{\partial}{\partial t} (U) - \pi \rho b^3 a \frac{\partial}{\partial t} (\dot{\theta}) \quad (5.35)$$

The total force is the summation of the circulatory lift (Eq.5.26) and the non-circulatory lift (Eq.5.35).

2<sup>nd</sup> region:

*1. Calculation of Downwash:*

The components of the translational velocity and the angular velocity of the airfoil for the second region are:

$$\vec{V} = (-U \cos \alpha, 0, U \sin \alpha) \quad (5.36)$$

$$\vec{\Omega} = (\dot{\phi}, \dot{\theta}, \dot{\psi}) = (0, \dot{\theta}, 0) \quad (5.37)$$

Then,

$$\vec{\Omega} \times \vec{r} = \begin{vmatrix} i & j & k \\ 0 & \dot{\theta} & 0 \\ x-ba & y & z \end{vmatrix} = (\dot{\theta}z, 0, -\dot{\theta}(x-ba)) \quad (5.38)$$

So the local downwash is given by:

$$w_a = U \sin \alpha - \dot{\theta} \cdot (x - ba) \quad (5.39)$$

The downwash at 3/4c location is:

$$w_{3/4c} = U \sin \alpha - \dot{\theta} \cdot b/2 \quad (5.40)$$

2. Calculation of the Circulatory Lift :

$$\begin{aligned} L_{\text{circulatory}} &= \pi \rho V(t) \cdot c \cdot \text{span} \cdot \left[ w_{3/4c}(0) \phi_w(s) + \int_0^s \frac{dw_{3/4c}}{d\sigma}(\sigma) \cdot \phi_w(s - \sigma) d\sigma \right] \\ &= \pi \rho V(t) \cdot c \cdot \text{span} \cdot [w_{3/4c} - X(s) - Y(s)] \end{aligned} \quad (5.41)$$

3. Calculation of the Non-Circulatory Lift:

For the 2<sup>nd</sup> region the lower surface is now at the top and upper surface is at the bottom. So the non-circulatory lift must be defined such that:

$$L_{NC} = - \int_{-b}^b (p_L - p_U) dx = -2\rho b \frac{\partial}{\partial t} \int_0^\pi \phi'_U \sin \theta d\theta \quad (5.42)$$

So for the 2<sup>nd</sup> region, the disturbance velocity potential  $\phi'_U$  is:

$$\begin{aligned} \phi'_U(\theta, t) &= - \frac{b}{\pi} \int_0^\pi \int_0^\pi \frac{w_a \sin^2 \phi d\phi d\theta}{(\cos \phi - \cos \theta)} \\ \phi'_U(\theta, t) &= - \frac{b}{\pi} (U \sin \alpha) (\pi \sin \theta) - \frac{b}{\pi} (-\dot{\theta}) (b \frac{\pi}{2} \sin \theta \cos \theta) - \frac{b}{\pi} (-\dot{\theta}) (-ba) \pi \sin \theta \end{aligned} \quad (5.43)$$

with local downwash  $w_a$  given by Eq.5.39.

$$\begin{aligned}
L_{NC} &= -2\rho b \frac{\partial}{\partial t} \int_0^\pi \left( -\frac{b}{\pi} (U \sin \alpha) (\pi \sin \theta) - \frac{b}{\pi} (-\dot{\theta}) \left( b \frac{\pi}{2} \sin \theta \cos \theta \right) - \frac{b}{\pi} (-\dot{\theta}) (-ba) \pi \sin \theta \right) \sin \theta d\theta \\
&= -2\rho b \frac{\partial}{\partial t} \left( -\frac{b}{\pi} (U \sin \alpha) \left( \frac{\pi^2}{2} \right) - \frac{b}{\pi} (-\dot{\theta}) (-ba) \left( \frac{\pi^2}{2} \right) \right) \\
&= -2\rho b \left( -\frac{b}{\pi} \right) \left( \frac{\pi^2}{2} \right) \frac{\partial}{\partial t} \left( (U \sin \alpha) + (-\dot{\theta}) (-ba) \right) \\
&= \pi \rho b^2 \sin \alpha \frac{\partial}{\partial t} (U) + \pi \rho b^3 a \frac{\partial}{\partial t} (\dot{\theta})
\end{aligned} \tag{5.44}$$

$$L_{NC} = \pi \rho b^2 \sin \alpha \frac{\partial}{\partial t} (U) + \pi \rho b^3 a \frac{\partial}{\partial t} (\dot{\theta}) \tag{5.45}$$

The total force is the summation of the circulatory lift (Eq.5.41) and the non-circulatory lift (Eq.5.45).

3<sup>rd</sup> region:

*1. Calculation of Downwash:*

The components of the translational velocity and the angular velocity of the airfoil for the third region are:

$$\vec{V}_o = (\dot{X}_o, \dot{Y}_o, \dot{Z}_o) = (-U \cos \alpha, 0, U \sin \alpha) \tag{5.46}$$

$$\vec{\Omega} = (\dot{\phi}, \dot{\theta}, \dot{\psi}) = (0, -\dot{\theta}, 0) \tag{5.47}$$

Then,

$$\vec{\Omega} \times \vec{r} = \begin{vmatrix} i & j & k \\ 0 & -\dot{\theta} & 0 \\ x-ba & y & z \end{vmatrix} = (-\dot{\theta}z, 0, \dot{\theta}(x-ba)) \tag{5.48}$$

So the local downwash is given by:

$$w_a = U \sin \alpha + \dot{\theta} \cdot (x - ba) \tag{5.49}$$

The downwash at 3/4c location is:

$$w_{3/4c} = U \sin \alpha + \dot{\theta} \cdot b/2 \quad (5.50)$$

2. Calculation of the Circulatory Lift :

$$\begin{aligned} L_{\text{circulatory}} &= \pi \rho V(t) \cdot c \cdot \text{span} \cdot \left[ w_{3/4c}(0) \phi_w(s) + \int_0^s \frac{dw_{3/4c}}{d\sigma}(\sigma) \cdot \phi_w(s - \sigma) d\sigma \right] \\ &= \pi \rho V(t) \cdot c \cdot \text{span} \cdot [w_{3/4c} - X(s) - Y(s)] \end{aligned} \quad (5.51)$$

3. Calculation of the Non-Circulatory Lift:

For the 3<sup>rd</sup> region the lower surface is now at the top and upper surface is at the bottom. So the non-circulatory lift must be defined such that:

$$L_{NC} = - \int_{-b}^b (p_L - p_U) dx = -2\rho b \frac{\partial}{\partial t} \int_0^\pi \phi'_U \sin \theta d\theta \quad (5.52)$$

So for the 3<sup>rd</sup> region, the disturbance velocity potential  $\phi'_U$  is:

$$\begin{aligned} \phi'_U(\theta, t) &= - \frac{b}{\pi} \int_0^\pi \int_0^\pi \frac{w_a \sin^2 \phi d\phi d\theta}{(\cos \phi - \cos \theta)} \\ \phi'_U(\theta, t) &= - \frac{b}{\pi} (U \sin \alpha) (\pi \sin \theta) - \frac{b}{\pi} (\dot{\theta}) \left( b \frac{\pi}{2} \sin \theta \cos \theta \right) - \frac{b}{\pi} (\dot{\theta}) (-ba) \pi \sin \theta \end{aligned} \quad (5.53)$$

with local downwash  $w_a$  given by Eq.5.49.

The non-circulatory lift is:

$$L_{NC} = - \int_{-b}^b (p_L - p_U) dx = -2\rho b \frac{\partial}{\partial t} \int_0^\pi \phi'_U \sin \theta d\theta \quad (5.54)$$



$$\begin{aligned}
L_{NC} &= -2\rho b \frac{\partial}{\partial t} \int_0^\pi \left( -\frac{b}{\pi} (U \sin \alpha) (\pi \sin \theta) - \frac{b}{\pi} (\dot{\theta}) \left( b \frac{\pi}{2} \sin \theta \cos \theta \right) - \frac{b}{\pi} (\dot{\theta}) (-ba) \pi \sin \theta \right) \sin \theta d\theta \\
&= -2\rho b \frac{\partial}{\partial t} \left( -\frac{b}{\pi} (U \sin \alpha) \left( \frac{\pi^2}{2} \right) - \frac{b}{\pi} (\dot{\theta}) (-ba) \left( \frac{\pi^2}{2} \right) \right) \\
&= -2\rho b \left( -\frac{b}{\pi} \right) \left( \frac{\pi^2}{2} \right) \frac{\partial}{\partial t} \left( (U \sin \alpha) + (\dot{\theta}) (-ba) \right) \\
&= \pi \rho b^2 \sin \alpha \frac{\partial}{\partial t} (U) - \pi \rho b^3 a \frac{\partial}{\partial t} (\dot{\theta})
\end{aligned} \tag{5.55}$$

$$L_{NC} = \pi \rho b^2 \sin \alpha \frac{\partial}{\partial t} (U) - \pi \rho b^3 a \frac{\partial}{\partial t} (\dot{\theta}) \tag{5.56}$$

The total force is the summation of the circulatory lift (Eq.5.51) and the non-circulatory lift (Eq.5.56).

4<sup>th</sup> region:

*1. Calculation of Downwash:*

The components of the translational velocity and the angular velocity of the airfoil for the fourth region are:

$$\vec{V} = (-U \cos \alpha, 0, -U \sin \alpha) \tag{5.57}$$

$$\vec{\Omega} = (\dot{\phi}, \dot{\theta}, \dot{\psi}) = (0, -\dot{\theta}, 0) \tag{5.58}$$

Then,

$$\vec{\Omega} \times \vec{r} = \begin{vmatrix} i & j & k \\ 0 & -\dot{\theta} & 0 \\ x-ba & y & z \end{vmatrix} = (-\dot{\theta}z, 0, \dot{\theta}(x-ba)) \tag{5.59}$$

So the local downwash is given by:

$$w_a = -U \sin \alpha + \dot{\theta} \cdot (x - ba) \tag{5.60}$$

The downwash at 3/4c location is:

$$w_{3/4c} = -U \sin \alpha + \dot{\theta} \cdot b/2 \tag{5.61}$$

2. Calculation of the Circulatory Lift:

$$L_{\text{circulatory}} = \pi\rho V(t) \cdot c \cdot \text{span} \cdot \left[ w_{3/4c}(0)\phi_w(s) + \int_0^s \frac{dw_{3/4c}}{d\sigma}(\sigma) \cdot \phi_w(s-\sigma)d\sigma \right] \quad (5.62)$$

$$= \pi\rho V(t) \cdot c \cdot \text{span} \cdot [w_{3/4c} - X(s) - Y(s)]$$

3. Calculation of the Non-Circulatory Lift:

For the 4<sup>th</sup> region, the disturbance velocity potential  $\phi'_U$  is:

$$\phi'_U(\theta, t) = -\frac{b}{\pi} \int_0^\pi \int_0^\pi \frac{w_a \sin^2 \phi d\phi d\theta}{(\cos \phi - \cos \theta)} \quad (5.63)$$

$$\phi'_U(\theta, t) = -\frac{b}{\pi} (-U \sin \alpha)(\pi \sin \theta) - \frac{b}{\pi} (\dot{\theta})(b \frac{\pi}{2} \sin \theta \cos \theta) - \frac{b}{\pi} (\dot{\theta})(-ba)\pi \sin \theta$$

with local downwash  $w_a$  given by Eq.5.60.

Then, the non-circulatory lift is:

$$L_{NC} = -\int_{-b}^b (p_U - p_L) dx = 2\rho b \frac{\partial}{\partial t} \int_0^\pi \phi'_U \sin \theta d\theta \quad (5.64)$$

$$L_{NC} = 2\rho b \frac{\partial}{\partial t} \int_0^\pi \left( -\frac{b}{\pi} (-U \sin \alpha)(\pi \sin \theta) - \frac{b}{\pi} (\dot{\theta})(b \frac{\pi}{2} \sin \theta \cos \theta) - \frac{b}{\pi} (\dot{\theta})(-ba)\pi \sin \theta \right) \sin \theta d\theta$$

$$= 2\rho b \frac{\partial}{\partial t} \left( -\frac{b}{\pi} (-U \sin \alpha) \left( \frac{\pi^2}{2} \right) - \frac{b}{\pi} (\dot{\theta})(-ba) \left( \frac{\pi^2}{2} \right) \right) \quad (5.65)$$

$$= 2\rho b \left( -\frac{b}{\pi} \right) \left( \frac{\pi^2}{2} \right) \frac{\partial}{\partial t} \left( (-U \sin \alpha) + (\dot{\theta})(-ba) \right)$$

$$= \pi\rho b^2 \sin \alpha \frac{\partial}{\partial t} (U) + \pi\rho b^3 a \frac{\partial}{\partial t} (\dot{\theta})$$

$$L_{NC} = \pi\rho b^2 \sin \alpha \frac{\partial}{\partial t} (U) + \pi\rho b^3 a \frac{\partial}{\partial t} (\dot{\theta}) \quad (5.66)$$

The total force is the summation of the circulatory lift (Eq.5.62) and the non-circulatory lift (Eq.5.66). The results are tabulated as a summary for all four regions in Table 5.1 where  $U$  and  $\dot{\theta}$  are in absolute value since their signs are already included in the calculations.

**Table 5.1** Summary of the calculations for local downwash and non-circulatory lift.

Region	$w_a$ (local downwash)	Non-circulatory lift
1	$w_a = -U \sin \alpha - \dot{\theta} \cdot (x - ba)$	$L_{NC} = \pi \rho b^2 \sin \alpha \frac{\partial}{\partial t}(U) - \pi \rho b^3 a \frac{\partial}{\partial t}(\dot{\theta})$
2	$w_a = U \sin \alpha - \dot{\theta} \cdot (x - ba)$	$L_{NC} = \pi \rho b^2 \sin \alpha \frac{\partial}{\partial t}(U) + \pi \rho b^3 a \frac{\partial}{\partial t}(\dot{\theta})$
3	$w_a = U \sin \alpha + \dot{\theta} \cdot (x - ba)$	$L_{NC} = \pi \rho b^2 \sin \alpha \frac{\partial}{\partial t}(U) - \pi \rho b^3 a \frac{\partial}{\partial t}(\dot{\theta})$
4	$w_a = -U \sin \alpha + \dot{\theta} \cdot (x - ba)$	$L_{NC} = \pi \rho b^2 \sin \alpha \frac{\partial}{\partial t}(U) + \pi \rho b^3 a \frac{\partial}{\partial t}(\dot{\theta})$

## 5.4 Results

### 5.4.1 Duhamel Integral with Wagner Function

Aerodynamic forces, especially instantaneous normal force coefficient, are calculated assuming the flow around the airfoil to be governed by the linearized partial differential equation and the linearized boundary conditions for a given unsteady motion. The approach used was to superimpose indicial aerodynamic responses, by use of a superposition integral, named as Duhamel integral in literature, so that the specified boundary conditions are satisfied throughout time and space. Arbitrary variations in free-stream are mostly implemented by use of Eq.5.67.

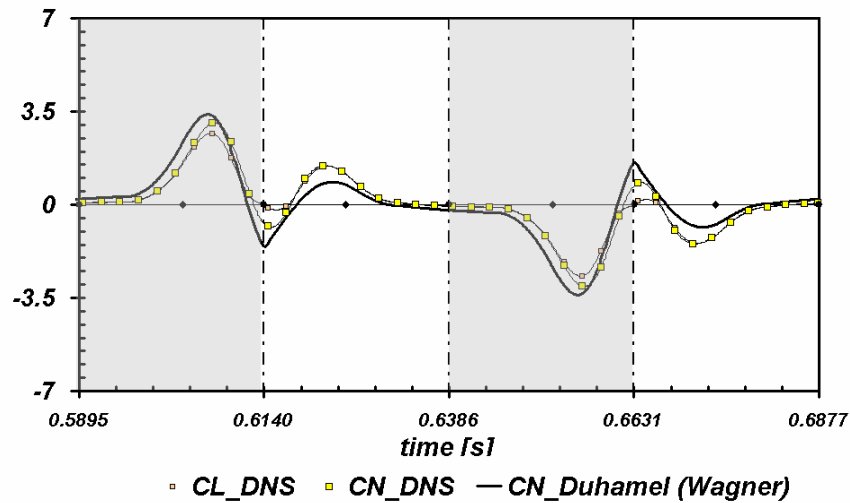
$$L_{circulatory} = \frac{C_{L\alpha}}{2} \rho V(t) \cdot S \cdot \left[ w_{3/4c}(0) \phi_w(s) + \int_0^s \frac{dw_{3/4c}}{d\sigma}(\sigma) \cdot \phi_w(s - \sigma) d\sigma \right] \quad (5.67)$$

In this study,  $\phi_w$  is taken to be the Wagner Function with  $s$  being the reduced time. For most of the studies in literature, the  $C_{L\alpha}$  term is taken to be equal to  $2\pi$ , the curve slope of the ideal fluid.

The non-circulatory or apparent mass terms are the results of instantaneous local accelerations.

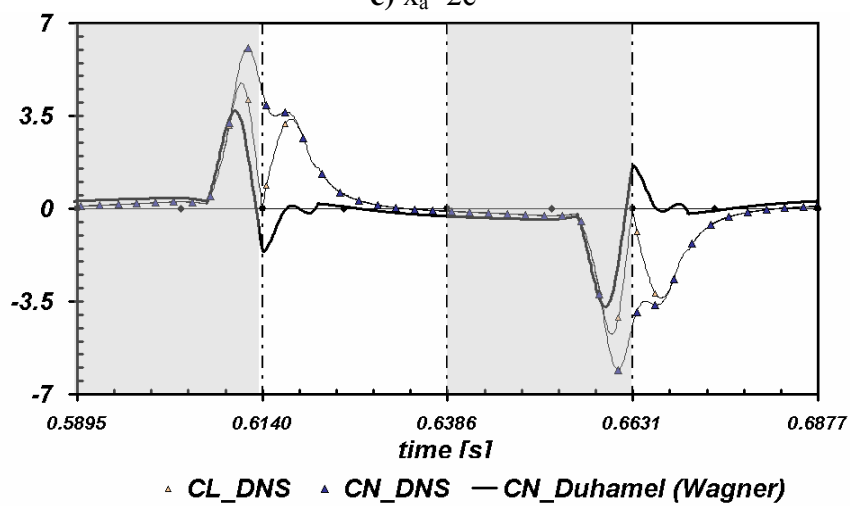
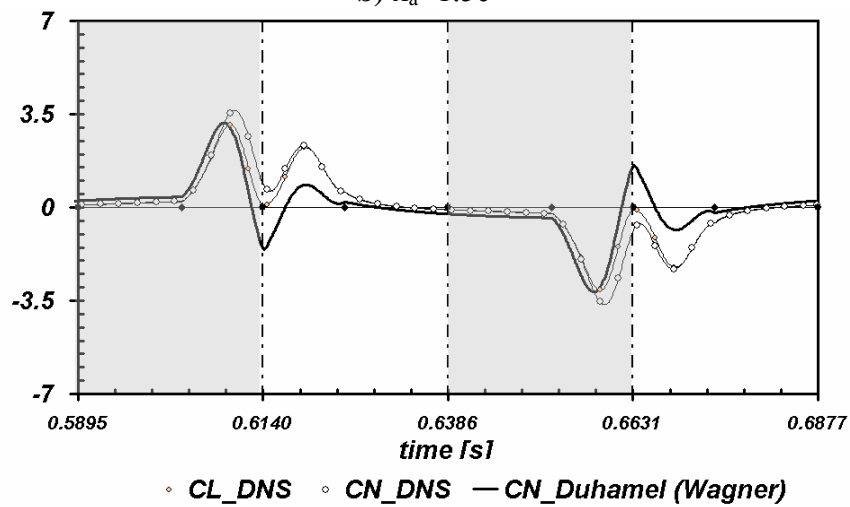
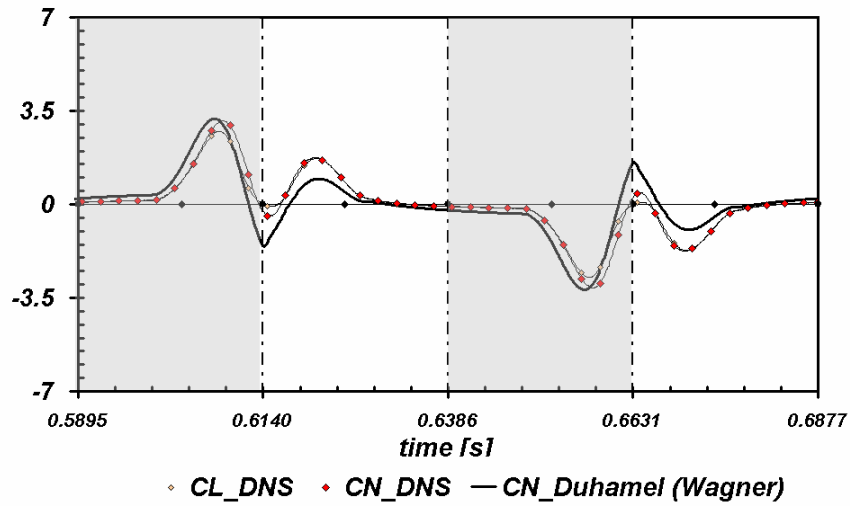
$$L_{NC} = \pi\rho b^2 \frac{\partial}{\partial t} (V \sin \alpha) + \pi\rho b^2 \frac{\partial}{\partial t} \left( \left| \dot{\theta} \right| \frac{b}{2} \right) \quad (5.68)$$

Figure 5.5 shows the results obtained by the above approach for a small starting angle of attack value of  $5^\circ$  by using Eq.5.67 and Eq.5.68 in order to calculate total normal force. The aerodynamic force coefficients are calculated with respect to the constant translational velocity.



a)  $x_a=1c$

**Figure 5.5** Lift coefficient, normal force coefficient and Duhamel Integral solution with Wagner function for  $\alpha=5^\circ$ ,  $x_v=2c$ ,  $Re=1000$  at  $1/4c$  rotation during 7<sup>th</sup> stroke using  $2\pi$  as curve slope.



**Figure 5.5 (continued)** Lift coefficient, normal force coefficient and Duhamel Integral solution with Wagner function for  $\alpha=5^\circ$ ,  $x_v=2c$ ,  $Re=1000$  at  $1/4c$  rotation during 7<sup>th</sup> stroke using  $2\pi$  as curve slope.

Since the angle of attack increase during the rotational region (which goes to 90° at the end of the stroke), the method does not respond very well in these regions and it is also observed that multiplication of this region with V(t) is not correct (V(t) goes to zero as the angle of attack goes to 90°). The first part of the circulatory lift is the steady state value at t=0. The Duhamel Integral calculates the lift by use of varying velocity and incidence data compared to this initial result. Since the lift is multiplied by V(t), the steady state lift value at s=0 is lost for V(t)≠V<sub>0</sub> so this value (named as L<sub>3</sub> in Eq.5.69) is added to the total circulatory lift value. The non circulatory lift is always taken to be as Eq.5.68. So the same configuration for Fig.5.5 is drawn with new correction term in circulatory lift in Fig.5.6 for always α=5°. The difference is observable only during the rotational region.

$$L_{circulatory} = \frac{C_{L\alpha}}{2} \rho V(t) \cdot S \cdot \left[ w_{3/4c}(0) \phi_w(s) + \int_0^s \frac{dw_{3/4c}}{d\sigma}(\sigma) \cdot \phi_w(s-\sigma) d\sigma \right] + L_3 \quad (5.69)$$

where L<sub>3</sub> is calculated as:

$$L_3 = L_{ss} \cdot \left( \frac{|V(0)| - |V(t)|}{|V(0)|} \right) \quad (5.70)$$

with L<sub>ss</sub> being the steady state value at initial position t=0 given by:

$$L_{ss} = \frac{C_{L\alpha}}{2} \rho \cdot (-|V(0)|) \cdot S \cdot [w_{3/4c}(0)] = \frac{C_{L\alpha}}{2} \rho \cdot (-|V(0)|) \cdot S \cdot [-|V(0)| \cdot \sin \alpha(0)] \quad (5.71)$$

The lift slope is taken to be equal to 2π in this section. The results are highly good for 5° angle of attack for all x<sub>a</sub> values during the translational phase. The results of the analytical model for the rotational region are similar to the DNS results mostly for small x<sub>a</sub> values.

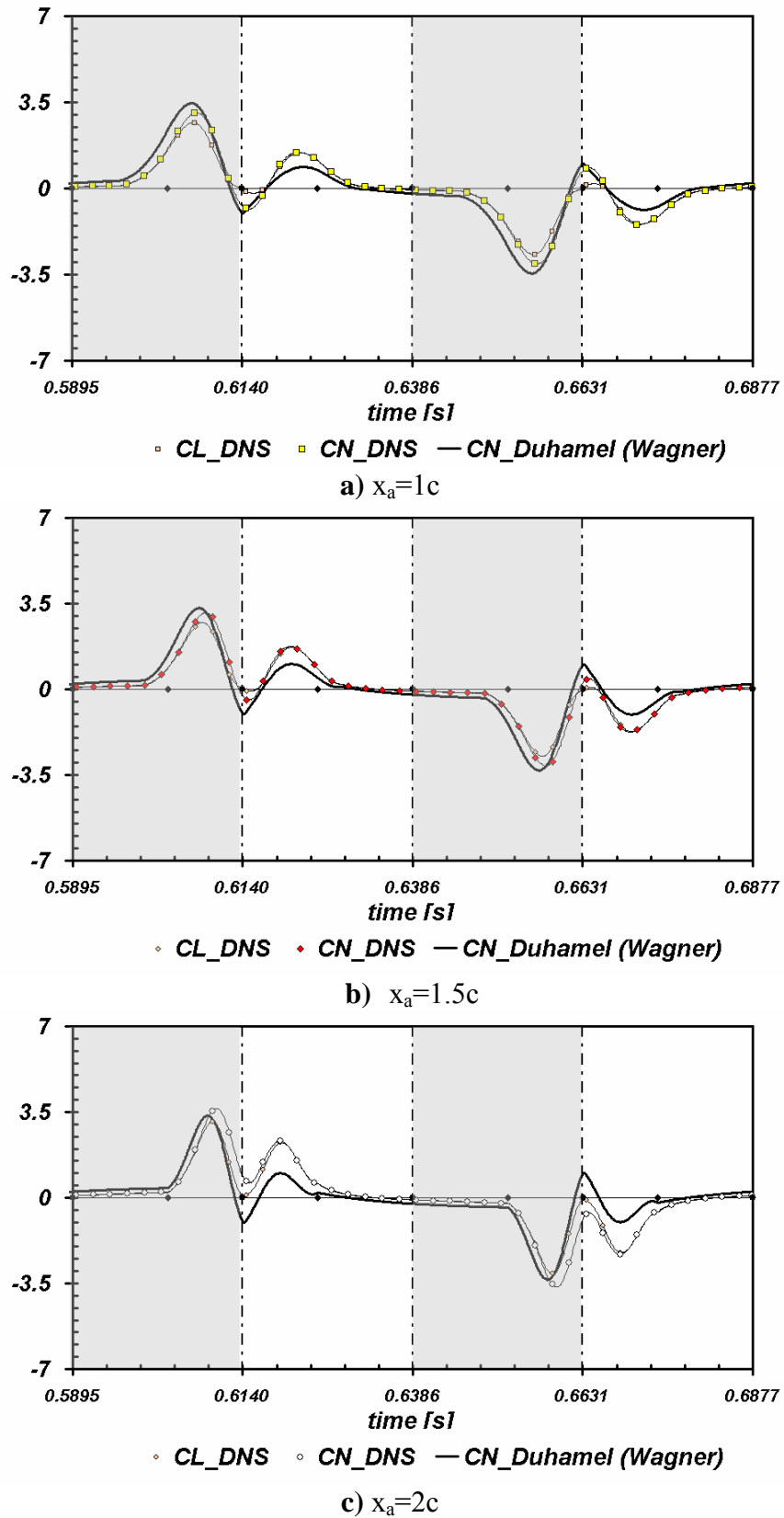


**Figure 5.6** Lift coefficient, normal force coefficient and Duhamel Integral solution with Wagner function for  $\alpha=5^\circ$ ,  $x_v=2c$ ,  $Re=1000$  at  $1/4c$  rotation during 7<sup>th</sup> stroke using  $2\pi$  as curve slope.

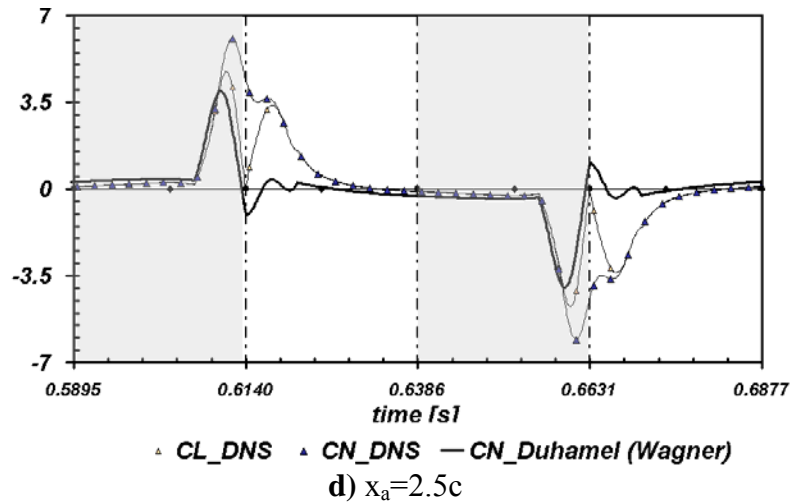


**Figure 5.6 (continue)** Lift coefficient, normal force coefficient and Duhamel Integral solution with Wagner function for  $\alpha=5^\circ$ ,  $x_v=2c$ ,  $Re=1000$  at  $1/4c$  rotation during 7<sup>th</sup> stroke using  $2\pi$  as curve slope.

The results for  $\alpha=30^\circ$  with different  $x_a$  values are shown in Fig.5.7 by using the correction term  $L_3$  in circulatory lift calculations. It is always observed that the results are not so close to the DNS results for high angles of attack where small angle of attack assumption is no longer valid during the translational phase.

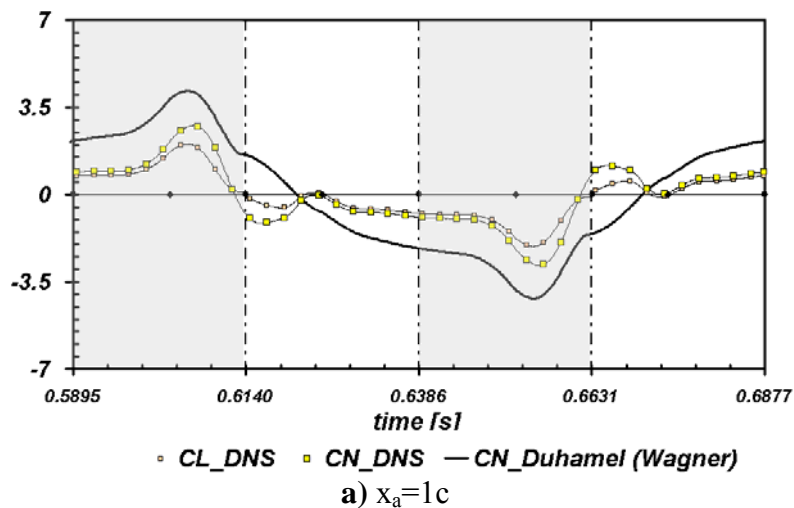
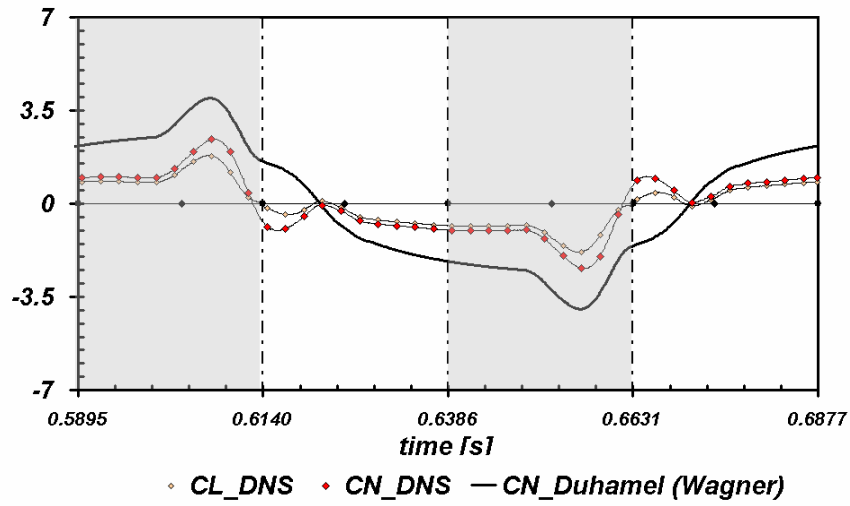
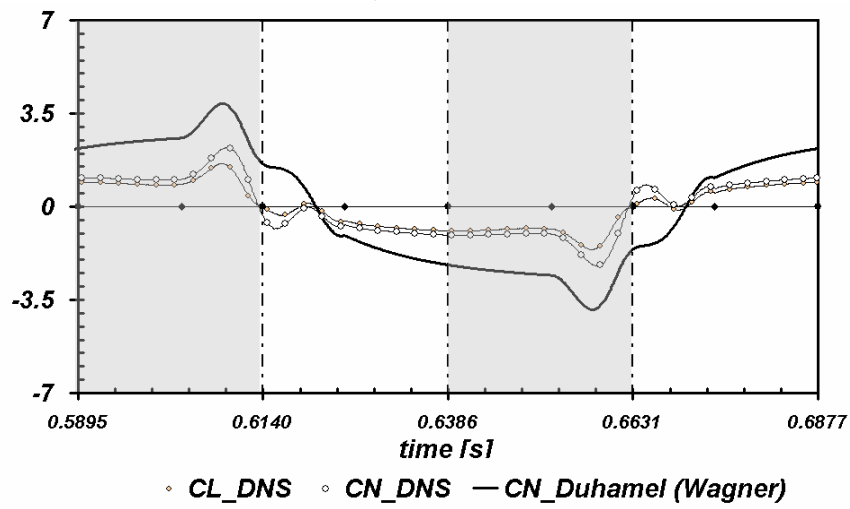


**Figure 5.7** Lift coefficient, normal force coefficient and Duhamel Integral solution with Wagner function for  $\alpha=30^\circ$ ,  $x_v=2c$ ,  $Re=1000$  at  $1/4c$  rotation during 7<sup>th</sup> stroke using  $2\pi$  as curve slope.

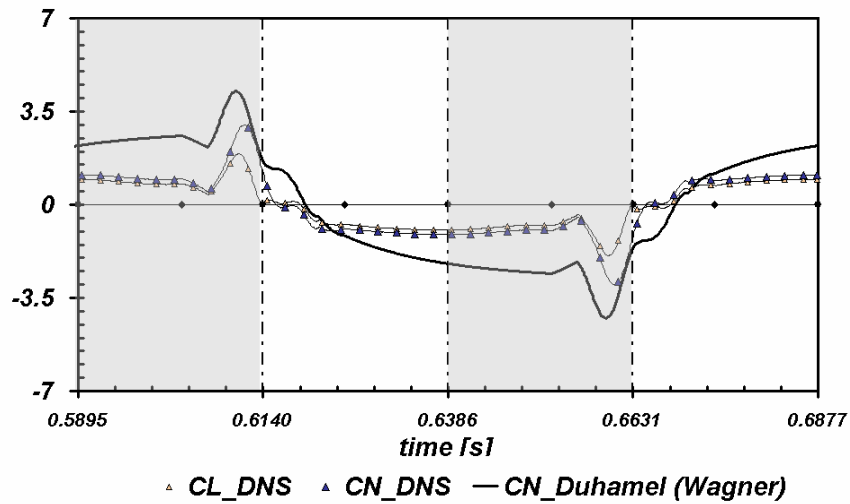




b)  $x_a=1.5c$



c)  $x_a=2c$



d)  $x_a=2.5c$

**Figure 5.7 (continued)** Lift coefficient, normal force coefficient and Duhamel Integral solution with Wagner function for  $\alpha=30^\circ$ ,  $x_v=2c$ ,  $Re=1000$  at  $1/4c$  rotation during 7<sup>th</sup> stroke using  $2\pi$  as curve slope.

### 5.4.2 Duhamel Integral with Wagner Function using DNS results

Since the results are not satisfactory for high starting angles of attack, the curve slope  $2\pi$  in the circulatory lift calculations is replaced by the DNS curve slope values since for high angle of attacks this curve slope is no longer valid. The curve slope implemented in Eq. 5.69 is the averaged normal force coefficient found from impulsive motion divided by  $\sin\alpha$ . (It is checked that starting location for averaging the normal force coefficient corresponds to a time value where the impulsive start effect on aerodynamic forces diminish its influence.) The non-circulatory equation (Eq.5.68) is always used in the calculations. Fig.5.8 and Fig.5.9 show the comparison of normal force coefficients obtained from the addition of these circulatory part and the non-circulatory part for  $5^\circ$  and  $30^\circ$  angle of attack values respectively. The results for high angles of attack are ameliorated as can be seen from Fig.5.9.

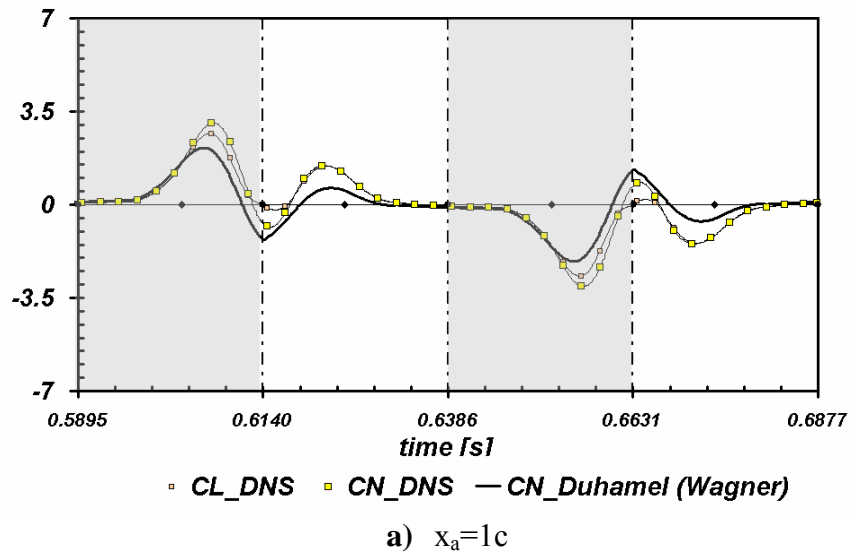
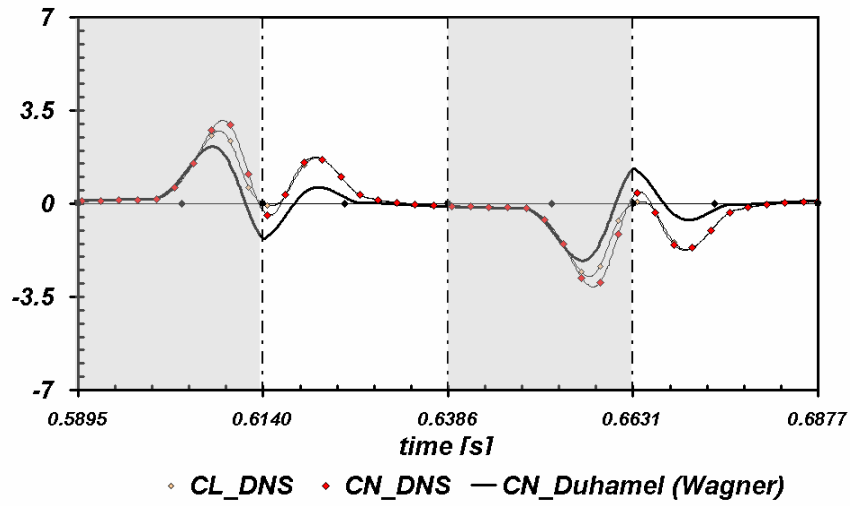
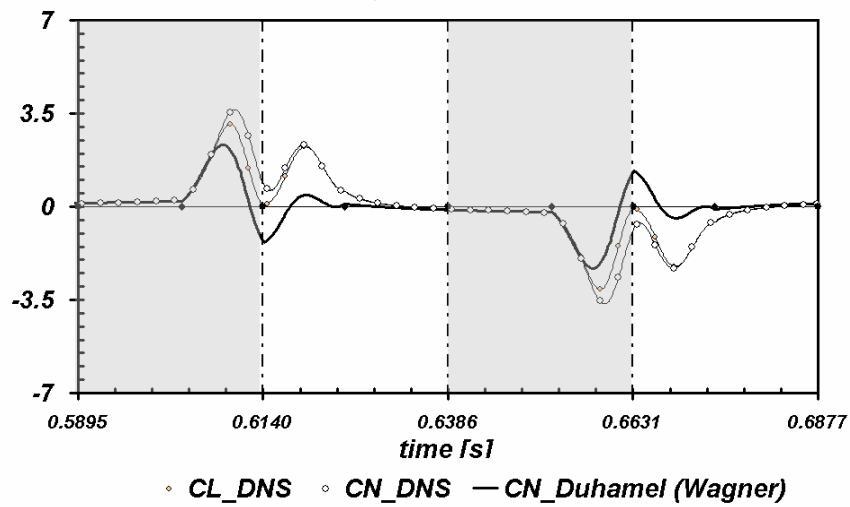


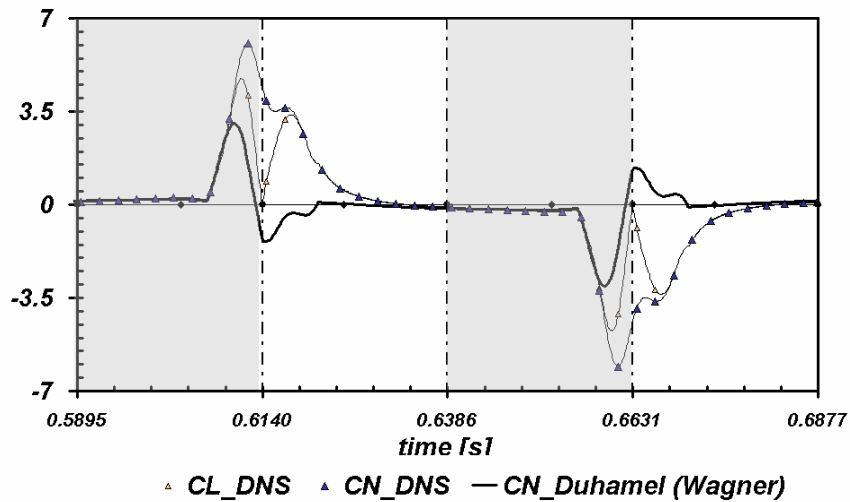
**Figure 5.8** Lift coefficient, normal force coefficient and Duhamel Integral solution with Wagner function for  $\alpha=5^\circ$ ,  $x_v=2c$ ,  $Re=1000$  at  $1/4c$  rotation during 7<sup>th</sup> stroke using DNS curve slope values.



b)  $x_a=1.5c$



c)  $x_a=2c$



d)  $x_a=2.5c$

**Figure 5.8 (continued)** Lift coefficient, normal force coefficient and Duhamel Integral solution with Wagner function for  $\alpha=5^\circ$ ,  $x_v=2c$ ,  $Re=1000$  at  $1/4c$  rotation during 7<sup>th</sup> stroke using DNS curve slope values.

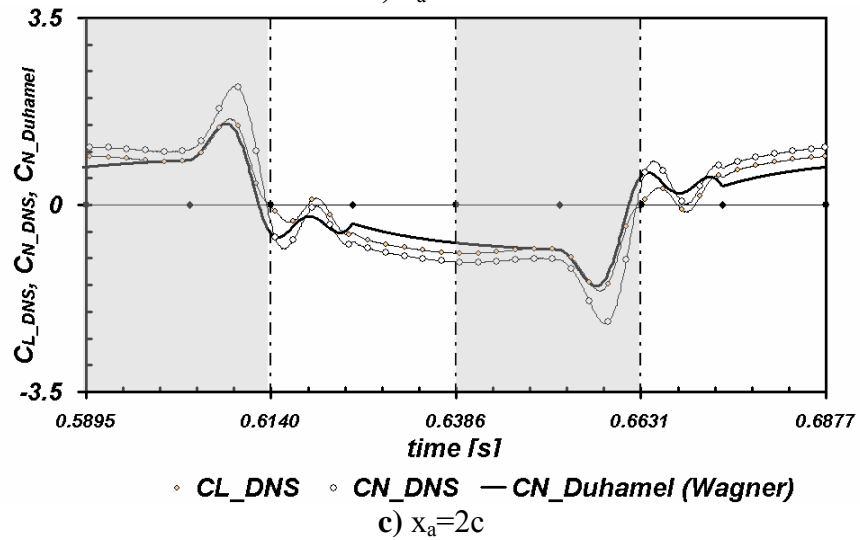
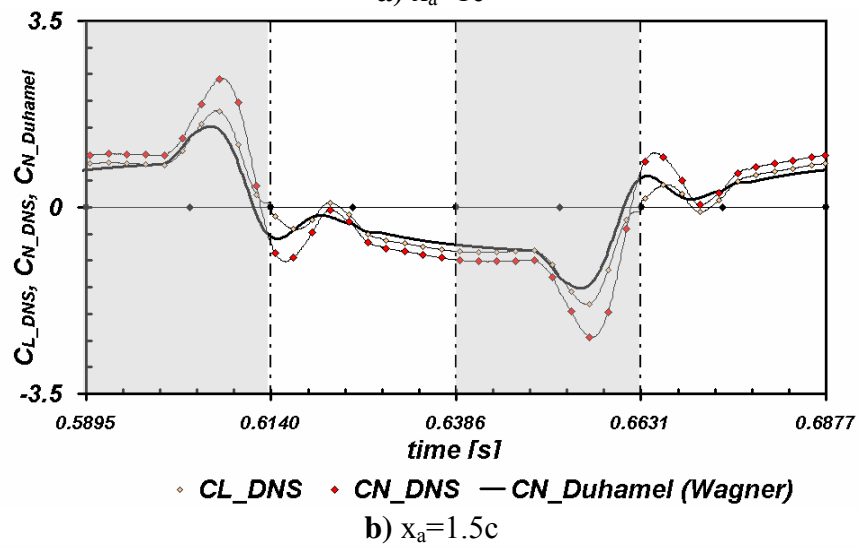
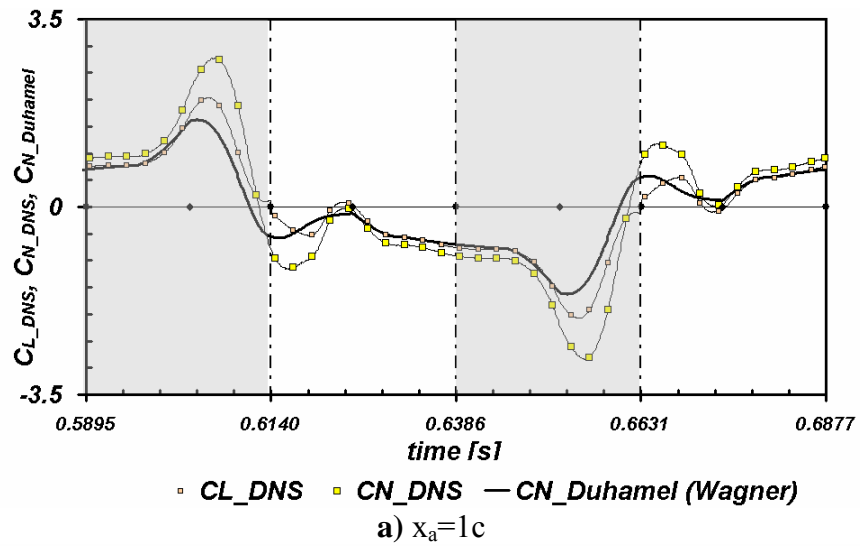


**Figure 5.9** Lift coefficient, normal force coefficient and Duhamel Integral solution with Wagner function for  $\alpha=30^\circ$ ,  $x_v=2c$ ,  $Re=1000$  at  $1/4c$  rotation during 7<sup>th</sup> stroke using DNS curve slope values.

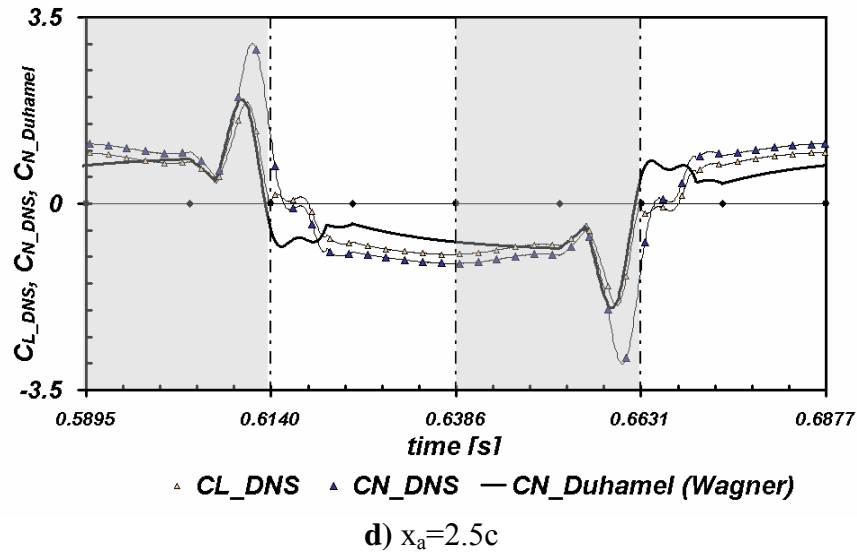


**Figure 5.9 (continued)** Lift coefficient, normal force coefficient and Duhamel Integral solution with Wagner function for  $\alpha=30^\circ$ ,  $x_v=2c$ ,  $Re=1000$  at  $1/4c$  rotation during 7<sup>th</sup> stroke using DNS curve slope values.

However, the results are not always satisfactory since we do not yet take into account the induced velocity region which is due to the previous semi-stroke. The airfoil enters to an induced velocity region caused by a previous semi-stroke which alters distribution of downwash velocity on the airfoil. In the following section, this velocity is assumed to be a constant vertical gust that the airfoil is subjected to.

#### 5.4.3 Duhamel Integral with Wagner and Kussner Function by use of Rankine-Froude Momentum Jet Using DNS Results

The hovering flight problem is commonly solved in literature by the actuator disk and its associated Rankine-Froude momentum jet. The theory assumes no vorticity in the body of the wake and also a well defined boundary with a thin vortex sheet where the mass and momentum is conserved. But for the case of flapping wings, the boundary of the wake is likely to break up which could not result a steady momentum jet. So, in the literature the actuator disk theory is mostly used to predict the induced fluid velocities predicted by momentum jet and the results are combined with other theories such as blade element theory [24]. For an insect of hummingbird the usual momentum-jet estimate may be between 10 and 15% too low [24]. So in

addition to the Wagner impulsive function, the sudden gust velocity change (Küssner function) is implemented into the program developed where the induced velocities for each case are approximated by use of the actuator disc theory. The weight is taken to be average lift during a period per unit span obtained from the DNS code (Table 5.2).

Feathering parameter,  $f$ , in Table 5.2 is defined in Section 1.2.1 and the values for different insects and birds are given in Table 1.3. It is found that the feathering parameter is very close to the values in Table 1.3

**Table 5.2** Induced velocity calculated by actuator disk theory using DNS average lift results for different cases for  $Re=1000$  and wing beat frequency,  $n=1/T=10.18$  Hz.

$\alpha$ [°]	$x_v$	$x_a$	$w_g$ [m/s]	$f$
5	2c	1c	0.14	0.013
5	2c	1.5c	0.12	0.001
5	2c	2c	0.01	0.006
5	2c	2.5c	0	0
30	2c	1c	0.25	0.043
30	2c	1.5c	0.25	0.043
30	2c	2c	0.25	0.043
30	2c	2.5c	0.26	0.044
45	2c	1c	0.27	0.049
45	2c	1.5c	0.27	0.05
45	2c	2c	0.28	0.052
45	2c	2.5c	0.30	0.06
60	2c	1c	0.27	0.048
60	2c	1.5c	0.27	0.05
60	2c	2c	0.28	0.052
60	2c	2.5c	0.29	0.056

The circulatory lift is given in Eq.5.72 with the summation of the Wagner function response and the Kussner function response.  $L_3$  is the correction term for the Duhamel integral with Wagner function and  $L_{3k}$  is the correction term corresponding

to the Duhamel integration with Küssner function defined similarly to  $L_3$  by replacing  $w_{g\_3/4c}$  instead of  $w_{3/4c}$  in equation 5.71.

$$L_{circulatory} = \frac{C_{L\alpha}}{2} \rho \cdot (-|V(t)|) \cdot S \cdot \left[ w_{3/4c}(0) \phi(s) + \int_0^s \frac{dw_{3/4c}}{d\sigma}(\sigma) \cdot \phi(s-\sigma) \right] + L_3 + \frac{C_{L\alpha}}{2} \rho \cdot (-|V(t)|) \cdot S \cdot \quad (5.72)$$

$$\left[ w_{g\_3/4c}(0) \psi(s) + \int_0^s \frac{dw_{3/4c}}{d\sigma}(\sigma) \cdot \phi(s-\sigma) + \int_0^s \frac{dw_{g\_3/4c}}{d\sigma}(\sigma) \cdot \psi(s-\sigma) \right] + L_{3k}$$

$$w_g = \sqrt{\frac{Mg}{2\rho A}} = \sqrt{\frac{\bar{L}'}{2\rho \cdot 6c}} \quad (5.73)$$

where the area  $A$  is taken to be rectangular region covered by the airfoil during its overall motion. The calculated  $w_g$  value is taken to be constant all over the motion, where it is assumed that all the time the airfoil enters to a constant gust with a velocity of  $w_g$ . The effect of this velocity in normal direction of the airfoil at  $3/4c$  location is  $w_{g\_3/4c} = w_g \cos \alpha(t)$  and this gust velocity is implemented in circulatory lift calculations with Küssner function. It must be paid attention that although the gust velocity where the airfoil is assumed to be entered during the motion is taken to be a constant value through the motion, the  $w_{g\_3/4c}$  value changes as the angle of attack change.

This gust velocity also has influence in non-circulatory lift which is also implemented in the program written in Fortran90. But it is observed that, order of magnitude of this effect is very small and can be neglected since the time derivative of  $\cos \alpha$  implement  $\dot{\alpha} \cdot \sin \alpha$  term where when the angular velocity is increasing  $\sin \alpha$  term goes to zero, since angle of attack goes to  $90^\circ$  and all other times mostly the angle of attack remains constant so angular velocity is zero or very small.

$$L_{NC} = \pi \rho b^2 \frac{\partial}{\partial t} (|V \sin \alpha|) + \pi \rho b^2 \frac{\partial}{\partial t} \left( \left| \dot{\theta} \right| \frac{b}{2} \right) + \pi \rho b^2 \frac{\partial}{\partial t} (w_g \cos \alpha) \quad (5.81)$$

The total normal force coefficient obtained by sum of Eq.5.79 and Eq.5.81 are shown for  $\alpha=5^\circ$  in Fig.5.10 and for  $\alpha=30^\circ$  in Fig.5.12. The results are especially good for small  $x_a$  values. For  $x_a=2.5c$  the rotational velocity is too big since in  $0.5c$  it is expected to have a rotation of a constant  $\alpha$  value to  $90^\circ$  angle of attack so the nonlinearities are much bigger for these cases during rotational phase and Duhamel Integral does not respond very well for this situation for both small and high angle of attack values. This case is also the only case between four cases of  $x_a$  where the translational velocity change position  $x_v=2c$  is smaller than the change of the angular velocity position  $x_a=2.5c$ . The program responds well for  $x_a \geq x_a$ .

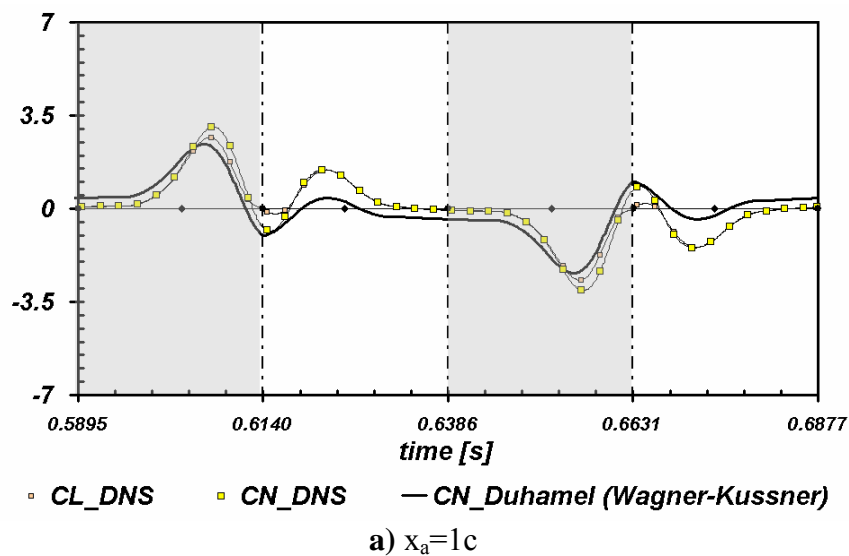
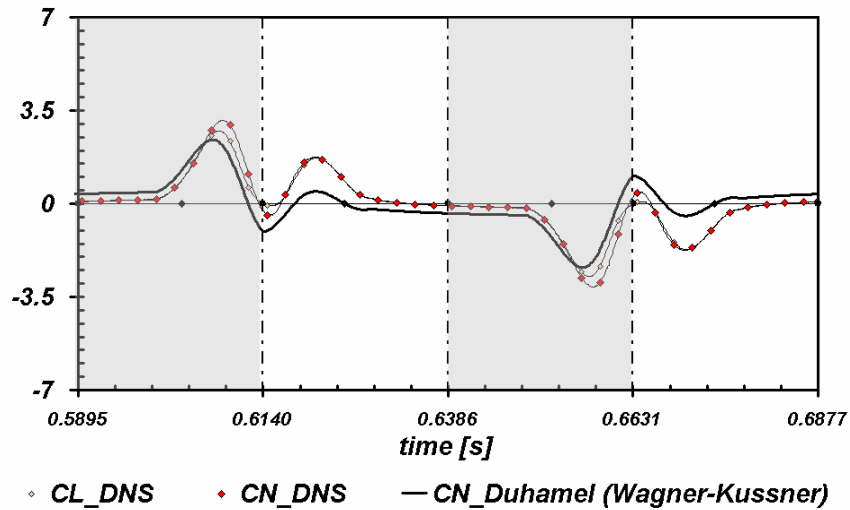
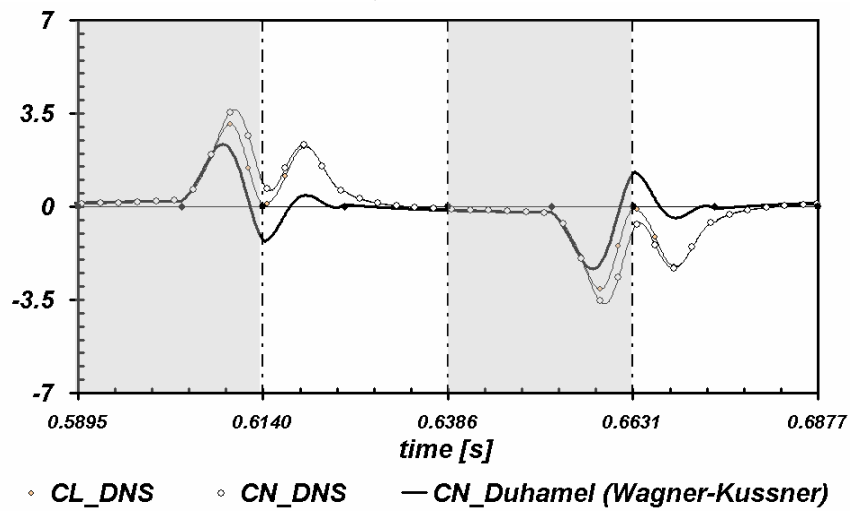


**Figure 5.10** Lift coefficient, normal force coefficient and Duhamel Integral solution with Wagner and Küssner function for  $\alpha=5^\circ$ ,  $x_v=2c$ ,  $Re=1000$  at  $1/4c$  rotation during 7<sup>th</sup> stroke using DNS curve slope values.

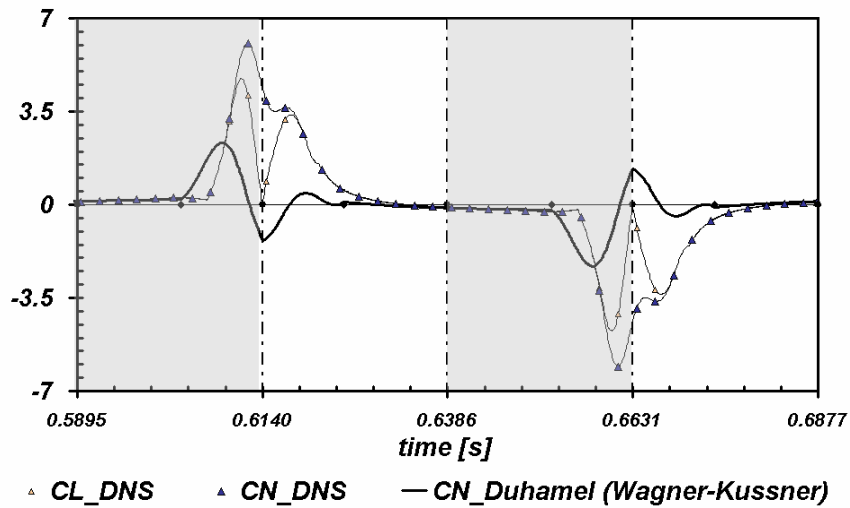




b)  $x_a=1.5c$



c)  $x_a=2c$



d)  $x_a=2.5c$

**Figure 5.10 (continued)** Lift coefficient, normal force coefficient and Duhamel Integral solution with Wagner and Küssner function for  $\alpha=5^\circ$ ,  $x_v=2c$ ,  $Re=1000$  at  $1/4c$  rotation during 7<sup>th</sup> stroke using DNS curve slope values.

Fig.5.11 is drawn for the same configurations as Fig.5.12 but without correction terms  $L_3$  and  $L_{3k}$  for  $30^\circ$  angle of attack for comparison purpose. It is observed that for the regions where translational acceleration and deceleration occurs (i.e.  $V(t) \neq V_0$ ), the normal force coefficients are closer to DNS results when correction terms are added.

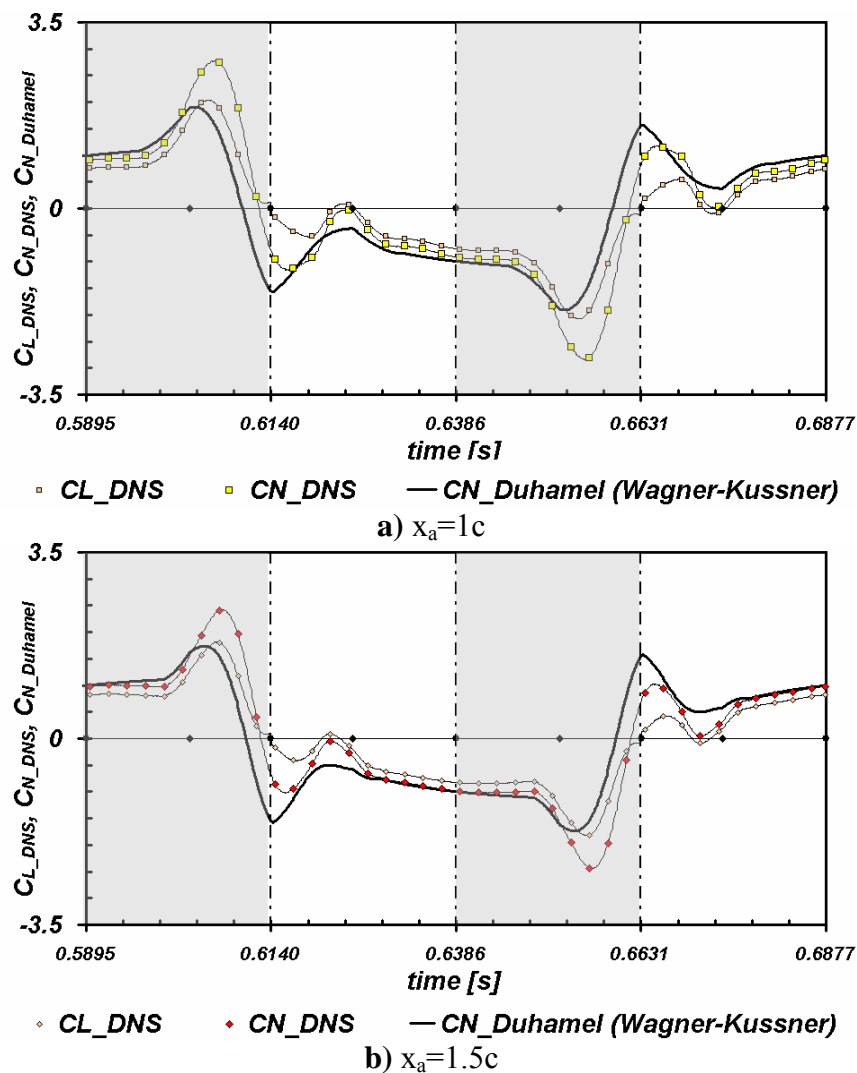


**Figure 5.11** Lift coefficient, normal force coefficient and Duhamel Integral solution with Wagner and Küssner function for  $\alpha=30^\circ$ ,  $x_v=2c$ ,  $Re=1000$  at  $1/4c$  rotation during 7<sup>th</sup> stroke using DNS curve slope values without additional correction terms  $L_3$  and  $L_{3k}$ .

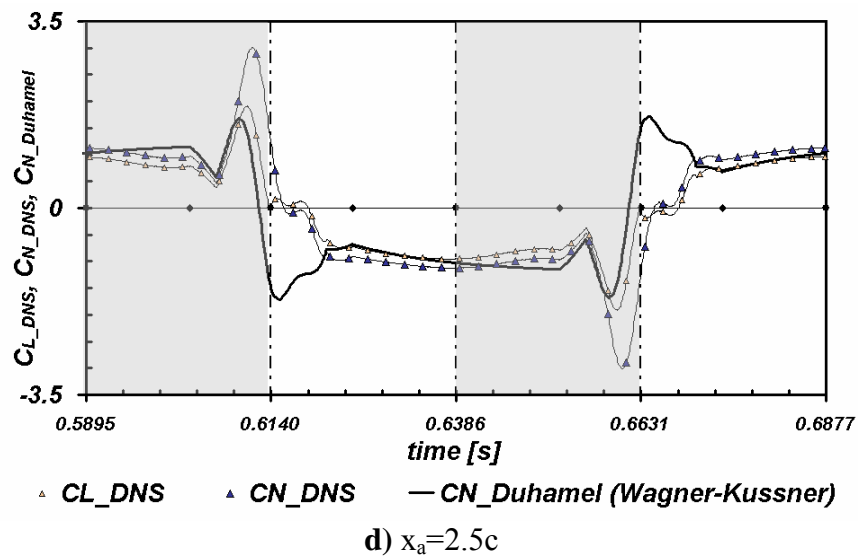
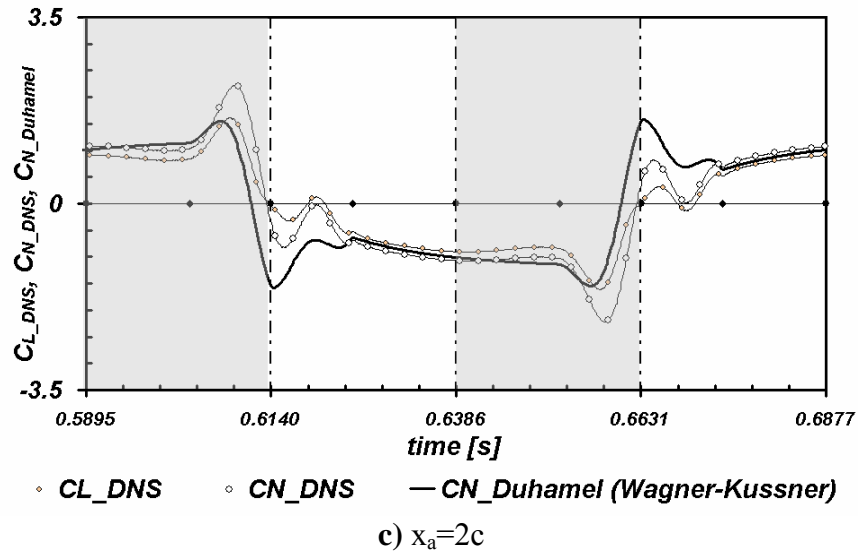
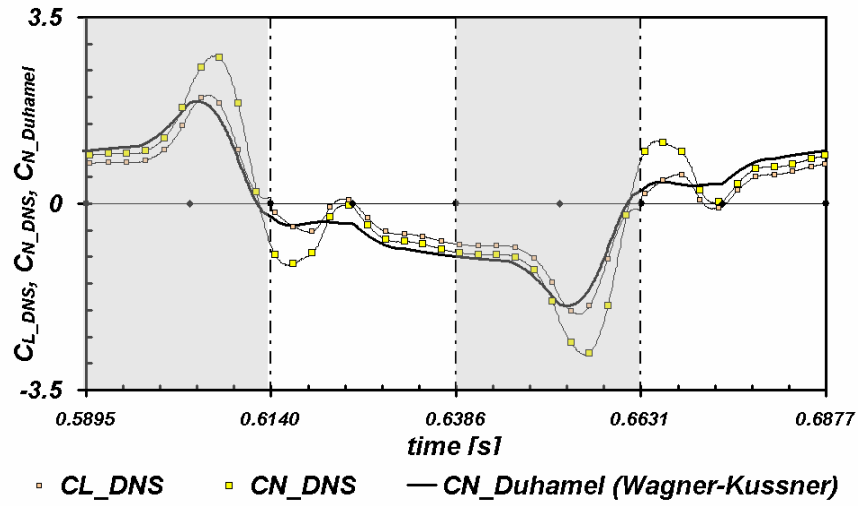
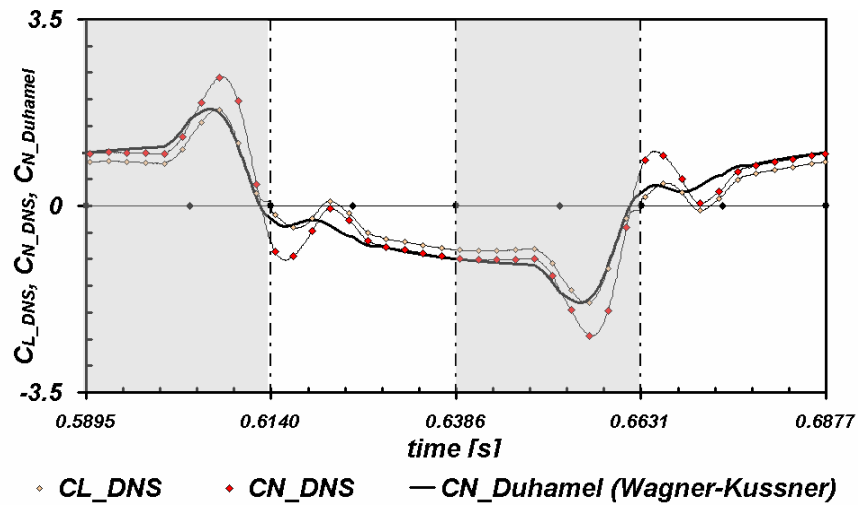


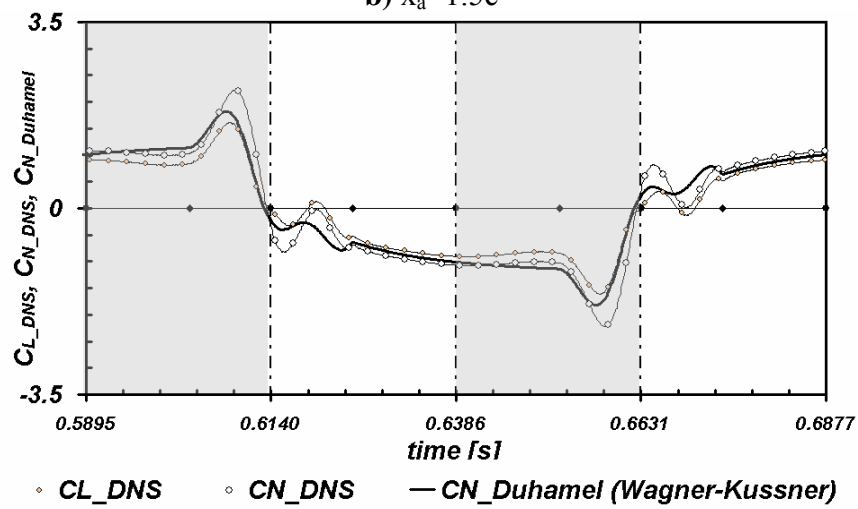
**Figure 5.11 (continued)** Lift coefficient, normal force coefficient and Duhamel Integral solution with Wagner and Küssner function for  $\alpha=30^\circ$ ,  $x_v=2c$ ,  $Re=1000$  at  $1/4c$  rotation during 7<sup>th</sup> stroke using DNS curve slope values without additional correction terms  $L_3$  and  $L_{3k}$ .



a)  $x_a=1c$



b)  $x_a=1.5c$



c)  $x_a=2c$

**Figure 5.12** Lift coefficient, normal force coefficient and Duhamel Integral solution with Wagner and Küssner function for  $\alpha=30^\circ$ ,  $x_v=2c$ ,  $Re=1000$  at  $1/4c$  rotation during 7<sup>th</sup> stroke using DNS curve slope values.

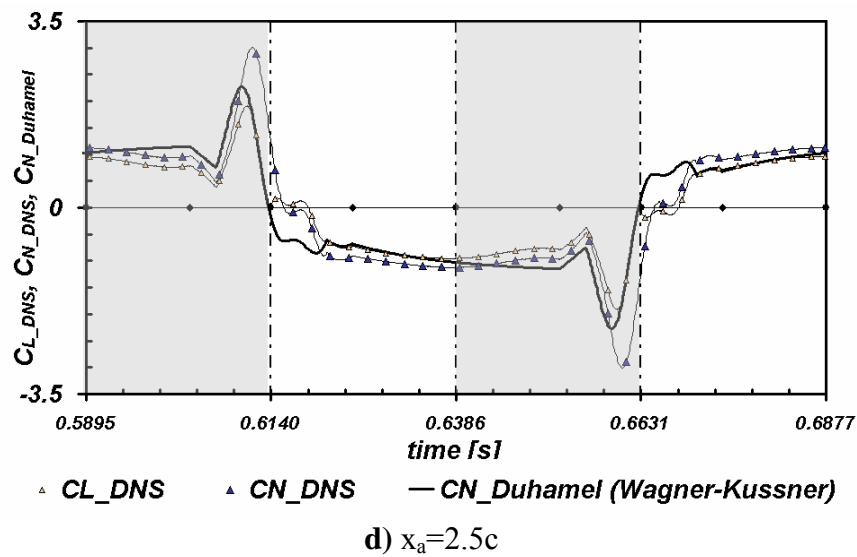


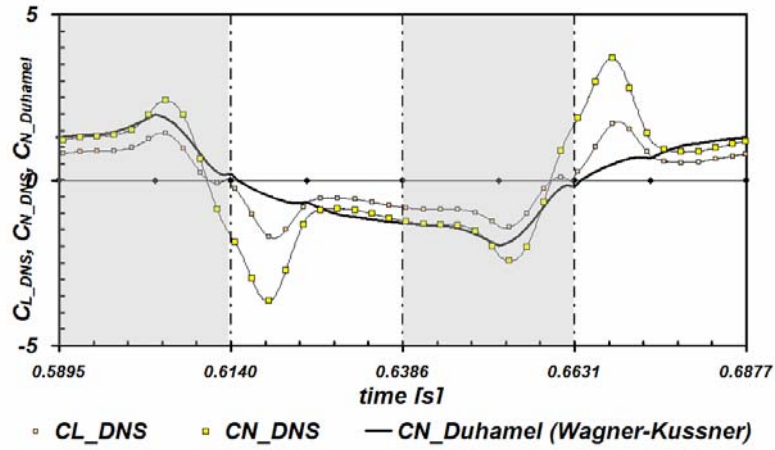
**Figure 5.12 (continued)** Lift coefficient, normal force coefficient and Duhamel Integral solution with Wagner and Küssner function for  $\alpha=30^\circ$ ,  $x_v=2c$ ,  $Re=1000$  at  $1/4c$  rotation during 7<sup>th</sup> stroke using DNS curve slope values.

This improvement has a very big inconvenience due to the necessity of the estimation of the average lift which results the loss of the autonomy of the model. One possibility is to estimate this corrective term  $w_g$  from a first estimation of the lift (or normal force) using only the results with the Wagner function. This method could eventually be implemented in the model in an iterative way.

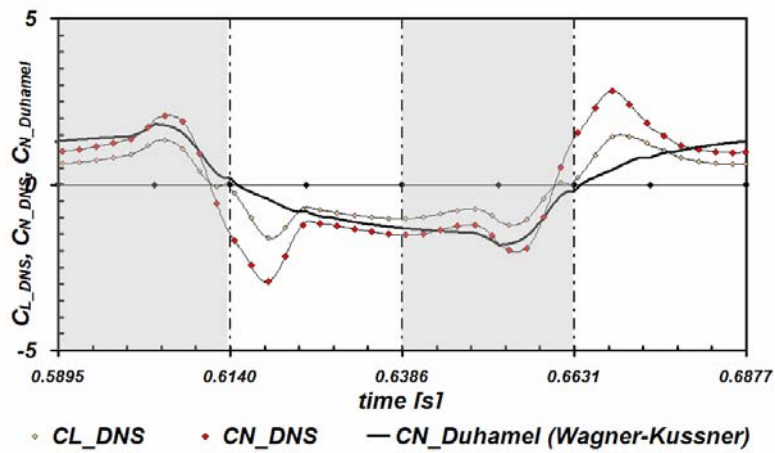
#### 5.4.4 Discussion of the Results for High Angles of Attack

The Duhamel integral approach given in section 5.4.3 is also applied to angle of attacks higher than  $30^\circ$  where the airfoil enters to a region of highly energetical vortices in return.

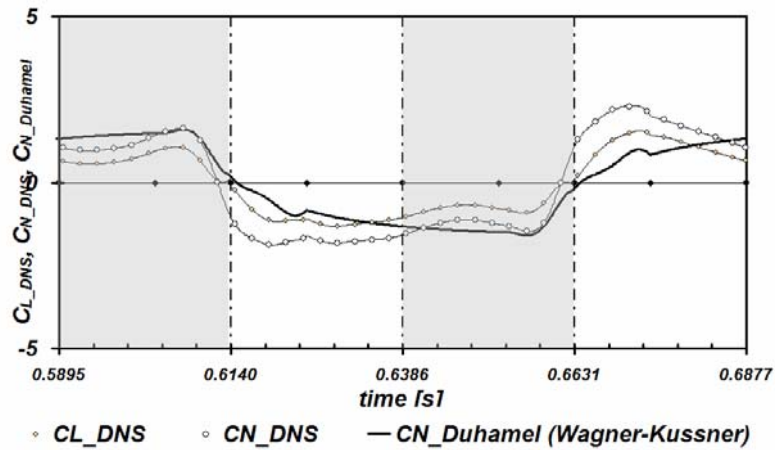
Figure 5.13 shows the results for  $45^\circ$  angle of attack and Figure 5.14 represents the results for  $60^\circ$  angle of attack for different  $x_a$  values.



a)  $x_a=1c$



b)  $x_a=1.5c$



c)  $x_a=2c$

**Figure 5.13** Lift coefficient, normal force coefficient and Duhamel Integral solution with Wagner and Küssner function for  $\alpha=45^\circ$ ,  $x_v=2c$ ,  $Re=1000$  at  $1/4c$  rotation during 7<sup>th</sup> stroke using DNS curve slope values.

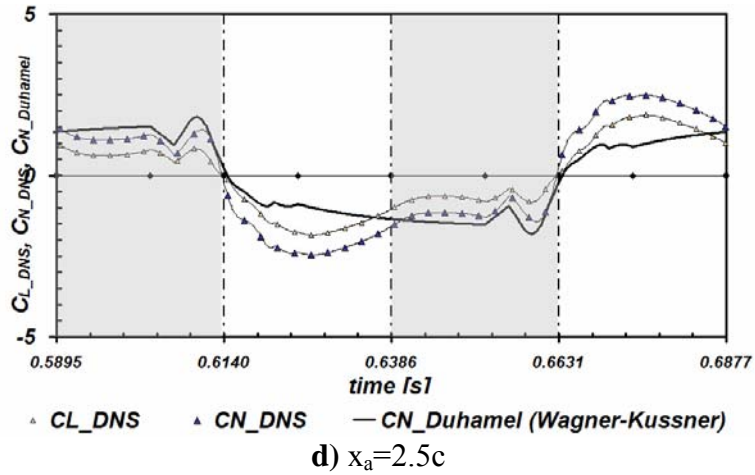


**Figure 5.13 (continued)** Lift coefficient, normal force coefficient and Duhamel Integral solution with Wagner and Küssner function for  $\alpha=45^\circ$ ,  $x_v=2c$ ,  $Re=1000$  at  $1/4c$  rotation during 7<sup>th</sup> stroke using DNS curve slope values.

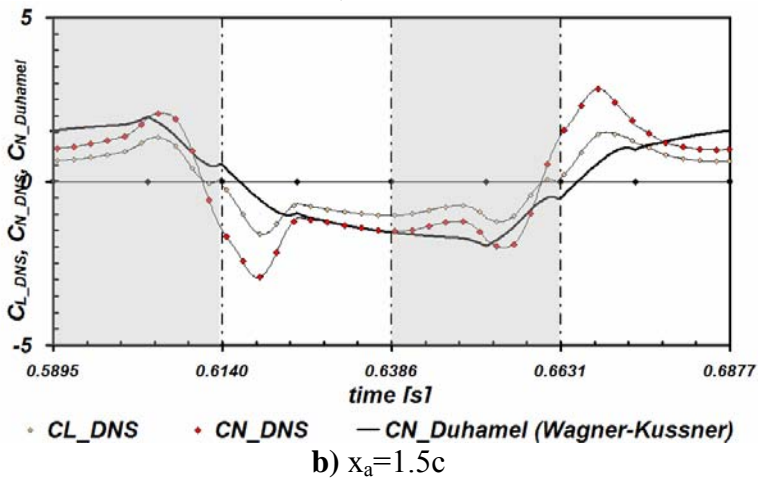
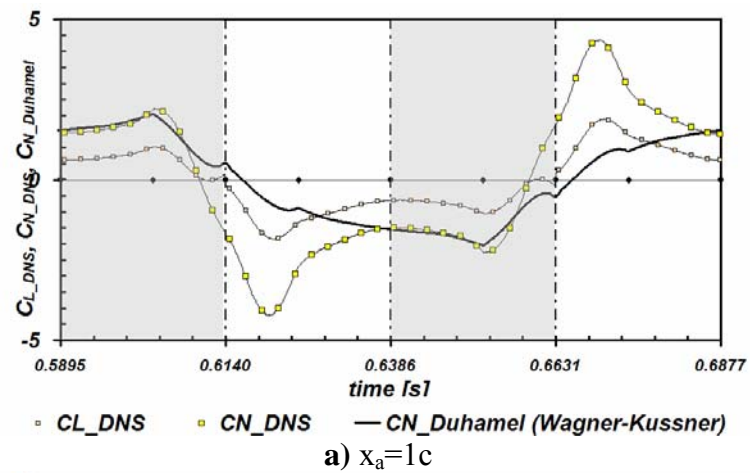


**Figure 5.14** Lift coefficient, normal force coefficient and Duhamel Integral solution with Wagner and Küssner function for  $\alpha=60^\circ$ ,  $x_v=2c$ ,  $Re=1000$  at  $1/4c$  rotation during 7<sup>th</sup> stroke using DNS curve slope values.

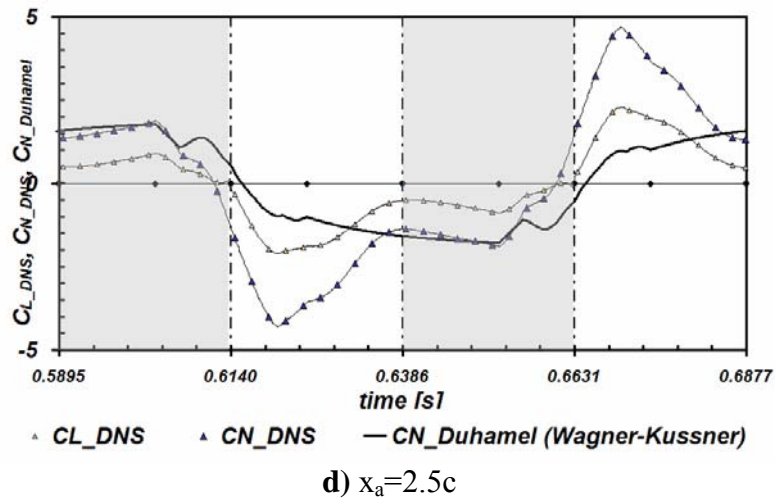
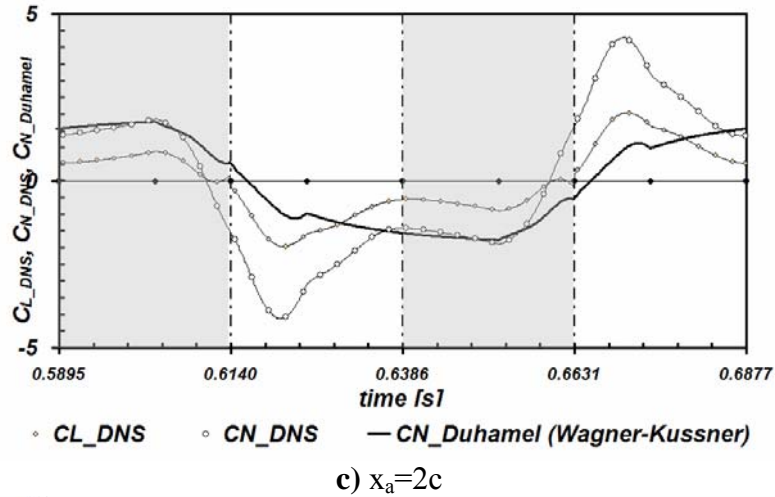


**Figure 5.14 (continued)** Lift coefficient, normal force coefficient and Duhamel Integral solution with Wagner and Küssner function for  $\alpha=60^\circ$ ,  $x_v=2c$ ,  $Re=1000$  at  $1/4c$  rotation during 7<sup>th</sup> stroke using DNS curve slope values.

Although 1<sup>st</sup> and 3<sup>rd</sup> regions are similar to the numerical simulations, the peak of the 2<sup>nd</sup> and 4<sup>th</sup> regions cannot be found by the analytical model. Wagner function is an increasing function, so it cannot capture the peak at the 2<sup>nd</sup> and 4<sup>th</sup> regions of the flapping motion. The results are not satisfactory for these high incidences in particular for the second part of the rotation. Another trial has been done by using the impulsive solution obtained from the DNS calculations instead of the Wagner function for these high angles of attack.



It is found that although this second peak is captured in rotational phase, the analytical model is not good in this way compared to the Wagner solution during the translational phase. Figure 5.15 shows the comparison of the Wagner solution and the numerical impulsive solution for  $\alpha=60^\circ$ ,  $x_v=2c$ ,  $x_a=2c$ ,  $Re=1000$  at  $1/4c$  rotation case. Figure 5.16 shows different solutions with analytical model for  $45^\circ$  angle of attack with  $x_v=2c$  and  $x_a=1c$ . Impulsive solution capture the slope of the lift force coefficient with time during rotation phase of 2<sup>nd</sup> and 4<sup>th</sup> regions but the decrease of the force coefficient during the translational phase cannot be captured.

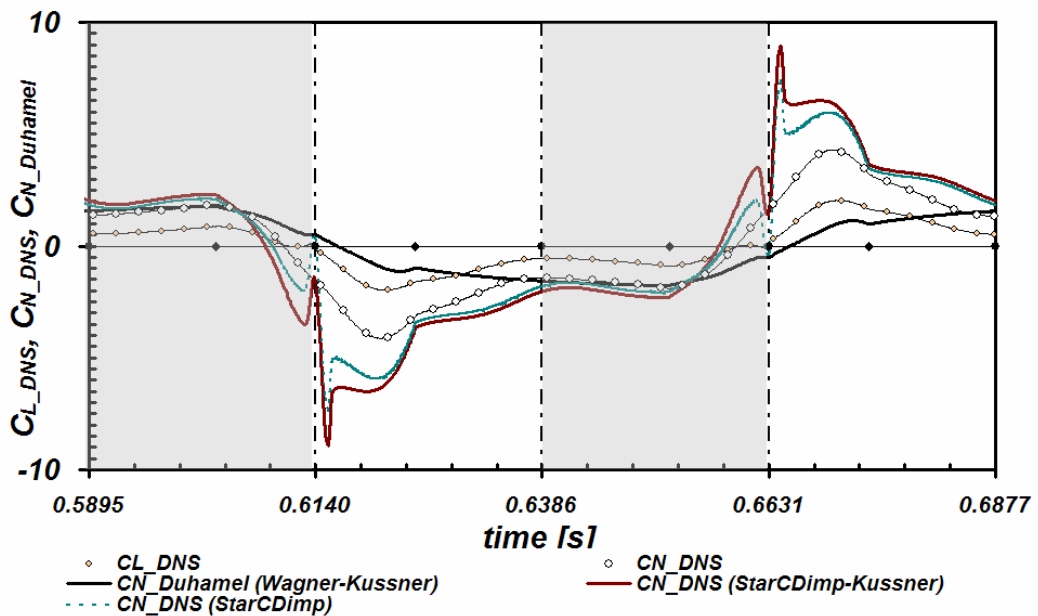
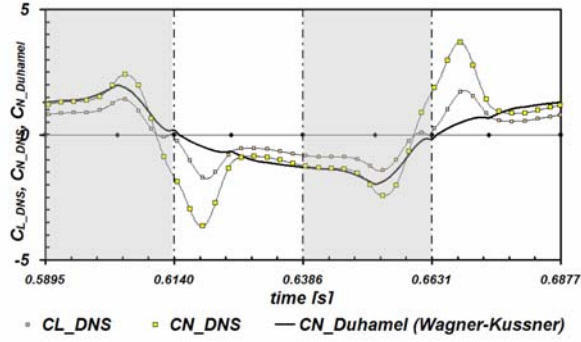
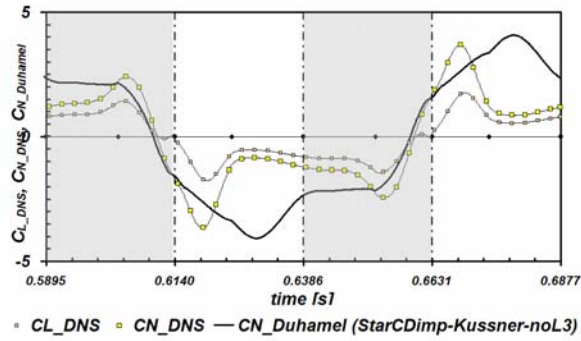


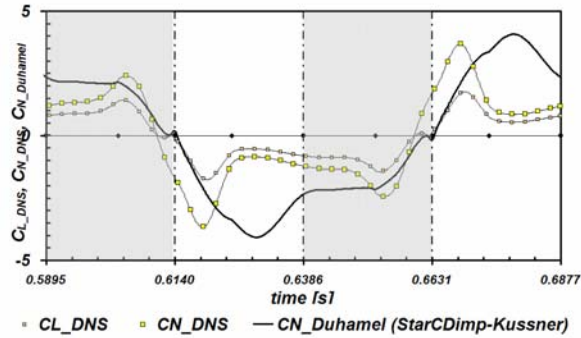
**Figure 5.15** Lift coefficient, normal force coefficient and Duhamel Integral solution comparisons function for  $\alpha=60^\circ$ ,  $x_v=2c$ ,  $x_a=2c$ ,  $Re=1000$  at  $1/4c$  rotation during 7<sup>th</sup> stroke using DNS curve slope values.



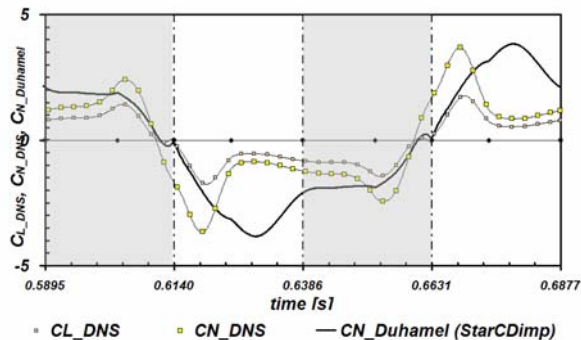
a) Duhamel Integral with Wagner and Kussner function



b) Duhamel Integral with DNS impulsive solution and Kussner function (without correction term  $L_3$  and  $L_{3k}$ )



c) Duhamel Integral with DNS impulsive solution and Kussner function



d) Duhamel Integral with DNS impulsive solution without Kussner function

**Figure 5.16** Lift coefficient, normal force coefficient and Duhamel Integral solution comparisons function for  $\alpha=45^\circ$ ,  $x_v=2c$ ,  $x_a=1c$ ,  $Re=1000$  at  $1/4c$  rotation during 7<sup>th</sup> stroke using DNS curve slope values.

During the beginning of 2<sup>nd</sup> and 4<sup>th</sup> regions, the airfoil enters to trace of the leading edge vortex, translational vortex and rotational vortex that was generated before the return (Figure 5.17). Although this effect is implemented in the model via the Küssner function with an very approximate way of constant induced velocity, at angles of attack higher than 30° the effect of the downwash due to the leading edge vortex is stronger and this result a peak on lift coefficient graphs in 2<sup>nd</sup> and 4<sup>th</sup> regions. The instantaneous points corresponding to the pictures in Fig.5.17 are shown on aerodynamic forces versus time graph in Fig. 5.18.

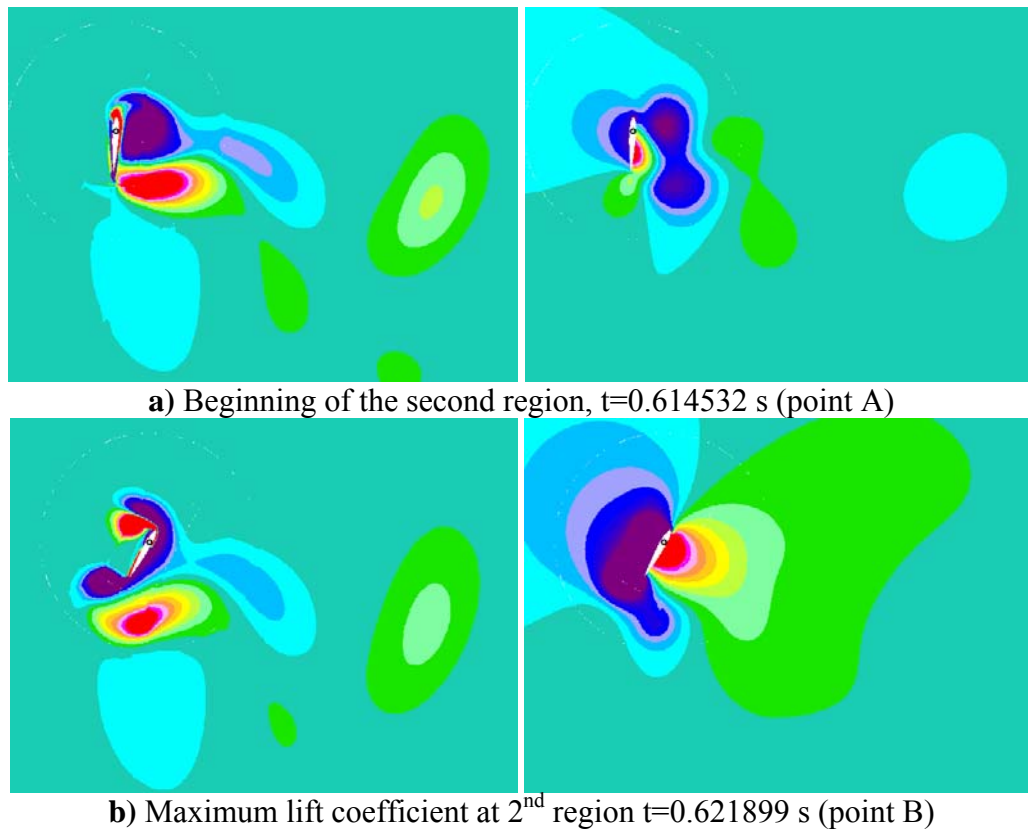
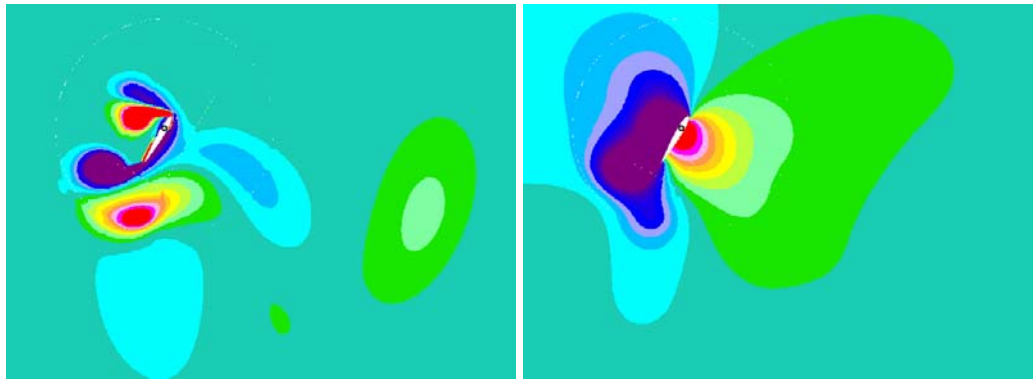
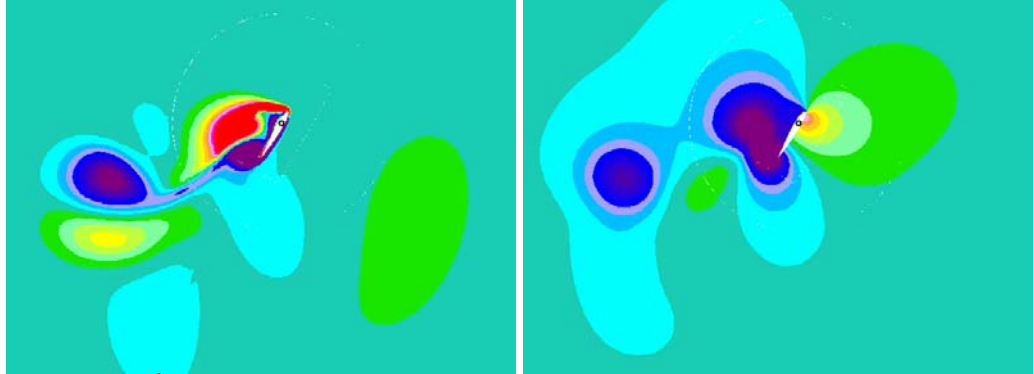


**Figure 5.17** Vorticity contours (1<sup>st</sup> row) and Pressure contours (2<sup>nd</sup> row) for  $\alpha=60^\circ$ ,  $x_v=2c^\circ$ ,  $x_a=2c$ ,  $Re=1000$  at  $1/4c$  rotation during 7<sup>th</sup> stroke.



c) End of the rotation and variable velocity region ( $x_a=x_v$ )  $t=0.624355$  s (point C)



d) End of 2<sup>nd</sup> region during pure translation ( $x=0$  location)  $t=0.639089$  s (Point D)  
**Figure 5.17 (continued)** Vorticity contours (1<sup>st</sup> row) and Pressure contours (2<sup>nd</sup> row) for  $\alpha=60^\circ$ ,  $x_v=2c$ ,  $x_a=2c$ ,  $Re=1000$  at  $1/4c$  rotation during 7<sup>th</sup> stroke.

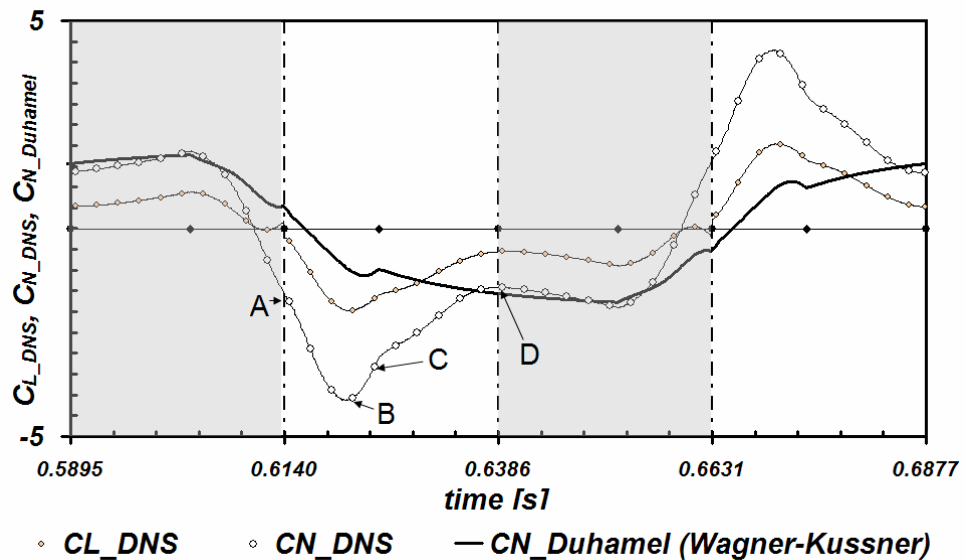


**Figure 5.18** Aerodynamic force coefficients obtained numerically and analytically (Wagner-Kussner) for  $\alpha=60^\circ$ ,  $x_v=2c$ ,  $x_a=2c$ ,  $Re=1000$  at  $1/4c$  rotation during 7<sup>th</sup> stroke using DNS curve slope values. (Location of the points A, B, C, D of Figure 5.14 are represented).

As the angle of attack increases the counter-clockwise leading edge vortex (blue) gets bigger. There is also formation of a second leading edge vortex clockwise (red) near the leading edge which is more distinguishable as the starting angle of attack increases. The clockwise translational vortex gets bigger with increase of  $\alpha$ .

The lift and drag coefficients for different angles of attack are represented in Figure 5.19 and Figure 5.20 respectively where four different time instants (A, B, C, D) are emphasized and the vortex contours are drawn in Figure 5.21 to Figure 5.24. It is previously stated that the lift coefficient becomes positive throughout the period after  $30^\circ$  and there is a formation of a second peak in 2<sup>nd</sup> region at higher angle of attack values. Point B represent a time instant where the lift coefficient is zero for the  $5^\circ$  however is a very big value for  $60^\circ$  angle of attack. The difference between these two cases comes from the formation of a strong opposite clockwise leading edge vortex inside a counterclockwise vortex (Figure 5.22). As seen also from Figure 5.23 during the pure translation this clockwise leading edge vortex is detached from the airfoil for  $45^\circ$  and  $60^\circ$  angles of attack.

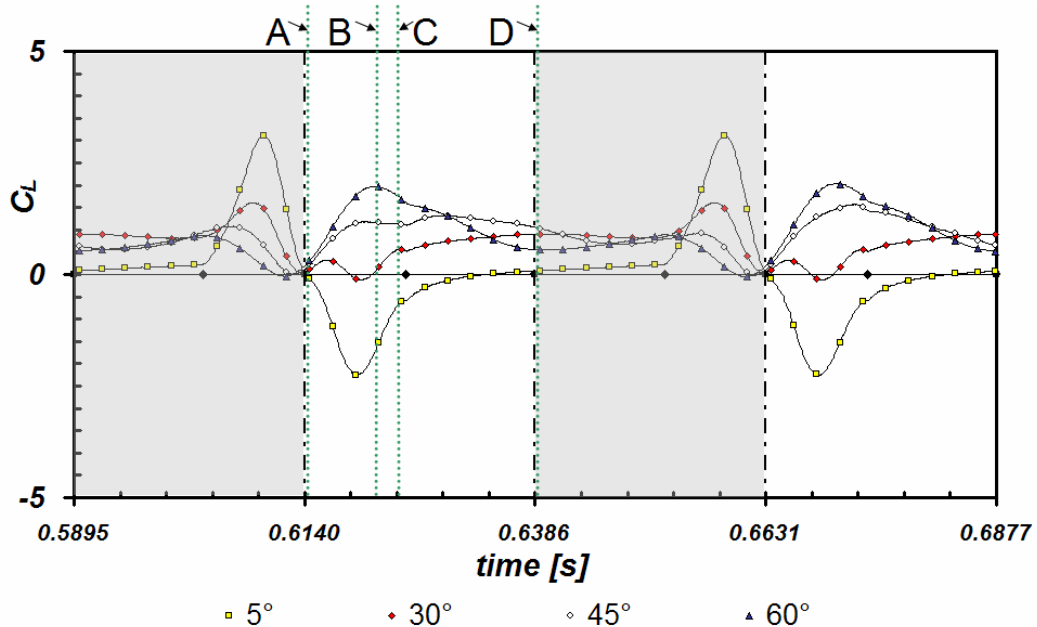


**Figure 5.19** Lift coefficient for different  $\alpha$  having  $x_v=2c$ ,  $x_a=2c$ ,  $Re=1000$  at  $1/4c$  rotation during 7<sup>th</sup> stroke. (Location of the points A, B, C, D of Figures 5.20 to 5.23 are represented).

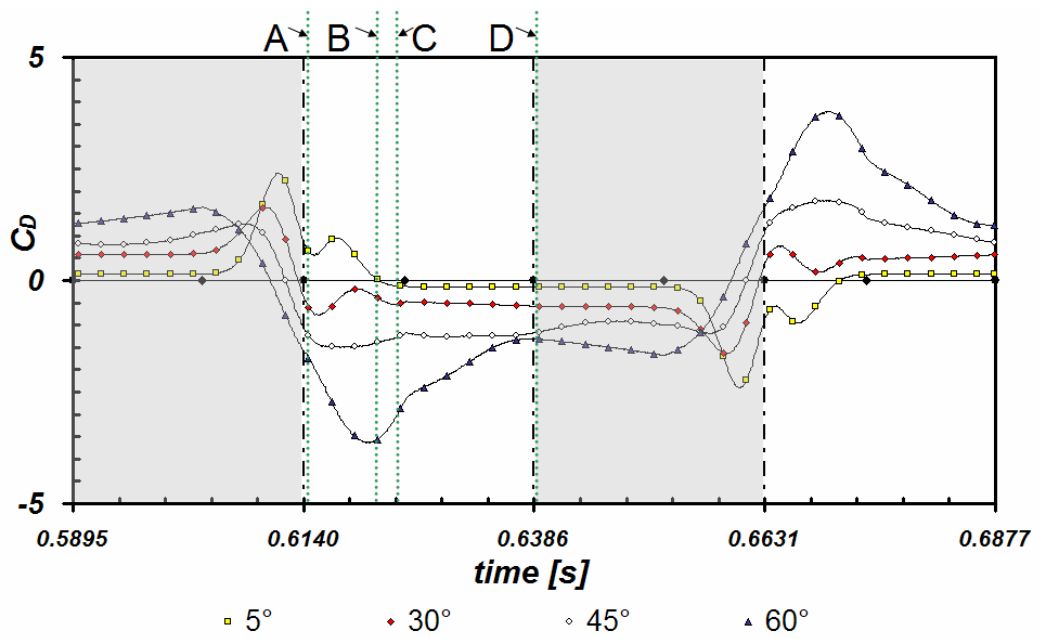


**Figure 5.20** Drag coefficient for different  $\alpha$  having  $x_v=2c$ ,  $x_a=2c$ ,  $Re=1000$  at  $1/4c$  rotation during 7<sup>th</sup> stroke. (Location of the points A, B, C, D of Figures 5.20 to 5.23 are represented).

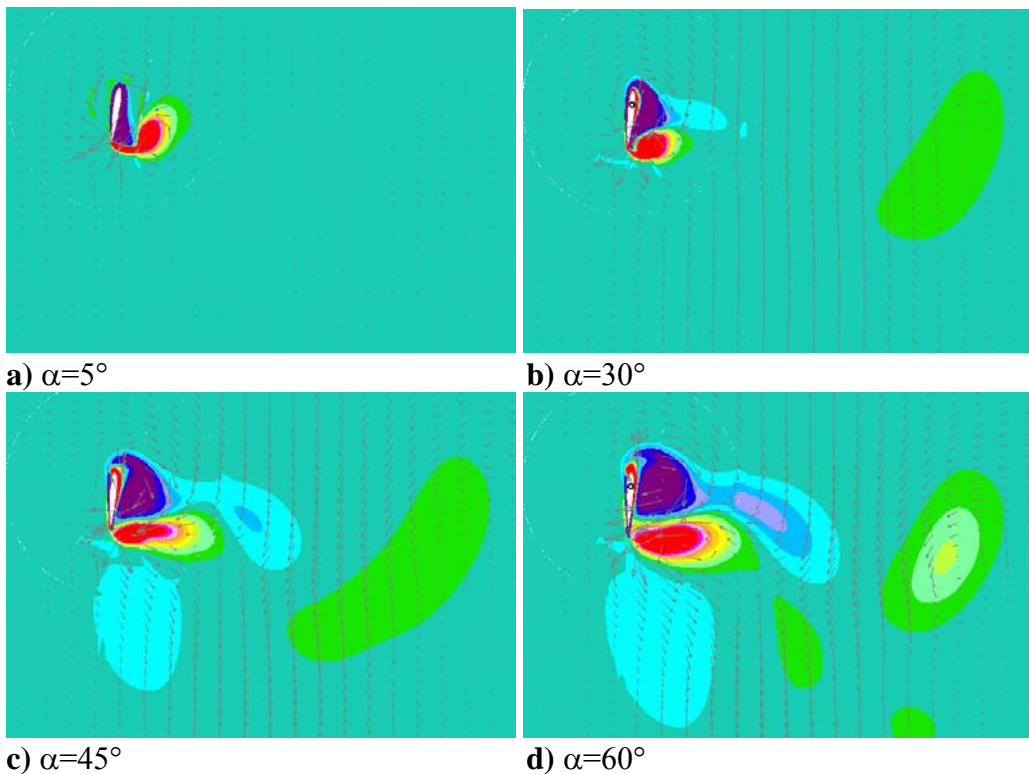


**Figure 5.21** Vorticity contours for different  $\alpha$  values with  $x_v=2c$ ,  $x_a=2c$ ,  $Re=1000$  at  $1/4c$  rotation at the beginning of the second region,  $t=0.614532$  s, during 7<sup>th</sup> stroke (point A).

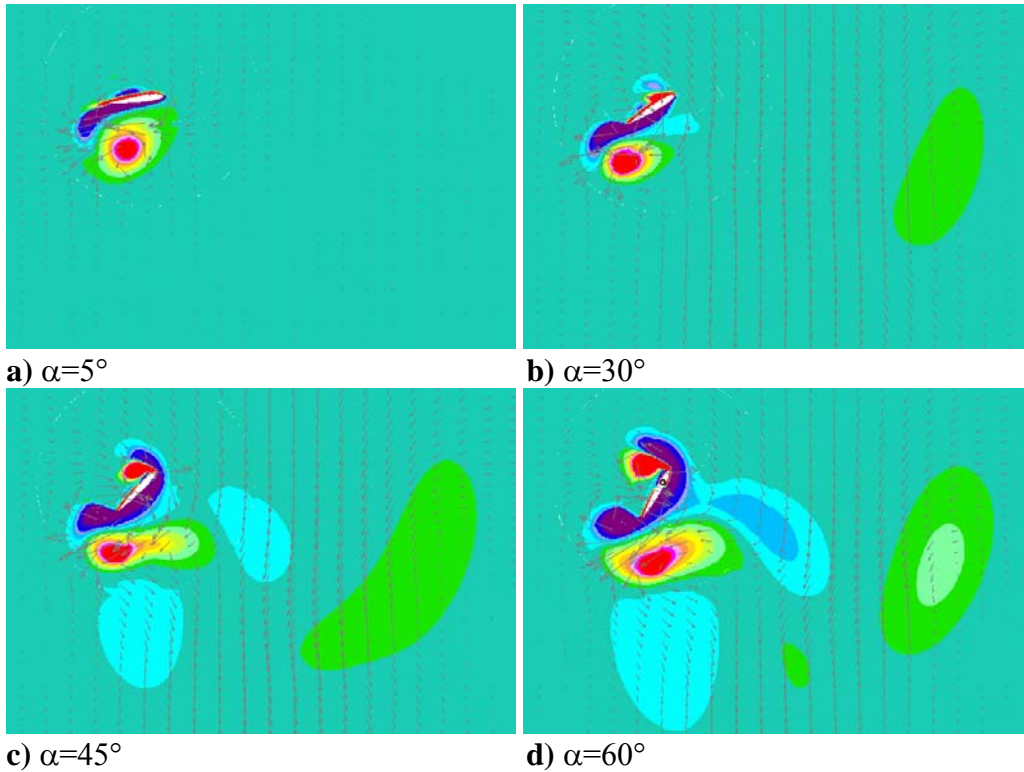


**Figure 5.22** Vorticity contours for different  $\alpha$  values with  $x_v=2c$ ,  $x_a=2c$ ,  $Re=1000$  at  $1/4c$  rotation at the maximum lift coefficient location for  $60^\circ$  angle of attack at 2<sup>nd</sup> region,  $t=0.621899$  s during 7<sup>th</sup> stroke (point B).

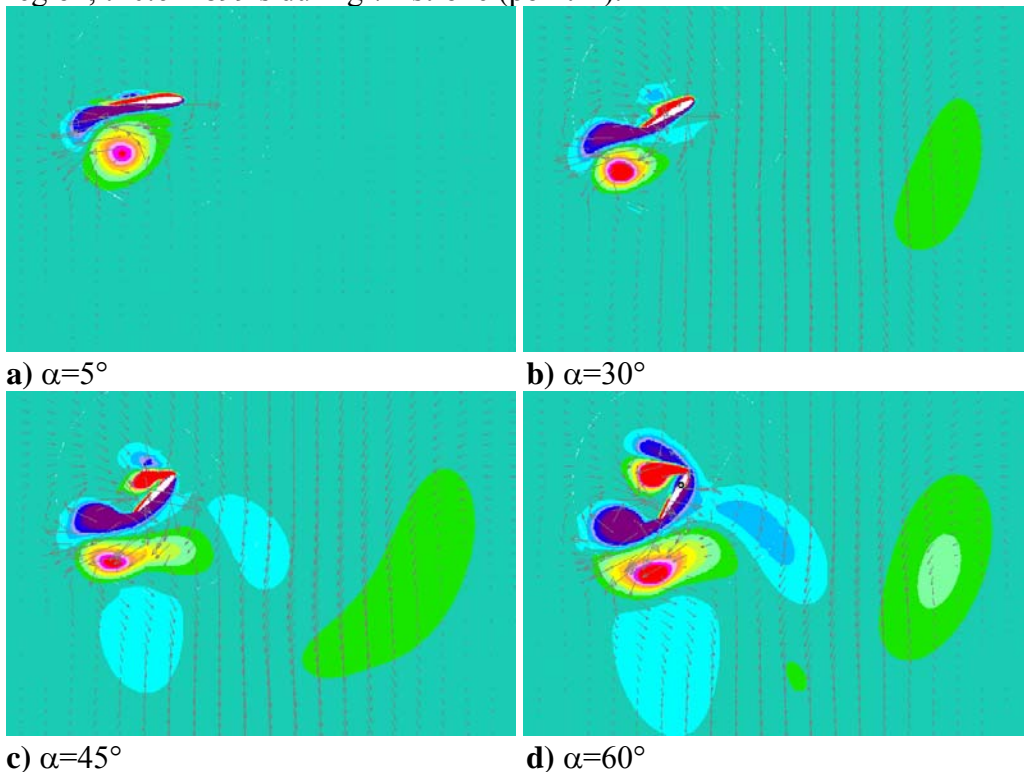


**Figure 5.23** Vorticity contours for different  $\alpha$  values with  $x_v=2c$ ,  $x_a=2c$ ,  $Re=1000$  at  $1/4c$  rotation at the end of the rotation and variable velocity region ( $x_a=x_v$ ),  $t=0.624355$  s, during 7<sup>th</sup> stroke (point C).

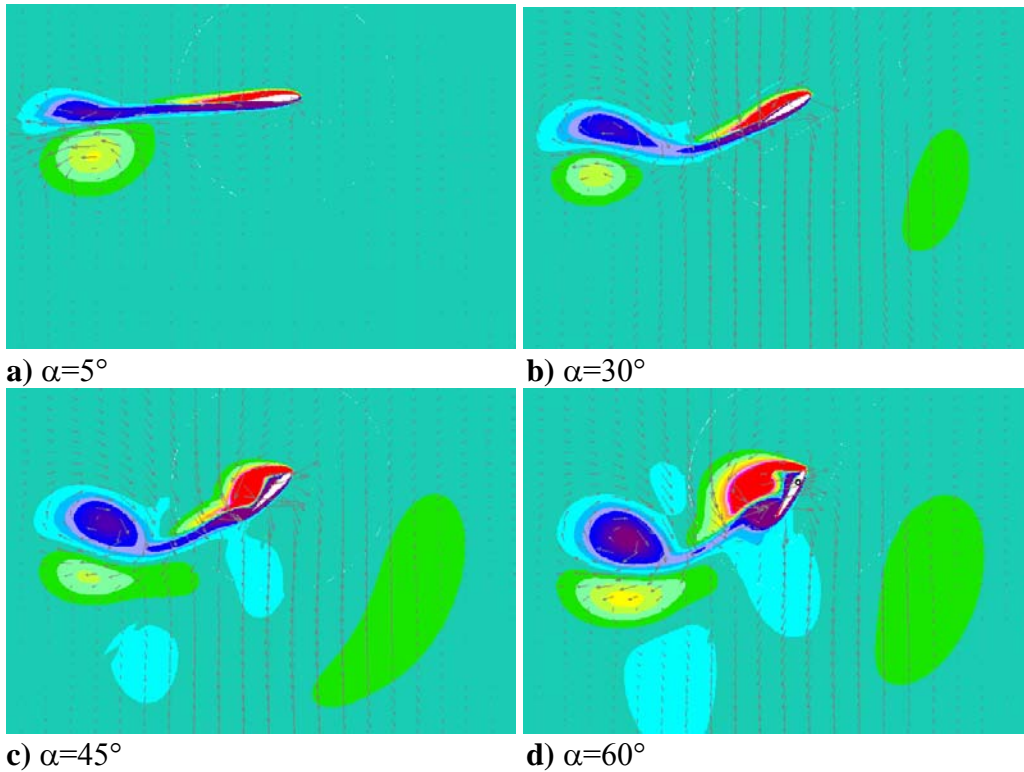


**Figure 5.24** Vorticity contours for different  $\alpha$  values with  $x_v=2c$ ,  $x_a=2c$ ,  $Re=1000$  at  $1/4c$  rotation at the end of 2<sup>nd</sup> region during pure translation ( $x=0$  location),  $t=0.639089$  s, during 7<sup>th</sup> stroke (point D).

#### 5.4.5 Conclusion

The models which are existing in the literature as Zbikowski [50], Leishman [4, 49], are improved by taking into account the realistical curve slope  $C_{L\alpha}$ , the correction terms and the introduction of an induced velocity from a previous stroke. We could consider that the results are acceptable until  $30^\circ$  angles of attack. For higher angles, the translational phase and the first rotational phase are captured but the second part of the rotational region cannot be obtained satisfactorily. The effects of the vortex interactions at high incidences could not be captured by the analytical model.



## CHAPTER 6

### CONCLUSION

#### **6.1 Objective of the Study and the Analysis Tools**

In this study, the flapping motion aerodynamics is considered for a symmetrical hovering case in the use of future Micro Air Vehicle applications. The inspiration from the bio-aerodynamics results an idea for the researches to have MAV's resembling to insects and small birds such as hummingbird with flapping wings. The complexity of the problem raises the necessity of a simplified model. So a two-dimensional model is investigated with a symmetrical airfoil with variable velocity and angular velocity laws.

The objective of this simplified model is to describe the physics of the phenomena and to develop an analytical model which could be usable for an optimization purpose.

The analysis tools used for the description of the phenomena are the numerical simulations and the experimental investigations. The numerical simulations are performed with a DNS code with a capability of moving grid option. The experimental results are performed separately, one with the laser sheet visualization and the other one with Particle Image Velocimetry (PIV) measurements.

## 6.2 General Conclusion

Firstly, a numerical simulation for the parametrical study is performed to get a first idea of the parameters which influence the flapping motion study. It is concluded that the most influencing parameter is the starting angle of attack. For small angles, the lift coefficient has both negative and positive values which give average force coefficients close to zero. As the angle of attack is increased to  $30^\circ$ , these negative peaks disappear and at  $45^\circ$  positive peaks are observable. The second important parameter is the center of rotation. The other parameters as the change of position of the velocity and angle of attack and Re number are found to be less important. It is observed that at  $a = \frac{1}{2} c$  axis of rotation at  $45^\circ$  angle of attacks there exist high values of total force coefficient which is due to the high drag coefficient values. The total force coefficient is on the order of 2.5 in average on a period, which is approximately three times bigger than the maximum aerodynamic force coefficients in steady state for this airfoil at the same Reynolds number. The numerical part of this study is presented in different conferences [65-67].

The experimental visualizations with laser sheet are firstly performed to see if the vortices generated in the numerical simulations are also observable in real flows. It is concluded that they have the same appearance especially the more energetical vortices close the airfoil are highly visible both in numerical simulations and experimental visualizations. After concluding that the results are highly comparable, PIV measurements are performed to obtain quantitative data of the flow domain. Different vortex identification techniques such as Q and  $\lambda$  criterions in addition to the vorticity distribution are used. The vortices generated are classified for the whole motion. Since the Q contours are the laplacian of the pressure, the vortices observed experimentally are correlated with the pressure distribution and aerodynamic force coefficients of the numerical results for each time instants. The numerical and experimental visualizations are compared in order to better understand the vortex generation mechanism during the motion in consideration and to reason the unsteady effects generated by these vortices on the airfoil in terms of the aerodynamic force coefficients and pressure distribution. The experimental results are a part the

validation of the numerical simulations. The visualizations and Q contours are the indirect validation of the aerodynamic force calculations of these numerical simulations.

Lastly, an analytical model is developed with the Duhamel Integral and using Wagner and Küssner functions by implementation of the actuator disk theory for the circulatory term. The total normal force is calculated as the summation of the circulatory term and the non-circulatory term due to the added mass effect. The results are compared with the numerical simulation aerodynamic force coefficients. The model is highly satisfactory for the angles of attack until  $30^\circ$ . However, the model which is defined cannot take into account the interactions of the vortices around the airfoil so it gives poor results at the second part of the rotation for high angles of attack.

### **6.3 Perspective**

The analytical model can be more developed by taking into account the Translational Vortex TV, Rotational Stopping Vortex RSV and Leading Edge Vortex LEV observed in front of the airfoil during rotational motion. For this purpose a literature survey of vortex-wall interaction is also carried out from the References [68]-[75]. This point is difficult but very important to improve the model for high angles of attack. So, it is a necessity for the use of our model in an optimization process as a genetic algorithm.

Hummingbird and several insects use normal hovering where the wings are moving through a large angle in an approximately horizontal plane making a figure-of-eight motion with a symmetrical half-strokes. In hovering bats and birds the stroke plane is more tilted and this hovering is named as asymmetrical hovering where most of the lift is generated during downstroke. Always in the case of two dimensional problems, a third degree of freedom could be added with a figure-of-eight. This allows changing the plane of the upstroke and the downstroke. Some first calculations are performed for this purpose. The same angular velocity and the translational velocity

laws could be used for the calculations by adding a displacement law in the normal direction which could be out of phase with the rotation. This motion will allow using the total force as the lift due to the ability of the change of the stroke plane angle and position during the whole motion. This could also be implemented in the analytical model in a straight forward manner.

At long terms, if we want to build a system of flapping motion, the 3D effects must be taken into consideration. For three dimensional simulations, the velocity at the tip of the airfoil is very high and important. A 3D model is more realistic so three dimensional simulations and experiments have to be done. The behavior of the vortices in 3D views must be compared to the 2D solutions to have a better idea of the flow. 2D results represented here could be a base for understanding the flapping motion mechanism with three-dimensional experiments and numerical results. Analytical model developed could also be modified for three dimensional simulations.

## REFERENCES

- [1] McMichael, J. M., Francis, M. S., “Micro Air Vehicles - Toward a New Dimension in Flight,” [http://www.darpa.mil/tto/mav/mav\\_auvsi.html](http://www.darpa.mil/tto/mav/mav_auvsi.html), 1997.
- [2] Aerovironment, “Development of Breakthrough Aerial Vehicles,” <http://www.aerovironment.com/area-aircraft/unmanned.html>, 2005.
- [3] Choy, P., DGA-ONERA, “Concours international universitaire de drones miniatures,” Presentation faite aux Journée Micro-Drones, Toulouse, [http://concours-drones.onera.fr/page\\_8/ConcoursDrones\\_fr.pdf](http://concours-drones.onera.fr/page_8/ConcoursDrones_fr.pdf), 2003.
- [4] Leishman, J. G., “Principles of Helicopter Aerodynamics”, Cambridge Aerospace Series, 2002.
- [5] Weis-Fogh, T., “Dimensional Analysis of Hovering Flight”, Scale effects in Animal Location by T. J. Pedley, 1977.
- [6] Maxworthy, T., “The Fluid Dynamics of Insect Flight,” *Ann. Rev. Fluid. Mech.*, 1981, 13, 329-50, 1981.
- [7] Weis-Fogh, T., “Quick estimates of flight fitness in hovering animals, including novel mechanisms for lift production,” *J. Exp. Biol.*, 59, 169-230, 1973.
- [8] Lighthill, M., “On Weis-Fogh mechanism of lift generation,” *J. Fluid Mech.* 60, 1-17, 1973.
- [9] Maxworthy, T., “Experiments on the Weis-Fogh mechanism of lift generation by insects in hovering flight”, Part 1. Dynamics of the ‘fling’, *J. Fluid Mech.*, 1979, Vol. 93, Part 1, pp 47-63.

- [10] Sane, S. P., "The aerodynamics of insect flight," *Journal of Experimental Biology* 206, 4191-4208, 2003.
- [11] Triantafyllou, M. S., Triantafyllou, G. S., Yue, D. K. P., "Hydrodynamics of Fishlike Swimming," *Annu. Rev. Fluid Mech.*, 2000, 32:32-53.
- [12] Bennett, A. G., Obye, R. C.; and Jeglum, P.M., "Ornithopter Aerodynamic Experiments," *Swimming and Flying in Nature*, edited by T.Y.T. Wu, C.J.Brokaw, and C. Brennen, Vol.2, Plenum New York, pg.985-1000, 1975.
- [13] Liu, H., Ellington, C. P., Kawachi, K., van der Berg, C., Wilmlmott, A. P., "A Computational Fluid Dynamic Study of Hawkmoth Hovering", *J. Exp.Biol*, 201, 461-77, 1998.
- [14] Birch, J. M., Dickinson, M. H., "Spanwise flow and the attachment of the leading-edge vortex on insect wings", *Nature* 412, 729-733; 2001.
- [15] Van den Berg, C., Ellington, C. P., "The three-dimensional leading-edge vortex of a 'hovering' model hawkmoth"; *Phil. Trans. R. Soc. Lond. B* 352, 329-340, 1997.
- [16] Dickinson, M. H., "The Effects of Wing Rotation on Unsteady Aerodynamics Performance at Low Reynolds Numbers," *Journal of Experimental Biology*, Vol 192, Issue 1 179-206, 1994.
- [17] Sane, S., Dickinson, M. H., "The Control of Flight Force by a Flapping Wing: Lift and Drag Production," *J. of Exp.Biology*; 204; pg. 2607-2626, 2001.
- [18] Dickinson, M. H.; Lehmann Fritz-Olaf ; Sane S., P.; Sane; "Wing Rotation and the Aerodynamic Basis of Insect Flight," *Science*, Vol.284, pg. 1954-60,1999.
- [19] Dickinson, M.H., Götz, K. G., "Unsteady Aerodynamic Performance of Model Wings at Low Reynolds Numbers," *J.exp. Biol.*; Vol.174, pg. 45-64; 1993.

- [20] Dickinson, M. H., Farley C. T., Full, R. J., Koehl, M. A. R., Kram R., Lehman, S., "How Animals Move: An Integrative View," Vol.288, Science, 2000.
- [21] Wang, Z. J., "Vortex Shedding and Frequency Selection in Flapping Flight," Journal Fluid Mechanics, 410, 323, 2000.
- [22] Lissaman, P. B. S., "Low-Reynolds-Number Airfoils", Ann. Rev. Fluid. Mech., 15, 223-39, 1983.
- [23] Shy, W., Berg, M., Ljungqvist, D., "Flapping and Flexible Wings for Biological and Micro Air Vehicles", Progress in Aerospace Sciences, Vol.35; pg 455-505, 1999.
- [24] Rayner, J. M. V., "A Vortex Theory of Animal Flight Part I, The Vortex Wake of a Hovering Animal," J. Fluid Mech., Vol. 91, Part 4, pp 697-730, 1979.
- [25] Lai, J., Platzer M.F., "Characteristics of a Plunging Airfoil at Zero Freestream Velocity", AIAA Journal, Vol. 39, No.3, 2001.
- [26] Jones, K. D, Platzer, M. F., "Numerical Computation of Flapping Wing Propulsion and Power Extraction", AIAA-97-0826, 1997.
- [27] Jones, K. D., Dohring, C. M., Platzer, M.F. "Wake Structures Behind Plunging Airfoils: A Comparison of Numerical and Experimental Results," AIAA-96-0078, 1996.
- [28] Jones, K. D., "Numerical Wake Visualization for Airfoils Undergoing Forced and Aeroelastic Motions," AIAA-96-0055, 1996.
- [29] Jones, K. D., Platzer, M. F., "On the Prediction of Dynamic Stall Onset On Airfoils in Low Speed Flow," 8th International Symposium on Unsteady Aerodynamics and Aeroelasticity of Turbomachines, Stockholm, Sweden, Sept., 1997.

- [30] Jones, K. D., Lai, J. C. S., Tuncer, I. H., Platzer, M. F., "Computational and Experimental Investigation of Flapping-Foil Propulsion," 1<sup>st</sup> International Symposium on Aqua Bio-Mechanisms, August 27-30, 2000.
- [31] Jones, K. D., Castro, B. M., Mahmoud, O., Neef, M. F., Goret, K., Hummel, D., "A Collaborative Numerical and Experimental Investigation of Flapping-Wing Propulsion," AIAA-2002-0706, 2002.
- [32] Jones, K. D., Platzer, M. F., "An Experimental and Numerical Investigation of Flapping-Wing Propulsion," AIAA-99-0995, 1999.
- [33] Jones, K. D., Lund, T. C., Platzer, M. F., "Experimental and Computational Investigation of Flapping Wing Propulsion for Micro Air Vehicles," Fixed and Flapping Wing Aerodynamics for Micro Air Vehicle Applications by Thomas J. Mueller.
- [34] Jones, K. D., Dohring, C. M., Platzer, M. F., "Experimental and Computational Investigation of the Knoller-Betz Effect, AIAA Journal, Vol. 36, No. 7, July 1998.
- [35] Jones, K. D., Castro, B. M., Mahmoud O., Platzer M. F., "A Numerical and Experimental Investigation of Flapping Wing Propulsion in Ground Effect," AIAA-2002-0866, 2002.
- [36] Anderson, J. M., Streitlien, K., Borrett D. S.; Triantafyllou M.S.; "Oscillating Foils of High Propulsive Efficiency", J. Fluid Mech., Vol. 360, pp. 41-72,1998.
- [37] Isogai, K., Shinmoto, Y., Watonobe, Y., "Effects of Dynamic Stall on Propulsive Efficiency and Thrust of a Flapping Airfoil," AIAA Journal, Vol. 37. No 10, Oct. 1999.
- [38] Neef, M. F., Hummel, D., " Euler Solution for a Finite-Span Flapping Wing," Conference on fixed, flapping and rotary wing vehicles at very low Reynolds number, University of Notre Dame, June 2000.
- [39] Koochesfahani, M. M., "Vortical Patterns in the Wake of an Oscillating Airfoil," AIAA Journal Vol 27, No.9, Sept. 1989.



- [40] Lai, J. C. S., Platzer, M. F., "Jet Characteristics of a Plunging Airfoil", AIAA Journal, Vol. 37, No. 2, Dec. 1999.
- [41] Tuncer, I. H., Platzer, M. F., "Thrust Generation due to Airfoil Flapping," AIAA Journal, Vol. 34, No. 2, Feb. 1996.
- [42] Freymuth, P., "Thrust Generation by an Airfoil Hover Modes," Experiments in Fluids 9, 17-24, 1990.
- [43] Wagner, H., "Über die Entstehung des Dynamischen Auftriebes von Tragflügeln," Zeitschr. F. Angew. Math. U. Mech., Bd. 5., 1925.
- [44] Theodorsen, T., "General Theory of Aerodynamic Instability and the Mechanism of Flutter," NACA Report 496, pp. 23, 1935.
- [45] Küssner H. G., "Zusammenfassender Bericht über den instationären Auftrieb von Flügeln", Luftfahrtforschung, Vol. 13, pp 410-424, 1936.
- [46] Von Karman, T., Sears, W. R., "Airfoil Theory for non-uniform motion," J. Aero. Sci., 5 (10): 379-390, 1938.
- [47] Garrick, I. E., "Propulsion of a Flapping and Oscillating Airfoil," NACA Report 567, 1937.
- [48] Beddoes, T. S., "Practical computation of unsteady lift," Vertica, Vol. 8, No.1, pp 55-71, Pergamon Press Ltd. UK, 1984.
- [49] Leishman, J. G., "Challenges in Modeling the Unsteady Aerodynamics of Wind Turbines," AIAA 2002-0037, 21st ASME Wind Energy Symposium and the 40th AIAA Aerospace Sciences Meeting, Reno, NV, 2002.
- [50] Zbikowski, R., "On Aerodynamic Modeling of an Insect like Flapping Wing in Hover for Micro Air Vehicles," Phil. Trans. R. Soc. London; A 360, pg. 273-290; 2002.
- [51] Klein, V., Noderer K. D., "Modeling of Aircraft Unsteady Aerodynamic Characteristics Part1-Postulated Models," NASA Technical Memorandum 106120, 1994.

- [52] Parameswaran, V., Baeder, J. D., "Indicial Aerodynamics in Compressible Flow - Direct Calculations," *Journal of Aircraft*, Vol.34, No. 1, Jan-Feb 1997.
- [53] Reisenthel, P. H., "Prediction of Unsteady Aerodynamic Forces via Nonlinear Kernel Identification," CEAS/AIAA/ICASE/NASA Longley International Forum on Aeroelasticity and Structural Dynamics; Williamsburg; VA; June 22-25; 1999.
- [54] Leishman, J. G., Nguyen, K. Q., "State-Space Representation of Unsteady Airfoil Behavior," *AIAA Journal*; Vol.28; No.5; 1989.
- [55] Lomax, H., "Indicial Aerodynamics," AGARD Manual on Aeroelasticity Part 2 Aerodynamic Aspects, Chapter 6, Nasa Ames Research Center, pp.1-58, November 1960.
- [56] Hunt, J. C. R., Wray, A. A., Moin, P., "Eddies, stream, and convergence zones in turbulent flows," Report CTR-S88, Center For Turbulence Research, 1988.
- [57] Jeong, J., Hussain, F., "On the identification of a vortex," *J. Fluid Mech.* Vol. 285, pp. 69-94, 1995.
- [58] Dubief, Y., Delcayre, F., "On coherent-vortex identification in turbulence," *J.Turbulence* , Vol.1, 011, 2000.
- [59] Cucitore, R., Quadrio, M., Baron, A., "On the effectiveness and limitations of local criteria for the identification of a vortex," *Eur. J. Mech. B* 18 261-82, 1999.
- [60] Yinlong,S.,[http://www.cs.purdue.edu/homes/sun/Teach/530\\_03F/LectureNotes/09a\\_flowVis\\_introduction.pdf](http://www.cs.purdue.edu/homes/sun/Teach/530_03F/LectureNotes/09a_flowVis_introduction.pdf), 2003
- [61] Détery, J., "Points singuliers, décollement tridimensionnel et formation des tourbillons," Département d'Aérodynamique Fondamentale et Expérimentale Onera, Séminaire LEA – ENSMA Futuroscope, 3 Avril 2003.
- [62] Bisplinghoff R. L., Ashley, H., "Principles of Aeroelasticity," Dover Publications, 1996.

- [63] Katz, J., Plotkin, A., "Low-Speed Aerodynamics - Second Edition," Cambridge University Press, NY, 2000.
- [64] Schlichting, H., Boundary Layer Theory, Seventh ed., McGraw Hill, 1979.
- [65] Kurtulus D. F., Farcy A., Alemdaroglu N., "Numerical Calculation and Analytical Modelization of Flapping Motion," 1st European Micro Air Vehicle conference and Flight Competition, Braunschweig, Germany, 13-14 July 2004.
- [66] Kurtulus D. F., Farcy A., Alemdaroglu N., "Unsteady Aerodynamics of Flapping Airfoil in Hovering Flight at Low Reynolds Numbers," 43rd AIAA Aerospace Sciences Meeting and Exhibit, AIAA-2005-1356, Reno, Nevada, 10 - 13 Jan 2005.
- [67] Kurtulus D. F., Farcy A., Alemdaroglu N., "Havada Asılı Konumdaki Çırpın Kanat Profilinin Sayısal ve Analitik Modellemesi", HİTEK organized by Turkish Air Force Academy, 9-10 December 2004.
- [68] Sarpkaya, T., " Vortex Element Methods for Flow Simulation," In Advances in Applied Mechanics, (Ed. Th. Wu and A Hutchinson), Vol. 31, pp. 113-247, Academic Press, London, 1994.
- [69] Whitehouse, G. R. , Brown, R. E., "Modeling the Mutual Distortions of Interacting Helicopter and Aircraft Wakes," , Journal of Aircraft, Vol. 40, No. 3, pp. 440-449, May–June 2003.
- [70] Sitaraman, J., Baeder, J. D., "Computational-Fluid-Dynamics-Based Enhanced Indicial Aerodynamic Models", Journal of Aircraft, Vol. 41, No. 4, pp. 798-810, July-August 2004.
- [71] Barba, L. A. , Leonard, A., Allen, C. B., "Advances in viscous vortex methods-meshless spatial adaption based on radial basis function interpolation," International Journal Journal for Numerical Methods in Fluids, Int. J. Numer. Meth. Fluids, 46:001–0032, 2004.
- [72] Sarpkaya T., "Computational methods with vortices," Journal of Fluids Engineering, Vol. 11, pp. 5–52, 1989.

- [73] Puckett, E., G., "Vortex methods: An introduction and survey of selected research topics", In *Incompressible Computational Fluid Dynamics: Trends and Advances*, Gunzburger, M. D., Nicolaides, R. A. (eds.). Cambridge University Press, pp. 335–408, 1993.
  
- [74] Bene, J., Brocheler, S., Lustfeld, H., "Simulating 2D Flows with Viscous Vortex Dynamics," *Journal of Statistical Physics*, Vol. 101, Nos. 1/2, 2000.
  
- [75] Yeung, W. W. H., Parkinson, G. V., "Analysis and Modeling of Pressure Recovery for Separated Reattaching Flows," *Journal of Fluids Engineering*, Vol. 126 , pp. 355-361 , May 2004.

## APPENDIX A

### PRELIMINARY TESTS

#### A.1 Impulsively Started Flat Plate

The motion of a viscous fluid caused by the suddenly accelerated plane wall is termed as Stokes's first problem by Schlichting (Ref.[64], pg. 90). The motion is started impulsively from rest and moves in its own plane with a constant velocity  $U_0$ . Selecting the x-axis along the wall in the direction of  $U_0$ , one gets the simplified Navier-Stokes equation (Eq.A.1).

$$\frac{\partial u}{\partial t} = \nu \frac{\partial^2 u}{\partial y^2} \quad (\text{A.1})$$

The pressure in the whole space is constant, and the boundary conditions are:

$$\begin{aligned} u &= 0 \text{ for all } y & t &\leq 0 \\ u &= U_0 \text{ for } y=0; u=0 \text{ for } y=\infty & t &> 0 \end{aligned} \quad (\text{A.2})$$

The partial differential equation (A.1) can be reduced to an ordinary differential equation by the substitution:

$$\eta = \frac{y}{2\sqrt{\nu t}} \quad (\text{A.3})$$

Assuming

$$u = U_0 f(\eta) \quad (\text{A.4})$$

one gets the ordinary differential equation for  $f(\eta)$ :

$$f'' + 2\eta f' = 0 \quad (\text{A.5})$$

with the boundary conditions  $f=1$  at  $\eta=0$  and  $f=0$  at  $\eta=\infty$ .

The solution is:

$$u = U_o \operatorname{erfc}(\eta) \quad (\text{A.6})$$

where

$$\operatorname{erfc}(\eta) = \frac{2}{\sqrt{\pi}} \int_{\eta}^{\infty} \exp(-\eta^2) d\eta = 1 - \operatorname{erf}(\eta) = 1 - \frac{2}{\sqrt{\pi}} \int_0^{\eta} \exp(-\eta^2) d\eta \quad (\text{A.7})$$

is the complementary error function.

The boundary conditions shown in Figure A.1 are set such that the blue sides are symmetric boundary conditions, the cyan color representing the flat plate at the bottom of the grid domain is defined by the wall boundary condition. The top side of the grid domain is represented by the pressure boundary conditions and the left and right sides are defined as the cyclic boundary conditions. Different velocity profiles for different time values are represented in Figure A.2. The velocity profiles for varying times are similar meaning that they can be reduced to the same curve by scaling  $\eta$ . Central differencing scheme is used in the calculations of Star-CD with an implicit time discretization. The time increment used is  $\Delta t = 0.5 \times 10^{-5}$  sec with a 5000 time steps. The comparison of the numerical results obtained by Star-CD and Eq. (A.6) is shown in Figure A.3.

By using the definition of  $\eta$  (Eq.A.3), (Eq.A.6) and the complementary error function (Eq.A.7), the shear stress at the wall of the impulsively starting flat plate is:

$$\tau_w = \mu \cdot \left( \frac{\partial u}{\partial y} \right)_{y=0} = \mu \cdot \frac{1}{2\sqrt{\nu \cdot t}} \cdot \left( \frac{\partial u}{\partial \eta} \right)_{\eta=0} \quad (\text{A.8})$$

where

$$\begin{aligned} \frac{\partial u}{\partial \eta} &= U_o \cdot \operatorname{erfc}(\eta) = U_o \cdot \frac{\partial}{\partial \eta} \left( 1 - \frac{2}{\sqrt{\pi}} \int_0^\eta \exp(-\eta^2) d\eta \right) \\ &= -U_o \cdot \frac{2}{\sqrt{\pi}} \cdot \exp(-\eta^2) \end{aligned} \quad (\text{A.9})$$

$$\left( \frac{\partial u}{\partial \eta} \right)_o = -U_o \cdot \frac{2}{\sqrt{\pi}} \quad (\text{A.10})$$

then

$$\tau_w = \mu \cdot \left( \frac{\partial u}{\partial y} \right)_{y=0} = \mu \cdot \frac{1}{2\sqrt{\nu \cdot t}} \cdot \left( \frac{\partial u}{\partial \eta} \right)_{\eta=0} = -\frac{\mu \cdot U_o}{\sqrt{\pi \cdot \nu \cdot t}} \quad (\text{A.11})$$

For a flat plate, the drag is calculated by the product of the shear stress with the area  $S$  of the plate. So the drag coefficient is:

$$C_d = \frac{D}{\frac{1}{2} \rho U_o^2 \cdot S} = -\frac{\mu U_o \cdot S}{\frac{1}{2} \rho U_o^2 \cdot S \cdot \sqrt{\pi \nu t}} = -\frac{2}{U_o} \sqrt{\frac{\nu}{\pi \cdot t}} \quad (\text{A.12})$$

Figure A.4 shows the comparison of the results obtained by the Navier-Stokes code and the exact solution (Eq.A.12).

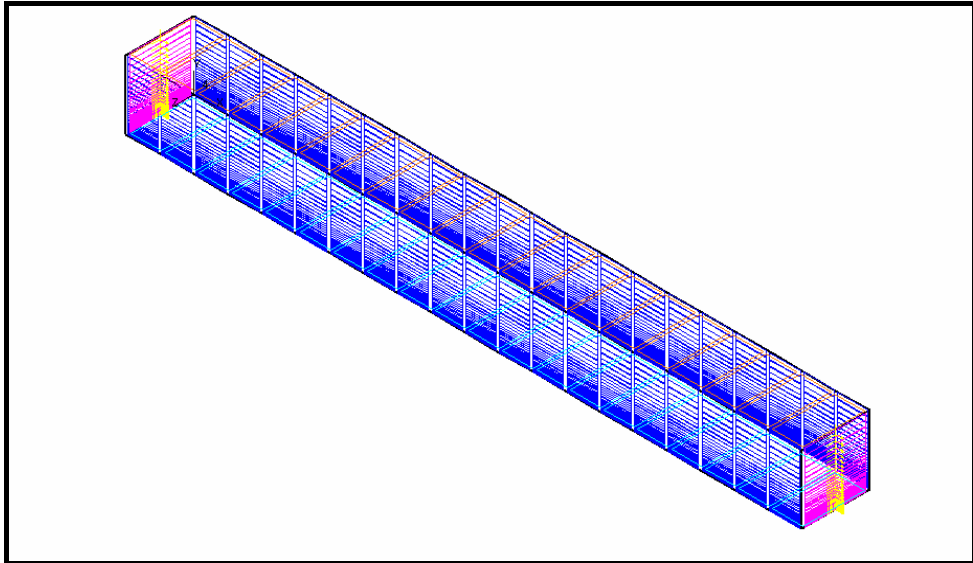


**Figure A.1** Boundary conditions of the grid domain for a flat plate.

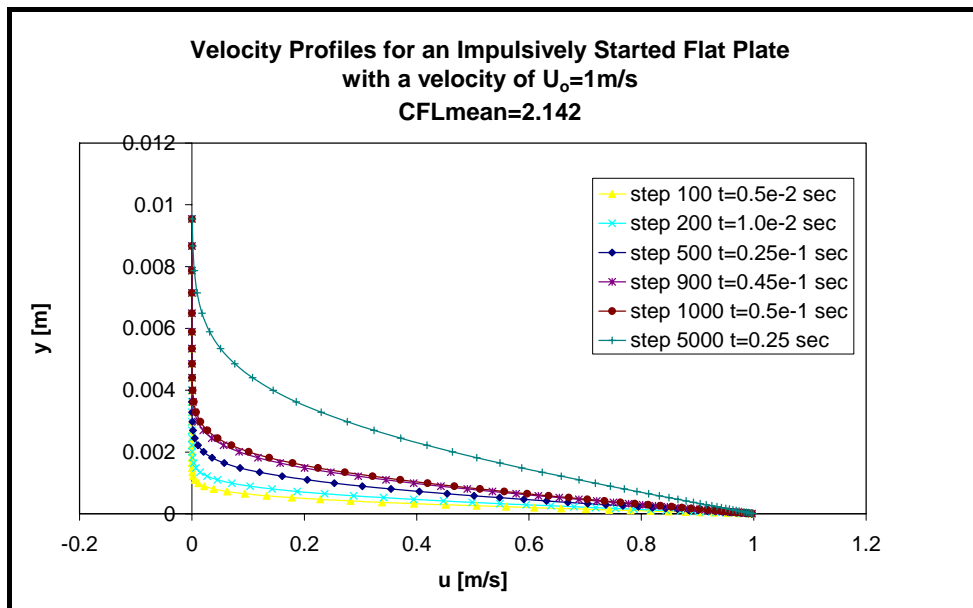


**Figure A.2** Dimensional velocity profile of an impulsively started flat plate with  $U_0=1\text{m/s}$  for different time steps.



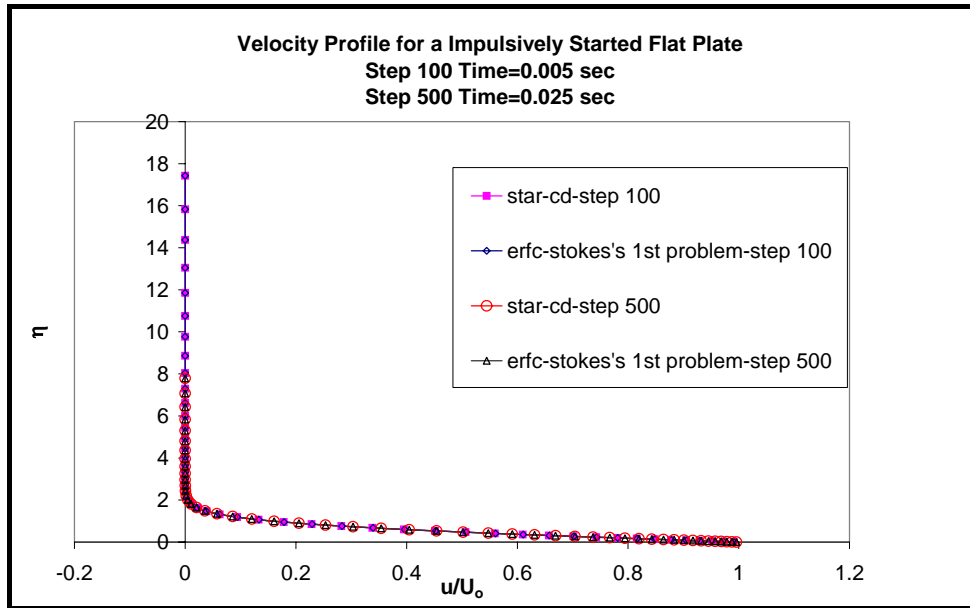


**Figure A.3** Non-dimensional velocity profile of an impulsively started flat plate with  $U_0=1\text{m/s}$  for different time steps.

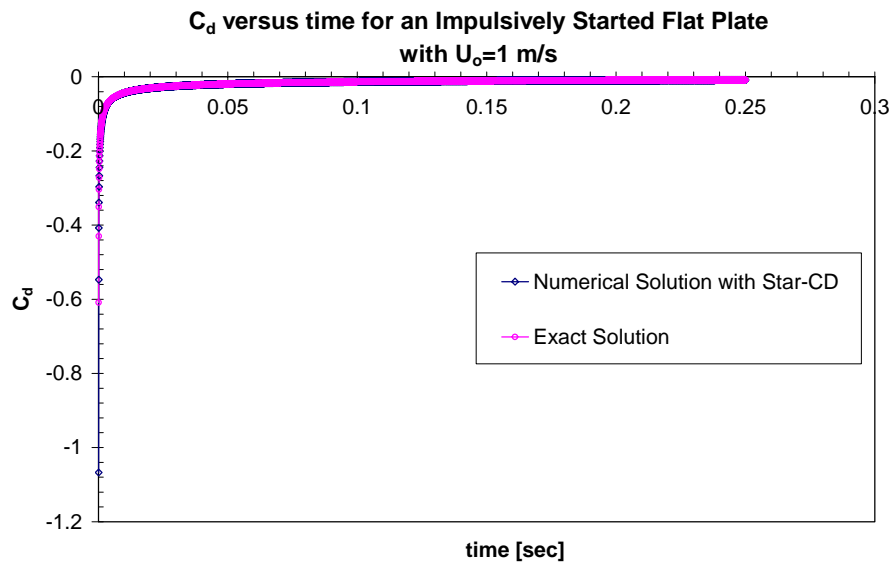


**Figure A.4** Comparison of the drag coefficient  $C_d$  between the numerical and exact solutions of impulsively started flat plate with  $U_0=1\text{m/s}$ .

## A.2 Oscillating Flat Plate

The exact solution, the numerical solution obtained by the Navier-Stokes code and the Duhamel's integral solution by analytical integration are calculated for an oscillating flat plate. The velocity profiles for the Navier-Stokes code are given in Figure A.5. The drag coefficient is compared in Figure A.6 for all calculations. The same grid domain is used as case of the impulsively started flat plate case.

For this case, the boundary conditions are given as:

$$\begin{aligned} u=0 \text{ for all } y & \quad t \leq 0 \\ u=\omega A \cos(\omega t) \text{ for } y=0; u=0 \text{ for } y=\infty & \quad t > 0 \end{aligned} \quad (\text{A.13})$$

Exact solution is given in Ref.[64] as:

$$u(y,t) = \omega A e^{-ky} \cos(\omega t - ky) \quad (\text{A.14})$$

with

$$k = \sqrt{\frac{\omega}{2\nu}} \text{ and } \omega = \frac{2\pi}{T} \quad (\text{A.15})$$

where T is the period and A is the amplitude of the oscillation.

In the numerical calculations carried in Star-CD, amplitude of oscillation is taken to be 0.02m and the period is 0.1sec.

By doing similar calculations for shear stress and by differentiating the velocity with respect to y:

$$\begin{aligned} \left( \frac{\partial u}{\partial y} \right) &= -k\omega A e^{-ky} \cos(\omega t - ky) + k\omega A e^{-ky} \sin(\omega t - ky) \\ &= k\omega A e^{-ky} (\sin(\omega t - ky) - \cos(\omega t - ky)) \quad (\text{A.16}) \\ \tau_w = \mu \left( \frac{\partial u}{\partial y} \right)_{y=0} &= \mu k \omega A (\sin(\omega t) - \cos(\omega t)) = A \omega^{3/2} \frac{\sqrt{\rho \mu}}{\sqrt{2}} (\sin(\omega t) - \cos(\omega t)) \end{aligned}$$

$$\begin{aligned}
C_D &= \frac{D}{\frac{1}{2}\rho(A\omega)^2 S} = \frac{\tau_w S}{\frac{1}{2}\rho(A\omega)^2 S} = \frac{A\omega^{3/2} \frac{\sqrt{\rho\mu}}{\sqrt{2}} (\sin(\omega t) - \cos(\omega t))}{\frac{1}{2}\rho(A\omega)^2} \\
&= \frac{1}{A} \sqrt{\frac{2\nu}{\omega}} (\sin(\omega t) - \cos(\omega t))
\end{aligned} \tag{A.17}$$

Analytical Duhamel Integration from impulsively starting flat plate in order to obtain oscillating flat plate result:

$$C_{Dosc}(t) = f(0) \cdot C_{Dimp} + \int_0^t \frac{d}{d\tau} f(\tau) \cdot C_{Dimp}(t-\tau) d\tau \tag{A.18}$$

$$\begin{aligned}
f(t) &= A\omega \cdot \cos(\omega t) \\
\frac{d}{dt} f(t) &= -A\omega^2 \sin(\omega t)
\end{aligned} \tag{A.19}$$

$$C_{Dimp}(t) = -2 \frac{1}{U_o} \sqrt{\frac{\nu}{\pi t}} \tag{A.20}$$

$$\begin{aligned}
C_{Dosc}(t) &= -2 \cdot A\omega \cdot \frac{1}{U_o} \sqrt{\frac{\nu}{\pi t}} + \int_0^t -A\omega^2 \sin(\omega\tau) \cdot \left[ -2 \frac{1}{U_o} \sqrt{\frac{\nu}{\pi(t-\tau)}} \right] d\tau \\
&= -2 \cdot A\omega \cdot \frac{1}{U_o} \sqrt{\frac{\nu}{\pi t}} + \int_0^t \frac{2A\omega^2}{U_o} \sqrt{\frac{\nu}{\pi}} \frac{\sin(\omega\tau)}{\sqrt{(t-\tau)}} d\tau
\end{aligned} \tag{A.21}$$

If we do a change of variables with

$$u = \sqrt{t-\tau} \quad \text{and} \quad du = -\frac{1}{2\sqrt{t-\tau}} = -\frac{1}{2u} \tag{A.22}$$

then we have

$$\int_0^t \frac{\sin \omega t}{\sqrt{t-\tau}} = \int_{\sqrt{t}}^0 \sin(\omega[t-u^2]) \cdot (-2) \cdot du \quad \text{where } t > \tau \quad (\text{A.23})$$

$$C_{Dosc}(t) = -2 \cdot A \omega \cdot \frac{1}{U_o} \sqrt{\frac{v}{\pi}} + \frac{2A\omega^2}{U_o} \sqrt{\frac{v}{\pi}} \cdot \left[ 2 \sin(\omega t) \int_0^{\sqrt{t}} \cos(\omega u^2) du - 2 \cos(\omega t) \int_0^{\sqrt{t}} \sin(\omega u^2) du \right] \quad (\text{A.24})$$

$$= -2 \cdot A \omega \cdot \frac{1}{U_o} \sqrt{\frac{v}{\pi}} +$$

$$\frac{2A\omega^2}{U_o} \sqrt{\frac{v}{\pi}} \cdot \left[ 2 \sin(\omega t) \frac{1}{2} \sqrt{\frac{2\pi}{\omega}} \text{FresnelC} \left( \sqrt{\frac{2\omega}{\pi}} \cdot \sqrt{t} \right) - 2 \cos(\omega t) \frac{1}{2} \sqrt{\frac{2\pi}{\omega}} \text{FresnelS} \left( \sqrt{\frac{2\omega}{\pi}} \cdot \sqrt{t} \right) \right]$$

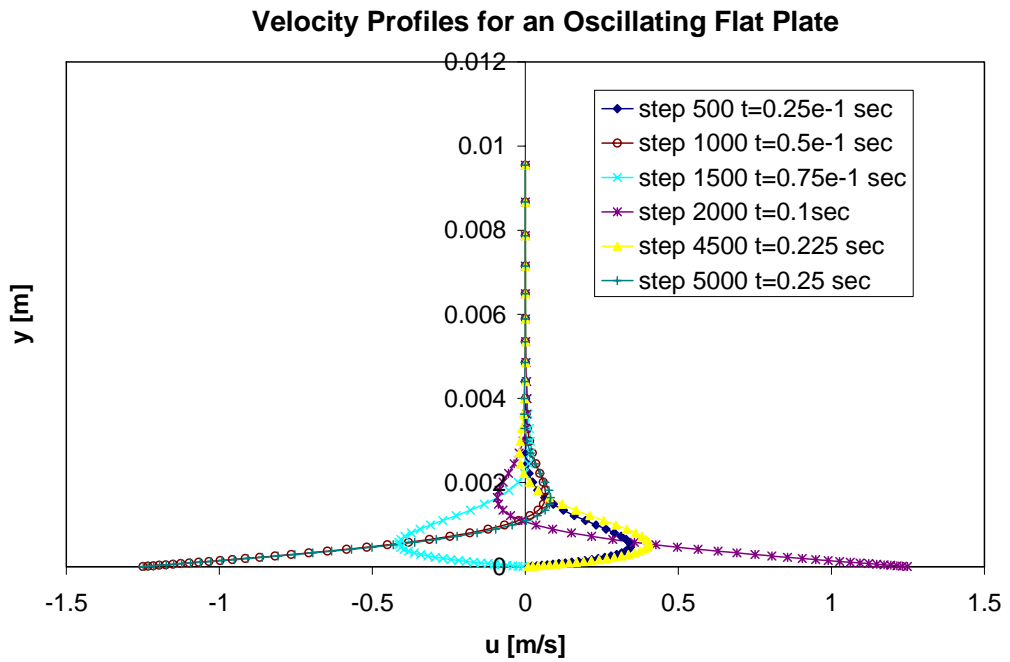


**Figure A.5** Velocity profile of an oscillatory flat plate for different time steps.

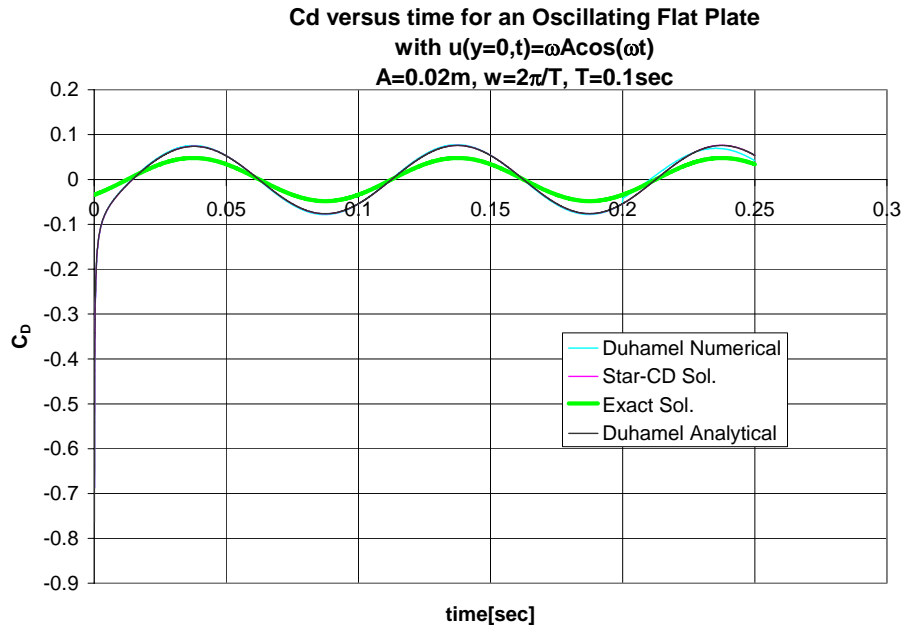


**Figure A.6** Drag coefficient  $C_d$  between the numerical and analytical compared to exact solutions of oscillating flat plate.

### A.3 Choice of the Difference Scheme

The velocity distribution over the oscillating flat plate for central difference and upward different schemes are compared with the exact solution (Fig.A.7) and the  $L_1$ ,  $L_2$  and  $L_\infty$  norms are calculated at  $t=0.5\text{sec}$  for period  $T=0.1\text{sec}$  and the amplitude of oscillation  $A$ , being equal to  $0.02\text{m}$  (Table A.1).

Both difference schemes give good results compared to the exact solution of the oscillating flat plate problem. For the numerical calculations, the upward difference scheme is used.

**Table A.1** Oscillating flat plate velocity error norms on the flat plate relative to the exact solution at  $t=0.5s$  for the comparison of central and upward difference schemes used in numerical calculations.

	Central Difference Scheme	Upward Difference scheme
$L_\infty$ norm	0.00972605	0.00972745
$L_1$ norm	0.00345752	0.00345785
$L_2$ norm	0.03387375	0.0338781

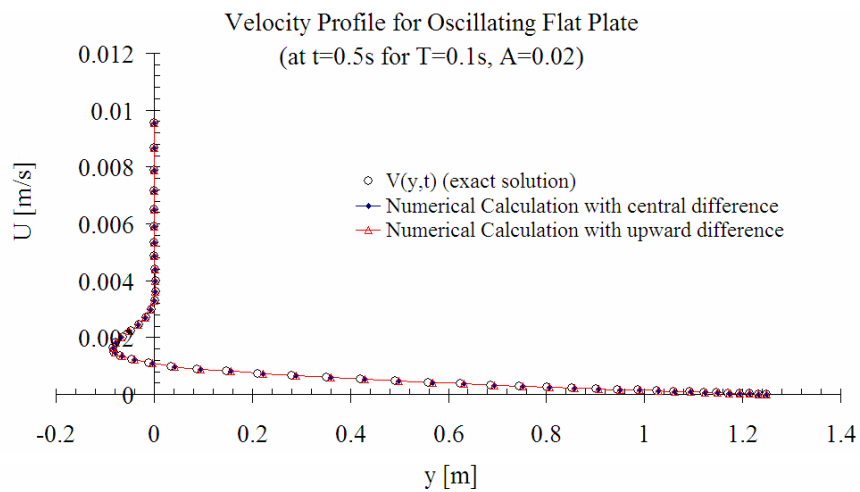


**Figure A.7** Velocity profiles for oscillating flat plate for central and upward difference schemes and comparison with exact solution.

#### A.4 Verification of Boundary Conditions

Pressure coefficient values along the airfoil surface for the steady solutions of Star-CD for 2 different boundary conditions (inlet/outlet & inlet/pressure) are compared with XFOIL results (Fig. A.8). Steady results are also compared with the impulsive start run (at iter=5000 where impulsive start effect was disappeared much earlier) of the same configuration and it is concluded that the impulsive start goes to its steady state value correctly (Fig.A.9). Table A.2 shows the force coefficients and the lift to drag ratio for these calculations.

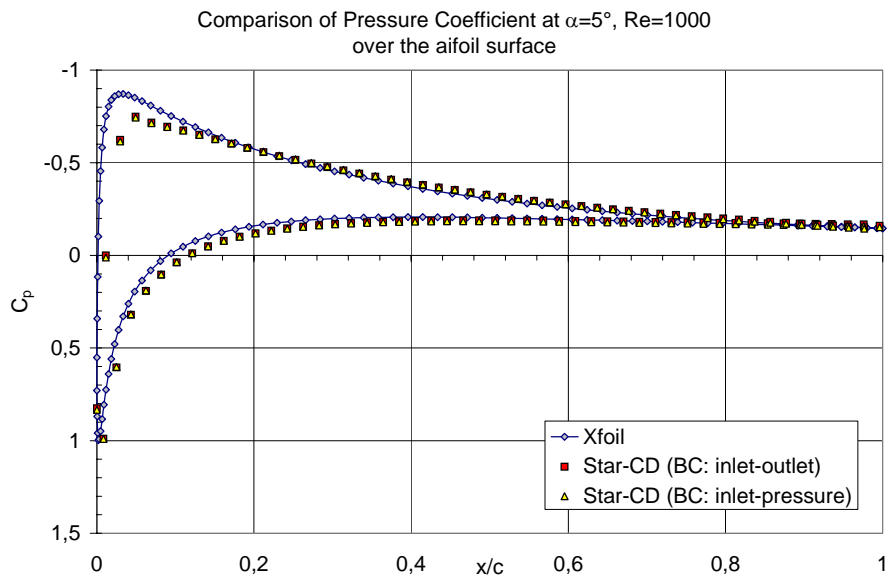


**Figure A.8** Steady state solutions.

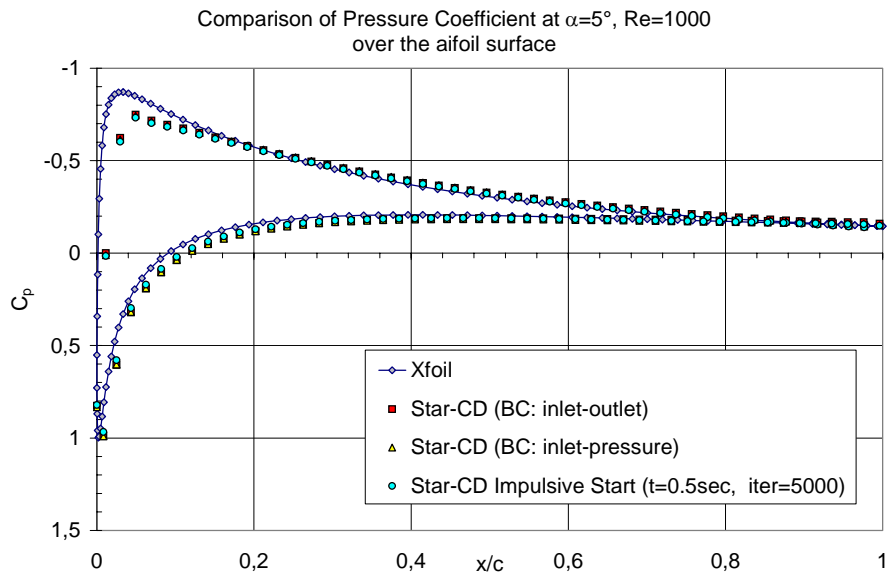


**Figure A.9** Comparison of steady state solutions with impulsive start result.

**Table A.2** Lift and Drag coefficients for steady state results and impulsive motion result.

<b>Program</b>	<b><math>C_L</math></b>	<b><math>C_D</math></b>	<b>L/D</b>
Xfoil	0.2414	0.1280	1.886
Star-CD (BC: inlet-outlet)	0.2512	0.1415	1.775
Star-CD (BC: inlet-pressure)	0.2548	0.1421	1.793
Star-CD (impulsive)	0.2485	0.1411	1.761



## APPENDIX B

### DIMENSIONAL ANALYSIS AND SIMILITUDE

#### B.1 Buckingham Pi Theorem

$$\bullet \quad \Pi_1 = \frac{F}{\rho^{x1} V^{y1} c^{z1}} = \frac{MT^{-2}}{M^{x1} L^{-3*x1} L^{y1} T^{-y1} L^{z1}} = \frac{MT^{-2}}{M^{x1} L^{-3*x1+y1+z1} T^{-y1}}$$

$$\begin{array}{ll} x1=1 & x1=1 \\ -y1=-2 & y1=2 \\ -3*x1+y1+z1=0 & z1=1 \end{array}$$

$$\Pi_1 = \frac{F}{\rho V^2 c} \quad (\text{non-dimensional force}) \quad (\text{B.1})$$

$$\bullet \quad \Pi_2 = \frac{\mu}{\rho^{x2} V^{y2} c^{z2}} = \frac{ML^{-1}T^{-1}}{M^{x2} L^{-3*x2+y2+z2} T^{-y2}}$$

$$\begin{array}{ll} x2=1 & x2=1 \\ -y2=-1 & y2=1 \\ -3*x2+y2+z2=0 & z2=1 \end{array}$$

$$\Pi_2 = \frac{\mu}{\rho V c} = \frac{1}{\text{Re}} \quad (\text{Reynolds number}) \quad (\text{B.2})$$

$$\bullet \quad \Pi_3 = \frac{T}{\rho^{x3} V^{y3} c^{z3}} = \frac{T^1}{M^{x3} L^{-3*x3+y3+z3} T^{-y3}}$$

$$\begin{array}{ll} x3=0 & x3=0 \\ -y3=1 & y3=-1 \\ -3*x3+y3+z3=0 & z3=1 \end{array}$$

$$\Pi_3 = \frac{TV}{c} \quad (\text{non-dimensional time}) \quad (\text{B.3})$$

$$\bullet \quad \Pi_4 = \frac{x_T}{\rho^{x_4} V^{y_4} c^{z_4}} = \frac{L^1}{M^{x_4} L^{-3x_4+y_4+z_4} T^{-y_4}}$$

$$x_4=0 \qquad x_4=0$$

$$-y_4=0 \qquad y_4=0$$

$$-3x_4+y_4+z_4=1 \qquad z_4=1$$

$$\Pi_4 = \frac{x_T}{c} \qquad \text{(geometrical similitude)} \qquad \text{(B.4)}$$

$$\bullet \quad \Pi_5 = \alpha \qquad \text{(angle of attack)} \qquad \text{(B.5)}$$

$$\bullet \quad \Pi_6 = \frac{\dot{\alpha}}{\rho^{x_6} V^{y_6} c^{z_6}} = \frac{T^{-1}}{M^{x_6} L^{-3x_6+y_6+z_6} T^{-y_6}}$$

$$x_6=0 \qquad x_6=0$$

$$-y_6=0 \qquad y_6=1$$

$$-3x_6+y_6+z_6=0 \qquad z_6=-1$$

$$\Pi_6 = \frac{\dot{\alpha} c}{V} \qquad \text{(reduced frequency)} \qquad \text{(B.6)}$$

$$f(\Pi_1, \Pi_2, \Pi_3, \Pi_4, \Pi_5, \Pi_6) = 0 \qquad \text{(B.7)}$$

For similitude calculations, subscript 1 stands for air and subscript 2 stands for water.

For air:

The STP (Standard temperature and pressure) conditions are used in the calculations

- Temperature : T=15°C=288.15K
- Pressure : p=101325 Pa
- Density :  $\rho_1=1.225 \text{ kg/m}^3$
- Dynamic viscosity :  $\mu_1=1.781 \cdot 10^{-5} \text{ kg/ms}$
- Kinematic viscosity :  $\nu_1=1.45388 \cdot 10^{-5} \text{ m}^2/\text{s}$
- Chord of the airfoil :  $c_1=0.01\text{m}$

For water:

- Density :  $\rho_2=1000 \text{ kg/m}^3$
- Dynamic viscosity :  $\mu_2=10^{-3} \text{ kg/ms}$
- Kinematic viscosity :  $\nu_2=10^{-6} \text{ m}^2/\text{s}$
- Chord of the airfoil :  $c_2=0.06\text{m}$

## APPENDIX C

### EXPERIMENTAL SETUP DETAILS

#### C.1 Specifications of the Setup

**Table C.1** Specifications of the step motors used for the setup.

	Motor 1 (Translation) MAC 23 of midi ingenieurie	Motor 2 (Rotation) 6600-20 version R034BIP of Sonceboz
Power supply	12 to 45 VDC	12 to 60 VDC
Holding torque	1.4 N.m	0.93 N.m
Maximum speed	4500 rpm at 45 VDC	4000 rpm
Resolution	200 positions per rotation	200 positions per rotation
Rotor inertia	0.44 kg.cm <sup>2</sup>	0.248 kg.cm <sup>2</sup>
	5V → 20 KHz ⇔ 10 rev/sec	5V → 1.2 KHz ⇔ 0.6 rev/sec

**Table C.2** Potentiometer readings.

Angle turned	0°	360°
Voltage	4.77 V	1.907 V
Voltage corresponding to 360° turning	2.863 V	
Degree corresponding to 1 V	$360/2.863=125.742^\circ$	
Position	0mm	360mm
Voltage	1.685V	2.25 V
Voltage corresponding to 360mm turning	0.565 V	
mm corresponding to 1 V	$360/0.565=637.168\text{mm}$	

**Table C.3** Specifications of the driver controlling the step motors.

<b>Product</b>	<b>MI 904A</b>
<b>Power supply</b>	22 V to 90 VDC
<b>Rms current by phase</b>	0.5A to 4A
<b>Type of motor</b>	Two-pole wiring (4 or 8 wires)
<b>Microstep resolution</b>	1, 2, 4, 5, 8, 10, 16, 20, 32, 40, 64 $\mu$ step/step
<b>Maximum input clock frequency</b>	500 kHz
<b>Size (in mm)</b>	160 x 100 x 45

The power stages move the motor one step for each received clock signal (Figure C.1).

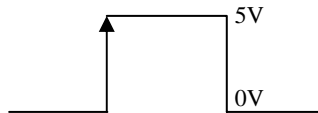


**Figure C.1** Clock Signal for drivers controlling step motors.

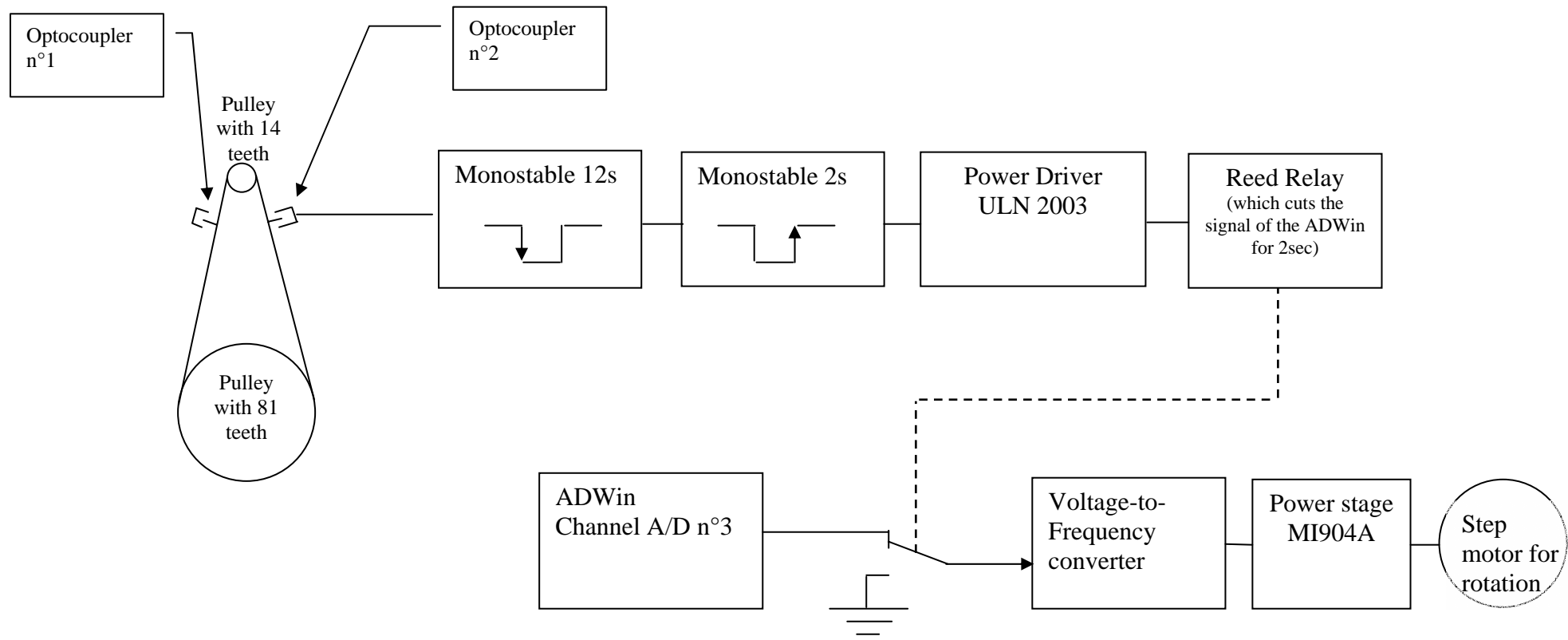


**Figure C.2** Basic Principle (Only the optocoupler n°2 is represented)

The frequency of the reading of the computer at for each line of the file created is measured as 130 Hz by sending only zero and one values to the computer. The controller measures the high and low signals and by sending only 0 and 1 values, so two data is implemented in a period (Figure C.3). The time corresponding to reading of one signal is the half of the period seen by the controller. So, in order to obtain the signal of the PC, the frequency ( $f_{PC} = \frac{1}{T_{contoroller}/2} = 2f_{controller}$ ) read from the controller must be multiplied by 2.

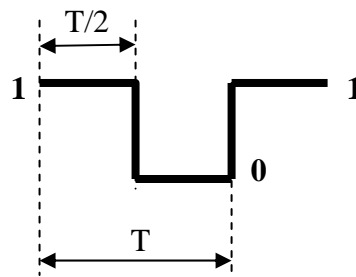


**Figure C.3** Signal send to computer to find the frequency of the PC.

The step motors consume 2 amps and in spite of the shielding of the cables, they radiate enormously. These situations disturb the voltage-to-frequency converters in the absence of significant voltage signal. It was necessary to correct the input voltage file in order to impose minimum voltage instead of zero value to the converters. So the minimum voltages are 0.005V and 0.01V for translation and rotation respectively. To avoid the parasites, the power supply (50V) and power driver (15V and 5V) are separated. Only the cables coming from module ADWin are not connected to the ground since in this case parasites coming from the ground would be induced on the mass of the signal. The emergency stop of the system is ensured by a knob connected on the cards MI 904A put to the ground connection of the input. To get the full power of the motors, the voltage supply of MI 904A card is carried with 30V (50V max).

## APPENDIX D

### VISUALIZATIONS OF THE CASE STUDY

The comparison of laser sheet visualizations, PIV measurements and numerical results during a period at different time values are represented in Figures from D.1 to D.24. Each figure represents:

- A. The experimental visualization with laser sheet,
- B. Non-dimensional vorticity contours for PIV measurements,
- C. Non-dimensional vorticity contours for numerical simulations,
- D. Non-dimensional Q contours for PIV measurements,
- E. Non-dimensional Q contours for numerical simulations,
- F. Pressure coefficient for the numerical simulations,
- G. Aerodynamic force coefficients for numerical simulations.

(The yellow texts on Figure A's correspond to the trace of vortices generated during the previous half-stroke. The white texts correspond to the vortices generated during the half-stroke in consideration.)

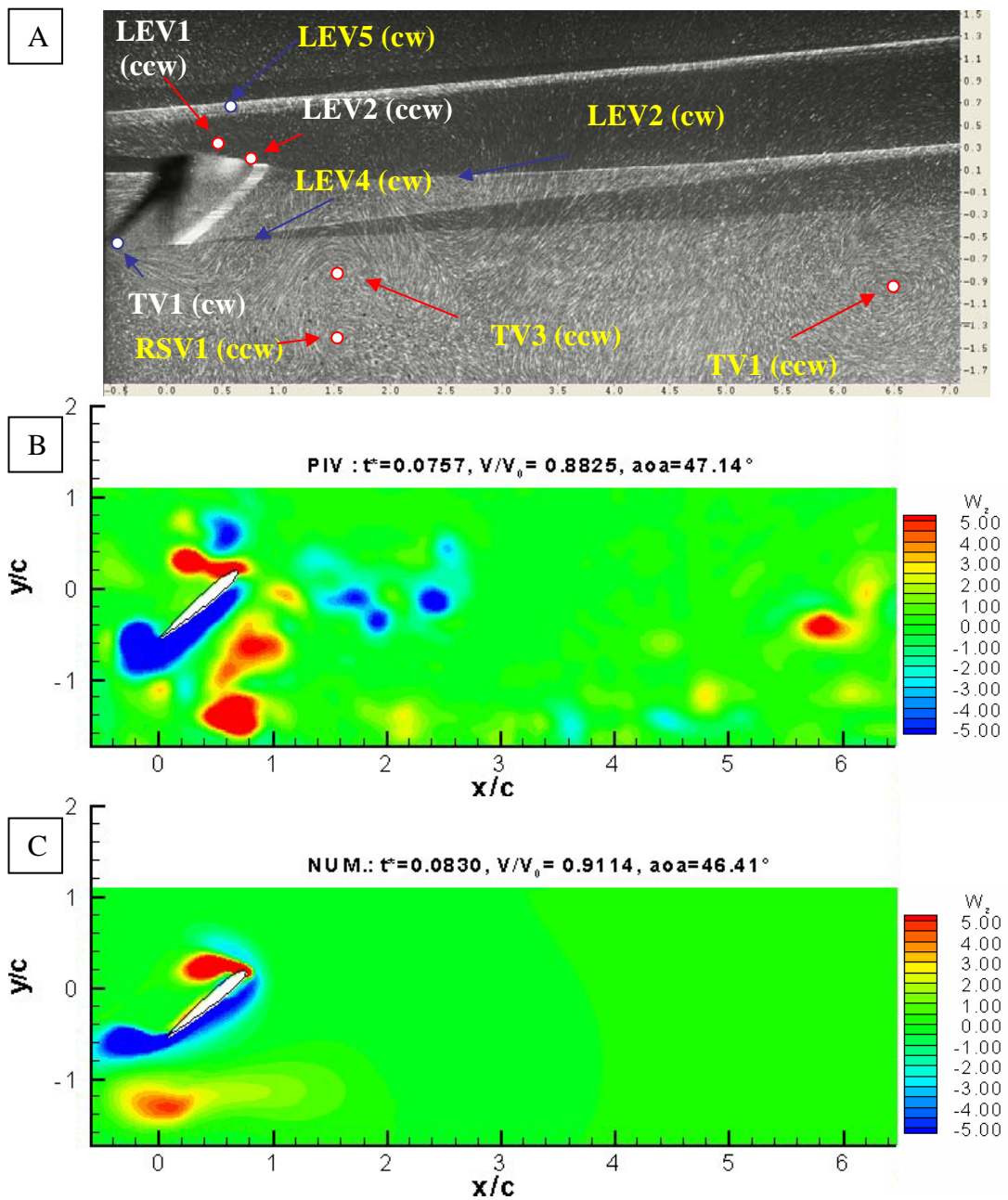


**Figure D.1** Experimental visualization at  $t^* = 0.08$ , comparison with the numerical solution and PIV measurements.



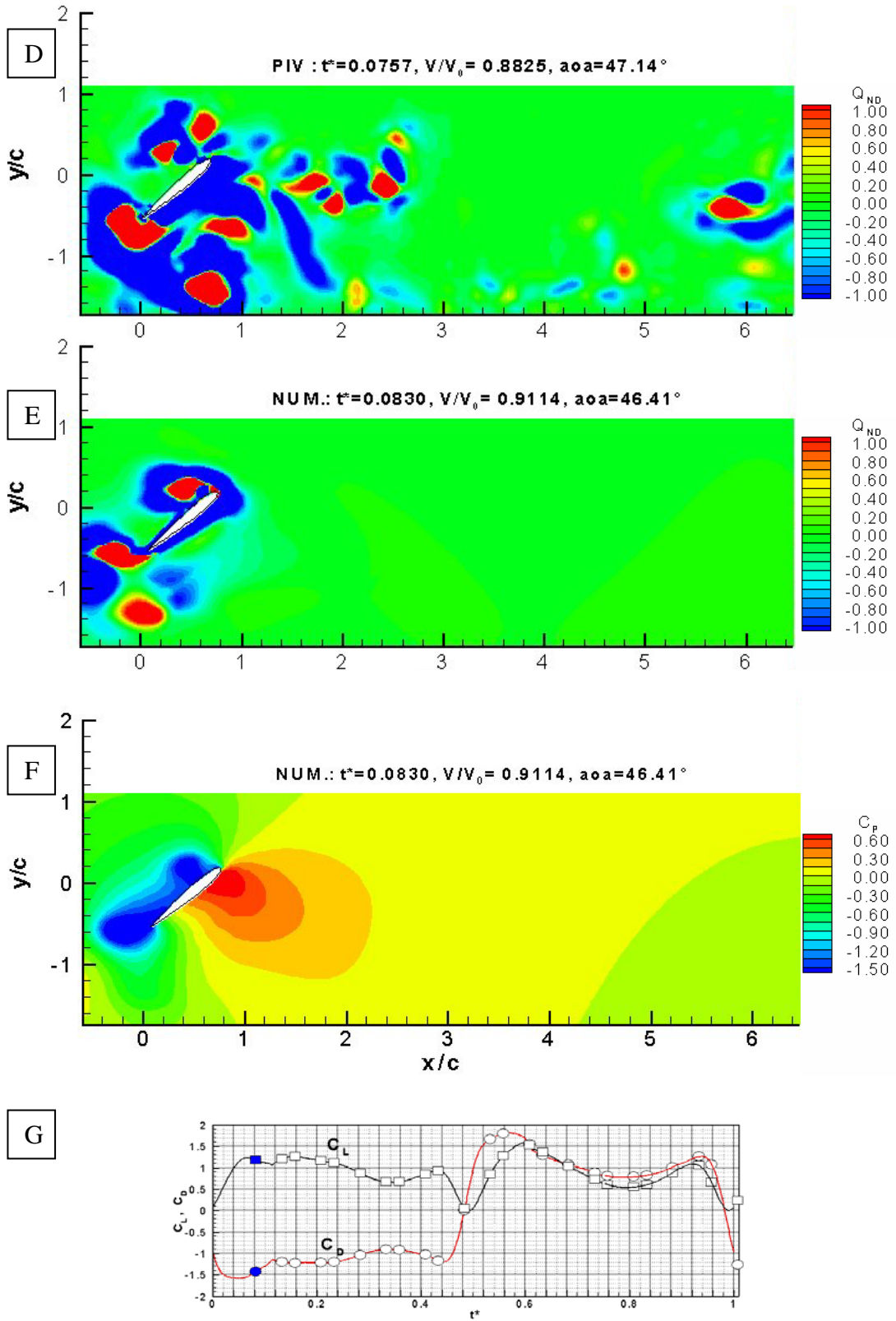


**Figure D.1 (continued)** Experimental visualization at  $t^* = 0.08$ , comparison with the numerical solution and PIV measurements.

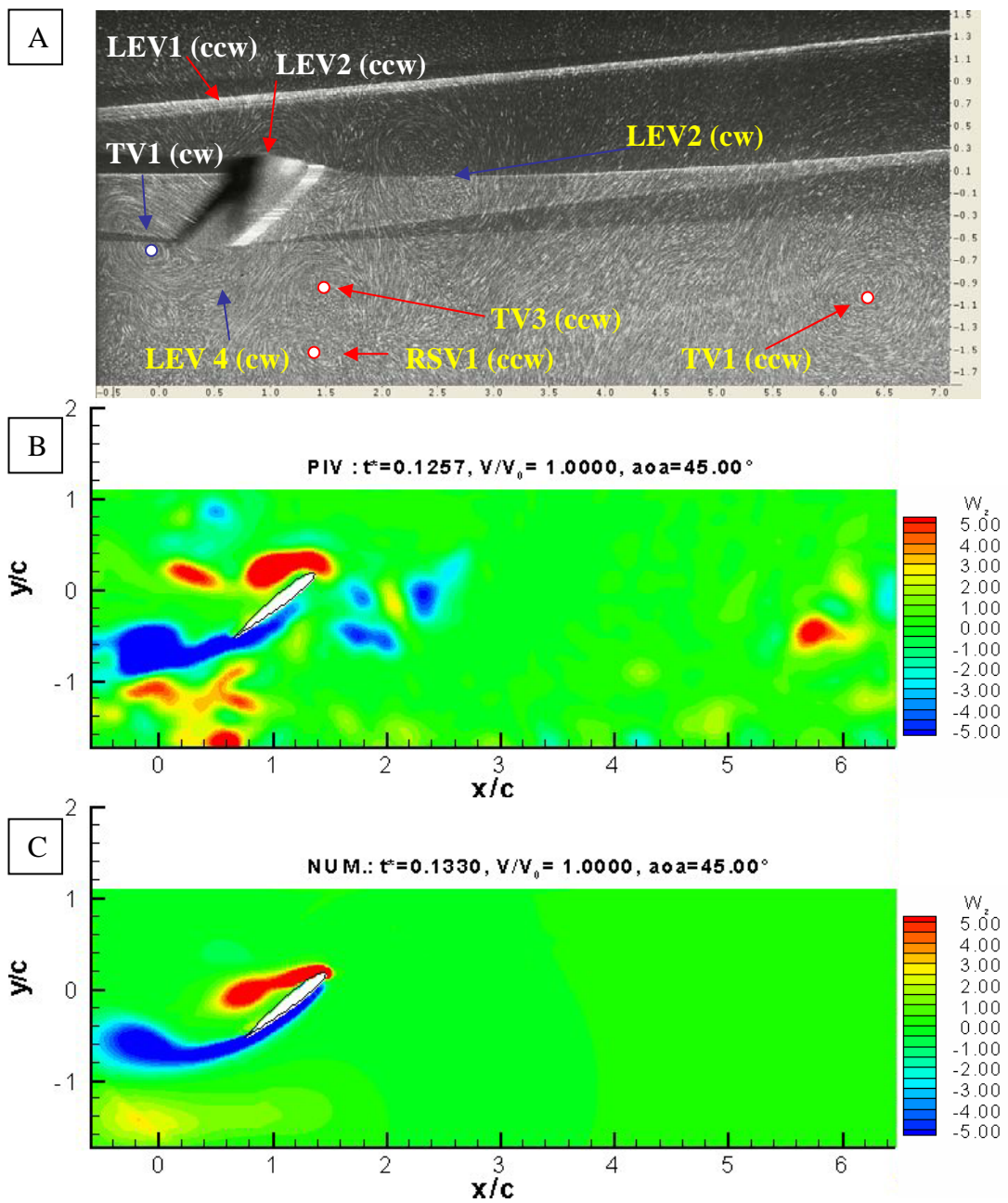


**Figure D.2** Experimental visualization at  $t^* = 0.12$ , comparison with the numerical solution and PIV measurements.

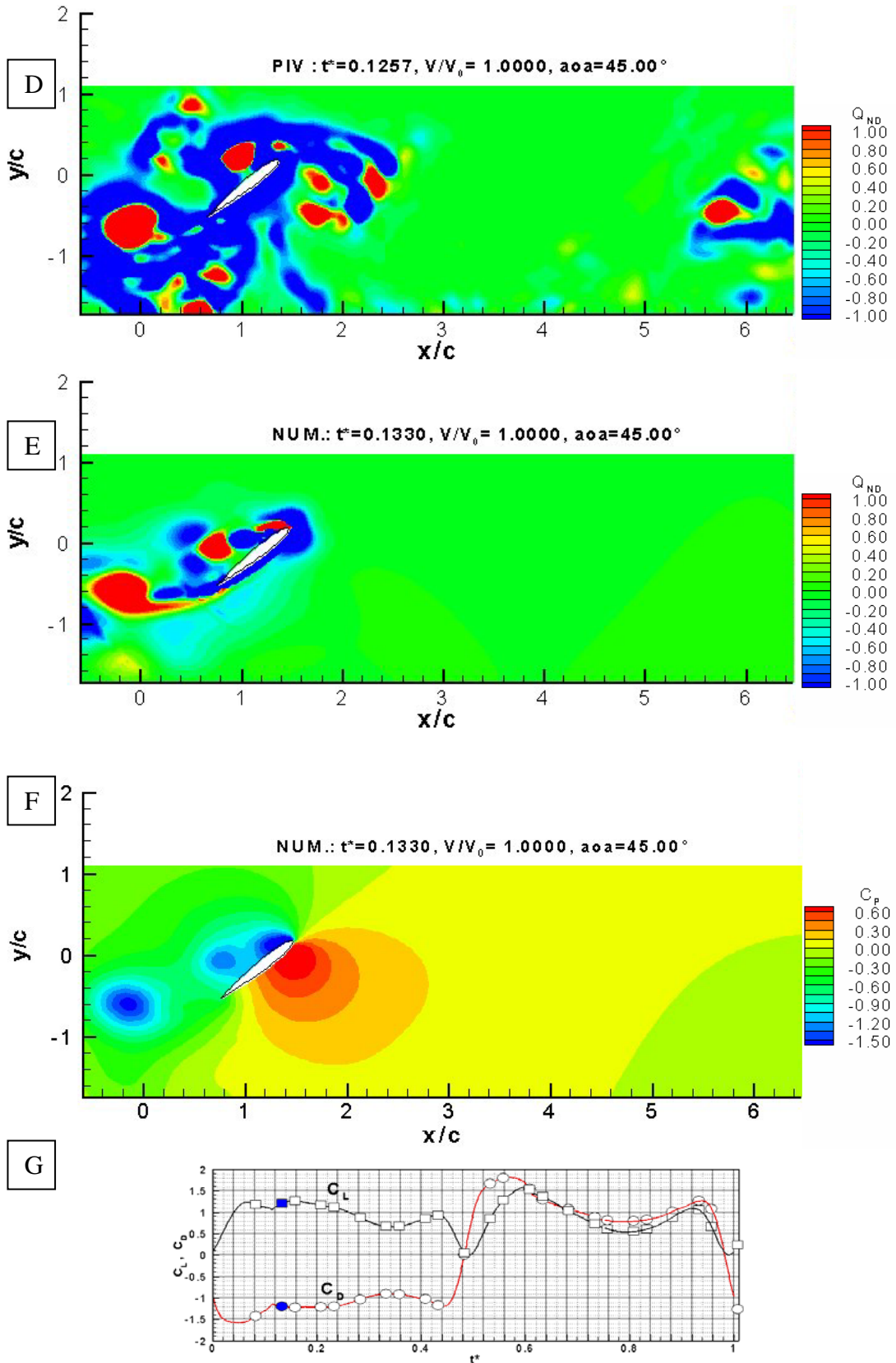
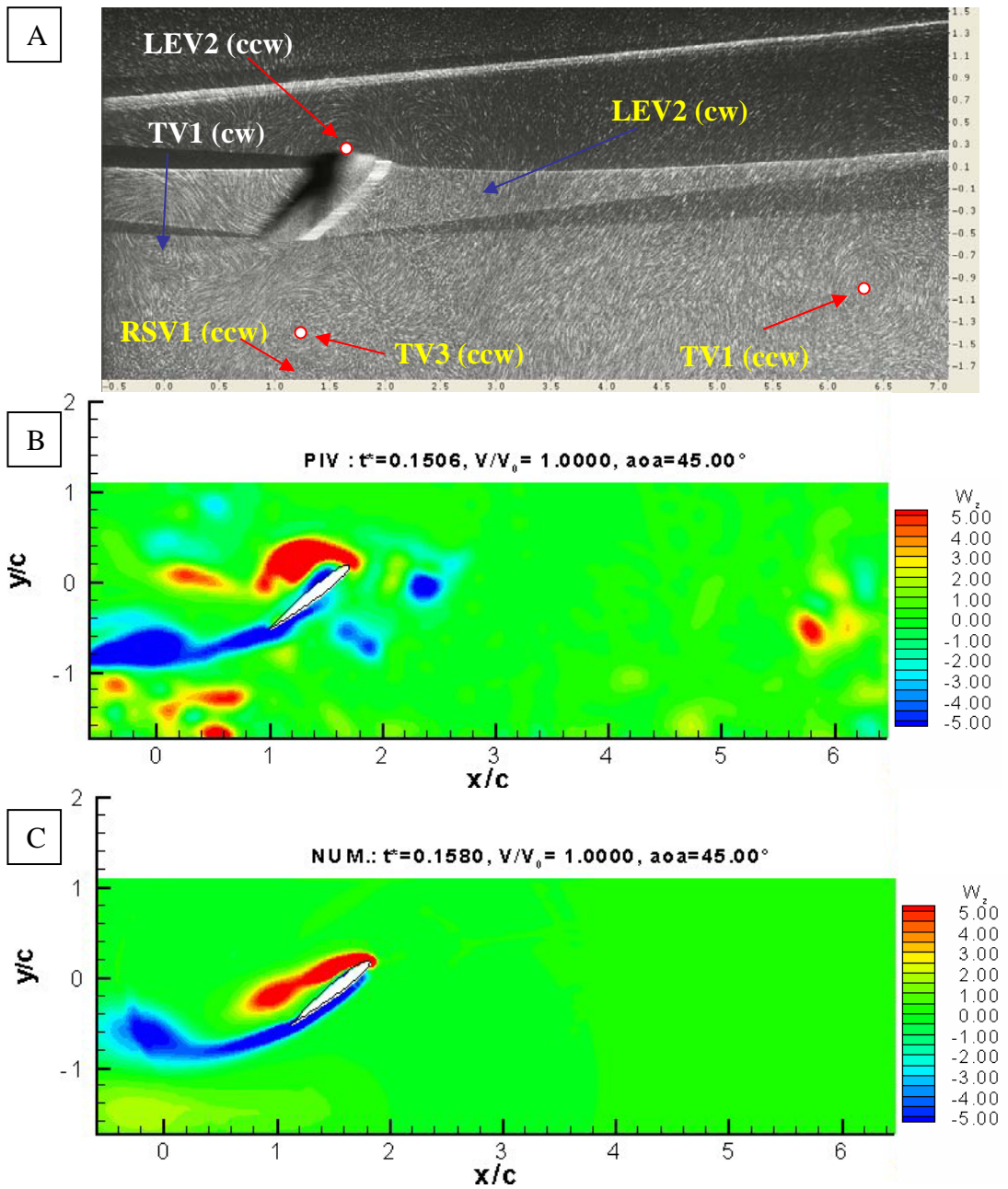


Figure D.2 (continued) Experimental visualization at  $t^*=0.12$ , comparison with the numerical solution and PIV measurements.



**Figure D.3** Experimental visualization at  $t^* = 0.16$ , comparison with the numerical solution and PIV measurements.

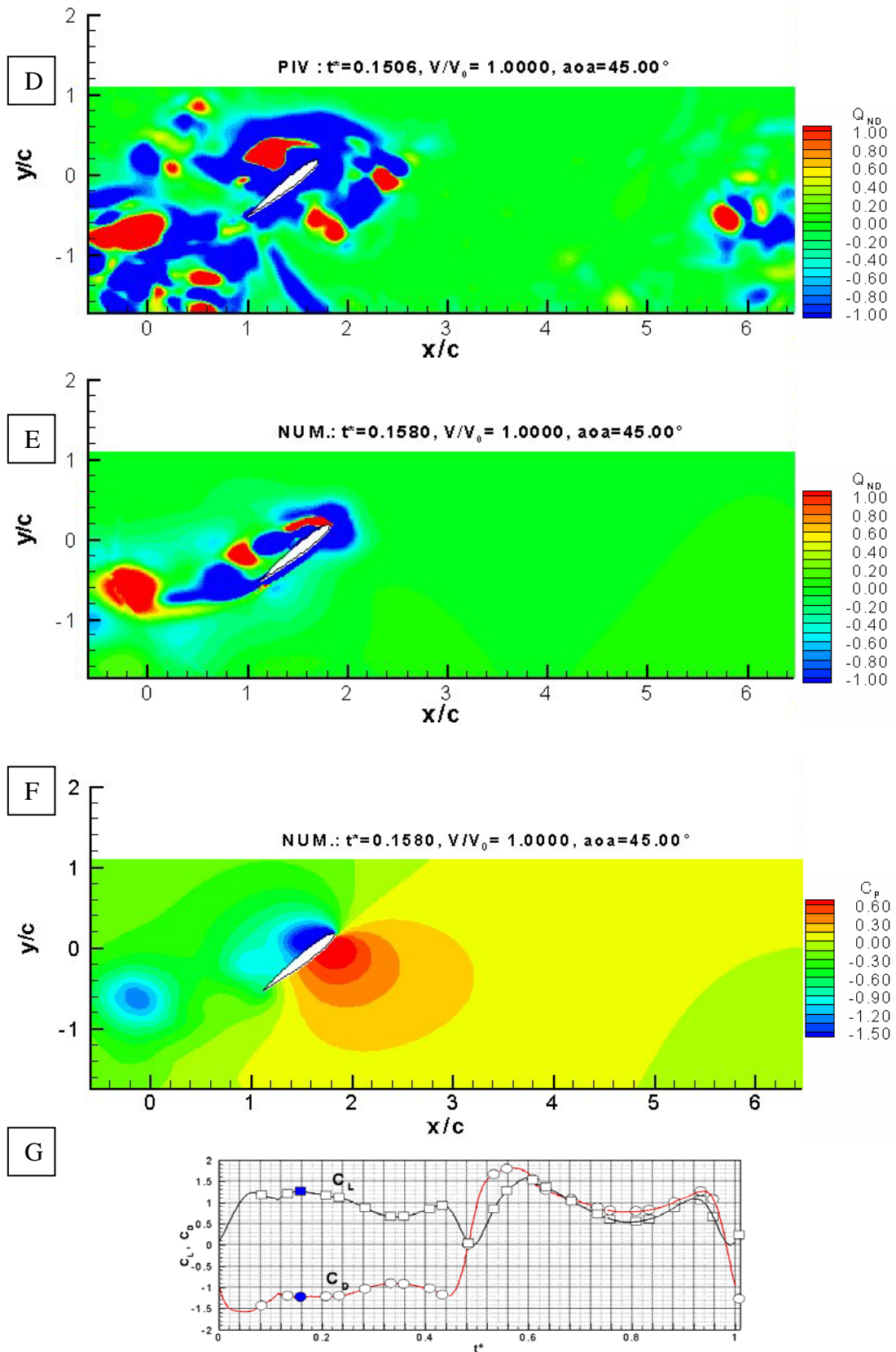
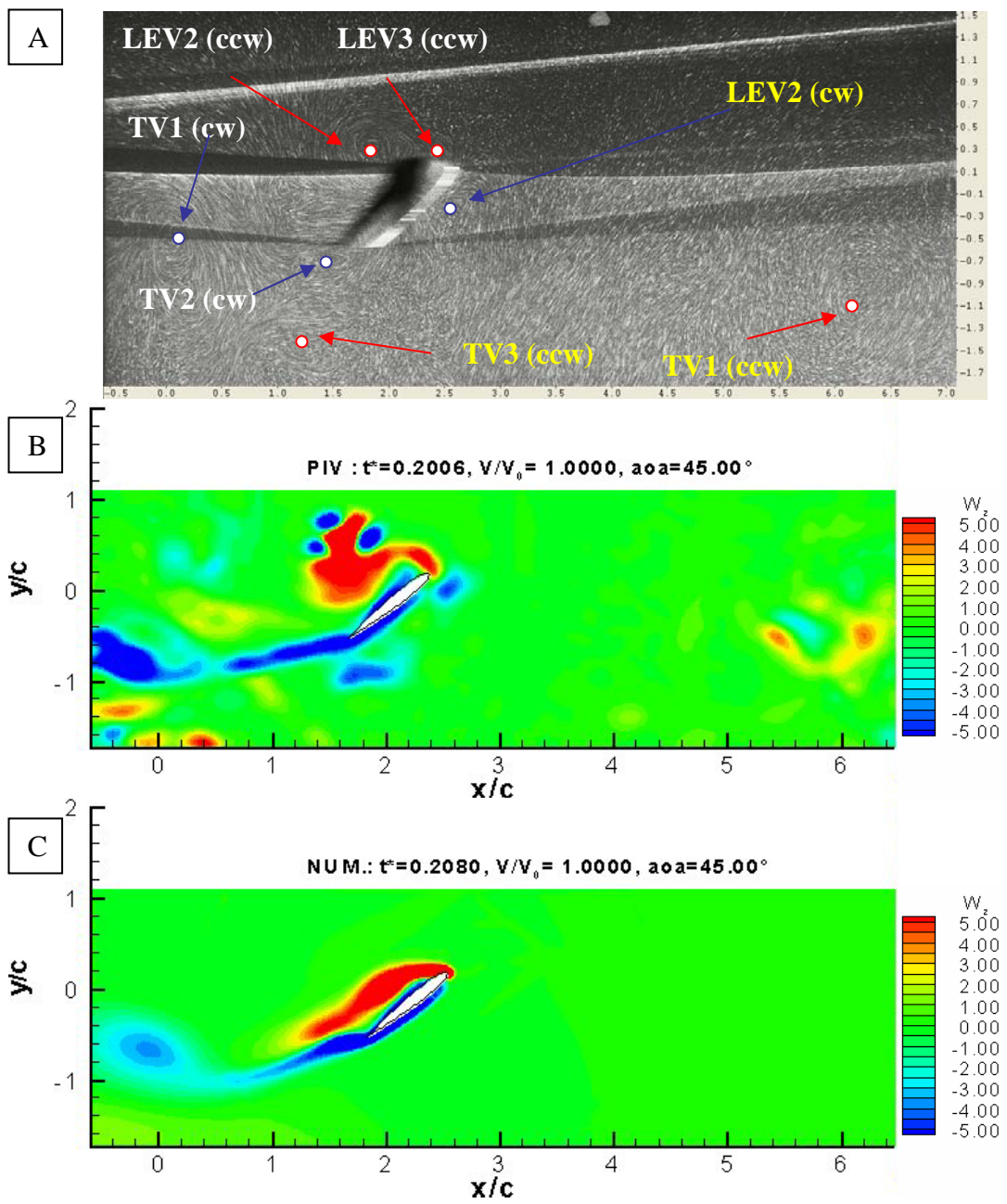
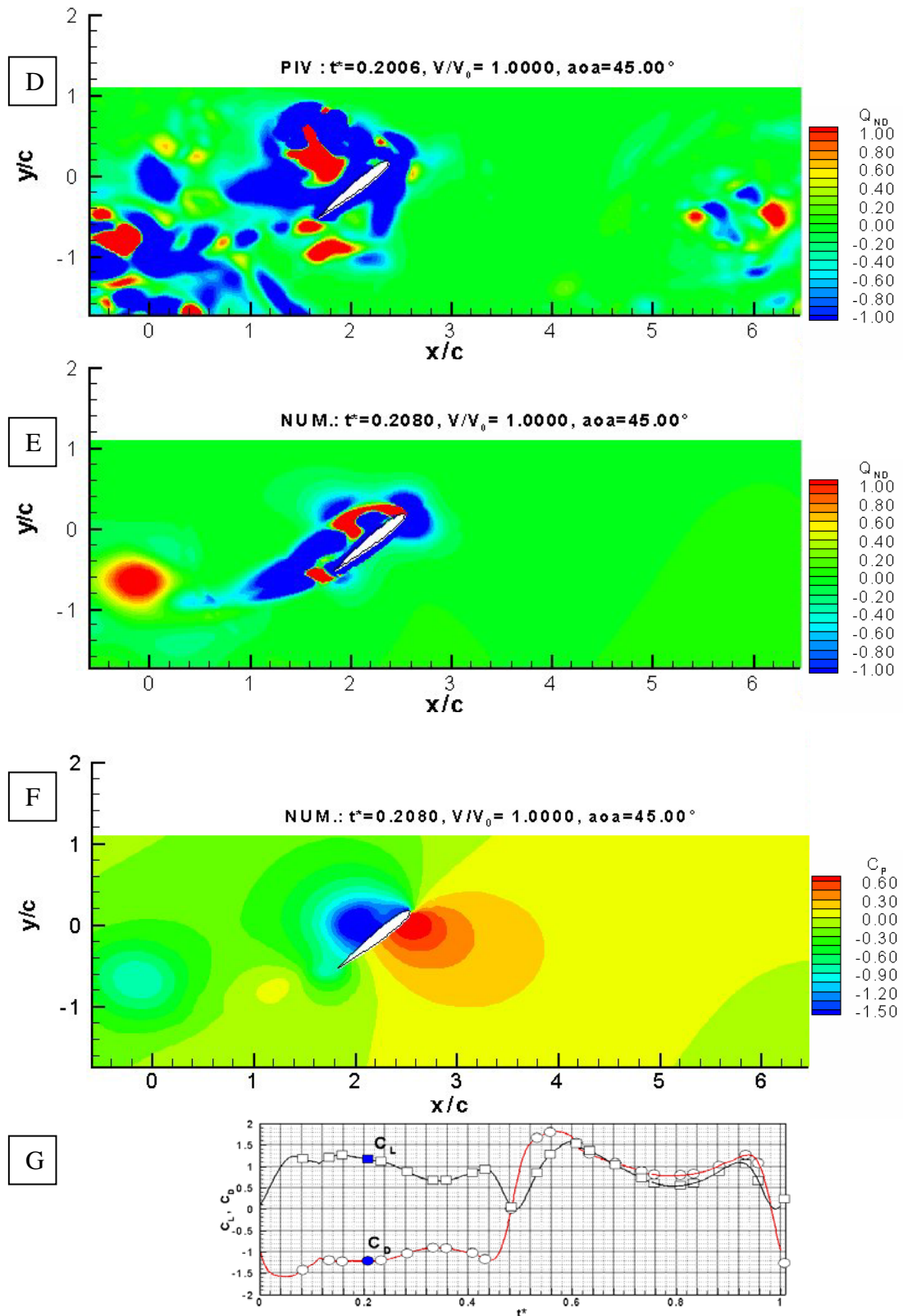


Figure D.3 (continued) Experimental visualization at  $t^*=0.16$ , comparison with the numerical solution and PIV measurements.



**Figure D.4** Experimental visualization at  $t^* = 0.20$ , comparison with the numerical solution and PIV measurements.



**Figure D.4 (continued)** Experimental visualization at  $t^* = 0.20$ , comparison with the numerical solution and PIV measurements.

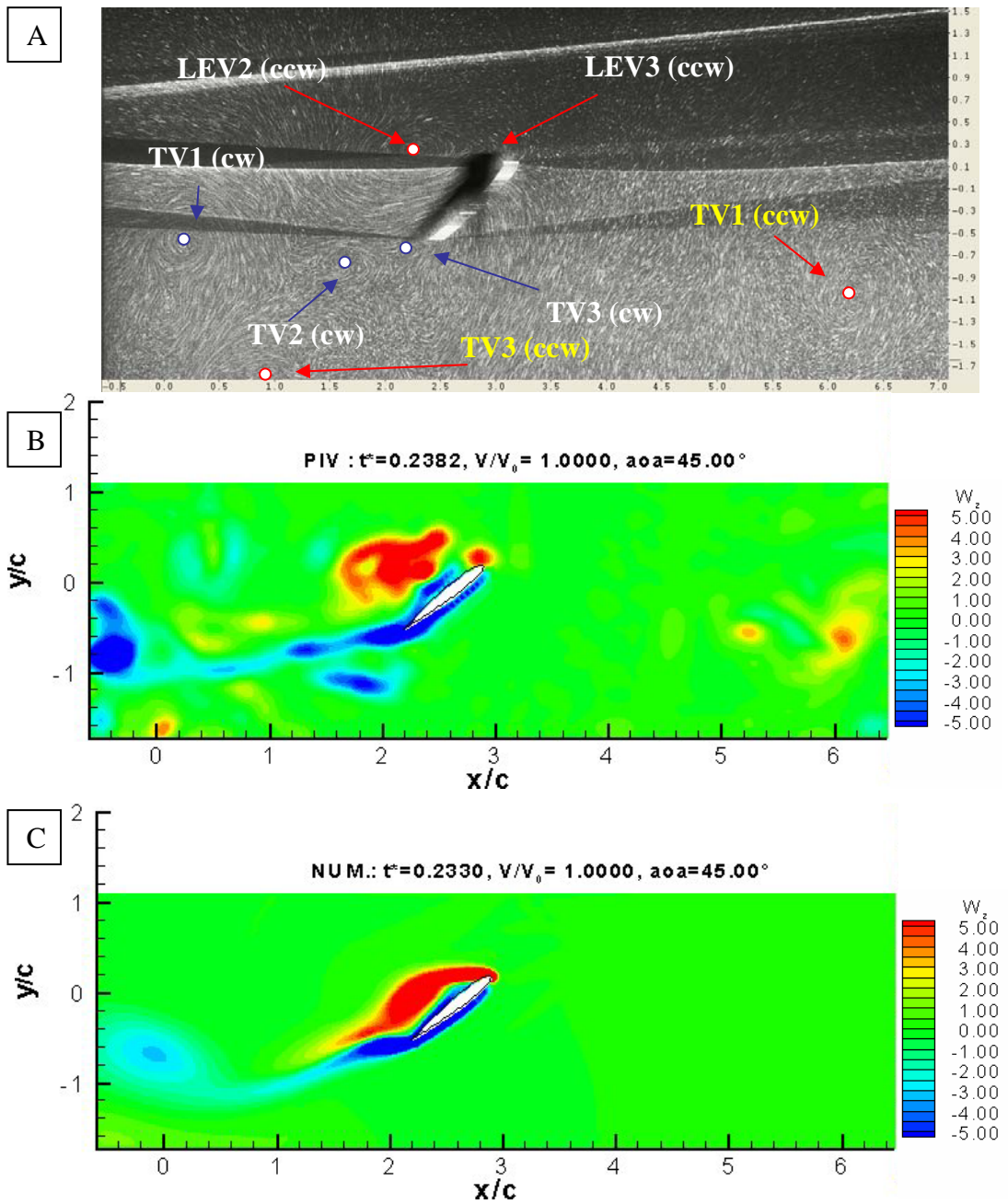


**Figure D.5** Experimental visualization at  $t^* = 0.24$ , comparison with the numerical solution and PIV measurements.



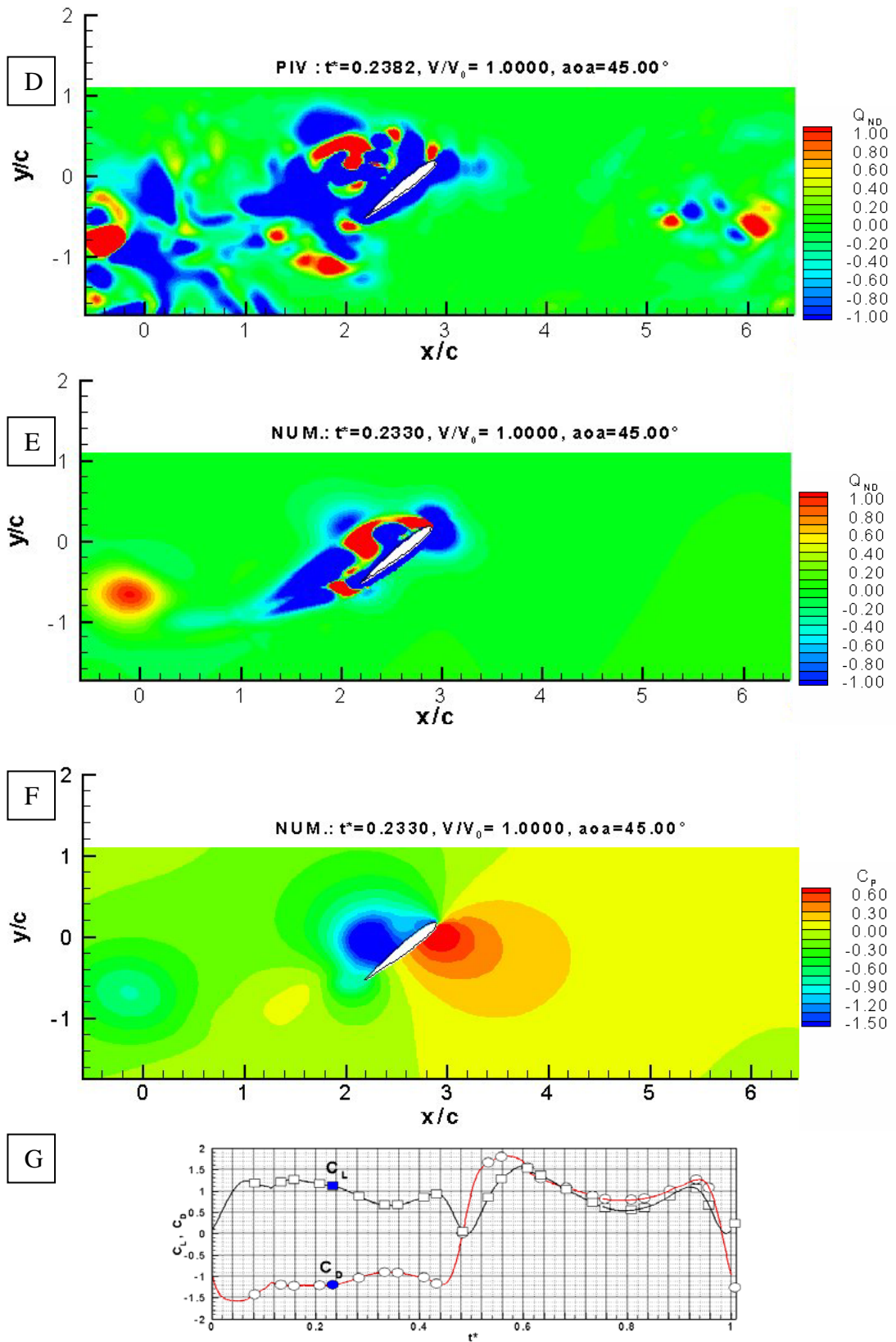


**Figure D.5 (continued)** Experimental visualization at  $t^*=0.24$ , comparison with the numerical solution and PIV measurements.

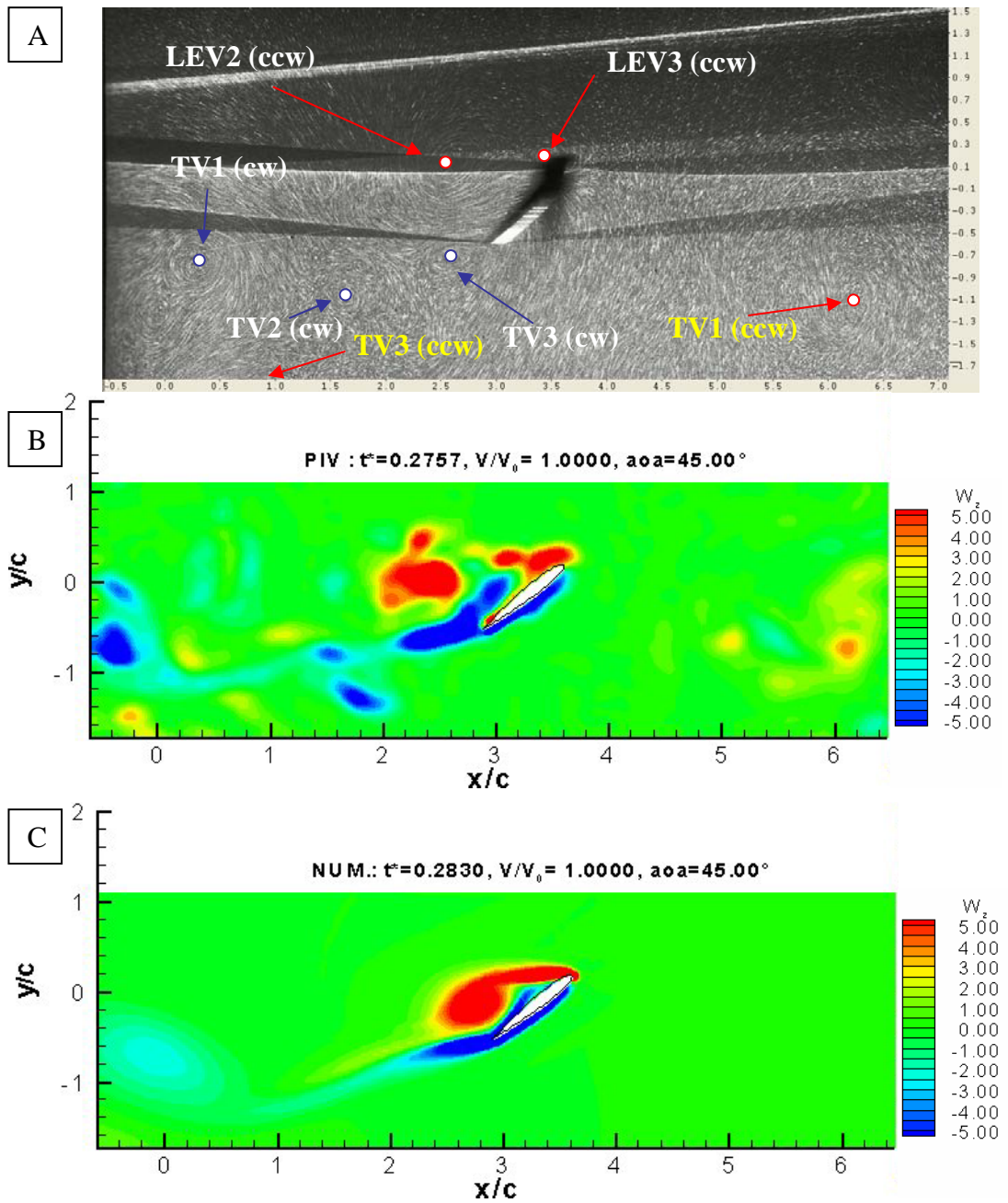


**Figure D.6** Experimental visualization at  $t^*=0.28$ , comparison with the numerical solution and PIV measurements.

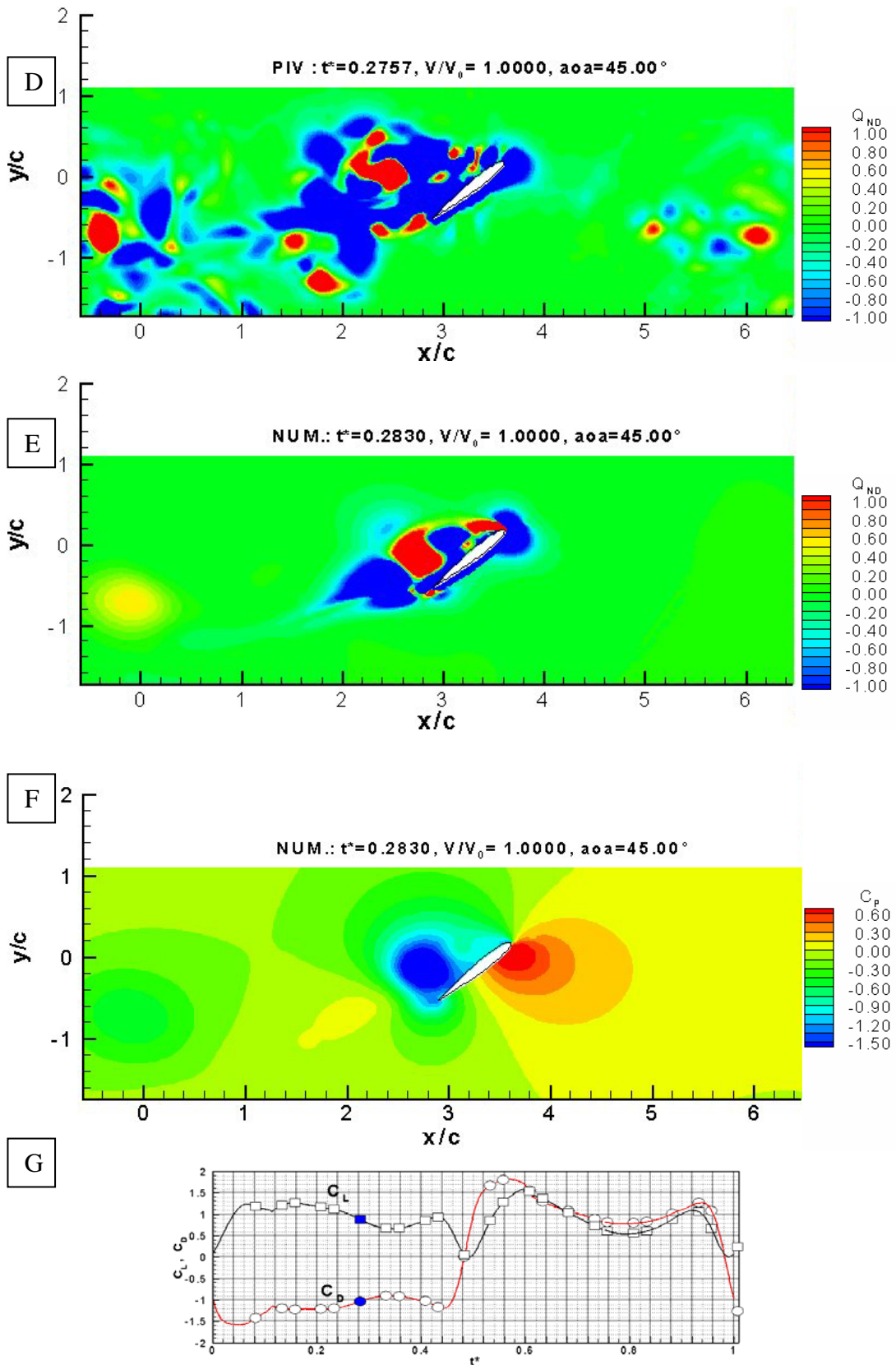


**Figure D.6 (continued)** Experimental visualization at  $t^*=0.28$ , comparison with the numerical solution and PIV measurements.

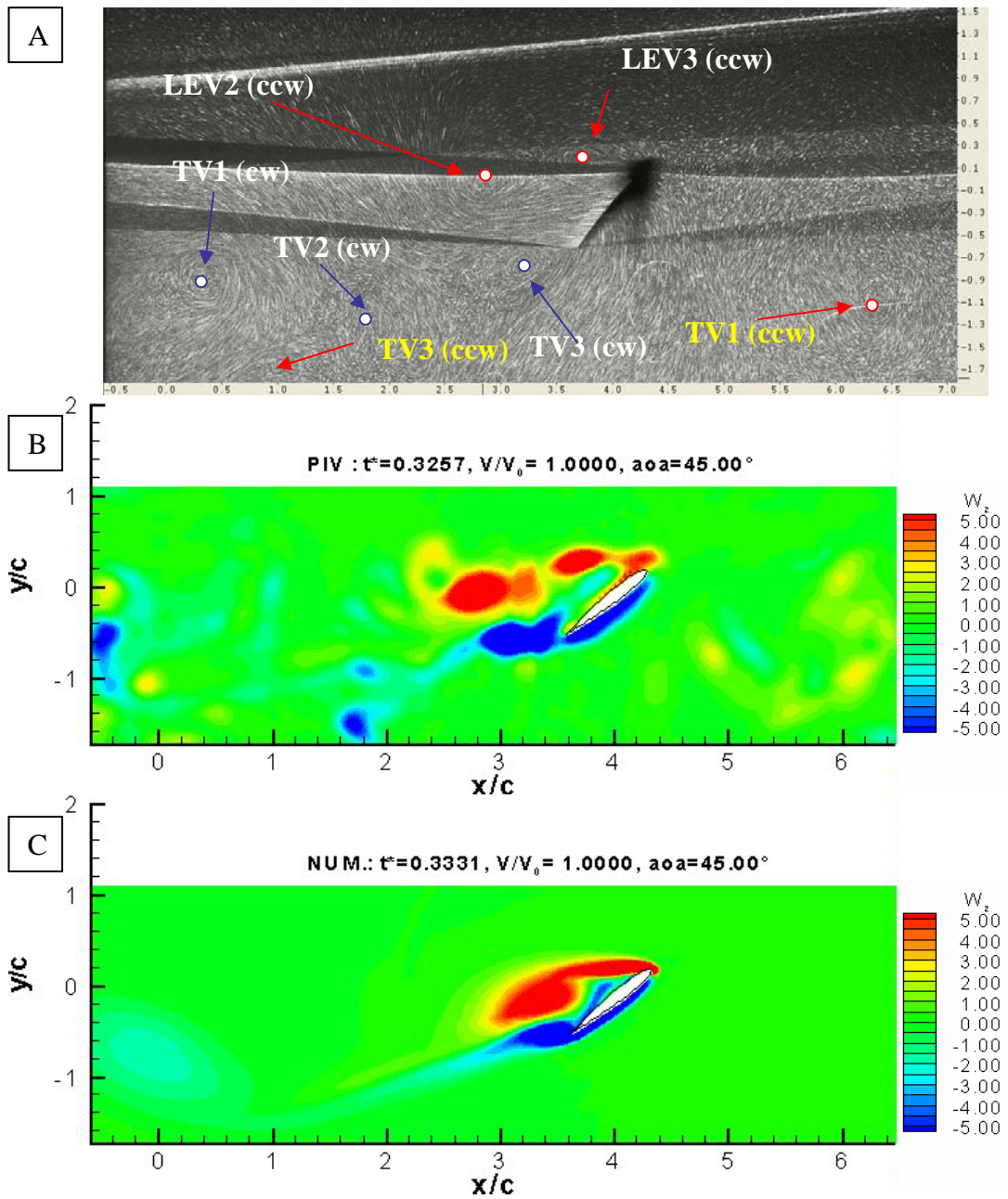


**Figure D.7** Experimental visualization at  $t^*=0.32$ , comparison with the numerical solution and PIV measurements.

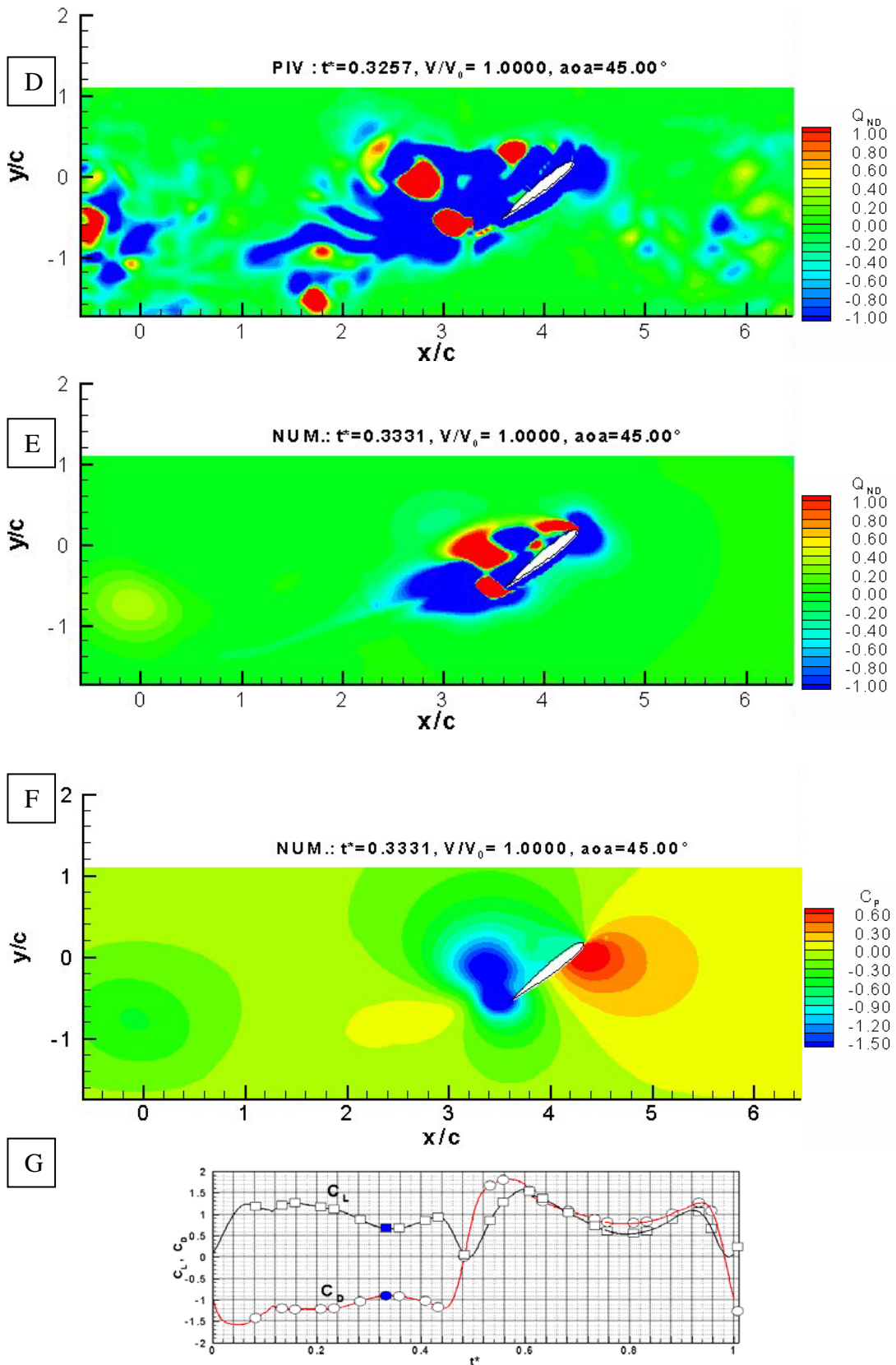


**Figure D.7 (continued)** Experimental visualization at  $t^* = 0.32$ , comparison with the numerical solution and PIV measurements.

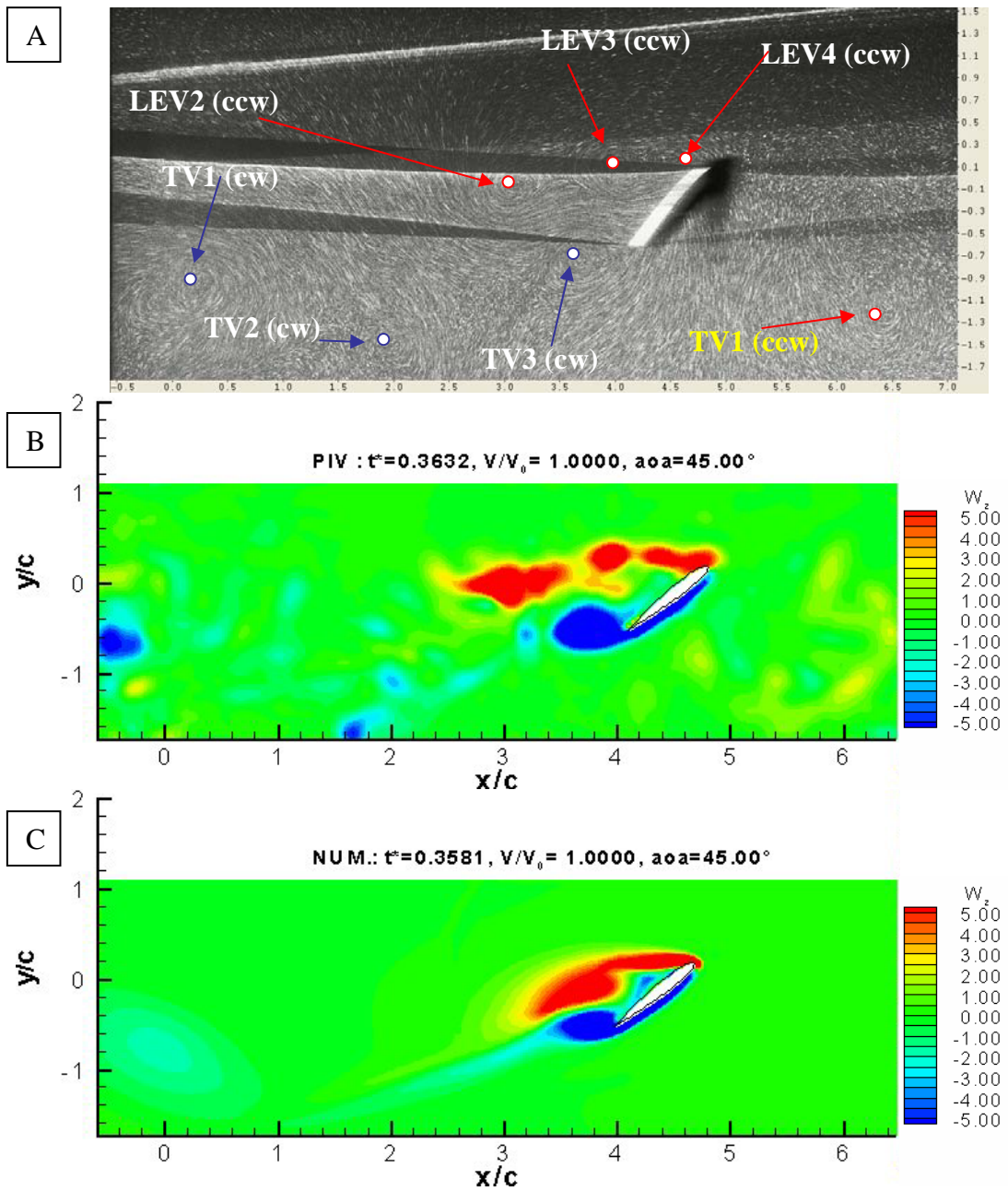


**Figure D.8** Experimental visualization at  $t^*=0.36$ , comparison with the numerical solution and PIV measurements.

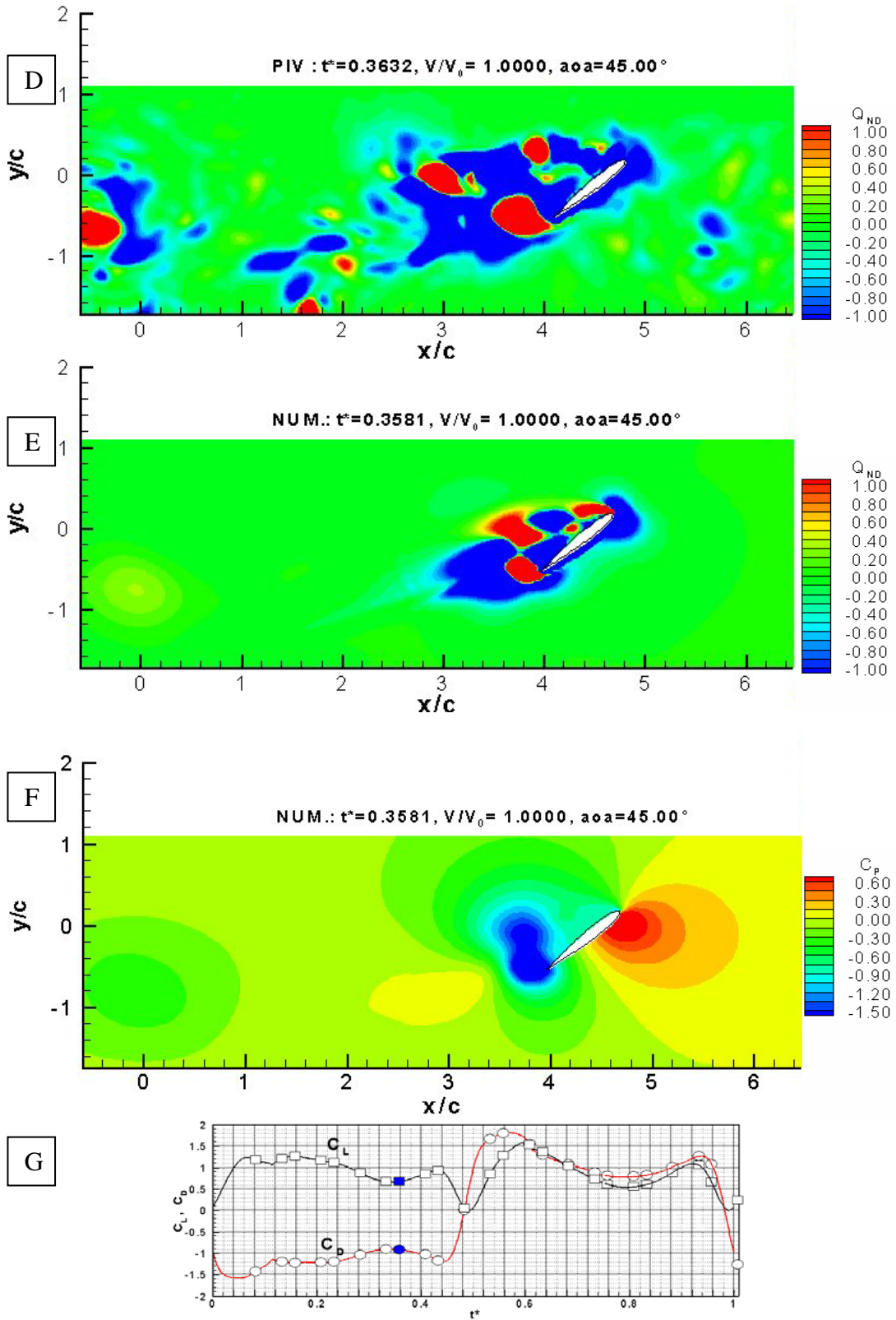


**Figure D.8 (continued)** Experimental visualization at  $t^* = 0.36$ , comparison with the numerical solution and PIV measurements.

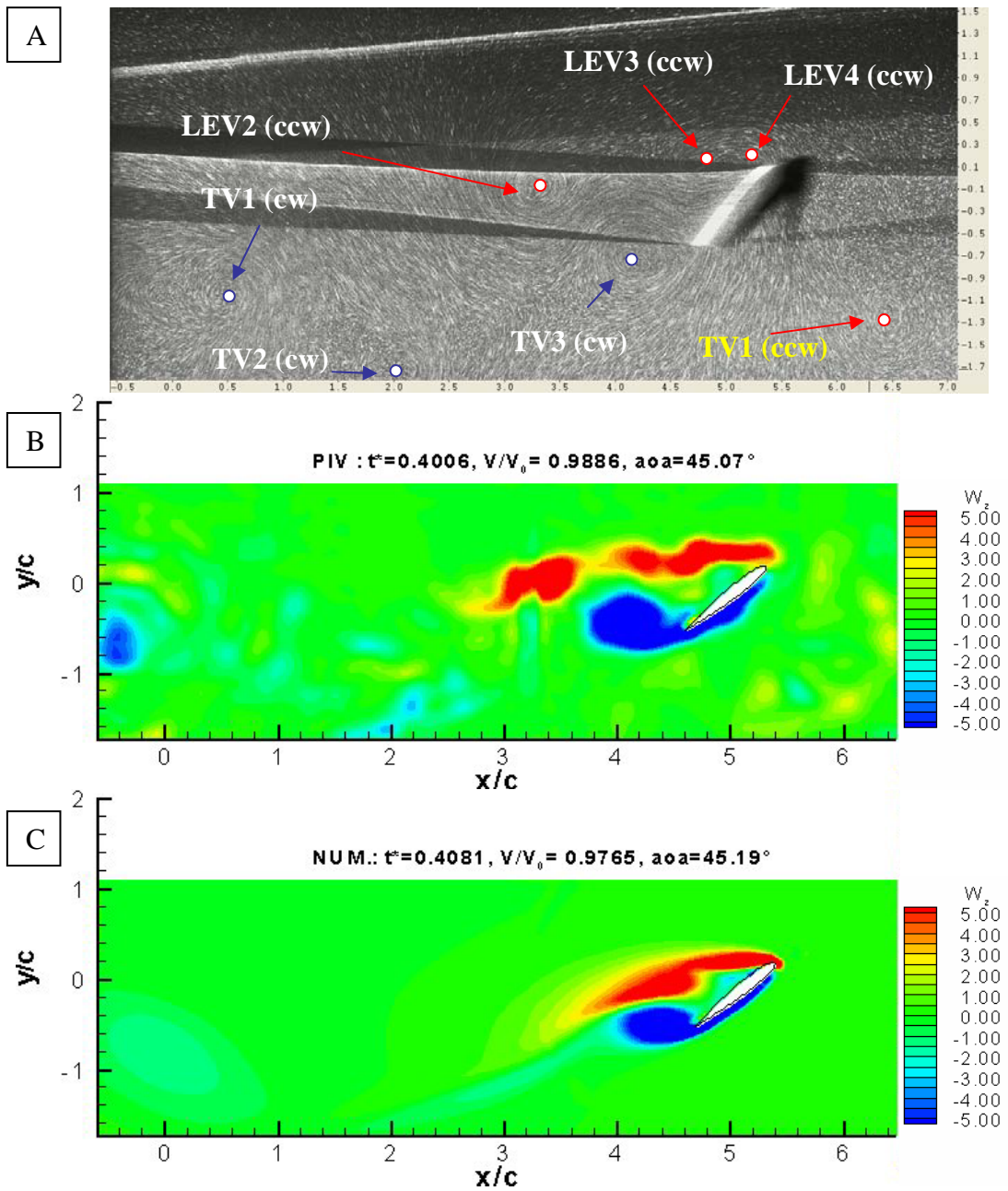


**Figure D.9** Experimental visualization at  $t^*=0.40$ , comparison with the numerical solution and PIV measurements.



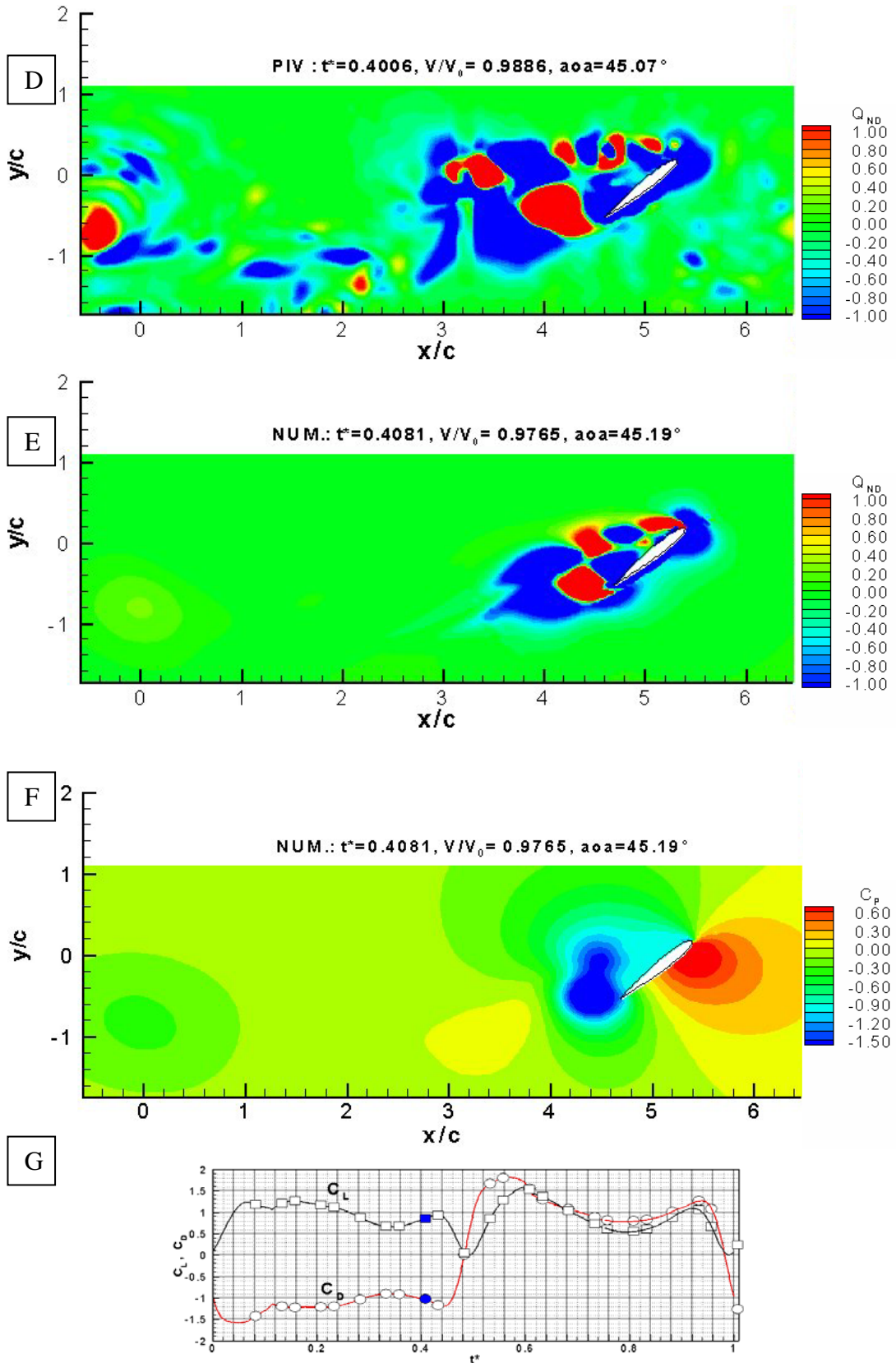


**Figure D.9 (continued)** Experimental visualization at  $t^* = 0.40$ , comparison with the numerical solution and PIV measurements.

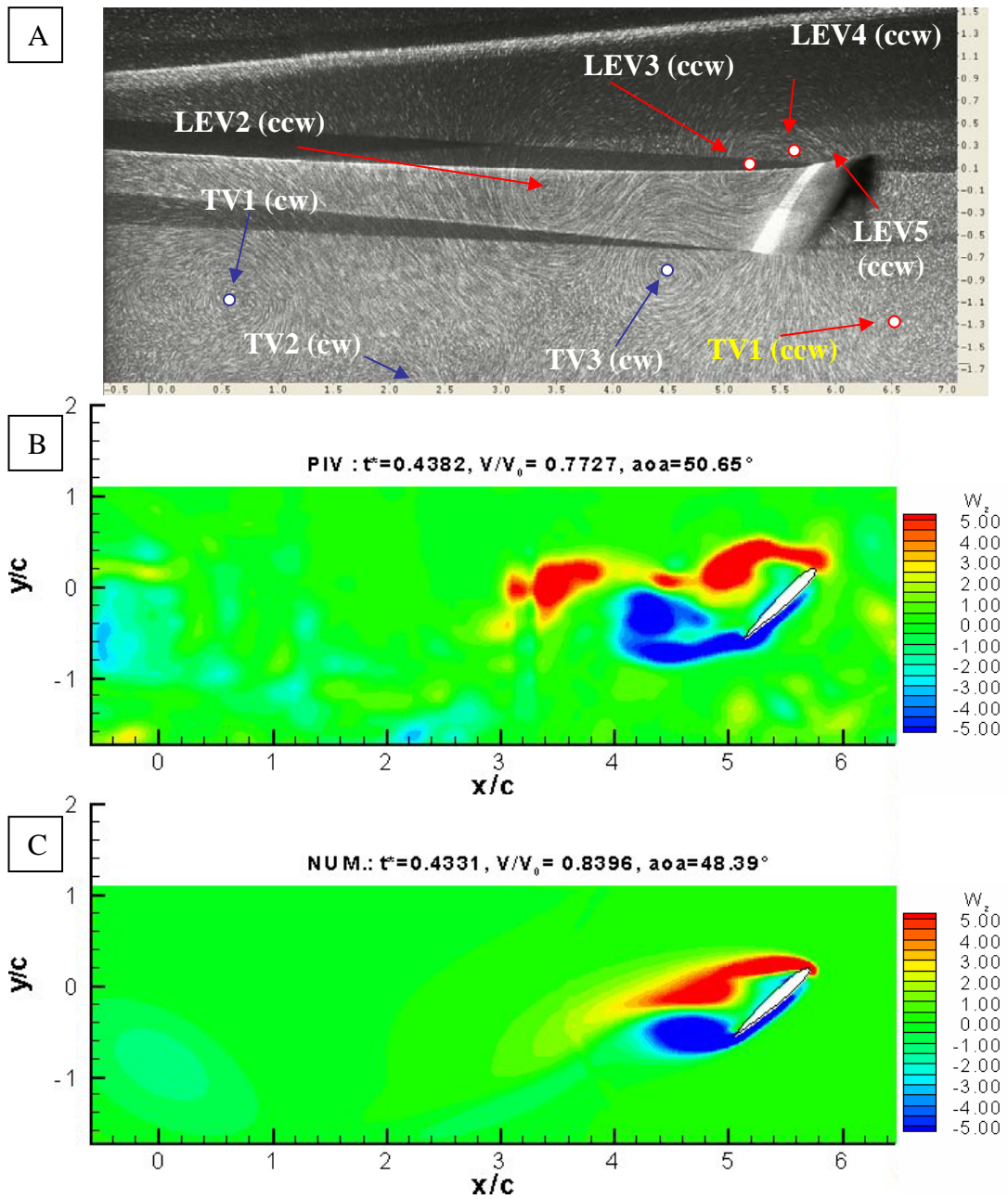


**Figure D.10** Experimental visualization at  $t^*=0.44$ , comparison with the numerical solution and PIV measurements.

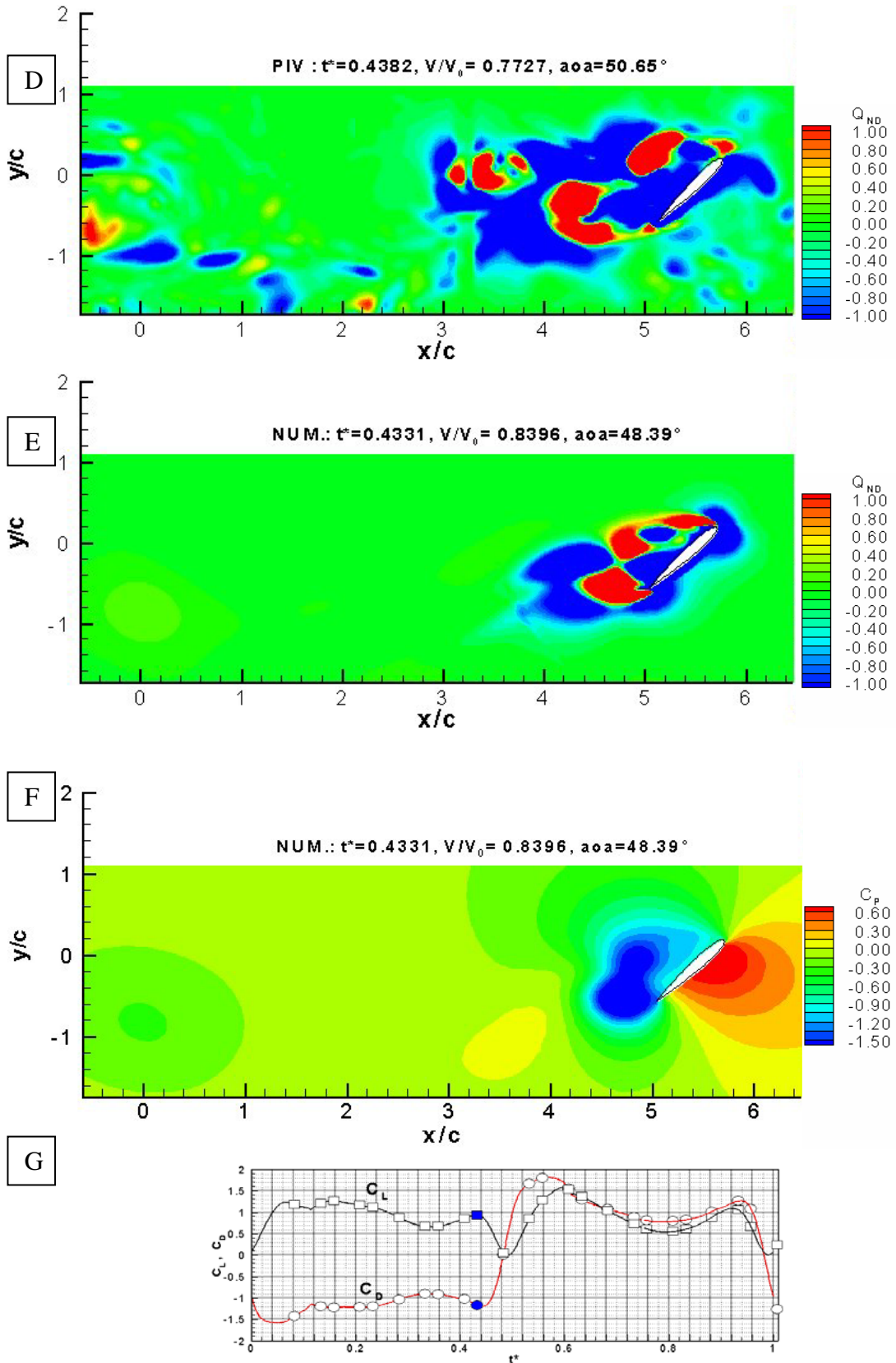


**Figure D.10 (continued)** Experimental visualization at  $t^* = 0.44$ , comparison with the numerical solution and PIV measurements.

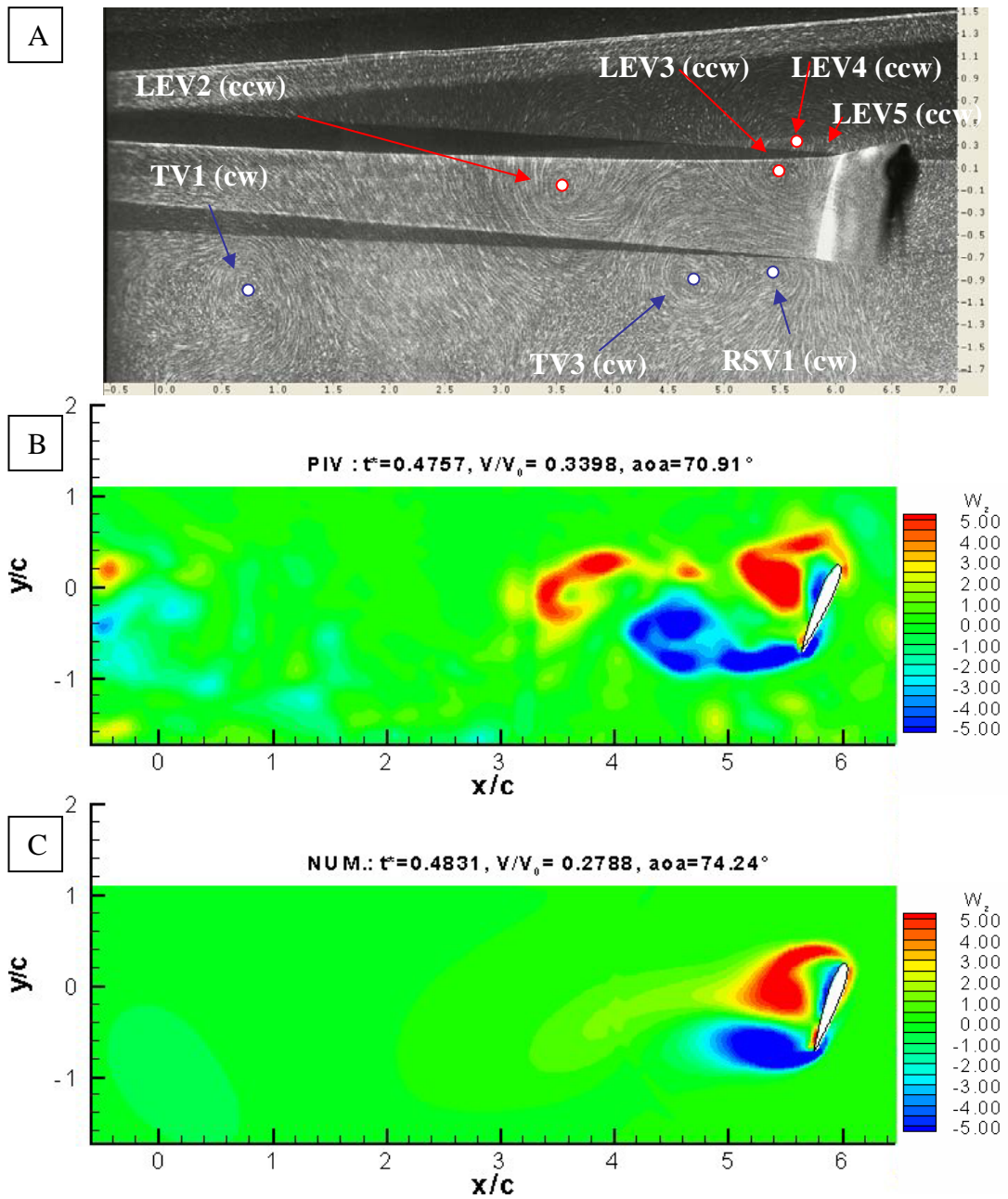


**Figure D.11** Experimental visualization at  $t^*=0.48$ , comparison with the numerical solution and PIV measurements.

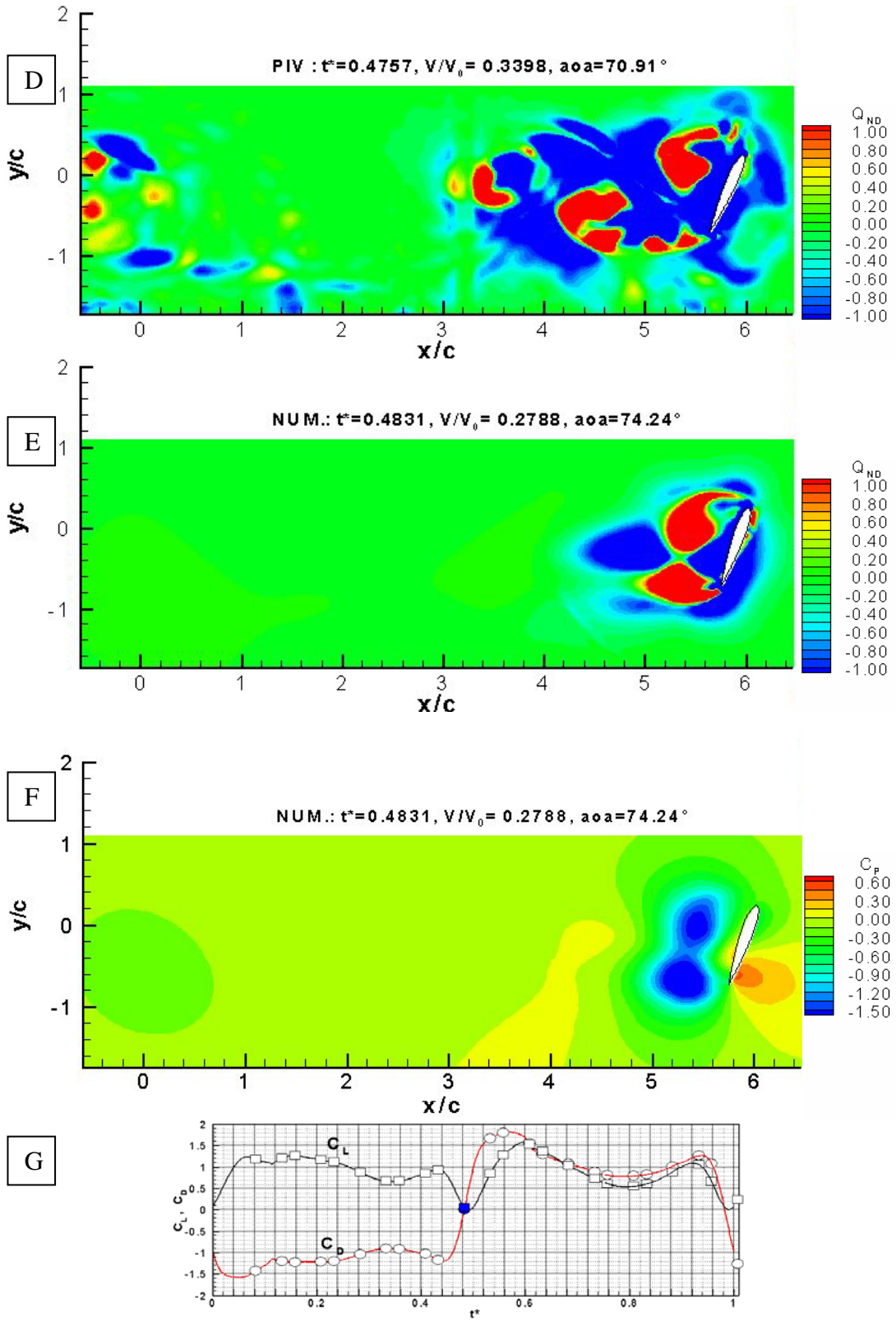


**Figure D.11 (continued)** Experimental visualization at  $t^*=0.48$ , comparison with the numerical solution and PIV measurements.

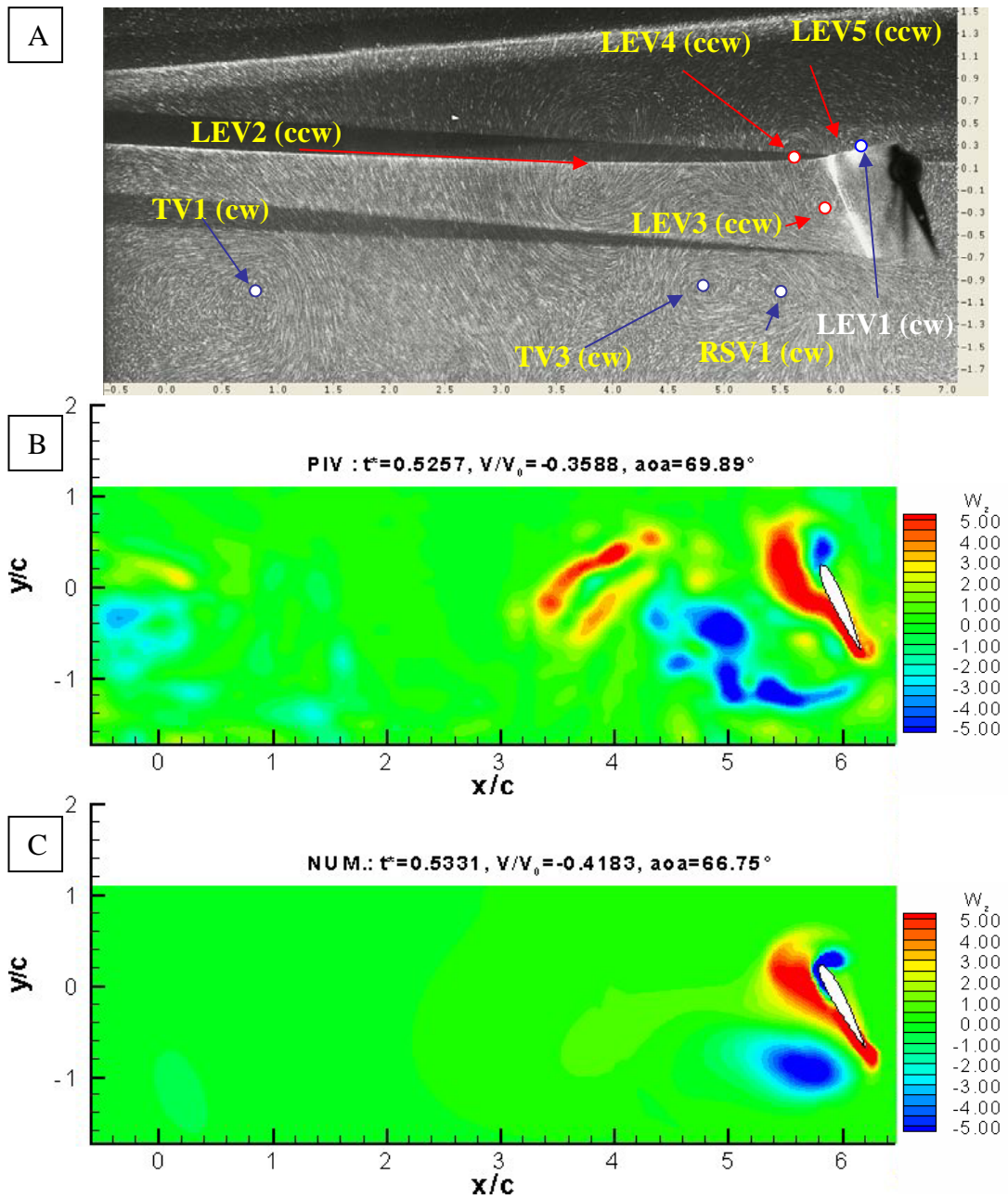


**Figure D.12** Experimental visualization at  $t^*=0.52$ , comparison with the numerical solution and PIV measurements.

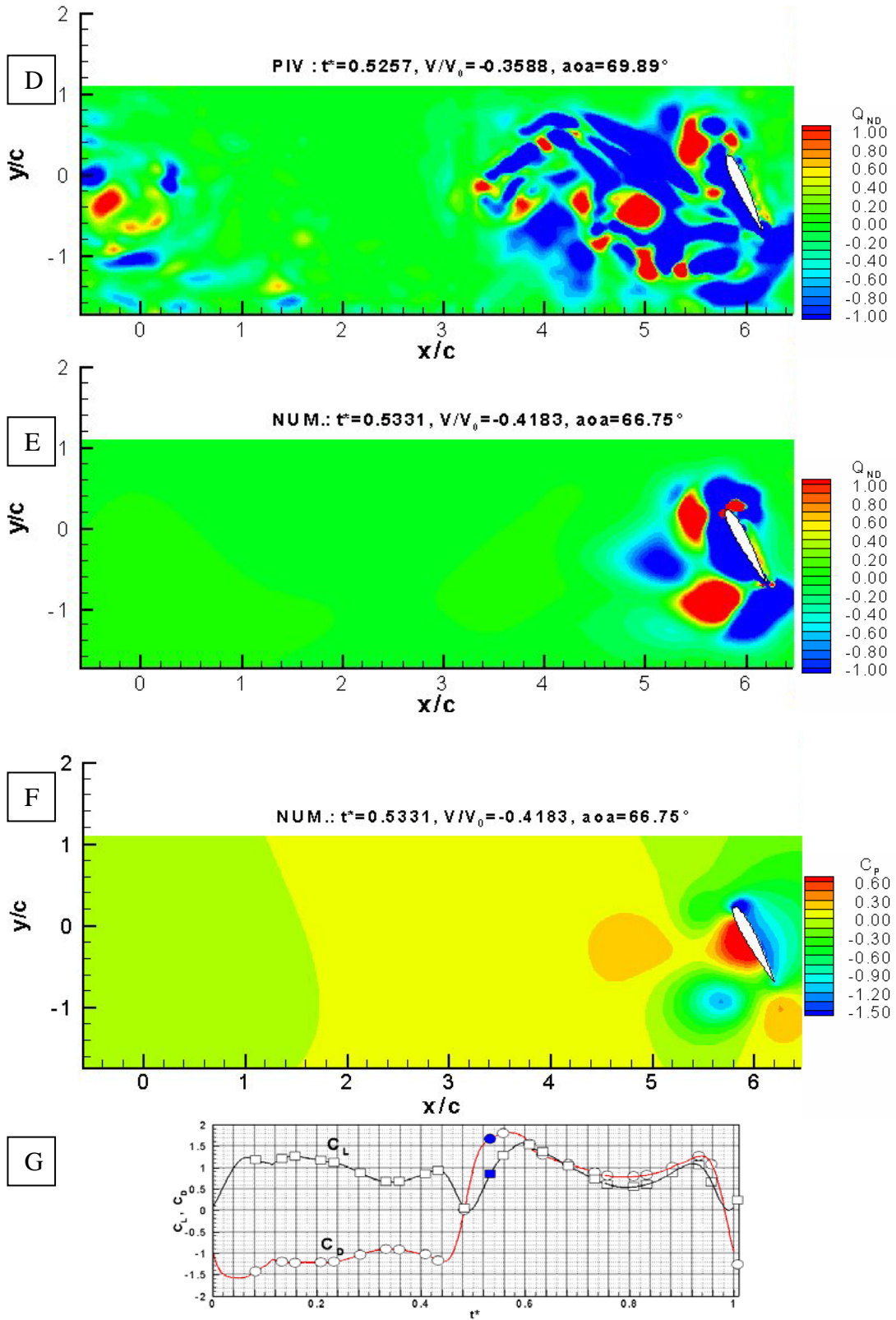


**Figure D.12 (continued)** Experimental visualization at  $t^*=0.52$ , comparison with the numerical solution and PIV measurements.

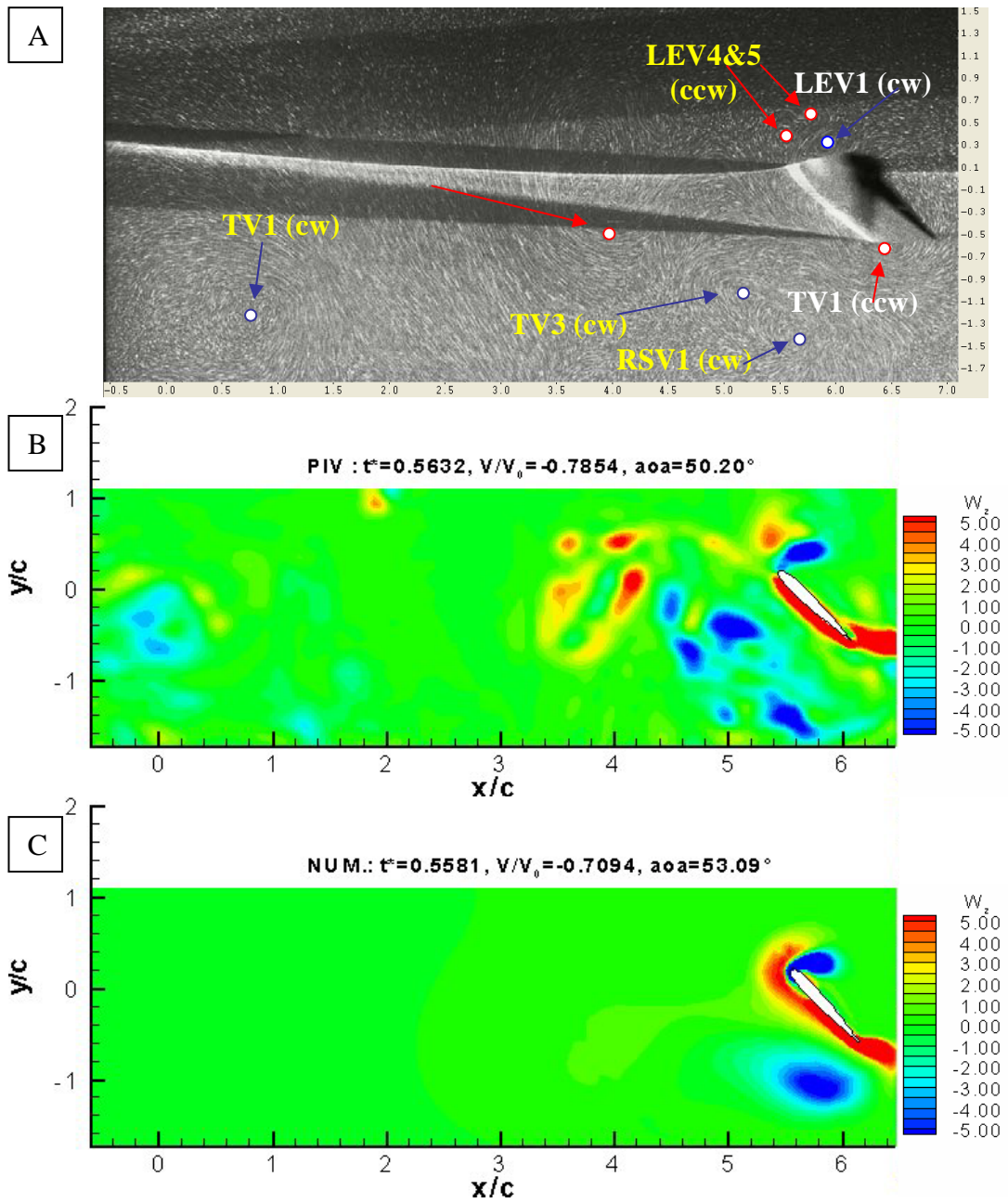


**Figure D.13** Experimental visualization at  $t^*=0.56$ , comparison with the numerical solution and PIV measurements.



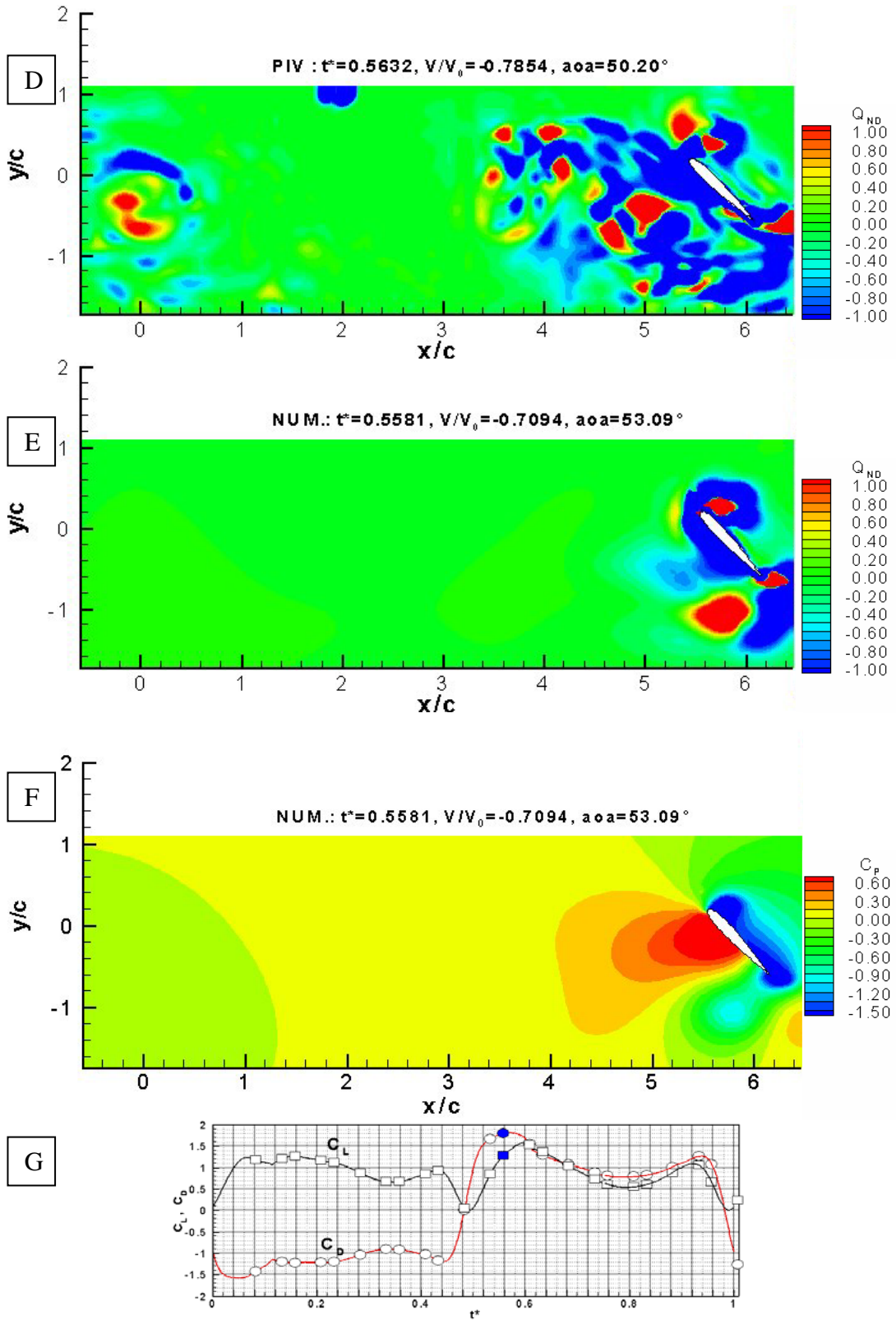
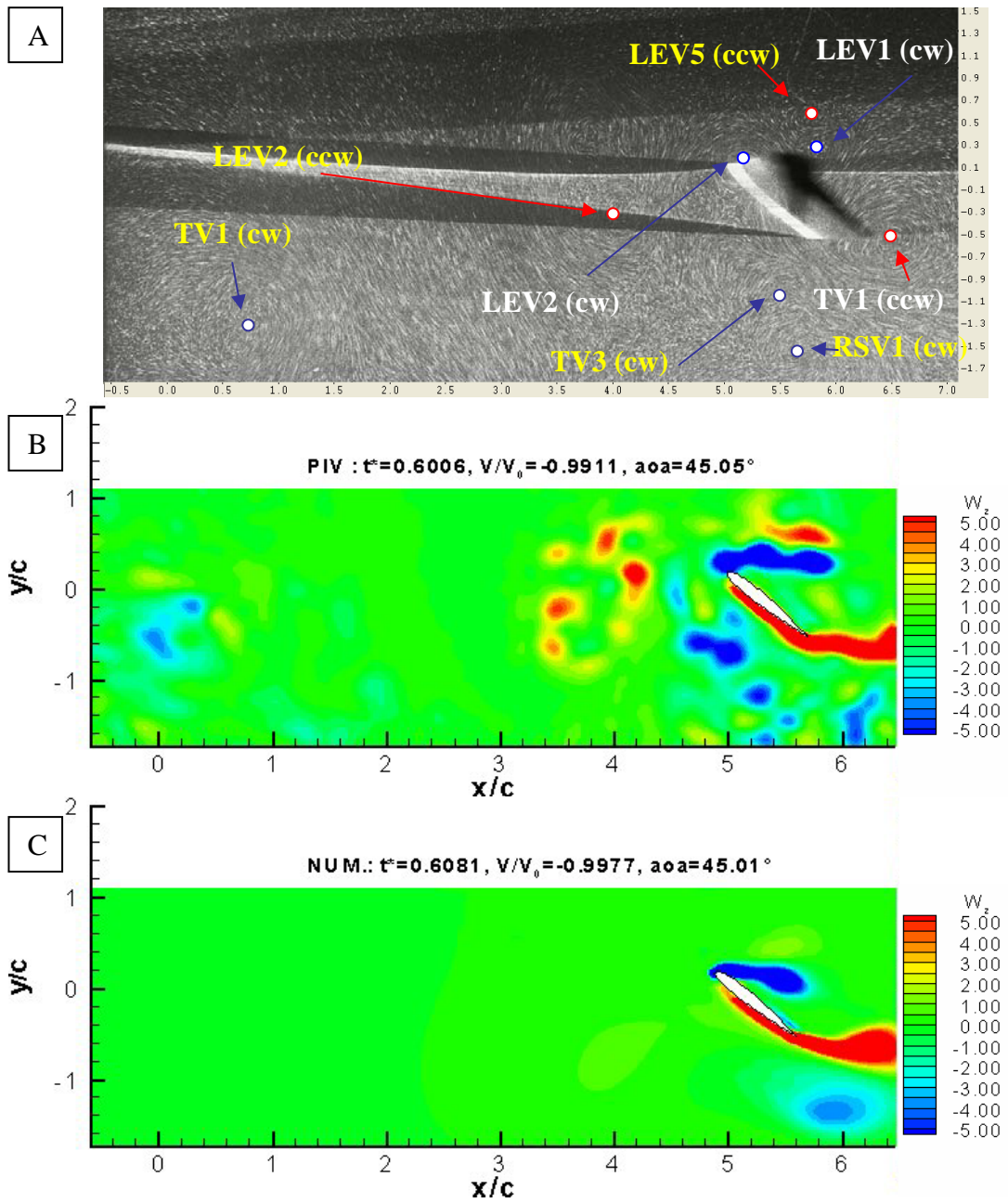
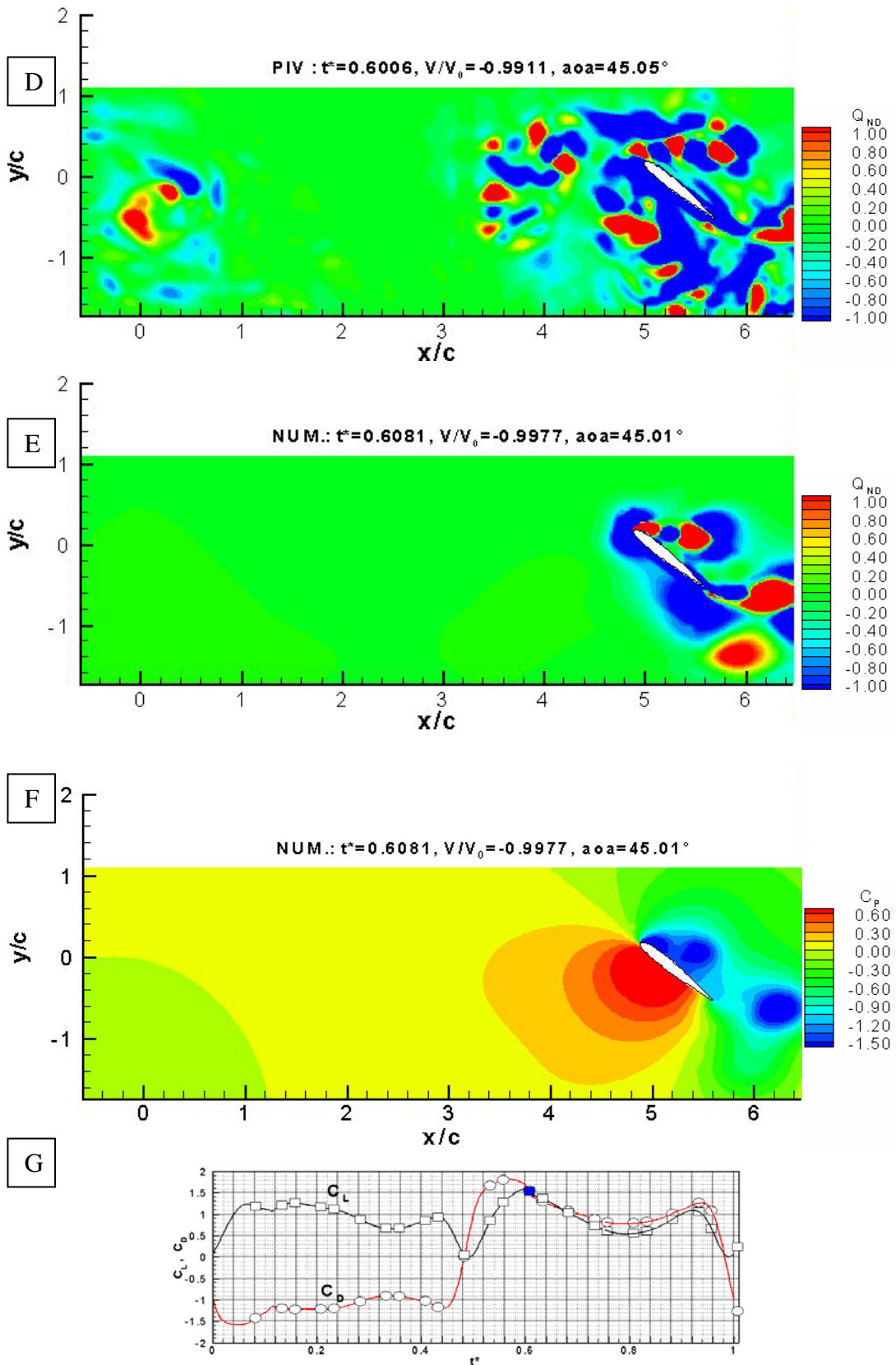


Figure D.13 (continued) Experimental visualization at  $t^*=0.56$ , comparison with the numerical solution and PIV measurements.



**Figure D.14** Experimental visualization at  $t^* = 0.60$ , comparison with the numerical solution and PIV measurements.



**Figure D.14 (continued)** Experimental visualization at  $t^*=0.60$ , comparison with the numerical solution and PIV measurements.

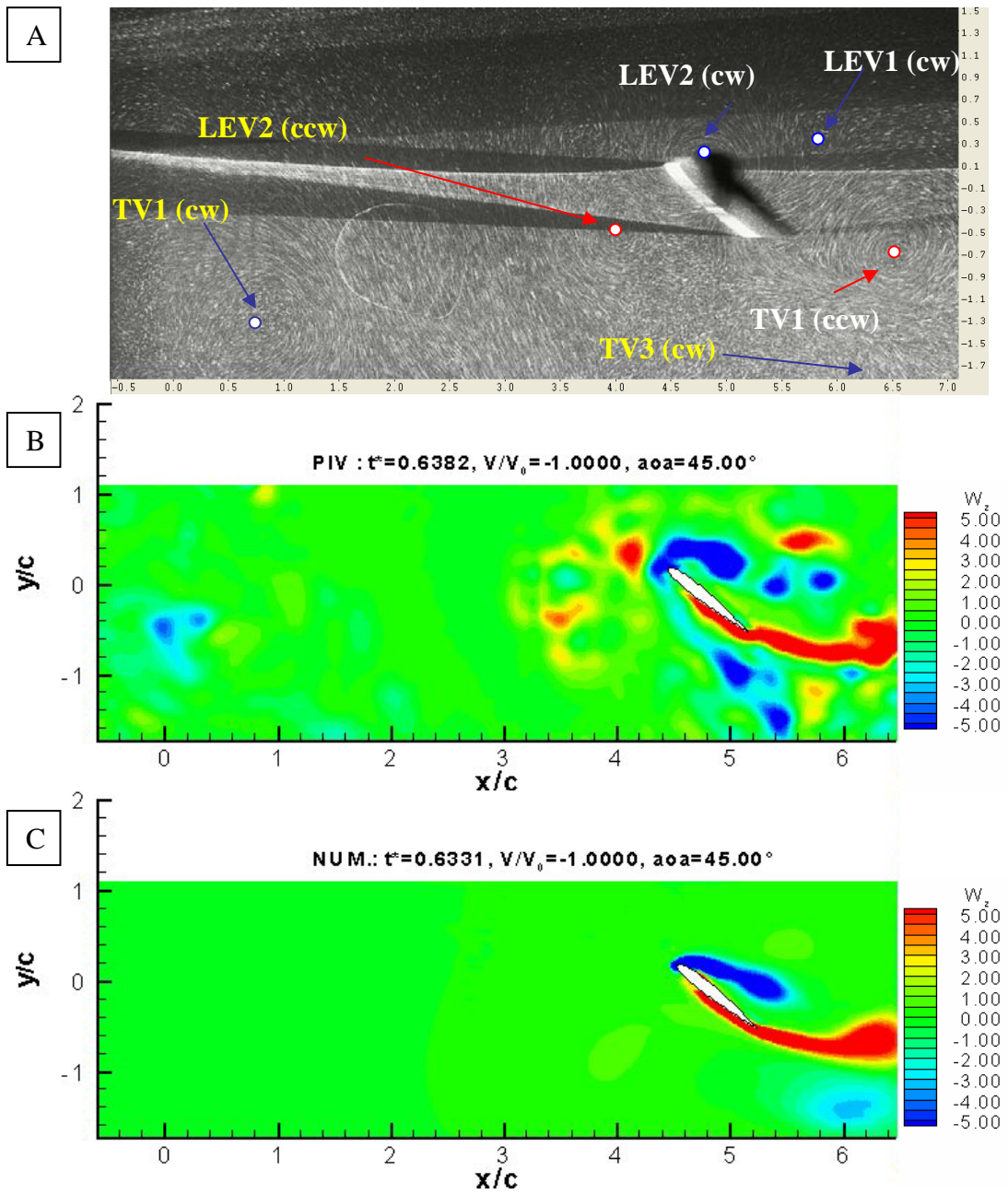


**Figure D.15** Experimental visualization at  $t^*=0.64$ , comparison with the numerical solution and PIV measurements.

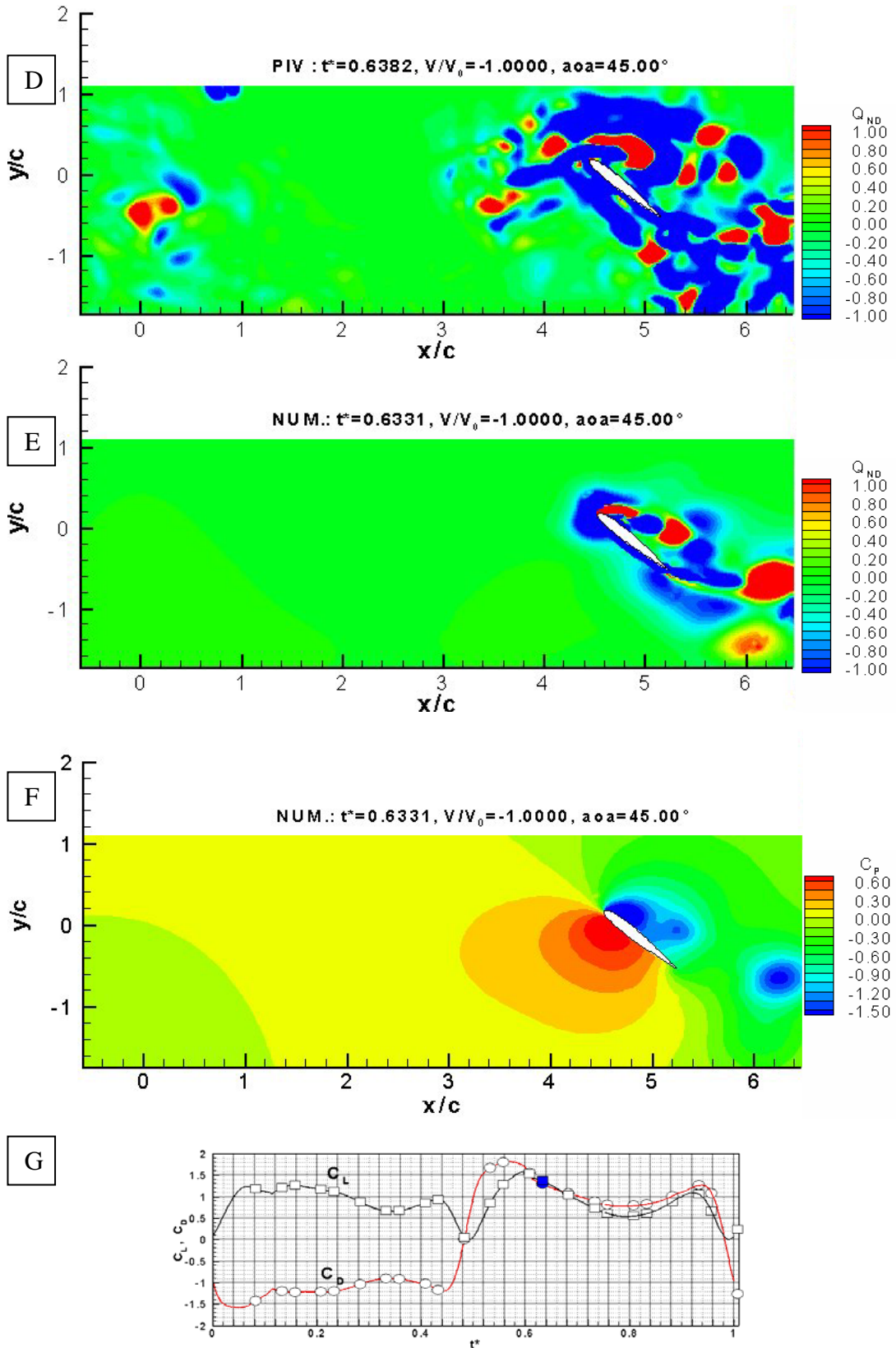


**Figure D.15 (continued)** Experimental visualization at  $t^* = 0.64$ , comparison with the numerical solution and PIV measurements.

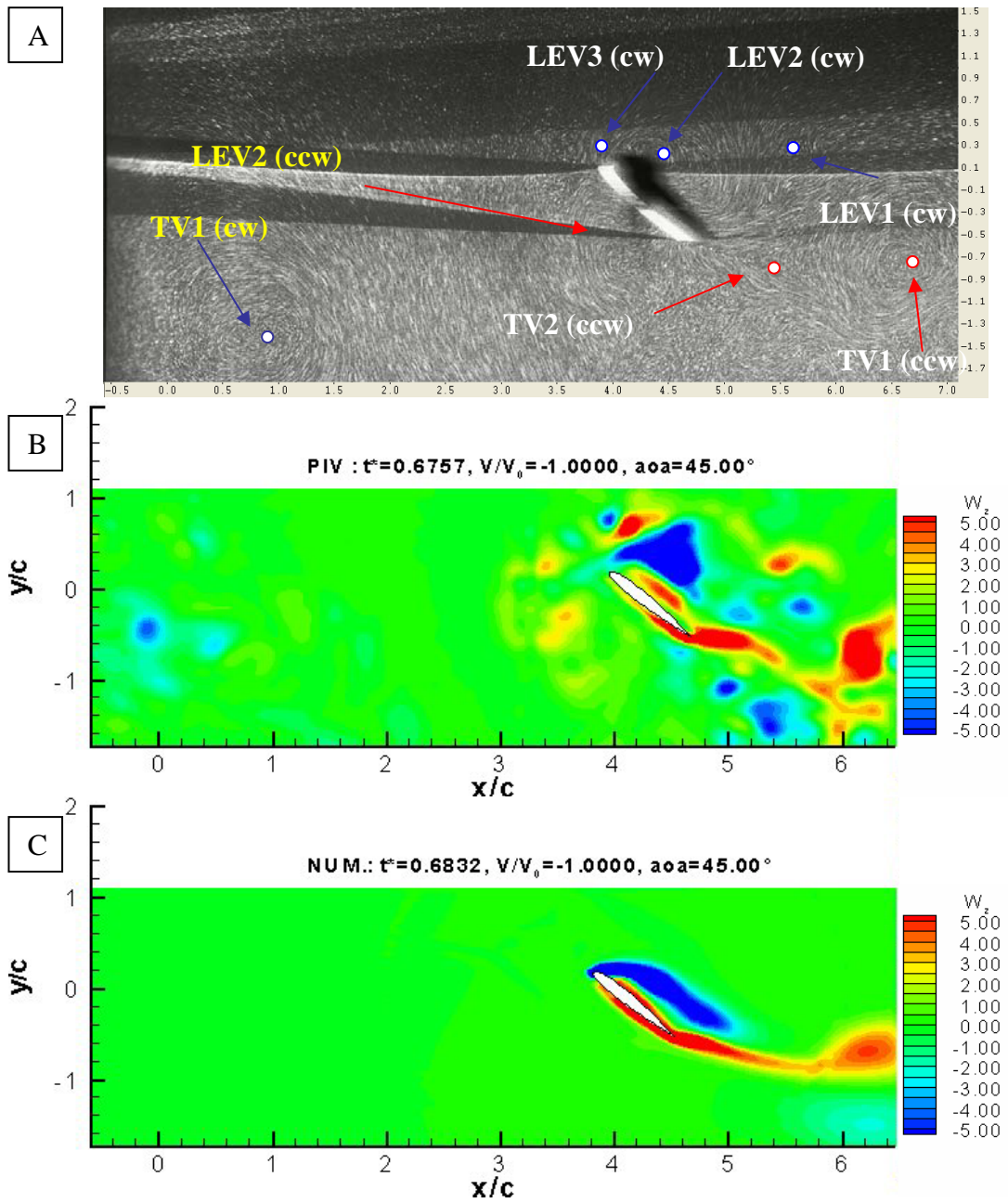


**Figure D.16** Experimental visualization at  $t^*=0.68$ , comparison with the numerical solution and PIV measurements.

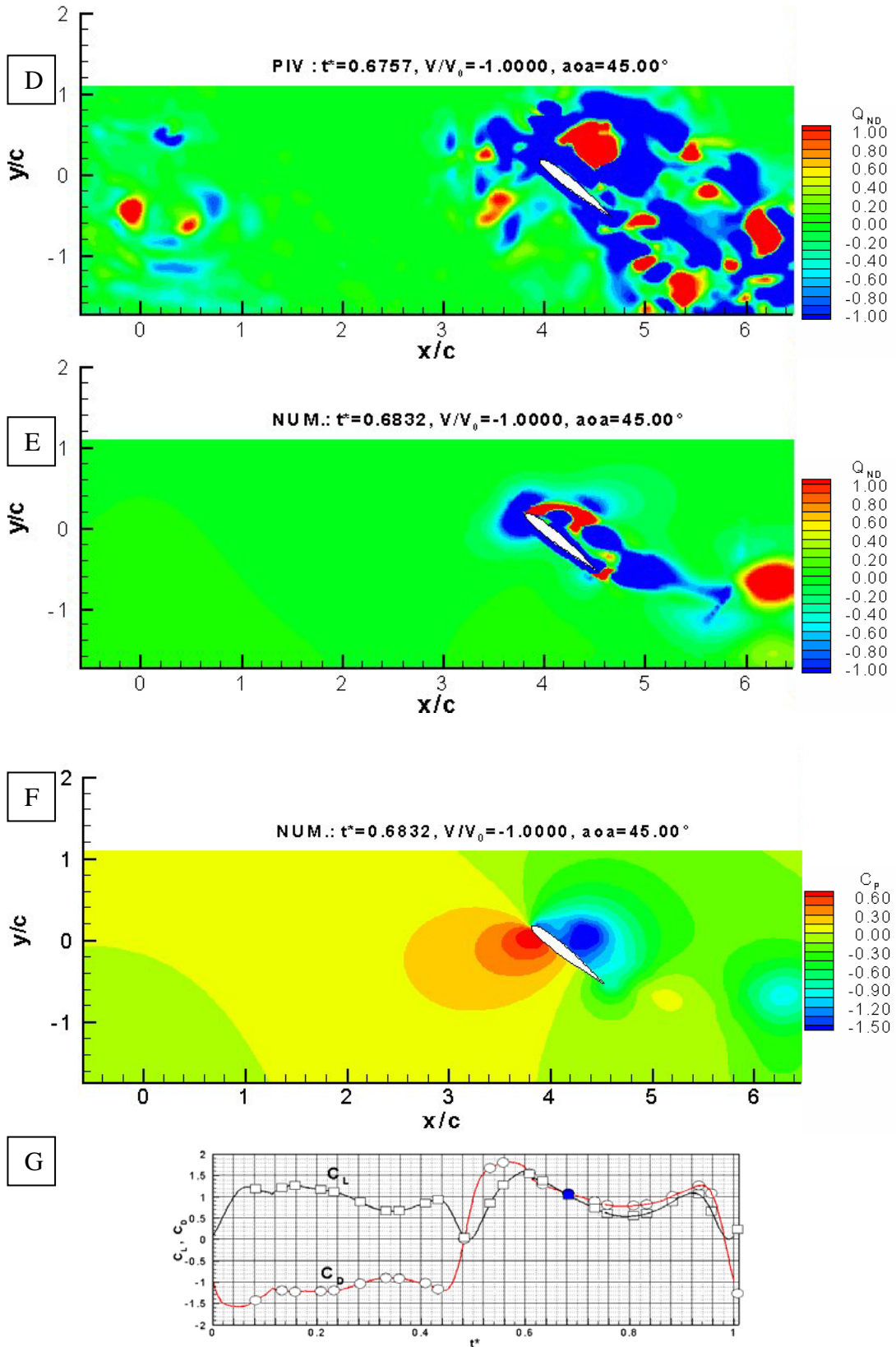


**Figure D.16 (continued)** Experimental visualization at  $t^*=0.68$ , comparison with the numerical solution and PIV measurements.

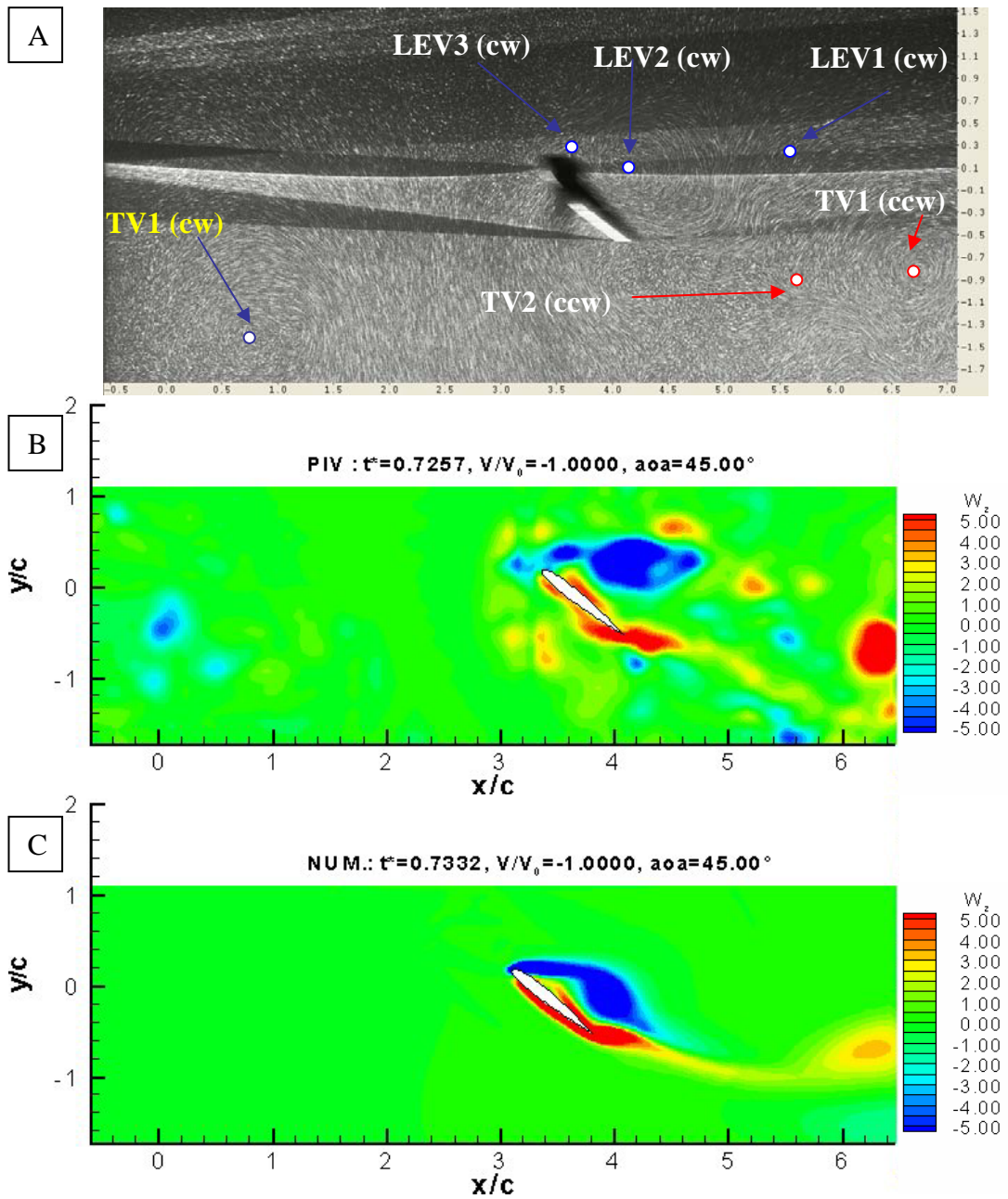


**Figure D.17** Experimental visualization at  $t^*=0.72$ , comparison with the numerical solution and PIV measurements.



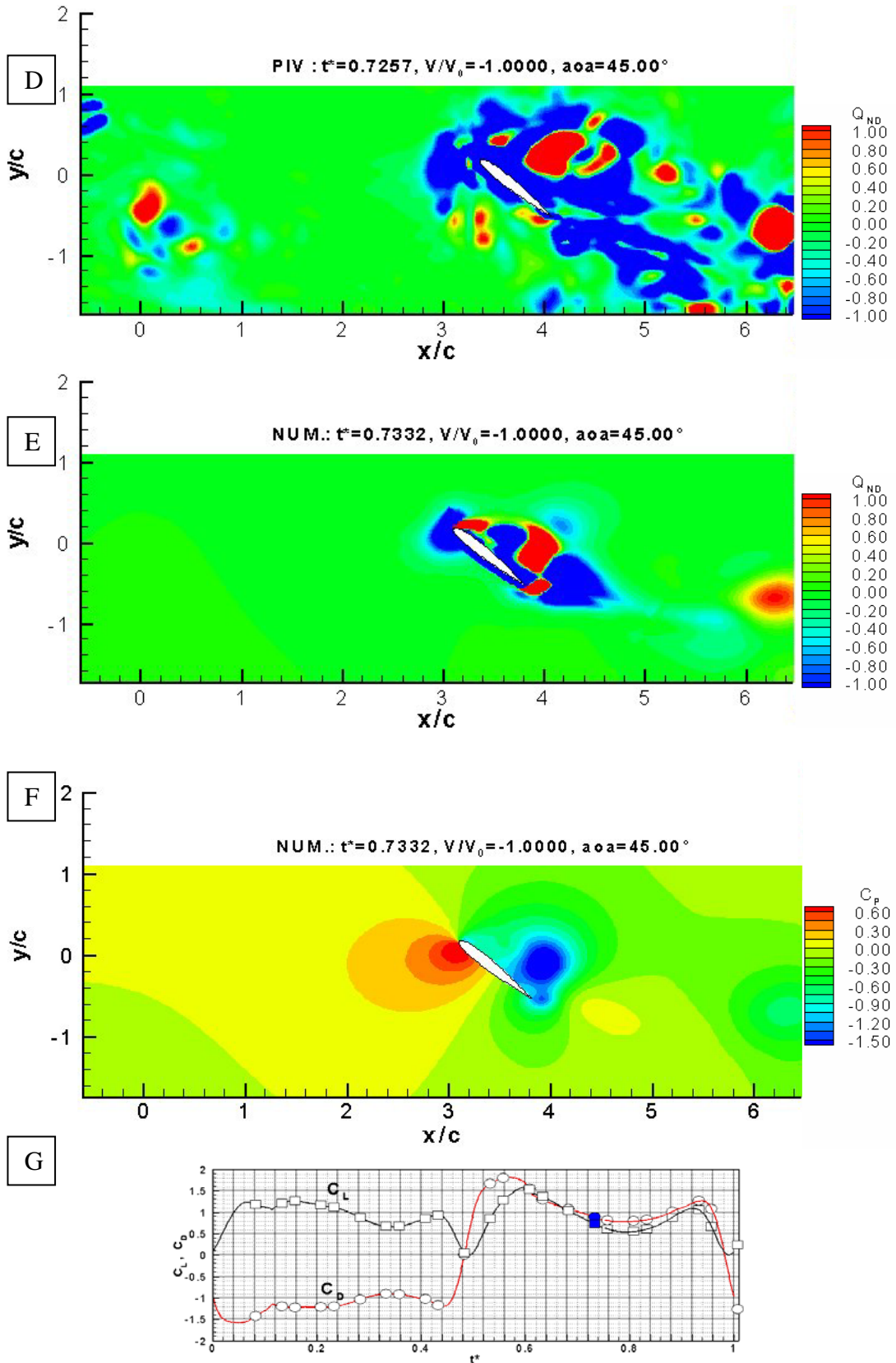


**Figure D.17 (continued)** Experimental visualization at  $t^* = 0.72$ , comparison with the numerical solution and PIV measurements.

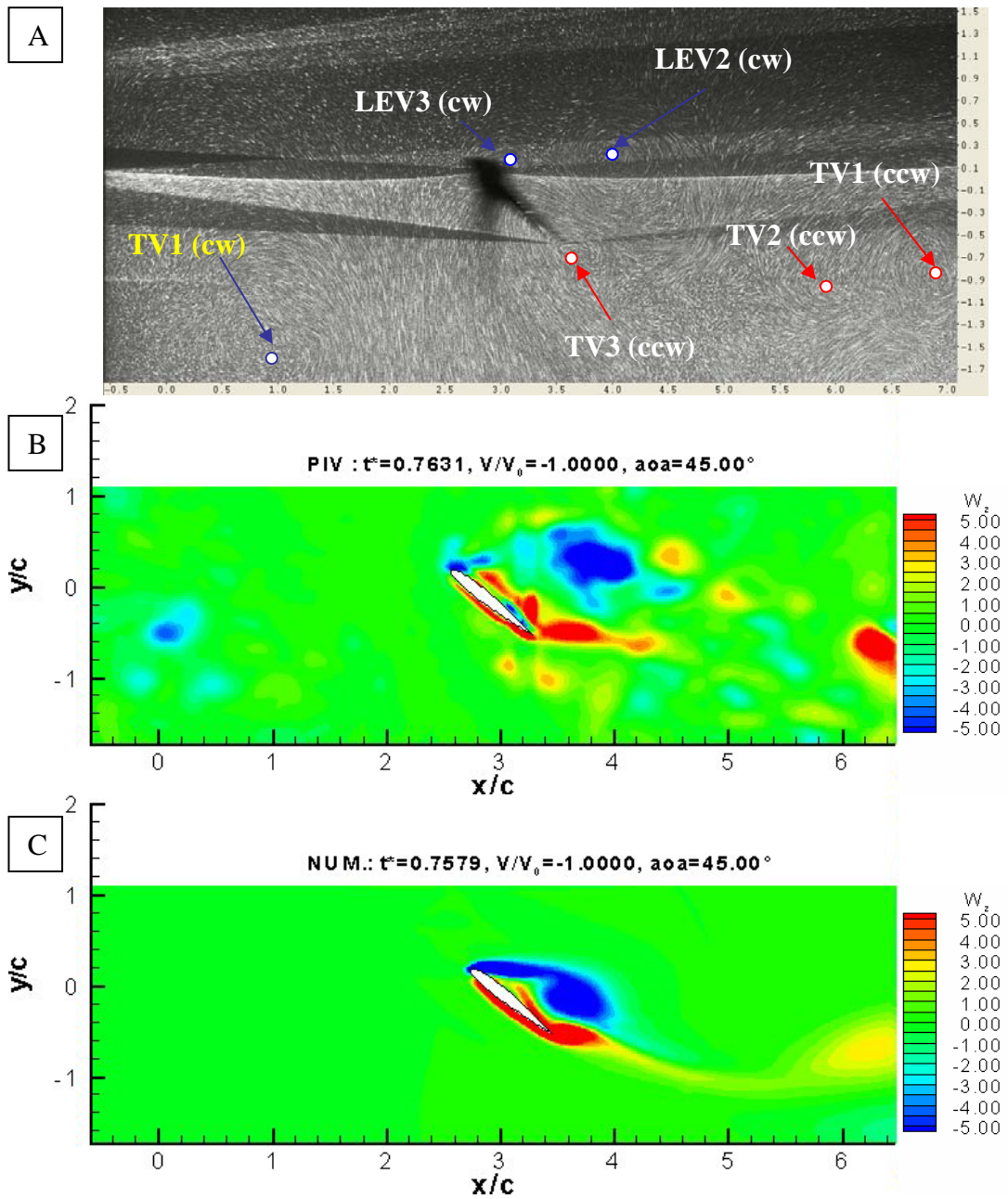


**Figure D.18** Experimental visualization at  $t^*=0.76$ , comparison with the numerical solution and PIV measurements.

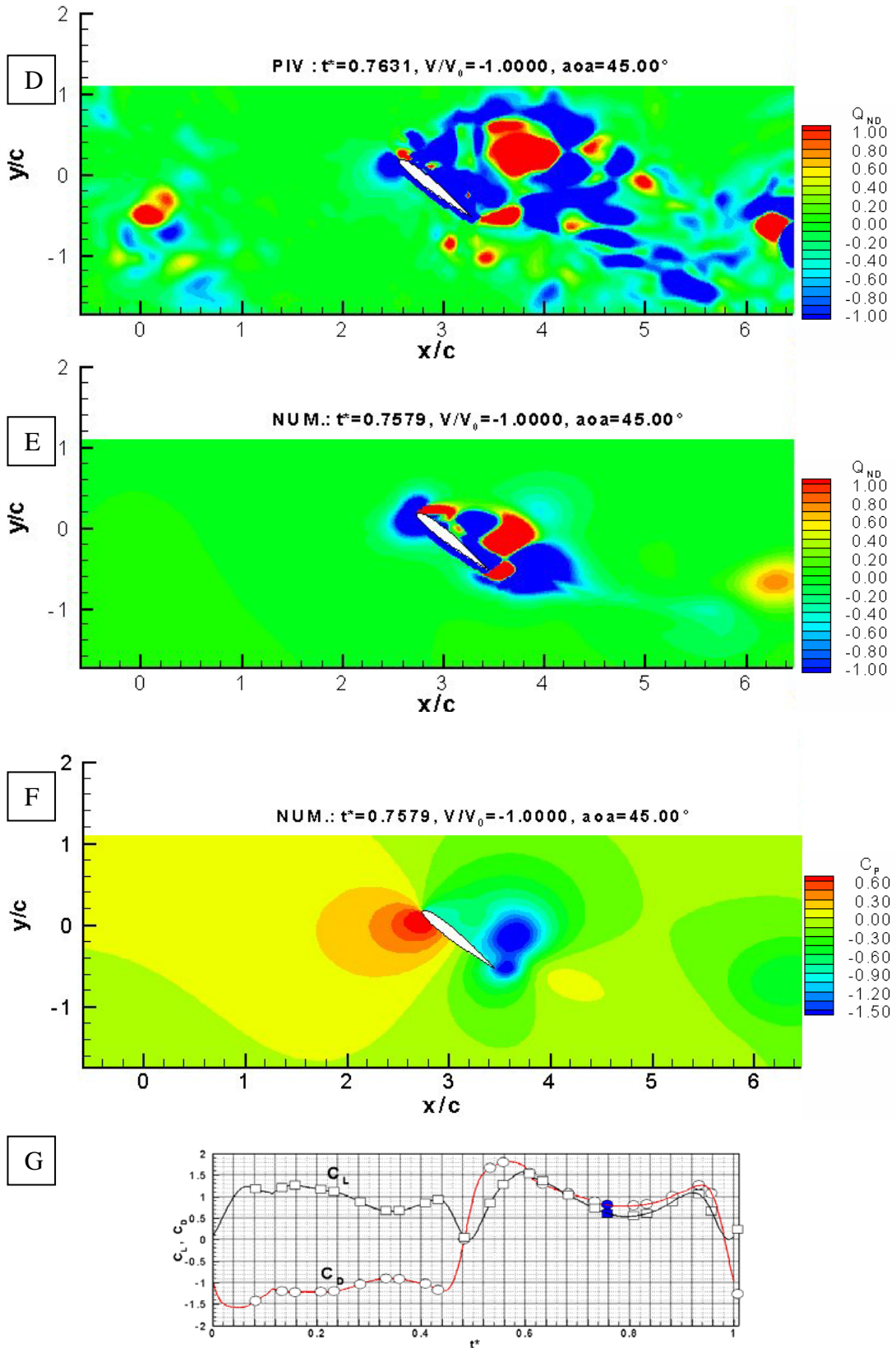


**Figure D.18 (continued)** Experimental visualization at  $t^* = 0.76$ , comparison with the numerical solution and PIV measurements.

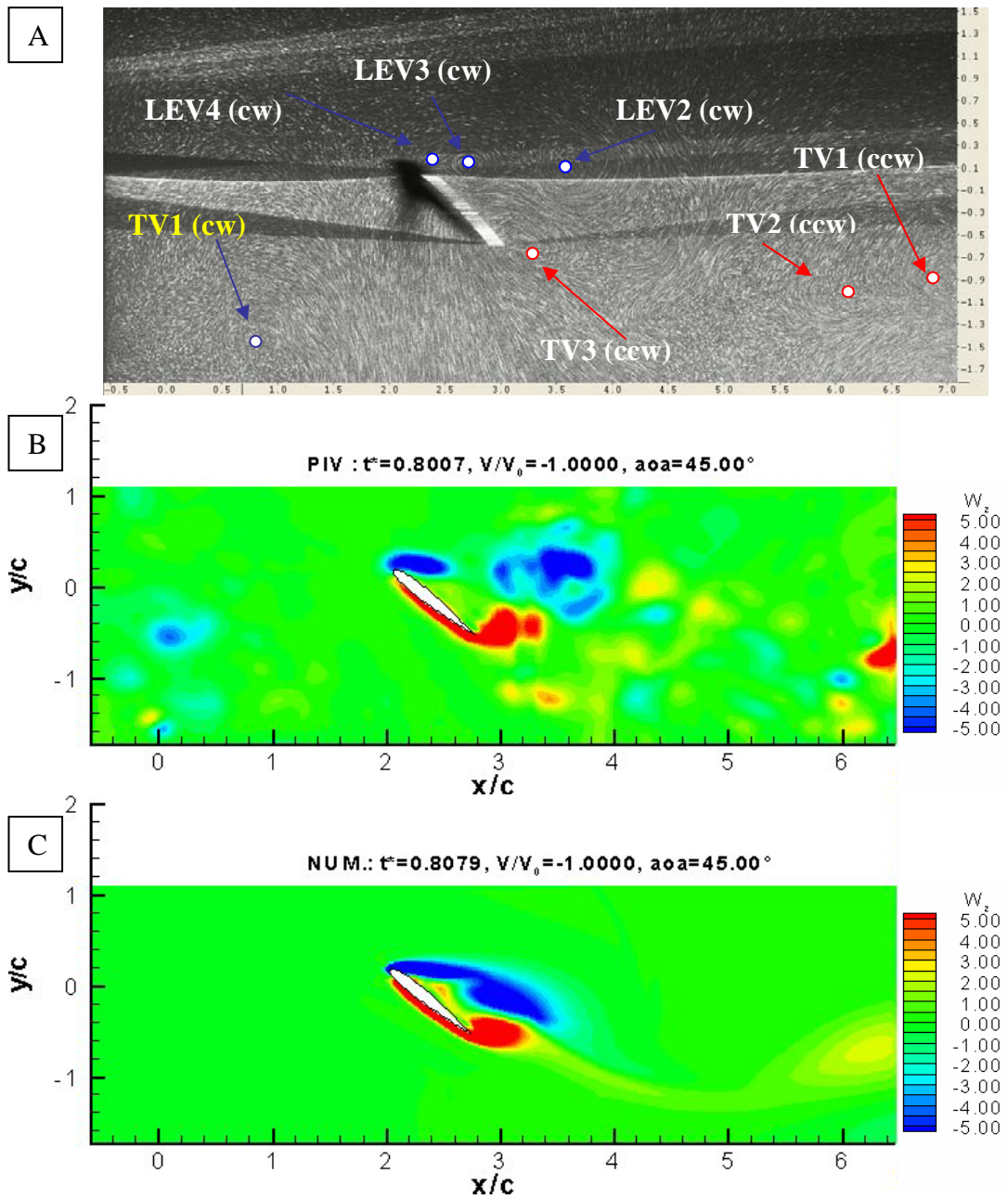


**Figure D.19** Experimental visualization at  $t^*=0.80$ , comparison with the numerical solution and PIV measurements.

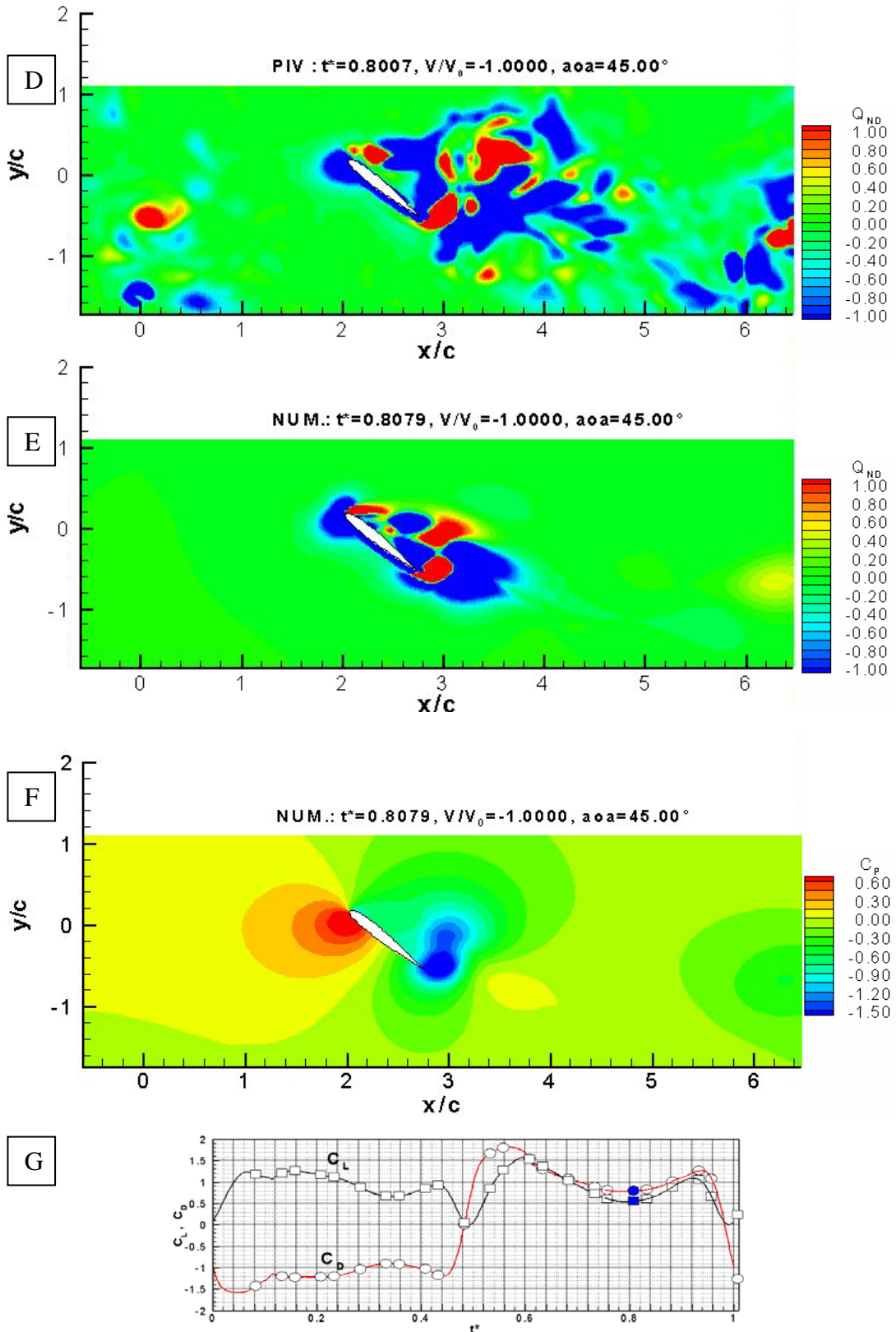


**Figure D.19 (continued)** Experimental visualization at  $t^*=0.80$ , comparison with the numerical solution and PIV measurements.

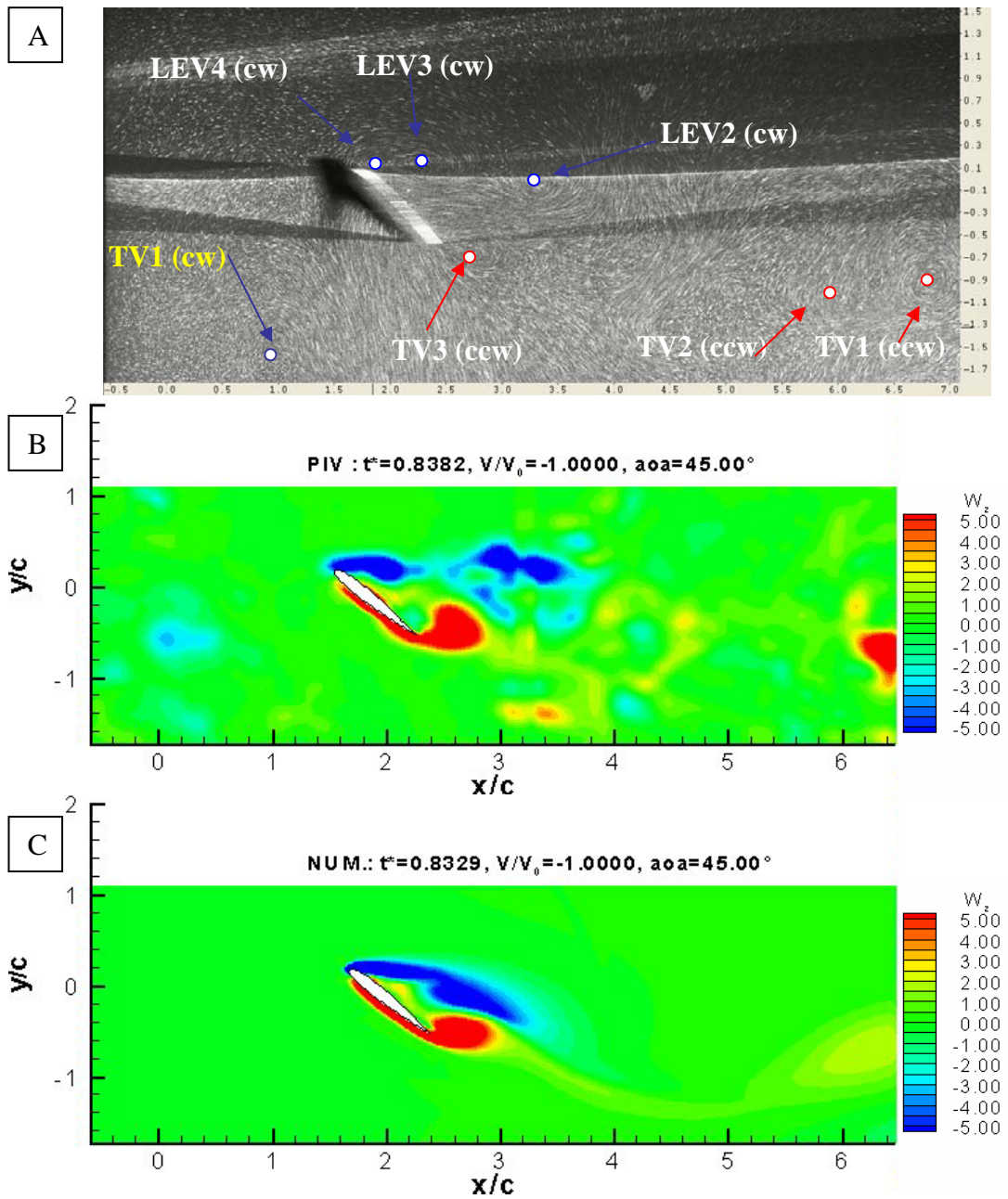


**Figure D.20** Experimental visualization at  $t^*=0.84$ , comparison with the numerical solution and PIV measurements.

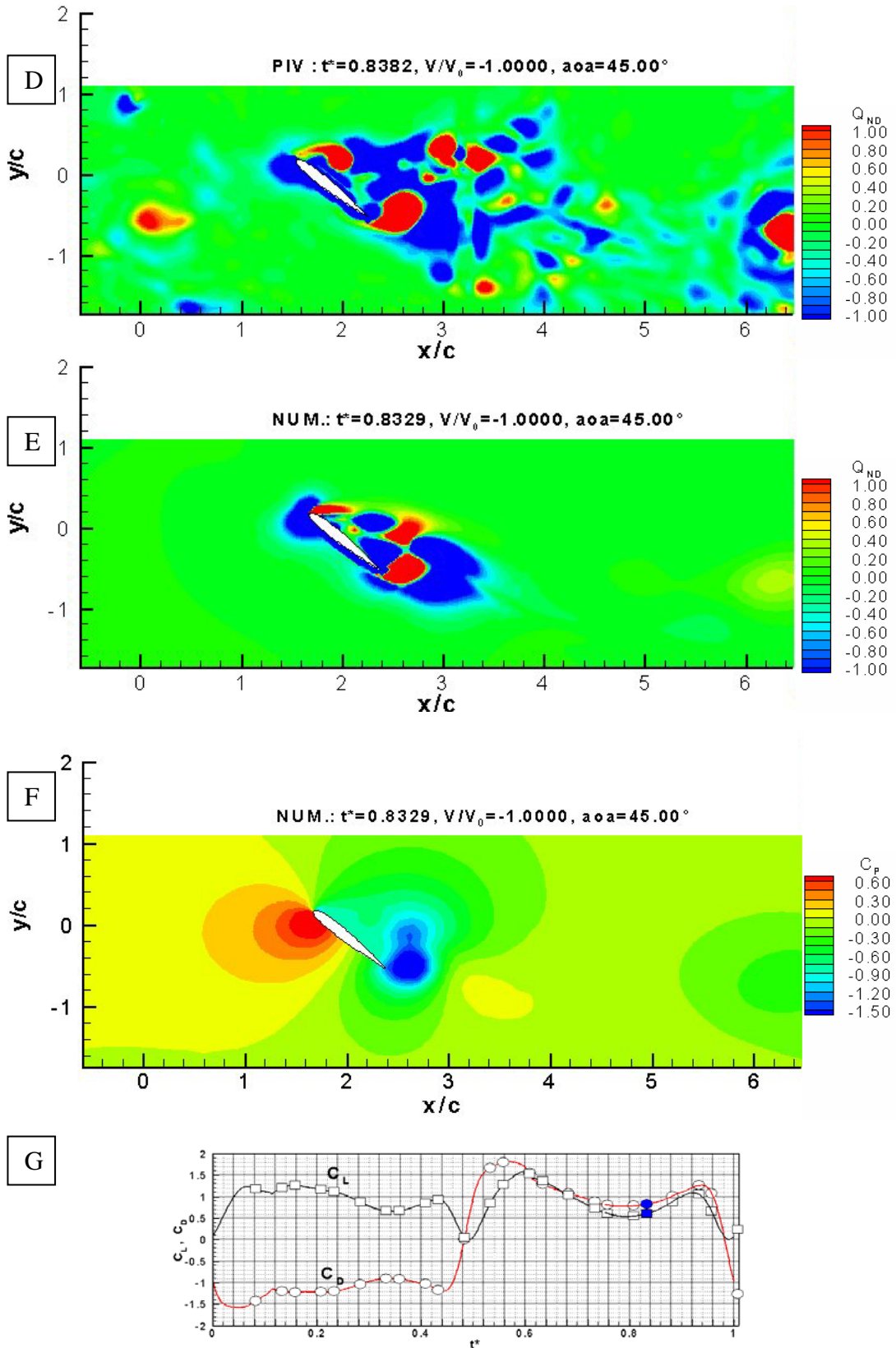


**Figure D.20 (continued)** Experimental visualization at  $t^* = 0.84$ , comparison with the numerical solution and PIV measurements.

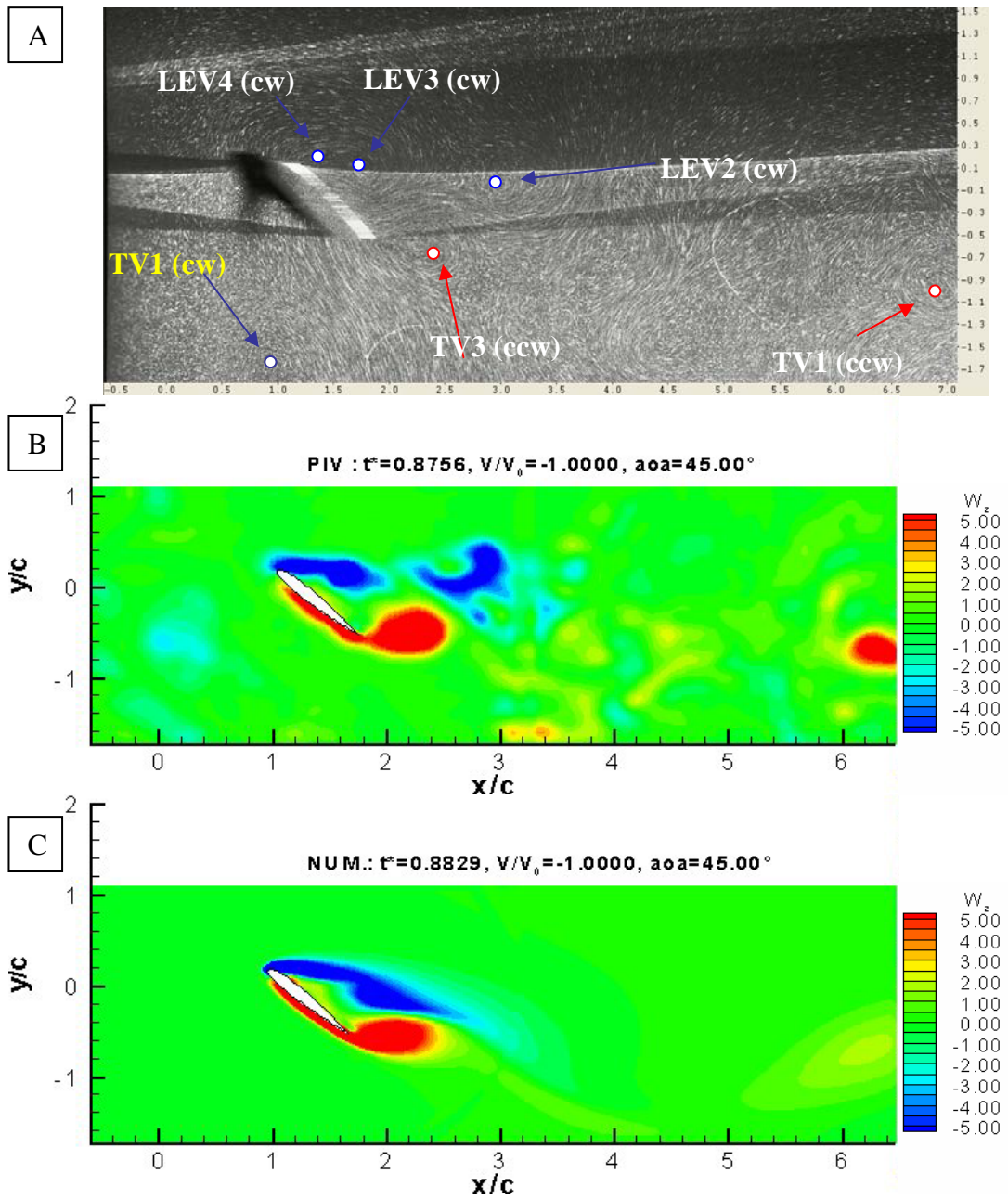


**Figure D.21** Experimental visualization at  $t^*=0.88$ , comparison with the numerical solution and PIV measurements.



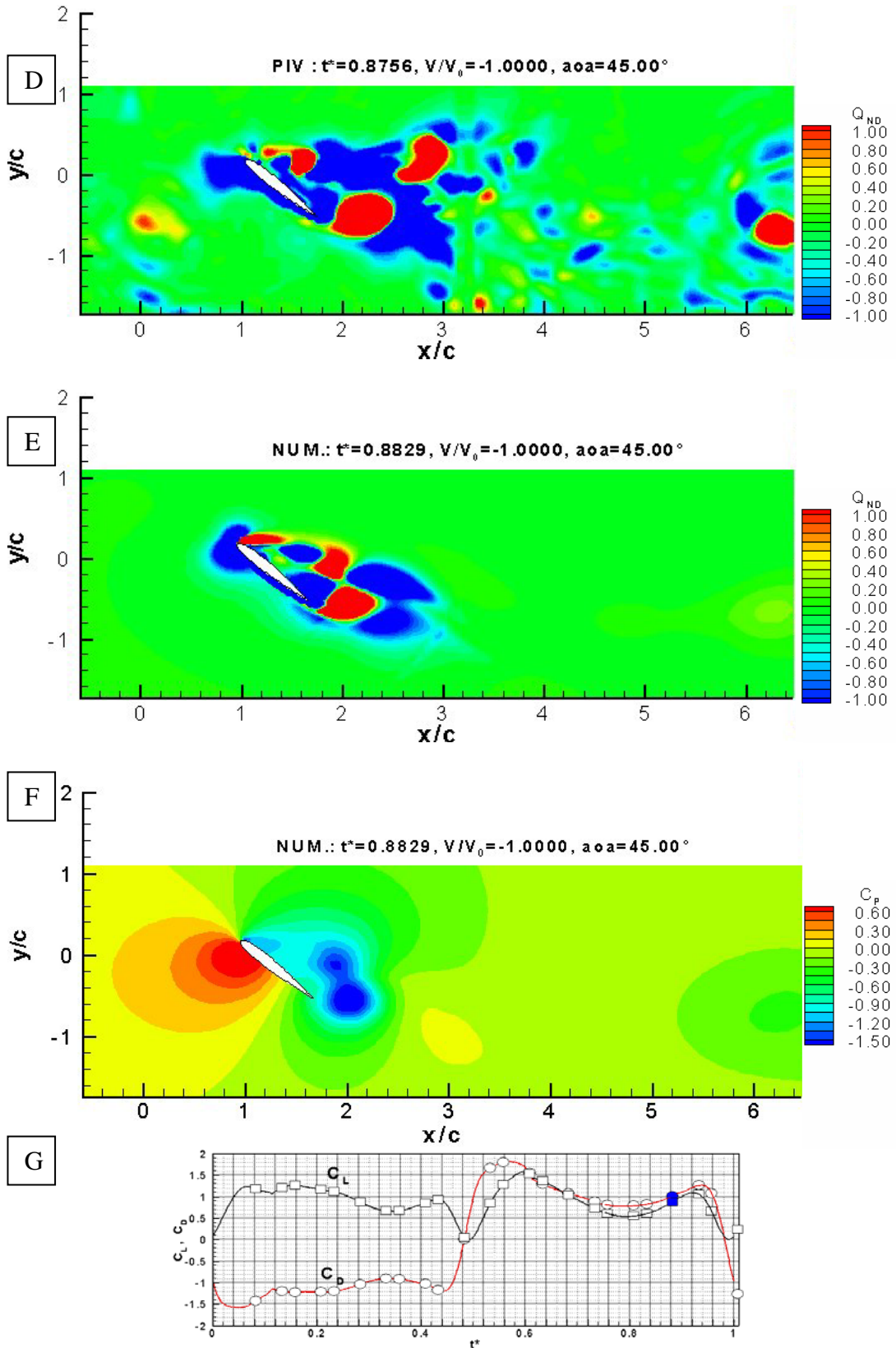


**Figure D.21 (continued)** Experimental visualization at  $t^*=0.88$ , comparison with the numerical solution and PIV measurements.

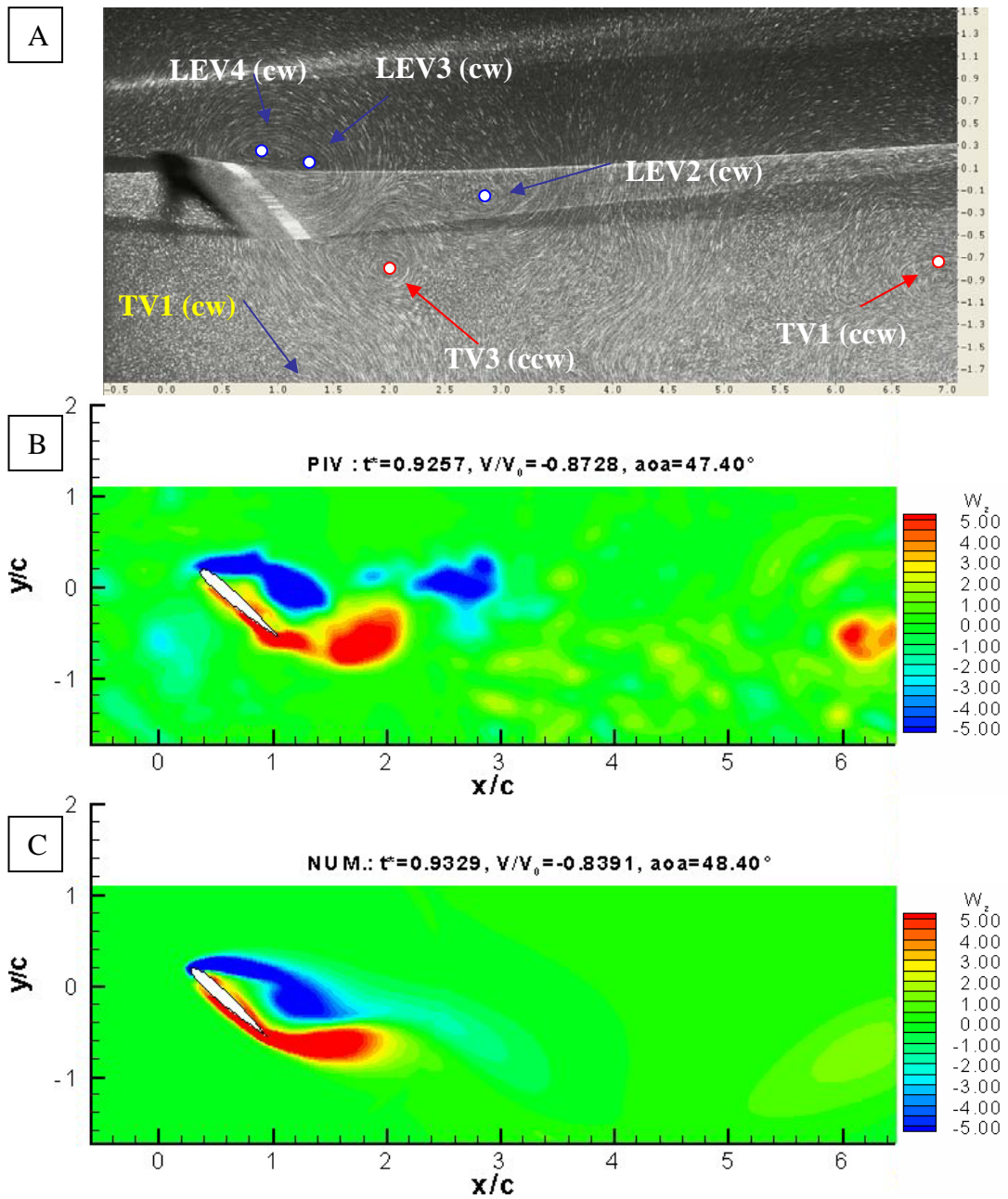


**Figure D.22** Experimental visualization at  $t^*=0.92$ , comparison with the numerical solution and PIV measurements.

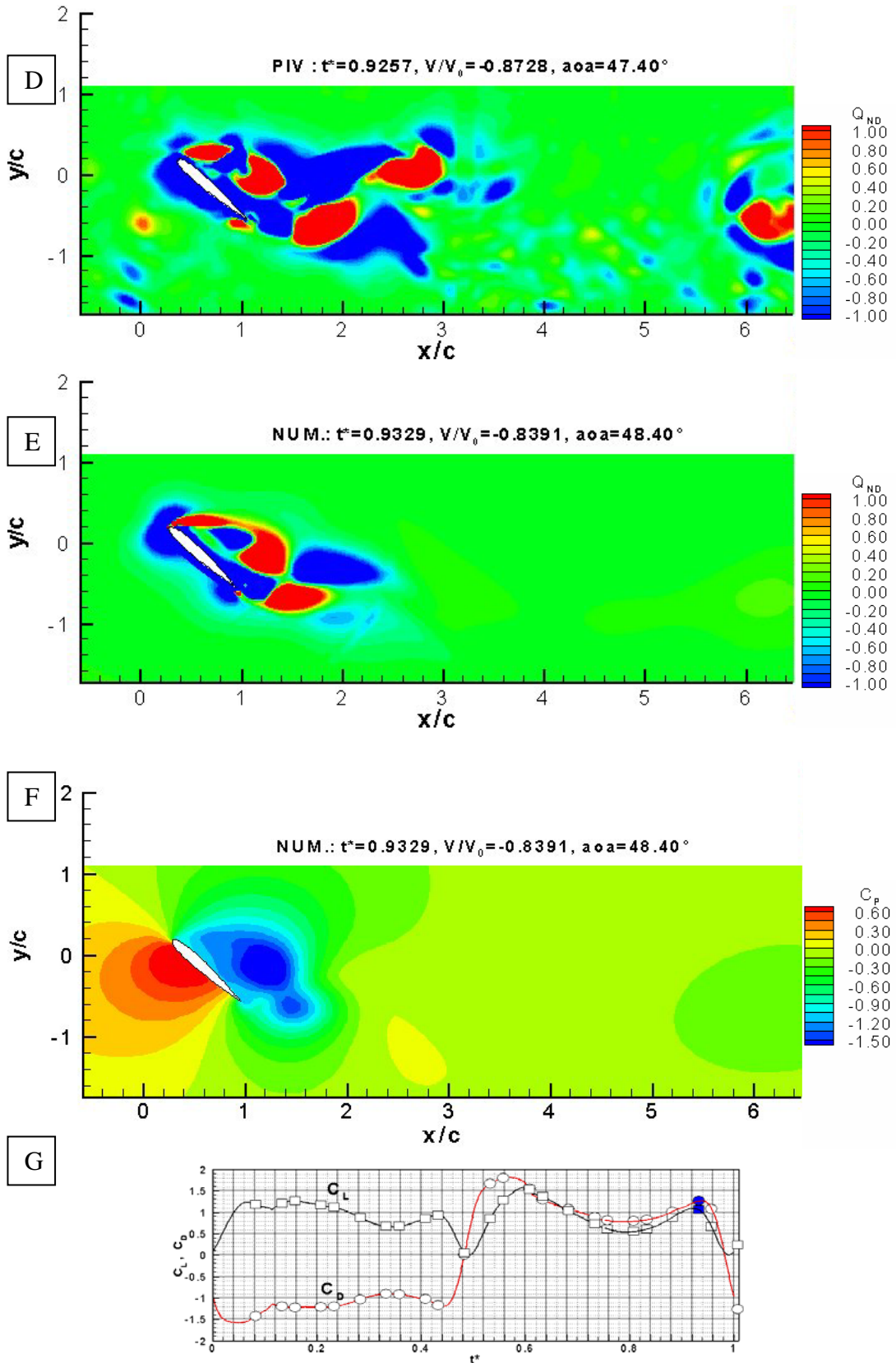
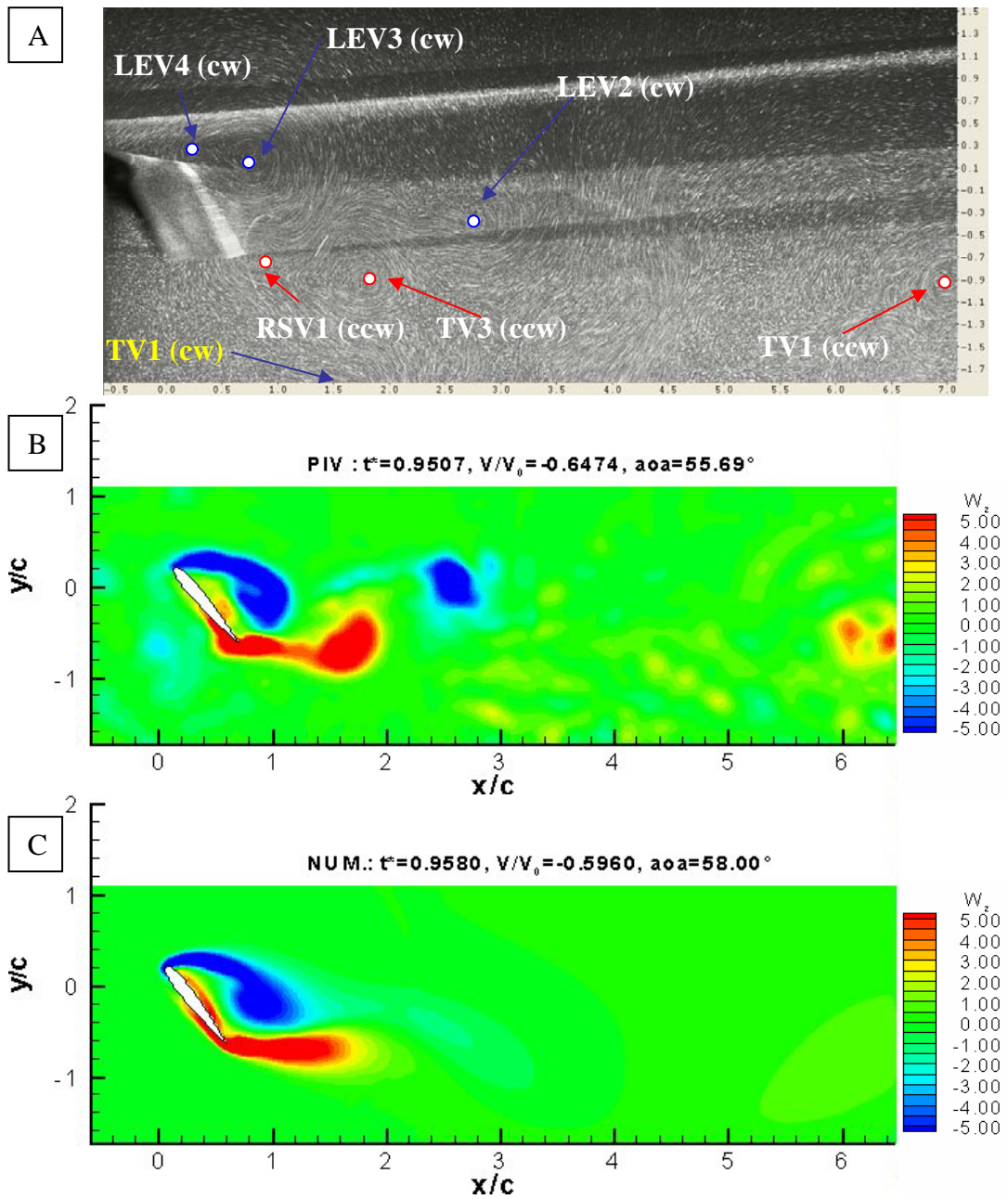
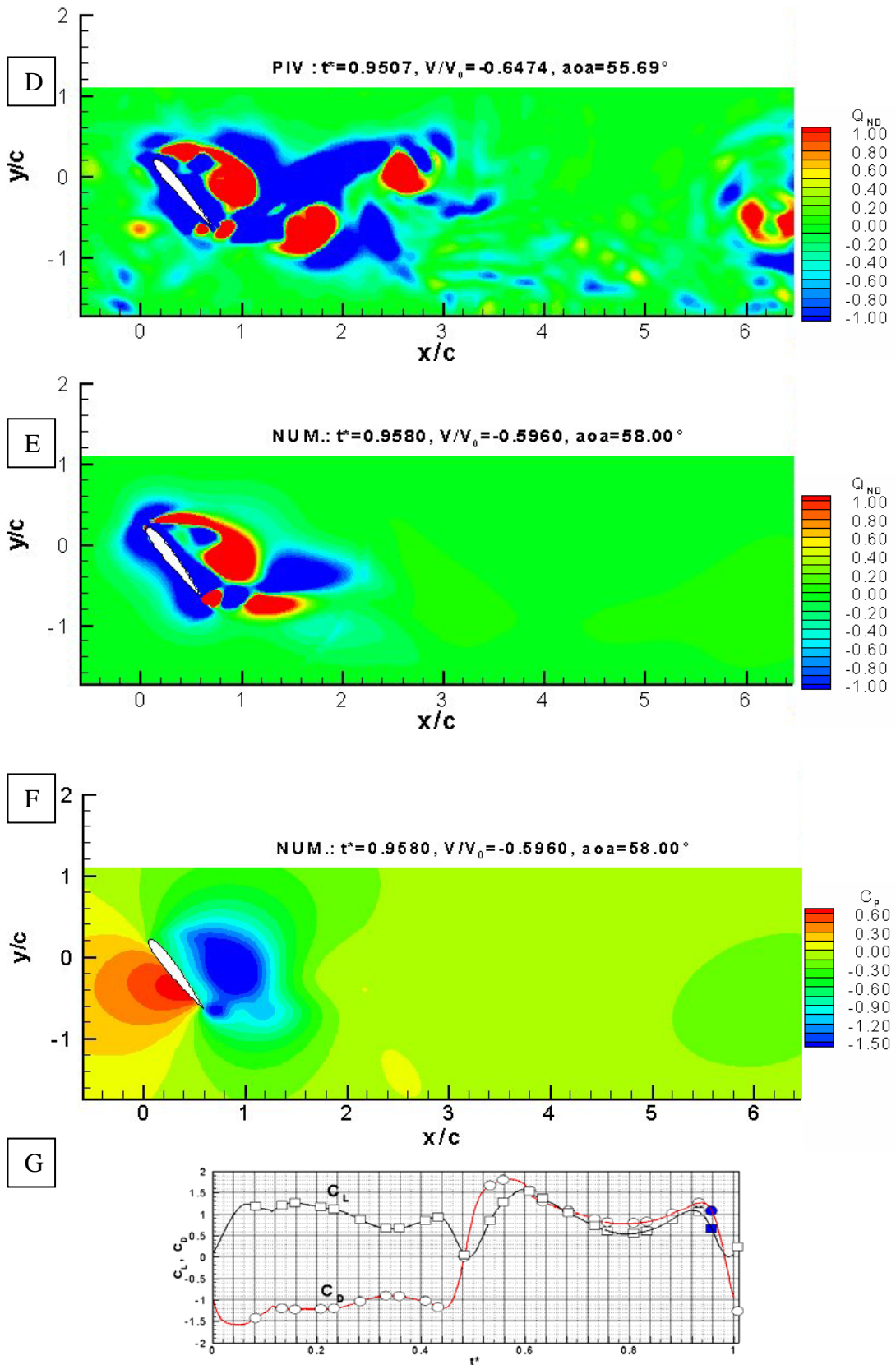


Figure D.22 (continued) Experimental visualization at  $t^* = 0.92$ , comparison with the numerical solution and PIV measurements.



**Figure D.23** Experimental visualization at  $t^*=0.96$ , comparison with the numerical solution and PIV measurements.



**Figure D.23 (continued)** Experimental visualization at  $t^*=0.96$ , comparison with the numerical solution and PIV measurements.

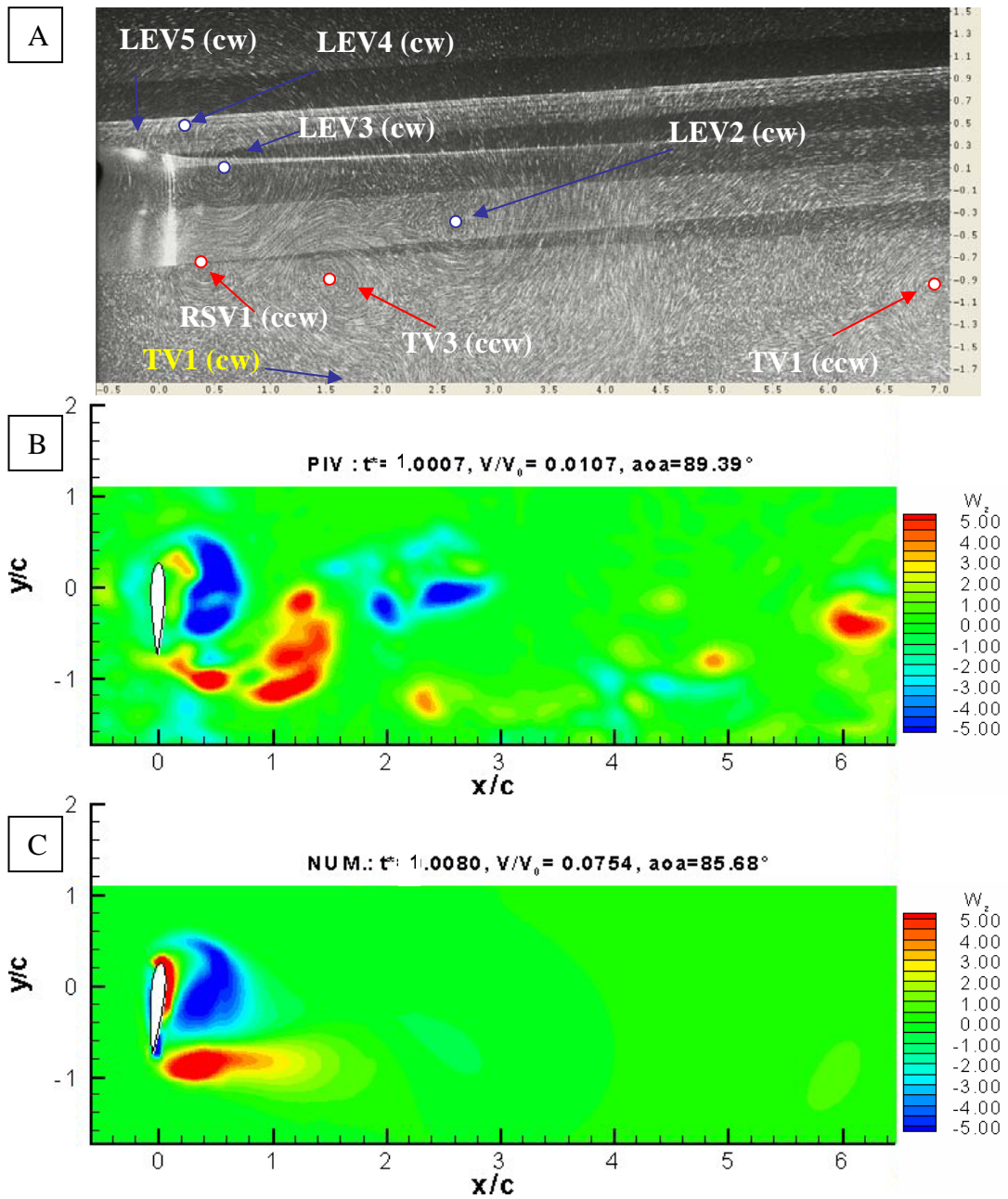


**Figure D.24** Experimental visualization at  $t^*=1.00$ , comparison with the numerical solution and PIV measurements.

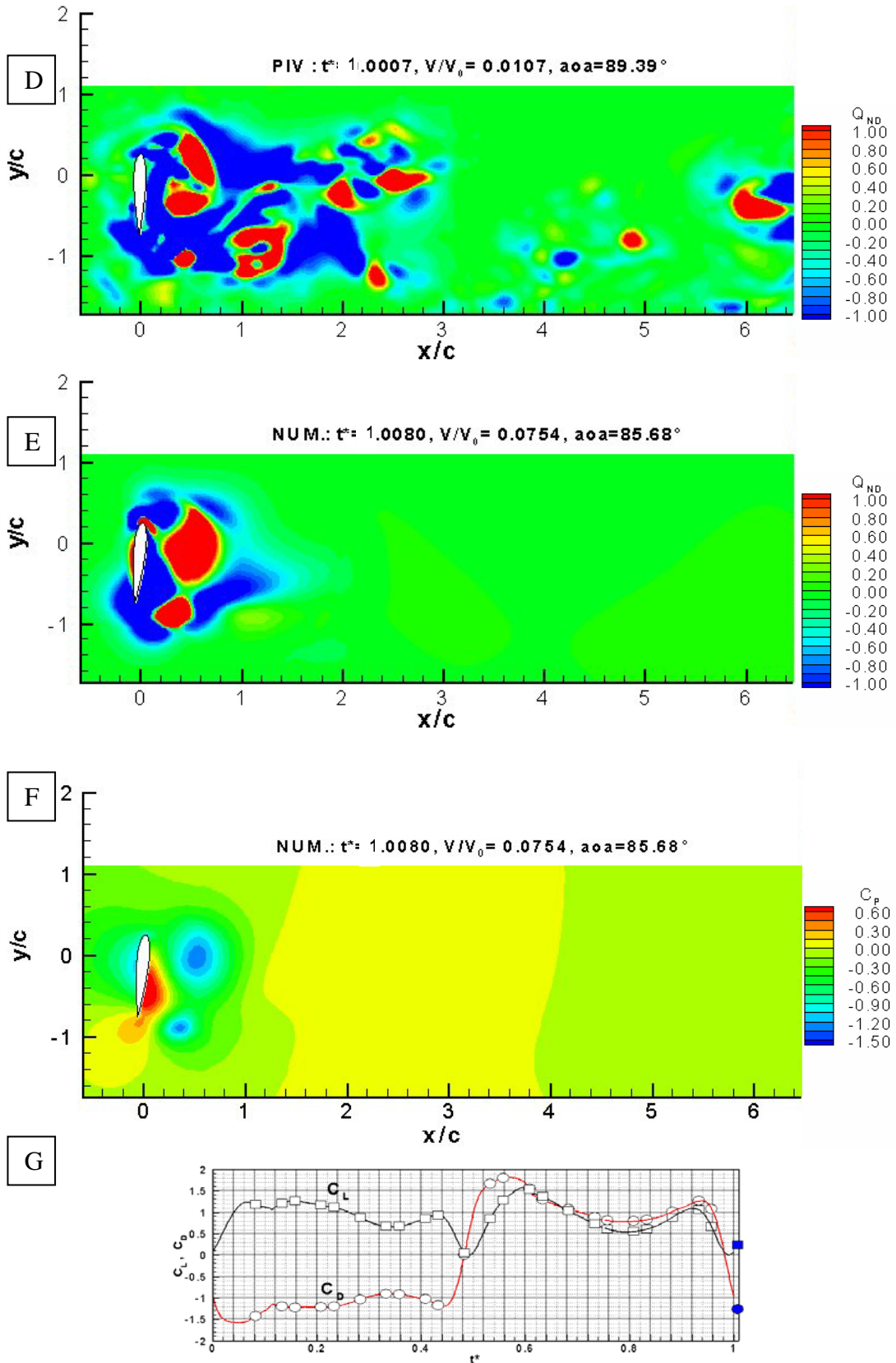


**Figure D.24 (continued)** Experimental visualization at  $t^*=1.00$ , comparison with the numerical solution and PIV measurements.

## VITA

Dilek Funda Kurtuluş was born in Ankara, in 1978. She received her BAC in 1995 from Lycée Tevfik Fikret d'Ankara, and graduated ranking first in her promotion. She graduated in June 2000 from Aerospace Engineering Department of Middle East Technical University, Ankara (CGPA:3.75/4.00) again ranking first in her promotion. She received her Master of Science degree from the same department in January 2002 (CGPA: 3.93/4.00). She is employed as a graduate research assistant in METU. She was awarded a Ph.D. scholarship from TUBITAK (Turkish National Scientific and Technical Council) and from the French Government for three years. As a consequence of this, she is now a joint Ph.D. student within the scope of a newly established Ph.D. program between ENSMA-Université de Poitiers (Poitiers, France) and METU (Ankara-Turkey). She is an Amelia Earhart Fellow of 2005 given by Zonta International (USA). She is awarded with “Course Performance Award 2005” by Gradual School of Natural and Applied Sciences of Middle East Technical University.